Doctoral Thesis

Surface Properties of Al_2O_3 for Understanding Metal-Support Interaction and Catalytic Properties of Al_2O_3-based Catalysts

Jaekyoung Lee

Department of Chemical Engineering

Graduate School of UNIST

2019

Surface Properties of Al_2O_3 for Understanding Metal-Support Interaction and Catalytic Properties of Al_2O_3-based Catalysts

Jaekyoung Lee

Department of Chemical Engineering

Graduate School of UNIST

Surface Properties of Al_2O_3 for Understanding Metal-Support Interaction and Catalytic Properties of Al_2O_3-based Catalysts

A thesis/dissertation
submitted to the Graduate School of UNIST
in partial fulfillment of the
requirements for the degree of
Doctor of Philosophy

Jaekyoung Lee

06/13/2019 of submission
Approved by

Advisor
Ja Hun Kwak

Surface Properties of Al_2O_3 for Understanding Metal-Support Interaction and Catalytic Properties of Al_2O_3-based Catalysts

Jaekyoung Lee

This certifies that the thesis/dissertation of Jaekyoung Lee is approved.

06/13/2019 of submission

signature

____

Advisor: Ja Hun Kwak

signature

____

Sang Hoon Joo: Thesis Committee Member #1

signature

____

Kwangjin An: Thesis Committee Member #2

signature

____

Hu Young Jeong: Thesis Committee Member #3

signature

____

Ji-Wook Jang: Thesis Committee Member #4;

Abstract

γ-Al_2O_3 is one of the most important heterogeneous catalytic materials that has been used as a support for a wide range of applications in petroleum chemistry and automobile emission control. Thanks to its intrinsic acidity, it can also participate in acid-catalyzed reactions such as alcohol dehydration. For decades, numerous studies have been devoted to understanding the fundamental nature of Al_2O_3 owing to its practical importance in catalysis. The catalytic properties of oxides, such as activity, selectivity, and distribution of active phases on the support, are significantly affected by their surface characteristics because chemical processes mainly occur on the surface. However, understanding the surface properties of aluminas have been challenging due to unresolved structures, mixed effects of various factors (morphology, phases, impurities, and additives), and difficulties of characterization. Therefore, comprehensive approaches should include the preparation of well-defined model aluminas and sensitive characterization tools. This thesis focuses on understanding the surface properties of aluminas and their role in the interaction with the active phases (Pt) and the corresponding catalytic behavior of Al_2O_3-based catalysts. By preparing the model aluminas for morphology, phase, additive and using ethanol TPD as a surface characterization tool, we studied the surface properties of Al_2O_3 with various modification and further investigated the interaction with Pt and its reduction behavior on alumina surfaces.

First, we synthesized a series of well-defined platelet γ-Al_2O_3 with the systematic change of (100) facets and investigated the catalytic role of (100) facets by ethanol dehydration. By controlling pH during the preparation of boehmite (γ-AlOOH), precursor for γ-Al_2O_3, (001) facet of boehmite increased under acidic condition. Topotactic transformation of boehmite into γ-Al_2O_3 maintained their morphologies, leading to platelet γ-Al_2O_3 with increased (100) facets of γ-Al_2O_3. Ethylene formation increased with increasing (100) facets, clearly demonstrating the critical role of (100) facets as active sites for ethanol dehydration on γ-Al_2O_3.

In chapter 3, We investigated the effect of morphology, phases, and additives on the surface properties of Al_2O_3 and which factors are the most important for surface properties of Al_2O_3 by preparing model aluminas with various modifications and using ethanol TPD. Ethanol TPD showed the desorption temperature (at a maximum rate of ethylene desorption, T_d) of dissociative ethanol was significantly dependent on morphology, crystalline phase, and additives. Here, the additives affected the desorption temperature of ethylene most significantly. Ethanol dehydration tests showed that ethylene formation rates, normalized with respect to the amount of dissociative ethanol (quantified by ethanol TPD), exhibited an inverse correlation with T_d on Al_2O_3 with various morphologies, crystalline phases, and additives, which suggests that T_d can be used as a descriptor for surface properties of Al_2O_3, irrespective of modification origins. The activities and activation barriers of various commercial Al_2O_3 on ethanol dehydration were also consistent with our empirical model.

Based on understanding for surface properties of Al_2O_3, we study how these surface properties of aluminas affect the active phases (Pt) and the catalytic behavior of Pt/Al_2O_3. We chose two sets of model alumina having different number of sites with the identical properties and different properties of sites with the same number based on ethanol TPD. With two model aluminas, how the number and properties of specific sites on alumina surfaces affect the specific interaction between Pt and alumina was investigated. Pt showed higher dispersion with increasing number of sites and interaction strength because the Pt atoms can interact with specific sites on alumina in greater numbers and more strongly. However, these Pt dispersion changes do not represent the gradual size change, but the relative population change of small (< 3 nm) and large agglomerated Pt clusters (>10 nm). The number of highly dispersed Pt clusters increased with increasing number of sites and interaction strength. When Pt showed higher dispersion from more number of sites and stronger interaction on alumina, Pt/Al_2O_3 showed higher activity for benzene hydrogenation due to more available highly dispersed Pt.

Finally, specific interaction between Pt and alumina strongly affected the reduction behavior of oxidized Pt on alumina. We studied the reduction of three-dimensional (3D) PtO_2, two-dimensional (2D) PtO_2, and atomically dispersed Pt on Pt/Al_2O_3. Under oxidizing atmosphere, morphologies and sizes of PtO_2 on Pt/Al_2O_3 are determined by the specific interaction between Pt and Al_2O_3 through Pt-O-Al bond, leading to highly dispersed Pt as ~1 nm 2D-raft PtO_2 and atomically dispersed Pt on Al_2O_3. When all the Pt atoms can't interact with anchoring sites on support under high Pt loading or SiO_2 which has very weak metal-support interaction, 3D PtO_2 was formed. Due to weak interaction with support, 3D PtO_2 was reduced earlier (-20~-60 ^oC) than 2D PtO_2 (~110 ^oC) and atomically dispersed Pt (>300 ^oC). Furthermore, when Pt/Al_2O_3 was calcined at 500-700 ^oC, PtO_2 was reduced without a reducing agent (auto-reduction) with Pt sintering. Interaction strength also influences auto-reduction when calcination temperature increases. 3D PtO_2 was auto-reduced after 550-600 ^oC calcination, but 2D PtO_2 was more difficult to be reduced (50 ^oC higher). So, the interaction strength with the support determines how long Pt oxide can maintain as Pt oxide rather Pt metal. These morphologies of Pt oxide also affect their sintering behavior. Because 3D PtO_2 is more easily auto-reduced than 2D PtO_2 and atomically dispersed Pt, 3D metallic Pt clusters become less mobile than 2D PtO_2 and atomically dispersed Pt (still, oxidized Pt). So, 3D PtO_2 showed more sinter-resistant behavior than 2D PtO_2 and atomically dispersed Pt. The metal-support interaction between Pt and alumina is important for the reduction of oxidized Pt on Pt/Al_2O_3, suggesting the guideline about a careful activation for the efficient utilization of metallic Pt for catalytic reactions.

Contents

1 Introduction

---

2 Critical role of (100) Facets on γ-Al_2O_3 for Ethanol Dehydration: Combined Efforts of Morphology-Controlled Synthesis and TEM Study

---

3 Acid-base properties of Al_2O_3: effects of morphology, crystalline phase, and additives

---

4 Effect of number and properties of specific sites on alumina surfaces for Pt-Al_2O_3 catalysts

---

5 Reduction behavior of Pt on alumina: effect of Pt loading and calcination

temperature

List of Tables

List of Figures

List of Abbreviations

2D	Two dimensional
3D	Three dimensional
Al_{IV}	Tetrahedral Al sites
Al_{V}	Pentahedral Al sites
Al_{VI}	Octahedral Al sites
BET	Brunauer Emmett Teller
BF-TEM	Bright filed-Transmission electron microscopy
DFT	Density Functional theory
DRIFTS	Diffuse reflectance infrared spectroscopy
E_s	Intrinsic activation barrier
E_{app}	Apparent activation barrier
FCC	Face-centered cubic
FID	Flame ionization detector
FT-IR	Fourier transform infrared
HAADF-STEM	High-angle annular dark-field scanning transmission electron microscopy
HCP	Hexagonal close-packed
HR-TEM	High-resolution transmission electron microscopy
IR	Infrared
MAS-NMR	Magic angle spinning nuclear magnetic resonance
NMR	Nuclear magnetic resonance
RT	Room temperature
SAED	Selected area electron diffraction
STEM	Scanning transmission electron microscopy
T_d	Maximum desorption temperature of dissociative ethanol
TEM	Transmission electron microscopy
TOF	Turnover frequency
TPD	Temperature programmed desorption
TPR	Temperature programmed reduction
XANES	X-ray absorption near edge structure
XRD	X-ray diffraction
ΔH	Heat of adsorption

1. Introduction

1.1. Alumina

1.1.1. Introduction to Alumina

Alumina, which is the common name of aluminum oxides, refers to four types of solid materials consisting of aluminum and oxygen.[1-4]

1) Aluminum trihydroxide ($Al(OH)_3$): gibbsite (γ-$Al(OH)_3$), bayerite (α-$Al(OH)_3$).

2) Aluminum oxyhydroxide (AlOOH): boehmite (γ-AlOOH), diaspore (α-AlOOH).

3) Transition alumina : η-Al_2O_3, γ-Al_2O_3, δ-Al_2O_3, θ-Al_2O_3, χ-Al_2O_3, κ-Al_2O_3.

4) Alpha alumina (or corundum): α-Al_2O_3

These various phases of alumina are interrelated because each phase can phase-transform into other phases depending on thermal-treatment. Detailed scheme for the phase transformation among various alumina polymorph is shown in **Figure 1.1**.[1, 3-4]

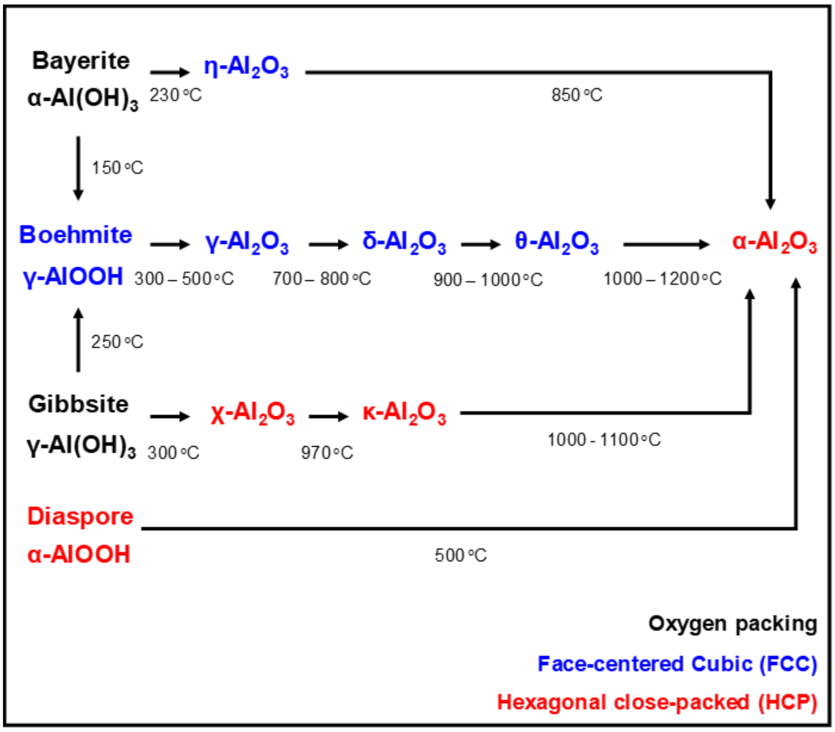

Figure 1.1. Phase transformation of various alumina polymorphs.

The initial precursors ($Al(OH)_3$ and AlOOH) evolves into different transition aluminas and finally become α-Al_2O_3, which is the most thermodynamically stable. α-Al_2O_3 consists of only octahedral aluminum and hexagonal close-packed (HCP) oxygen. Especially, the phase-transformation is known to be topotactic, which means the morphologies of initial precursors are maintained[3-6]. During the phase evolution of boehmite (γ-AlOOH) into θ-Al_2O_3 (γ-AlOOH→γ-Al_2O_3→δ-Al_2O_3→θ-Al_2O_3), oxygen lattice is maintained as face-centered cubic (ABCABC packing) and only Al^{3+} cations are redistributed.[1, 3-4] In order for oxygen anion to become hexagonal close-packed (ABAB), high temperature (1000-1100 °C) calcination is needed for θ-Al_2O_3 to become α-Al_2O_3.[1, 3-4] However, χ-Al_2O_3 and κ-Al_2O_3, whose oxygen packing is the same with α-Al_2O_3 as HCP, need also high temperature because structure and textural properties also affect the phase-transformation process.[3] Only diaspore (α-AlOOH) can phase-transform directly into α-Al_2O_3 at low temperature (500 °C).

1.1.2. Application as catalyst

The aluminas mostly used in the catalyst field are transition aluminas, which are derived from thermal decomposition of $Al(OH)_3$ or AlOOH. They have strong acid-base properties, high surface area, relatively low-cost, high thermal stability, and high mechanical strength.[1, 3] Thanks to their good properties, they are used in catalysts with three ways.

1) Support – to disperse the active phase and to adjust the acid-base properties of the catalysts.
2) Active component by using the acid-base properties of aluminas.
3) Binder – thanks to good mechanical and textural properties, they are added for catalyst formulation as beads, granules, and extrudes.

Mainly as support or the active component itself, aluminas are used in various chemical processes, which are shown in **Table 1.1**. Their intrinsic Lewis acid-base properties enable alumina to catalyze alcohol dehydration, one of typical acid-catalyzed reaction to produce olefin and ether.[7] Also, aluminas are used in the refinery to increase octane number by double bond isomerization and skeletal isomerization thanks to Lewis acid sites.[8] Finally, these Lewis acid sites act as anchoring sites for the active phases such as transition metal or metal oxide.[9-14] In addition, harsh reaction or regeneration condition (high temperature, pressure, and high moisture atmosphere) needs good thermal stability for the catalyst's long-term stability. δ, θ-Al_2O_3 are also utilized in automobile combustion control because they are more thermally stable and also have sufficient ability to disperse the transition metal (Pt, Pd).[15-16] However, strong Lewis acidity is not always needed when the reactants or products are too reactive, leading to side-reaction. In this case, θ-Al_2O_3 and α-Al_2O_3 are used because their weak acidities hinder the side reaction such as coke formation (propane dehydrogenation),[17] polymerizations (1,3-butadiene hydrogenation)[18] and decomposition of products (ethylene epoxidation).[19] Like this, which phases of aluminas are used critically depend on the kind of catalytic reactions and required functionalities for catalysts, which requires the fundamental understanding of the physicochemical properties of aluminas. In this thesis, I focus on γ-Al_2O_3 and related transition Al_2O_3 (δ-Al_2O_3, θ-Al_2O_3, α-Al_2O_3) because they are mostly used aluminas.

Table 1.1. Utilization of transition Al_2O_3 for various catalytic reactions.

Reaction	Catalyst	Key features of Al_2O_3	References
Claus process (S production)	κ,χ-Al_2O_3	Lewis acid-basicity	20
Alcohol dehydration	γ-Al_2O_3	Lewis acid-basicity	7
Isomerization	Pt/γ,η-Al_2O_3	Lewis acid-basicity	8
Reforming	PtRe/γ-Al_2O_3	Lewis acid-basicity, thermal stability	21
Hydrotreating	CoMo,NiMo/γ-Al_2O_3	Dispersion	22
Automobile combustion control	Pt,Pd/γ,δ,θ-Al_2O_3	Dispersion, thermal stability	16
Propane dehydrogenation	PtSn/θ-Al_2O_3	Dispersion, thermal stability, weak acidity - no side reaction	17
1,3-butadiene hydrogenation	Pd/α-Al_2O_3	Weak acidity - no side reaction	18
Ethylene epoxidation	Ag/α-Al_2O_3	Weak acidity - no side reaction	19

1.2. Structures and Characterization of γ-Al_2O_3

1.2.1. Bulk structures of γ-Al_2O_3

The bulk structures of γ-Al_2O_3 have been on the debate as spinel-based or non-spinel-based structure. Many studies studied the structure of γ-Al_2O_3 by X-ray diffraction,[23-24] neutron diffraction,[23, 25] transmission electron microscopy,[26-28] and simulation.[5, 29-30] Traditionally, γ-Al_2O_3 has been described as cubic defective spinel.[28] The ideal cubic spinel has AB_2O_4 stoichiometry (space group $Fd\bar{3}m$) where A^{2+} cation occupies tetrahedral (T_d) sites and B^{3+} cation does octahedral (O_h) sites with cubic close-packed oxygen anion. In Wyckoff positions, tetrahedral sites are T_d (8a) and octahedral sites are O_h (16d). In the case of the inverse spinel structure, A^{2+} cation occupies the half of octahedral (O_h) sites and B^{3+} cation does tetrahedral (T_d) sites and the remained half of the octahedral (O_h) sites.[1] As γ-Al_2O_3 has only Al^{3+} cation sites, cation vacancies are intrinsically needed with respect to the stoichiometry of spinel (compare Al_8O_{12} with $A_3B_6O_{12}$ spinel). The position of Al cation vacancies has been controversial as octahedral sites,[31] tetrahedral sites,[32] or both sites.[26, 33] Depending on the position of cation vacancies, the relative ratio of tetrahedral Al sites (Al_{IV}) to octahedral Al sites (Al_{VI}) varies from 25-37.5% theoretically,[1] which was also consistent with experimental results from ^{27}Al-NMR.[9, 34-36] However, non-spinel structures have been also reported for the bulk structure of γ-Al_2O_3.[5, 29-30, 34, 37-38] Rietveld analysis and simulation studies report that there exist non-spinel sites: other tetrahedral sites (8b and 48f) and octahedral sites (16c).[30, 38] Paglia et al. interpret these data as tetragonal bulk structure (space group $I4_1/amd$) for γ-Al_2O_3.[24, 39] Especially, Digne et al.[5, 37] and Krokidis et al.[29] proposed non-spinel structure (space group $P2_1/m$) from simulation results over the phase transformation from boehmite into γ-Al_2O_3. Among various structure models, non-spinel structure model by Digne et al. and Krokidis et al. has been the most popular one in the research field related to alumina. Still, the exact elucidation over the structure of γ-Al_2O_3 is the on-going challenge.

Continued controversy over the structure of γ-Al_2O_3 arises from the inherent complexity of γ-Al_2O_3. γ-Al_2O_3 has very small domain sizes around ~ 2 nm and highly disordered Al cations as shown in **Figure 1.2**, leading to broad diffraction peaks from X-ray and the subsequent Rietveld analysis based on X-ray diffraction is difficult.[25, 40] Electron diffraction can be a candidate for structural elucidation of γ-Al_2O_3.[27, 39, 41] However, as γ-Al_2O_3 is metastable phases rather than thermodynamically stable, electron-beam radiation can induce phase transformation of γ-Al_2O_3. Finally, the sample preparation for standard γ-Al_2O_3 adds complexity to the structural analysis. Various preparation protocols (temperature, precursor, and textural properties) affect the formation of γ-Al_2O_3, leading to different crystallinity, facets, etc.[1-3] Many structural studies for γ-Al_2O_3 have investigated γ-Al_2O_3 derived from different preparation protocols, which should be carefully considered.[28, 34, 38-39]

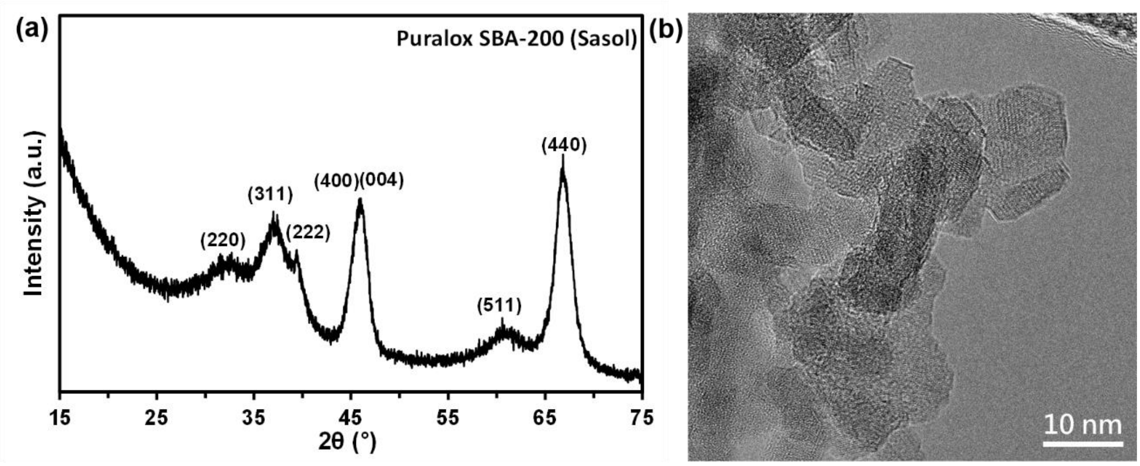

Figure 1.2. (a) XRD and (b) HR-TEM for Puralox SBA-200 (γ-Al_2O_3, Sasol).

1.2.2. *Surface chemistry of γ-Al_2O_3*

Although the bulk structures of γ-Al_2O_3 have not been fully established, whether the spinel or non-spinel structure is more stable or not doesn't directly provide the information about the origin of various catalytic properties of alumina-based catalysts. In general, the catalytic reaction proceeds on the surfaces, not the bulk. Specifically, the stability of the surface of alumina is more critical than the bulk stability in nanocrystalline powders.[42-43] McHale et al. reported that although α-Al_2O_3 is more stable than γ-Al_2O_3 in bulk, the surface of γ-Al_2O_3 is more stable than α-Al_2O_3, leading to energetically stable for γ-Al_2O_3 when the surface area is higher than 125 m^2/g.[42] Considering γ-Al_2O_3 utilized in catalytic process usually have sufficient surface area (> 100 m^2/g), the surface stabilities actually contribute most to the properties of Al_2O_3 based catalysts. Later, θ-Al_2O_3, derived from phase transformation of γ-Al_2O_3, was reported to have negative surface energies for specific facets under thicknesses larger than ~1 nm by theory, showing the surface stability similarly.[43]

γ-Al_2O_3 surfaces have under-coordinated Al sites and O sites, which act as Lewis acid sites (electron-accepting) and Lewis basic sites (electron-donating). In addition, OH groups derived from dissociative adsorption of water, act as Brønsted acid sites (proton-donating).[1, 3] Here, Brønsted acid sites and the Lewis basic sites usually are not straightforward than Lewis acidity of γ-Al_2O_3, I mainly focus on the Lewis acid sites of γ-Al_2O_3. These acid-base properties of γ-Al_2O_3 are key features of alumina-based catalysts because acid-base properties influence the interaction with active phases,[9-11, 44] stability related to sintering,[45] and catalytic activity itself.[46-48] So, there have been numerous studies devoted to understanding the acid-base properties of γ-Al_2O_3 by IR,[1, 49-50] NMR,[51] TPD,[46] TEM,[25, 52] and simulation.[48, 53-54]

γ-Al_2O_3 has various types of surface hydroxyls, which are intensively characterized by IR spectroscopy. Many surface models have been suggested to explain the origin of different OH groups, which are summarized in **Table 1.2**. Since Peri's study,[55] Tsygnanenko and Filimonov,[56] Morterra et al.,[57] and Knözinger and Ratnasamy[58] have tried to correlate OH vibration with the charges affected by the neighboring Al cation and oxygen anion. Among them, Knözinger and Ratnasamy model have been one of the most popular models.[58] This model considered (111), (110), and (100) surfaces and defined the net charge as the sum of negative charge of the anion and the strength of the electrostatic bonds (cation charge divided by the coordination number). Isolated OH, bridged OH, and triply bridged OH are assigned to 3790-3700 cm^{-1}. All the studies suggest that the more cations are coordinated to OH groups, the more the net charge becomes negative and the higher OH vibration frequencies shift, becoming more basic hydroxyls. Later, Busca et al. introduced the cation vacancy for explaining the splitting of OH vibrations.[59-60] The authors suggested the difference between isolated OH groups (Al_{IV}–OH and Al_{VI}–OH) became larger (~50 cm^{-1}) than that of Knözinger and Ratnasamy model (~20 cm^{-1}). Then, they assume the smaller splitting from the cation vacancy (3790 cm^{-1} for Al_{IV}–OH and 3770 cm^{-1} for [ ]–Al_{IV}–OH where [ ] is cation vacancy). Finally, Digne et al. proposed new assignments based on their new non-spinel structures by DFT simulation.[5, 37] The most contribution from their work is that they constituted the most realistic γ-Al_2O_3 surfaces where the surface reconstruction is considered. Previous models only consider ideal surfaces without the surface reconstruction. However, Digne et al.'s model considered the surface dehydroxylation, which were found to depend on both the crystal facet and the activation temperature.[5, 37] Their results showed that (100) facet are completely dehydrated above 327 °C, whereas (110) and (111) facet still remain high hydrated even at 727 °C. Under these reconstructed surfaces, OH vibrations were specific to exposed crystal facets of γ-Al_2O_3, suggesting that the crystal facets affect more critically than the cation vacancy by Busca et al.'s model. This model has been the most popular γ-Al_2O_3 surface model in Al_2O_3 research field. The challenge to understand the surfaces of γ-Al_2O_3 have been on-going.

Table 1.2. Suggested models for surface OH groups on γ-Al_2O_3. [ ] notes the cation vacancy. I and μ_1 = isolated; II and μ_2 = bridged; III and μ_3 = triply bridged.

OH frequency	**Model**			
	Tsyganenko and Filimonov[56]	**Knözinger and Ratnasamy**[58]	**Busca et al.**[59]	**Digne et al.**[5,37]
3800–3785	I	Ib (Al_{VI})	Al_{IV}	HO–μ_1–Al_{IV} (110)
3780–3760	I	Ia (Al_{IV})	[ ]–O–Al_{IV}	HO–μ_1–Al_{VI} (100)
3745	II	IIb (Al_{VI},Al_{VI})		HO–μ_3–Al_{VI} (111)
3735–3730	II	IIa (Al_{IV},Al_{VI})	Al_{VI}	HO–μ_2–Al_V (111), HO–μ_1–Al_V (110)
3710	III	III	[ ]–O–Al_{VI}	
3690	III	III	II	HO–μ_1–Al_V (110)
3590	H-bonded	H-bonded	III	HO–μ_3–Al_{VI} (100)

The acidity of various surface hydroxyls can be investigated by adsorbing acidic/basic probe molecules (pyridine, CO, CO_2, nitrile, etc.).[1, 61-63] Various surface models assume that the lower the OH vibration frequencies, the more acidic hydroxyls.[49, 55-56, 58-60] However, IR results showed the opposite results: The OH groups above 3700 cm^{-1} (3790, 3770, and 3730 cm^{-1}) are enough acidic to adsorb the weakly and strongly basic probes (CO, nitriles, and pyridine).[1] On the other hand, hydroxyls below 3700 cm^{-1}, which supposed to be acidic, are inactive in adsorption such as nitriles.[1, 61] Especially, surface hydroxyls at 3770 cm^{-1} showed the most reactivity among hydroxyls for various probes and OH-related reaction.[49, 64] Morterra et al.[62] and Busca et al.[1, 50] suggested that surface hydroxyls at 3770 cm^{-1} exist on the most exposed surfaces such as edge, corner or near defect sites (vacancy), leading to unique reactivity. HR-TEM and simulation also report the surface reconstruction of (110) facets into (111) facets, showing more exposed edge-like surfaces.[52, 65] However, the exact nature of defective surfaces has to be investigated in detail more.

The complexity of various surface hydroxyls indicates that Lewis acid sites are heterogeneous because Lewis acid sites on aluminas are usually formed after the dehydroxylation of these hydroxyls.[1, 3] Many studies report the heterogeneity of Lewis acidities on γ-Al_2O_3 surfaces.[48, 54, 61, 63, 66] Three kinds of Lewis acids sites were revealed by pyridine adsorption and also CO adsorption.[49, 61-63] Furthermore, five types of Al-O pair sites were reported to have different adsorption strength for water by simulation.[48] These heterogeneities of Lewis acid sites can result in different catalytic activities such as alcohol dehydration, one of typical acid-catalyzed reaction.[54]

Specifically, two Lewis acid sites are highlighted due to their unique activities. One is tri-coordinated Al site ($\mathrm{Al_{III}}$) on (110) facets formed after dehydroxylation of $\mathrm{Al_{IV}}$-OH and the other is penta-coordinated Al site ($\mathrm{Al_{V}}$) on (100) facets, which is formed after dehydroxylation of $\mathrm{Al_{VI}}$-OH, as shown in **Figure 1.3**.[37]

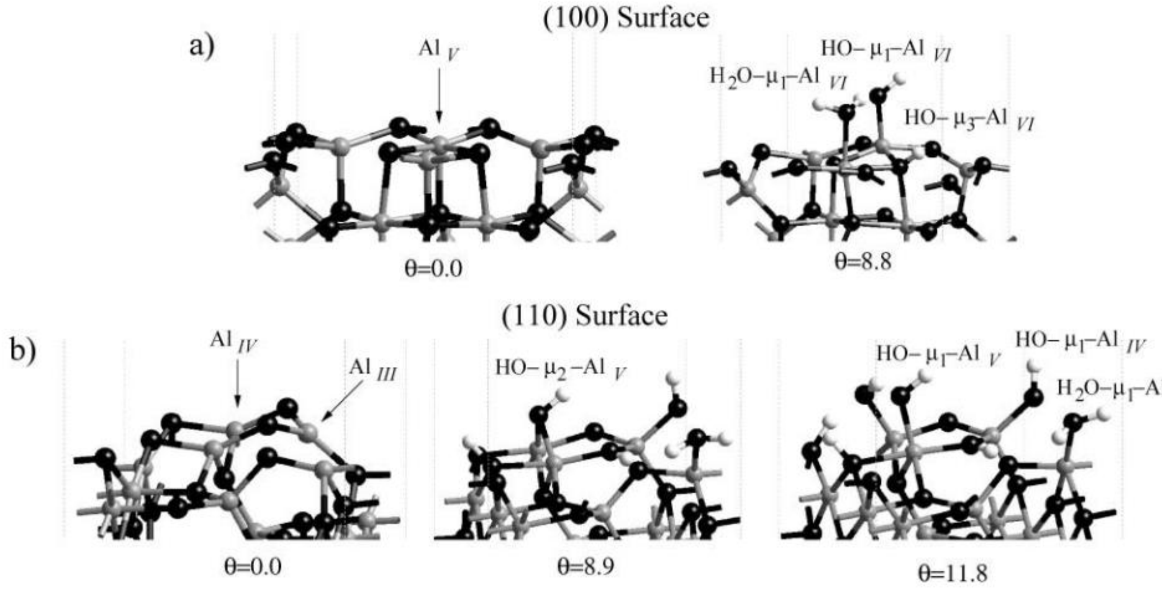

Figure 1.3. Relaxed configurations for (a) γ-$\mathrm{Al_2O_3}$(100) and (b) γ-$\mathrm{Al_2O_3}$(110) surfaces for different hydroxyl coverages (θ in OH·$\mathrm{nm^{-2}}$). (Black balls) O; (gray balls) Al; (white balls) H. Reprinted from ref 37. Copyright (2002), with permission from Elsevier.

First, $\mathrm{Al_{III}}$ site is the most acidic sites, but its existence in real has been questioned because (110) facets are still high hydrated even at 727 $^{\circ}$C.[5, 37] However, Wischert et al. found that the optimal surface hydration by activation at 700 $^{\circ}$C led to the expose of $\mathrm{Al_{III}}$ sites with the simultaneous stabilization of (110) surfaces by DFT simulation.[53] Interestingly, $\mathrm{Al_{III}}$ site can adsorb N_2 and $\mathrm{Al_{III}}$–O Lewis acid-base pair can activate H_2 and CH_4 (**Figure 1.4**).[48] Furthermore, $\mathrm{Al_{III}}$ sites also contribute to the metathesis of Re supported $\mathrm{Al_2O_3}$ catalysts.[44]

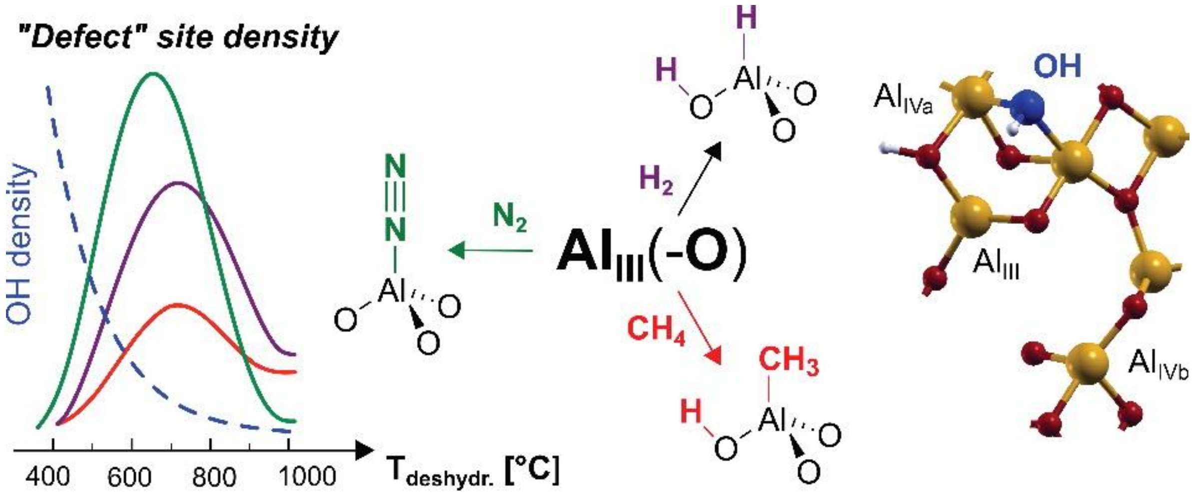

Figure 1.4. Scheme of activation of N_2, H_2, and CH_4 by Al_{III} sites. Reprinted with permission from ref 48. Copyright (2012) American Chemical Society.

Second, the role of penta-coordinated Al sites (Al_V) were investigated by ^{27}Al-NMR with ultrahigh magnetic field NMR.[9-11, 45, 51, 67] According to Digne et al's model, (100) facets are fully dehydroxylated at 327 °C, leading to formation of Al_V after dehydroxylation of Al_{VI}–OH.[5, 37] Kwak et al. confirmed the existence of Al_V on the alumina surfaces rather than bulk.[9] Serious of studies found the critical role of Al_V in catalytic properties of γ-Al_2O_3. Al_V sites are anchoring sites for the active phase (Pt, BaO, WO_x) evidenced by the decrease of Al_V sites with ^{27}Al-NMR after loading the active phases on **Figure 1.5a**.[9-11] PtO is suggested to be anchored on Al_V sites on (100) facets through Al_V-O-Pt bond by DFT simulation (**Figure 1.5b** and **1.5c**).[11] Furthermore, Al_V sites play a role in the phase transformation of γ-Al_2O_3.[67] Interestingly, despite the minor facets of (100) (<20%) in γ-Al_2O_3 rather than (110) facets (74%), Al_V sites are active for alcohol dehydration (**Figure 1.6a**).[46-47, 51] Kwak et al. performed ethanol temperature-programmed desorption (TPD) on γ-Al_2O_3 with changing the activation temperature.[46] **Figure 1.6b** showed that ethanol desorbed as ethylene (>150 °C) by dissociative adsorption as ethoxide on γ-Al_2O_3. Interestingly, the desorption of ethylene was sensitive to surface dehydroxylation of γ-Al_2O_3. The desorption of ethylene occurred at 250–260 °C after 100~200 °C activation, but shifted lower (225 °C) after 400~500 °C activation (**Figure 1.6c**). These results were interpreted; Ethylene was desorbed easily on the Lewis acid sites (Al_V) than Brønsted acid sites (Al-OH) on (100) facets, which were consistent with the model by Digne et al. showing the dehydroxylation of (100) facets above 327 °C.[5, 37] As (110) facets are always hydrated during 100~500 °C activation, change of ethylene desorption couldn't be explained on (110) facets.[5, 37] Furthermore, quantification of sites from ethanol TPD was comparable to that from ^{27}Al-NMR, suggesting the active sites are Al_V sites of (100) facets on γ-Al_2O_3.

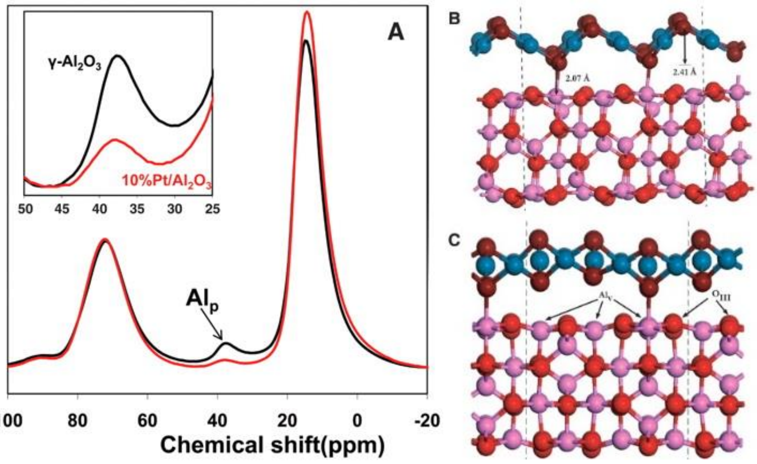

Figure 1.5. (a) ^{27}Al MAS-NMR for γ-Al_2O_3 (black) and 10 wt % Pt/γ-Al_2O_3 (red) after calcination at 573 K. (b), (c) Optimized PtO overlayer on γ-Al_2O_3 (100) by DFT simulation. Reprinted with permission from ref 11. Copyright (2009) American Association for the Advancement of Science.

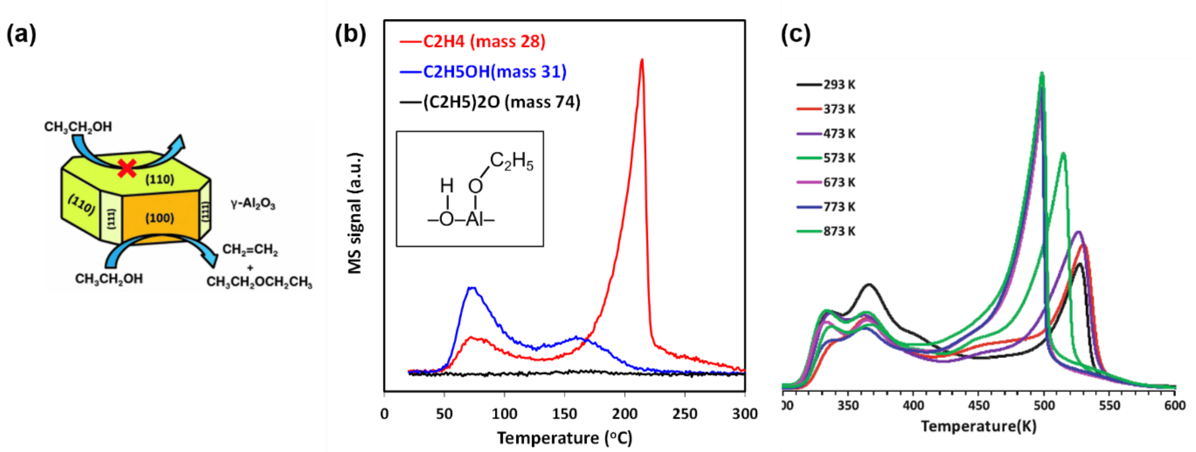

Figure 1.6. (a) Scheme of ethanol dehydration on (100) facets of γ-Al_2O_3. Reprinted by permission from SpringerNature: SpringerNature, Catalysis Letters (ref 46), Copyright (2011). (b) Ethanol TPD for Puralox SBA-200 (γ-Al_2O_3, Sasol) after 500 °C calcination, which was detected by mass spectrometry. The inlet showed a scheme for the dissociative adsorption of ethanol as ethoxide on γ-Al_2O_3 surfaces. (c) Ethanol TPD profiles on calcined at the indicated temperature after ethanol adsorption at room temperature. Reprinted by permission from SpringerNature: SpringerNature, Catalysis Letters (ref 46), Copyright (2011).

However, the formation of Lewis acid sites on γ-Al_2O_3 not always require dehydroxylation by pre-activation. Busca group suggests that if reactants have similar acidities with respect to water, reactants can substitute hydroxyls directly such as ethanol and water on **Figure 1.7**.[1, 50] The relative acidities between reactants and water are an important parameter to activate the Lewis acid sites on γ-Al_2O_3.

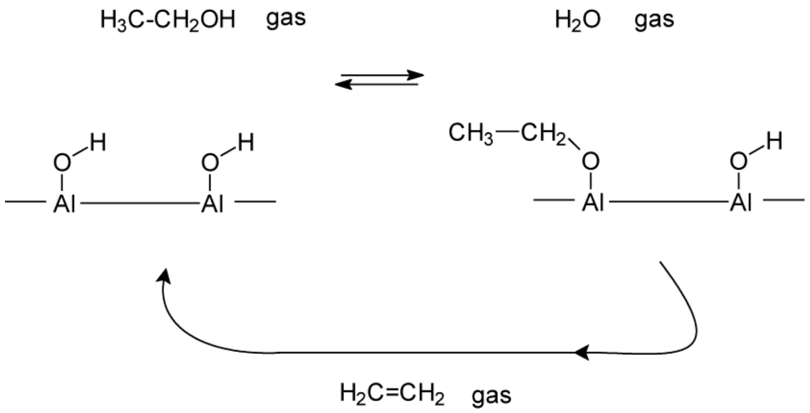

Figure 1.7. Scheme of ethanol adsorption and conversion into ethylene on alumina. Reprinted from ref 1. Copyright (2014), with permission from Elsevier.

In summary, γ-Al_2O_3 is very complex catalytic materials whose structures are not fully established despite numerous studies. However, surface properties of Al_2O_3 are most important because surface stability is critical than bulk stability in commercially utilized nano-sized Al_2O_3. The most key features of γ-Al_2O_3 arise from its Lewis acidity, which acts the anchoring sites for active phases and shows the unique catalytic activity itself. Various kinds of Lewis acid sites exist on γ-Al_2O_3 surfaces, leading to the complexity of understanding the surface chemistry of γ-Al_2O_3.

1.3. Factors to affect the surface properties of γ-Al_2O_3

Various factors such as morphology, crystalline phases, impurities, and additives affect the surface properties of γ-Al_2O_3. In particular, the influence of various factors is mixed, and each factor also affects each other. For example, the phase transformation of γ-Al_2O_3 are affected by both morphology and additives.[3, 68-69]

1.3.1. Morphology

Various morphologies (rhombus,[70-74] hexagon,[72] elongated platelets,[73, 75] cuboctahedrons,[70] rods,[71, 74] and fiber[72-73]) for γ-Al_2O_3 have been reported, as shown in **Figure 1.8**. As γ-Al_2O_3 with various morphologies have different crystal facet ratio in (110), (111), and (100) planes, and each facet has different surface properties such as dehydroxylation and strength of Lewis acid sites,[5, 37] they show different catalytic properties although their bulk structures are all the same as γ-Al_2O_3. First, each facet has different interaction strength with the catalytic active phases, leading to different dispersion for the active phase and also catalytic properties of the active phase.[11-14, 44, 70] Furthermore, their own catalytic activities such as alcohol dehydration and CH_4 activation are reported to be different.[46-48]

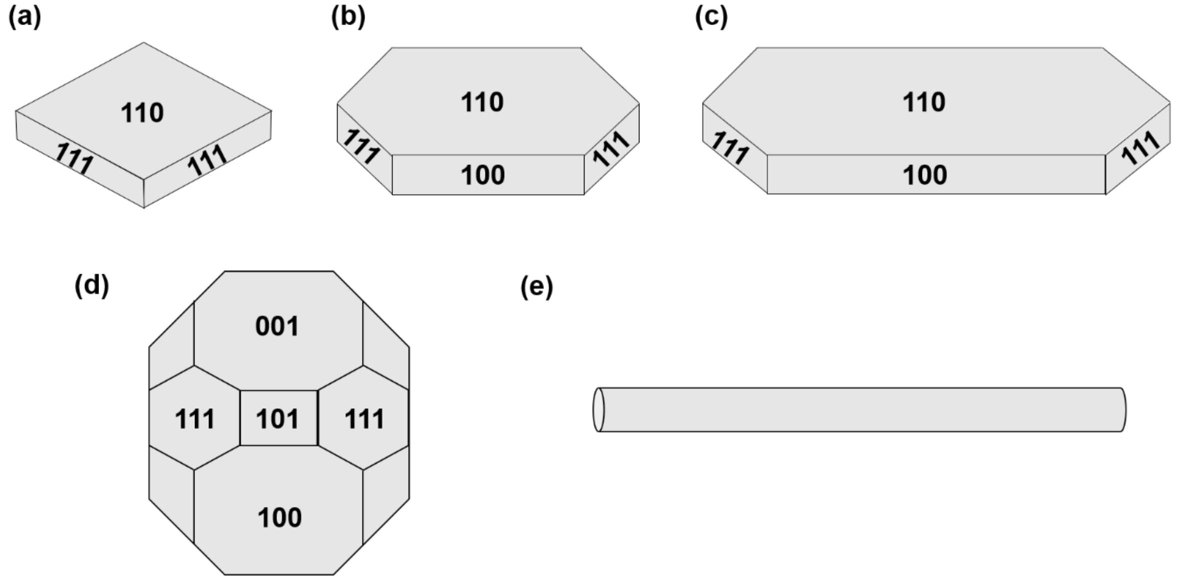

Figure 1.8. Scheme for γ-Al_2O_3 with various morphologies. (a) Rhombus platelet[70-74]; (b) hexagonal platelet[72]; (c) elongated platelet[73,75]; (d) cuboctahedral particles[70]; (e) rod/fibrous particles[71-74].

The critical role of morphologies for different catalytic properties suggests that controlling the morphology of γ-Al_2O_3 can be a promising way to design the catalytic performance of Al_2O_3-based catalysts. As the morphology of γ-Al_2O_3 inherits from their precursor (boehmite: γ-AlOOH)‒topotactic transformation (**Figure 1.9**),[5] many studies have devoted to controlling morphologies of boehmite. (010) plane of boehmite is the most stable irrespective of pH and normally becomes the most abundant plane.[76] The most abundant (010) plane became (110) plane after phase transformation into γ-Al_2O_3 and that's why γ-Al_2O_3 usually have (110) planes most.[5-6] By adjusting synthetic condition, other lateral planes ((110) and (111) planes) can grow, leading to different morphologies such as elongated platelet,[73, 75] rod,[71-72, 74] and fibrous γ-Al_2O_3.[72-73, 75] The morphology of γ-Al_2O_3/boehmite can be controlled by changing the pH condition,[71, 73-74] precursors (nitrate, chloride, sulfate),[73, 77] and additives.[78] Under the acidic condition, elongated morphologies are formed, but rhombus platelet is synthesized under basic condition.[71, 73-74] This is well correlated to the electrostatic state of the surface in solution.[73] Under the acidic condition, the surface of boehmite is positive and anion, whose source is Al precursors or additives, are adsorbed. Selective anion adsorption into (010), (001) planes led to preferential growth of boehmite along [100] direction and elongated morphologies are obtained.[73] The kinds of anion have different adsorption strength, leading to different growth rates and finally different facet ratio. Under the basic condition, the surfaces are negatively charged and the anion can't adsorb due to electro-repulsion. So, the kind of anion can't affect the morphology any more. That's why platelet particles are usually synthesized under basic condition, where the basal planes are most stable (010) plane (boehmite) and finally, (110) plane for γ-Al_2O_3.[73-74]

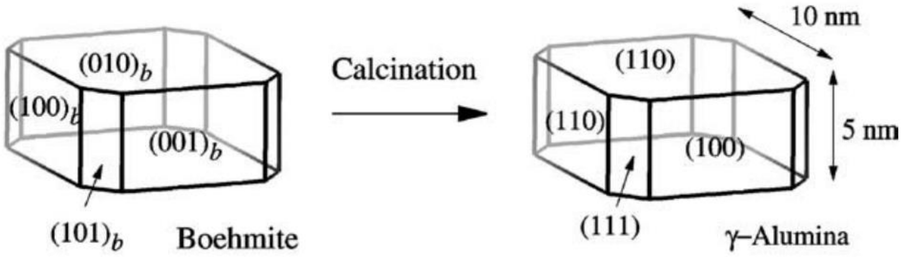

Figure 1.9. Topotactic transformation of γ-AlOOH into γ-Al_2O_3. Reprinted from ref 5. Copyright (2004), with permission from Elsevier.

Although many efforts devoted to controlling the morphology of alumina, two issues should be carefully considered. One is the remaining additives, which was used to control the morphology. As anion (chloride, sulfate) and cation (alkali metal) affect the surface properties of γ-Al_2O_3 (will be discussed in detail on 1.3.3 section), remaining additives should be washed clearly after synthesis of morphology-controlled Al_2O_3. The other is which planes are the real exposed planes. the γ-Al_2O_3 surface can be reconstructed, which is not easy to be correctly characterized. Kovarik et al. did HR-TEM study for rhombus platelet γ-Al_2O_3 with (110) and (111) planes with apparent morphology and reported that the (110) facets are actually reconstructed into (111) facets (**Figure 1.10**),[52] which was previously expected by simulation from Pinto et al.[65] These reconstruction of γ-Al_2O_3 surface suggests the difficulties of real exposed crystal facets on morphology-controlled γ-Al_2O_3.

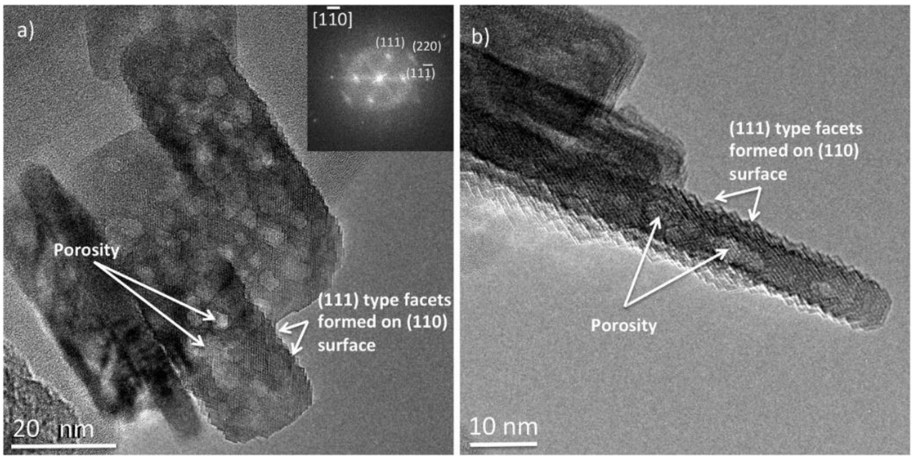

Figure 1.10. HR-TEM of (110) surfaces in edge-on orientation reveal that the surface is not atomically flat but, instead, consists of two sets of (111) type facets. The inset in panel a represents an indexed diffractogram (Fourier spectrum) that was obtained from the upper particle. Reprinted with permission from ref 52. Copyright (2013) American Chemical Society.

1.3.2. Crystalline phase

As γ-Al_2O_3 is metastable, high thermal treatment phase transform of γ-phase into δ-phase, θ-phase and finally α-phase.[1, 3] During this phase evolution, the physicochemical properties of Al_2O_3 vary and lead to different catalytic properties. For example, the strong Lewis acidities of γ-Al_2O_3 are useful in acid-catalyzed reaction, such as isomerization and alcohol dehydration.[7-8, 21] However, much less acidity of θ-Al_2O_3 and α-Al_2O_3 is desirable for suppressing the side reaction such as coke formation and polymerization.[17-19] The changes of Lewis acidity is due to the ordering of the cation sites on alumina surfaces during the phase transformation.[1, 3-4, 79] It has been known that the cation ordering increased gradually during phase evolution into θ-Al_2O_3 ($\gamma \rightarrow \delta \rightarrow \theta$) without no change of oxygen anion lattice (FCC).[1, 3-4] Especially, the number of tetrahedral Al sites (Al_{IV}) increased up to θ-Al_2O_3 (~50% for in theory) and then decreased due to the formation of α-Al_2O_3 having octahedral Al sites only.[35, 51] Increased cation ordering led to more homogenous Lewis acid sites for δ, θ-Al_2O_3 than γ-Al_2O_3. IR spectroscopy using probe molecules (CO and pyridine) showed the much narrow adsorption bands for Lewis acid sites.[1, 49, 80] However, CO and pyridine experiments show similar Lewis acid sites for γ-Al_2O_3 up to θ-Al_2O_3 qualitatively.[1, 49-50, 80] Only difference was δ, θ-Al_2O_3 has less number of Lewis acid sites than γ-Al_2O_3 due to lower surface areas after high thermal treatment. α-Al_2O_3 have Lewis acid sites from octahedral Al sites,[49, 80] but its contribution is small due to too low surface areas (< 5 m^2/g).

Several crystalline phases (γ-α phase) usually coexists: XRD and TEM showed transition Al_2O_3 had mixtures of at least two phases.[1, 3-4, 81-82] **Figure 1.11** showed the mixture of δ-Al_2O_3 and θ-Al_2O_3 after 1000 °C calcined platelet γ-Al_2O_3.[81] Tetrahedral Al sites should be ~50% for complete θ-Al_2O_3 in theory, but usually, θ-Al_2O_3 showed ~40% tetrahedral Al sites experimentally due to other phases.[35] The surface properties of transition aluminas are mixed from those of various crystalline phases. Therefore, understanding the transition aluminas is challenging because distinguishing how each phase contribute to the surface properties of transition aluminas is difficult. Furthermore, the presence as multiple phases in transition aluminas questions whether each phase exists on the surface only or in bulk. When the specific phase grows on the surface only, using bulk techniques only such as XRD should be careful.[83] Kwak et al. demonstrated the phase transformation of γ-Al_2O_3 into θ-Al_2O_3 initiates on the surfaces without no change of bulk phases as γ-Al_2O_3 by ethanol TPD.[84] 800 °C calcination of γ-Al_2O_3 showed the surface characteristics of θ-Al_2O_3 evidenced by ethanol desorption without no change of bulk structure by XRD. Therefore, surface-sensitive characterization such as ethanol TPD is needed for fully understanding the surface properties of transition Al_2O_3. Finally, thermal history of transition alumina should be carefully considered because each crystalline phase is metastable and continuously phase transform into other phases.[1-2, 4] Different thermal histories led to different mixtures of each crystalline phases among transition Al_2O_3.

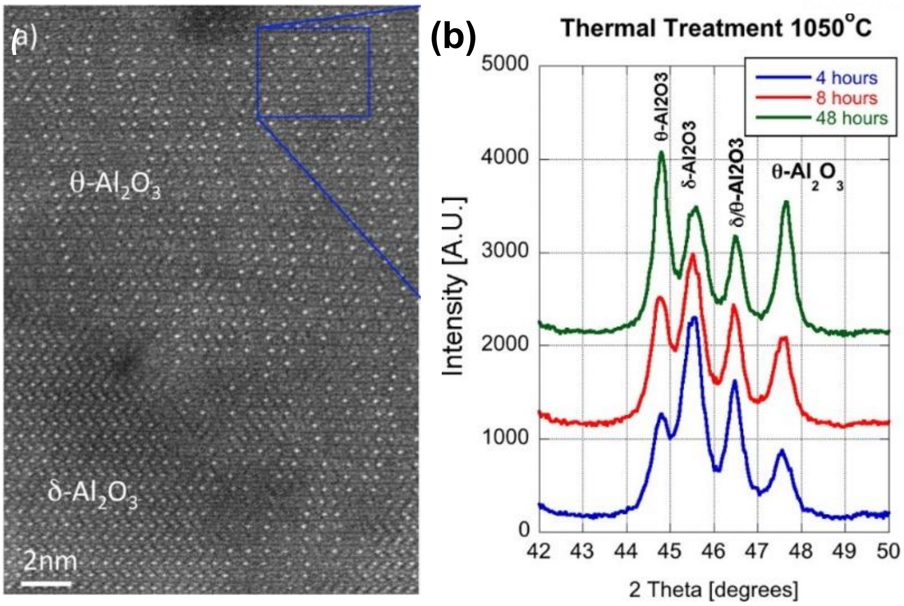

Figure. 1.11. (a) HAADF-STEM of a 1000 °C calcined γ-Al_2O_3, showing the formation of both θ-Al_2O_3 and δ-Al_2O_3. (b) XRD for 1050 °C calcined γ-Al_2O_3 (Sasol) during 4, 8, and 48 hr. Reprinted with permission from ref 81. Copyright (2015) American Chemical Society.

1.3.3. Impurities and additives

Al_2O_3 supported catalysts utilized in industries have remaining impurities (alkali metal or halogen) during preparation and various additives for modification of the catalysts.[1, 3] The effect of impurities and additives should be carefully considered because they affect the catalytic properties significantly by modifying the acidity and also the electronic properties of the active phases.[85-87] Commercial γ-Al_2O_3 are prepared by using various precursors.[1, 3] One is precipitation from $NaAl_2O_4$ salts, leading to several hundred ppm of Na (200-700 ppm).[88] The other is flame hydrolysis of $AlCl_3$, where Cl is remained (> 5000 ppm).[64] However, Sasol company produce pure γ-Al_2O_3 by alkoxide-based preparation by Ziegler process, where Na is ~20 ppm and Cl is non-detectable.[89] Especially, the effects of impurities are very sensitive because only small amounts of impurity affect the catalytic performances such as alcohol dehydration and reforming process.[3, 50, 88] **Figure 1.12** showed that the stability of reforming catalysts decreased twice when the catalysts with 300 ppm of Na were used compared to that with 100 ppm of Na. In this case, only pure Al_2O_3 prepared by the Ziegler process should be used.[3] Alkali metal (Na^+, K^+) and chlorine remove the most reactive hydroxyl at 3775 cm^{-1} and simultaneously modify the acidities of Al_2O_3.[50] Sodium reduces the number and titrates the strongest Lewis acid sites.[50, 64, 85, 88] Chlorine is usually known to promote the acidity of γ-Al_2O_3 for an acid-catalyzed reaction such as alkylation and isomerization.[90] Especially, chlorine is usually added from conventional metal precursors (H_2PtCl_6), contributing to higher dispersion and re-dispersion of transition metals such as Pt.[91-92] However, this chlorination sometime poison the activity of metals due to partial blockage of the active sites or formation of less active oxychlorinated species.[87]

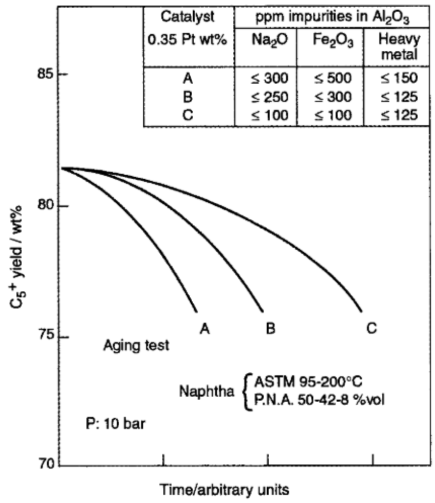

Figure. 1.12. Influence of Na impurities in γ-Al_2O_3 on the C_{5+} yield stability in the reforming process. Reprinted with permission from ref 3. Copyright (2008) Wiley-VCH Verlag GmbH & Co. KGaA, Weinheim.

High thermal temperature induces the phase evolution of γ-Al_2O_3 with the loss of surface area, which can be significantly suppressed by additives such as alkali metal, alkali earth-metal, and other elements (**Figure. 1.13**).[69, 93-94] These stabilized aluminas could improve the performance of the combustion catalyst.[94] However, these additives also modify the acid-base properties of γ-Al_2O_3. La_2O_3 and BaO are a well-known stabilizers for γ-Al_2O_3, but also titrates Lewis acid sites, showing the decreased activity for acid-catalyzed reaction.[95-96] It suggests that surface properties of γ-Al_2O_3 are affected by mixed effects of crystalline phases and additives.

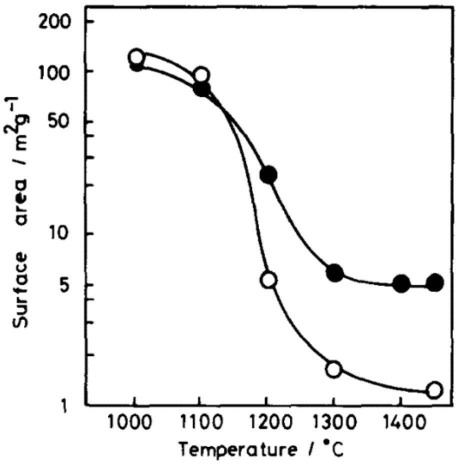

Figure 1.13. Temperature dependence of surface area for $(BaO)_{0.14}(Al_2O_3)_{0.86}$ (●), Al_2O_3 (○). Reprinted from ref 94. Copyright (1987), with permission from Elsevier.

1.4. Motivation

Thanks to the versatile utilization of industrial fields such as petroleum refining and automobile combustion, a fundamental understanding of the surface properties of Al_2O_3 is needed for the origin of the catalytic properties of Al_2O_3-based catalysts. This will provide guidelines for designing Al_2O_3-supported catalysts with improved activity and stability rather than trial and error methods. However, the surface properties of Al_2O_3 still need to be resolved because Al_2O_3-based catalysts are very complicated. The complexity of Al_2O_3-based catalysts is derived from the unresolved structures, various preparation conditions (precursors, pH, heat treatment and additives) and the combined effects of various factors (morphology, phases, impurity, additives, etc.). In addition, inherent low crystallinity with defective nature of Al_2O_3 makes conventional bulk characterization such as XRD difficult. Surface-oriented characterizations, such as spectroscopy using probe molecules (CO, pyridine, NH_3, CO_2), have been studied, but nonselective adsorption and broad signaling hinder distinguishing the effects of each factor on surface properties of Al_2O_3. To distinguish the role of each factor, comprehensive approaches should include the preparation of well-defined model Al_2O_3 and sensitive characterization tools for Al_2O_3 surface.

1.5. Outline

This thesis focuses on understanding the surface properties of Al_2O_3 and their role for the interaction with supported active phases (transition metal) and the corresponding catalytic behavior of Al_2O_3 supported catalysts. **Chapter 2** introduces a preparation of well–defined Al_2O_3 with different (100) facet ratios and their role for acid catalysis (ethanol dehydration). **Chapter 3** extends the preparation of model Al_2O_3 with controlled morphologies, phases, and additives and investigates which factor is the most critical for surface properties of Al_2O_3. Here, I use ethanol as the probe molecule by ethanol Temperature programmed desorption (TPD) for characterizing Al_2O_3 surfaces sensitively. Based on understanding the surface properties of Al_2O_3, **Chapter 4** shows how the number and properties of specific sites on Al_2O_3 affect the interaction between the supported active phase (Pt) and the catalytic behavior of Pt/Al_2O_3 by benzene hydrogenation. Finally, **Chapter 5** present how the metal support interaction affects the reduction behavior of oxidized Pt on the alumina surface.

1.6. References

[1] Busca, G. *Catal. Today* **2014**, *226*, 2-13.

[2] Trueba, M.; Trasatti, S. P. *Eur. J. Inorg. Chem.* **2005**, *2005*, 3393-3403.

[3] Euzen, P.; Raybaud, P.; Krokidis, X.; Toulhoat, H.; Le Loarer, J.-L.; Jolivet, J.-P.; Froidefond, C. Alumina. In Handbook of Porous Solids; Schüth, F., Sing, K. S. W., Weitkamp, J. Eds.; Wiley-VCH Verlag GmbH:Weinheim, 2002; Vol. 3, pp 1591-1677.

[4] Levin, I.; Brandon, D. *J. Am. Ceram. Soc.* **1998**, *81*, 1995-2012.

[5] Digne, M.; Sautet, P.; Raybaud, P.; Euzen, P.; Toulhoat, H. *J. Catal.* **2004**, *226*, 54-68.

[6] Nortier, P.; Fourre, P.; Saad, A. B. M.; Saur, O.; Lavalley, J. C. *Appl. Catal.* **1990**, *61*, 141-160.

[7] Knözinger, H. *Angew. Chem. Int. Ed.* **1968**, *7*, 791-805.

[8] de Klerk, A. In *Catalysis: Volume 23*, The Royal Society of Chemistry: **2011**; Vol. 23, pp 1-4.

[9] Kwak, J. H.; Hu, J.; Kim, D.; Szanyi, J.; Peden, C. *J. Catal.* **2007**, *251*, 189-194.

[10] Wan, C.; Hu, M. Y.; Jaegers, N. R.; Shi, D.; Wang, H.; Gao, F.; Qin, Z.; Wang, Y.; Hu, J. Z. *J. Phys. Chem. C* **2016**, *120*, 23093-23103.

[11] Kwak, J. H.; Hu, J.; Mei, D.; Yi, C.-W.; Kim, D. H.; Peden, C. H. F.; Allard, L. F.; Szanyi, J. *Science* **2009**, *325*, 1670-1673.

[12] Cai, W.; Zhang, S.; Lv, J.; Chen, J.; Yang, J.; Wang, Y.; Guo, X.; Peng, L.; Ding, W.; Chen, Y.; Lei, Y.; Chen, Z.; Yang, W.; Xie, Z. *ACS Catal.* **2017,** *7*, 4083-4092.

[13] Wang, Y.; Yang, J.; Gu, R.; Peng, L.; Guo, X.; Xue, N.; Zhu, Y.; Ding, W. *ACS Catal.* **2018,** *8*, 6419-6425.

[14] Bara, C.; Plais, L.; Larmier, K.; Devers, E.; Digne, M.; Lamic-Humblot, A.-F.; Pirngruber, G. D.; Carrier, X. *J. Am. Chem. Soc.* **2015,** *137*, 15915-15928.

[15] Koltsakis, G. C.; Stamatelos, A. M. *Prog. Energy Combust. Sci.* **1997**, 23, 1-39.

[16] Gélin, P.; Primet, M. *Appl. Catal., B* **2002,** *39*, 1-37.

[17] Sattler, J. J.; Ruiz-Martinez, J.; Santillan-Jimenez, E.; Weckhuysen, B. M., *Chem. Rev.* **2014,** *114*, 10613-10653.

[18] Boitiaux, J. P.; Cosyns, J.; Vasudevan, S. *Stud. Surf. Sci. Catal.* **1983**, *16*, 123-134.

[19] Lee, J. K.; Verykios, X. E.; Pitchai, R. *Appl.Catal.* **1988**, *44*, 223-237.

[20] Rhodes, C.; Riddel, S. A.; West, J.; Williams, B. P.; Hutchings, G. J. *Catal. Today* **2000**, *59*, 443-464.

[21] Rahimpour, M.R.; Jafari, M.; Iranshahi, D.; *Appl. Energy* **2013**, *109*, 79-93.

[22] Breysse, M.; Afanasiev, P.; Geantet, C.; Vrinat, M. *Catal. Today* **2003**, *86*, 5-16.

[23] Zhou, R.-S.; Snyder, R. L., *Acta Crystallogra.* **1991,** *B47*, 617-630.

[24] Paglia, G.; Buckley, C. E.; Rohl, A. L.; Hart, R. D.; Winter, K.; Studer, A. J.; Hunter, B. A.; Hanna, J. V. *Chem. Mater.* **2004,** *16*, 220-236.

[25] Rozita, Y .; Brydson, R.; Comyn, T. P.; Scott, A. J.; Hammond, C.; Brown, A.; Chauruka, S.; Hassanpour, A.; Young, N. P.; Kirkland, A. I.; Sawada, H.; Smith, R. I. *ChemCatChem* **2013,** *5*, 2695-2706.

[26] Wilson, S. J. *J. Solid State Chem.* **1979,** *30*, 247-255.

[27] Morrissey, K. J.; Czanderna, K. K.; Merrill, R. P.; Carter, C. B. *Ultramicroscopy* **1985,** *18*, 379-385.

[28] Lippens, B. C.; de Boer, J. H. *Acta Crystallogr.* **1964,** *17*, 1312-1321.

[29] Krokidis, X.; Raybaud, P.; Gobichon, A.-E.; Rebours, B.; Euzen, P.; Toulhoat, H. *J. Phys.*

Chem. B **2001,** *105*, 5121-5130.

[30] Paglia, G.; Rohl, A. L.; Buckley, C. E.; Gale, J. D. *Phys. Rev. B* **2005,** *71*, 224115.

[31] Sinha, K. P.; Sinha, A. P. B. *J. Phys. Chem.* **1957,** *61*, 758-761.

[32] Jayaram, V.; Levi, C. G. *Acta Metallurgica* **1989,** *37*, 569-578.

[33] Wang, J. A.; Bokhimi, X.; Morales, A.; Novaro, O.; López, T.; Gómez, R. *J. Phys. Chem. B* **1999,** *103*, 299-303.

[34] Samain, L.; Jaworski, A.; Edén, M.; Ladd, D. M.; Seo, D.-K.; Javier Garcia-Garcia, F.; Häussermann, U. *J. Solid State Chem.* **2014,** *217*, 1-8.

[35] Pecharroman, C.; Sobrados, I.; Iglesias, J.; Gonzalez-Carreno, T.; Sanz, J. *J. Phys. Chem. B* **1999,** *103*, 6160-6170.

[36] Lee, M. H.; Cheng, C.-F.; Heine, V.; Klinowski, J. *Chem. Phys. Lett.* **1997,** *265*, 673-676.

[37] Digne, M.; Sautet, P.; Raybaud, P.; Euzen, P.; Toulhoat, H. *J. Catal.* **2002,** *211*, 1-5.

[38] Smrcok, L.; Langer, V.; Krestan, J. *Acta Crystallogr. C* **2006,** *62*, i83-84.

[39] Paglia, G.; Buckley, C. E.; Rohl, A. L.; Hunter, B. A.; Hart, R. D.; Hanna, J. V.; Byrne, L. T. *Phys. Rev. B* **2003,** *68*, 144110.

[40] Pakharukova, V. P.; Yatsenko, D. A.; Gerasimov, E. Y.; Shalygin, A. S.; Martyanov, O. N.; Tsybulya, S. V. *J. Solid State Chem.* **2017,** *246*, 284-292.

[41] Bonevich, J. E.; Marks, L. D. *J. Mater. Res.* **1992,** *7*, 1489-1500.

[42] McHale, J. M.; Auroux, A.; Perrotta, A.J.; Navrotsky, A. *Science* **1997,** *277*, 788-791.

[43] Lodziana, Z.; Topsoe, N. Y.; Norskov, J. K. *Nat Mater* **2004,** *3*, 289-293.

[44] Valla, M.; Wischert, R.; Comas-Vives, A.; Conley, M. P.; Verel, R.; Copéret, C.; Sautet, P *J. Am. Chem. Soc* **2016,** *138*, 6774-6785.

[45] Mei, D.; Kwak, J. H.; Hu, J.; Cho, S. J.; Szanyi, J.; Allard, L. F.; Peden, C. H. F. *J. Phys. Chem. Lett.* **2010,** *1*, 2688-2691.

[46] Kwak, J. H.; Mei, D.; Peden, C. H. F.; Rousseau, R.; Szanyi, J. *Catal. Lett.* **2011,** *141*, 649-655.

[47] Larmier, K.; Chizallet, C.; Cadran, N.; Maury, S.; Abboud, J.; Lamic-Humblot, A.-F.; Marceau, E.; Lauron-Pernot, H. *ACS Catal.* **2015,** *5*, 4423-4437.

[48] Wischert, R.; Laurent, P.; Coperet, C.; Delbecq, F.; Sautet, P. *J. Am. Chem. Soc.* **2012,** *134*, 14430-14449.

[49] Morterra, C.; Magnacca, G. *Catal. Today* **1996,** *27*, 497-532.

[50] Phung, T. K.; Lagazzo, A.; Rivero Crespo, M. Á.; Sánchez Escribano, V.; Busca, G. *J. Catal.* **2014,** *311*, 102-113.

[51] Hu, J. Z.; Xu, S.; Kwak, J. H.; Hu, M. Y.; 23, C.; Zhao, Z.; Szanyi, J.; Bao, X.; Han, X.; Wang, Y.; Peden, C. H. F. *J. Catal.* **2016,** *336*, 85-93.

[52] Kovarik, L.; Genc, A.; Wang, C.; Qiu, A.; Peden, C. H. F.; Szanyi, J.; Kwak, J. H. *J. Phys.*

Chem. C **2013,** *117*, 179-186.

[53] Wischert, R.; Copéret, C.; Delbecq, F.; Sautet, P. *Angew. Chem. Int. Ed.* **2011,** *50*, 3202-3205.

[54] Jenness, G. R.; Christiansen, M. A.; Caratzoulas, S.; Vlachos, D. G.; Gorte, R. J. *J. Phys. Chem. C* **2014,** *118*, 12899-12907.

[55] Peri, J. B. *J. Phys. Chem.* **1965,** *69*, 220-230.

[56] Tsyganenko, A. A.; Filimonov, V. N. *J. Mol. Struct.* **1973,** *19*, 579-589.

[57] Zecchina, A.; Coluccia, S.; Morterra, C. *Appl. Spectrosc. Rev.* **1985,** *21*, 259-310.

[58] Knözinger, H.; Ratnasamy, P. *Catal. Rev. Sci. Eng.* **1978,** *17*, 31-70.

[59] Busca, G.; Lorenzelli, V.; Escribano, V.S.; Guidetti, R. *J. Catal.* **1991,** *131*, 167-177.

[60] Busca, G.; Lorenzelli, V.; Ramis, G.; Willey, R.J. *Langmuir* **1993,** *9*, 1492-1499.

[61] Liu, X.; Truitt, R. E. *J. Am. Chem. Soc* **1997,** *119*, 9856-9860.

[62] Morterra, C.; Bolis, V.; Magnacca, G. *Langmuir* **1994,** *10*, 1812-1824.

[63] Morterra, C.; Chiorino, A.; Ghiotti, G.; Garrone, E. *J. Chem. Soc., Faraday Trans. 1* **1979,** *75*, 271-288.

[64] Srinivasan, S.; Narayanan, C. R.; Datye, A. K. *Appl. Catal., A* **1995,** *132*, 289-308.

[65] Pinto, H. P.; Nieminen, R. M.; Elliott, S. D. *Phys. Rev. B* **2004,** *70*, 125402.

[66] Dyan, A.; Cenedese, P.; Dubot, P. *J. Phys. Chem. B* **2006,** *110*, 10041-10050.

[67] Kwak, J. H.; Hu, J.; Lukaski, A.; Kim, D. H.; Szanyi, J.; Peden, C. H. *J. Phys. Chem. C* **2008,** *112*, 9486-9492.

[68] Lee, J.; Jeon, H.; Oh, D. G.; Szanyi, J.; Kwak, J. H. *Appl. Catal., A* **2015,** *500*, 58-68.

[69] Arai, H.; Machida, M. *Appl. Catal., A* **1996,** *138*, 161-176.

[70] Sakashita, Y.; Araki, Y.; Shimada, H. *Appl. Catal., A* **2001,** *215*, 101-110.

[71] Chen, X. Y.; Zhang, Z. J.; Li, X. L.; Lee, S. W. *Solid State Commun.* **2008,** *145*, 368-373.

[72] Jiao, W.; Wu, X.; Xue, T.; Li, G.; Wang, W.; Wang, Y.; Wang, Y.; Tang, Y.; He, M.-Y. *Cryst. Growth Des.* **2016,** *16*, 5166-5173.

[73] He, T.; Xiang, L.; Zhu, S. *CrystEngComm* **2009,** *11*, 1338-1342.

[74] Chen, X. Y.; Huh, H. S.; Lee, S. W. *Nanotechnology* **2007,** *18*, 285608.

[75] Zhang, L.; Jiao, X.; Chen, D.; Jiao, M., *Eur. J. Inorg. Chem.* **2011,** *2011*, 5258-5264.

[76] Jolivet, J.-P.; Froidefond, C.; Pottier, A.; Chanéac, C.; Cassaignon, S.; Tronc, E.; Euzen, P. *J. Mater. Chem.* **2004,** *14*, 3281-3288.

[77] Xia, Y.; Jiao, X.; Liu, Y.; Chen, D.; Zhang, L.; Qin, Z. *J. Phys. Chem. C* **2013,** *117*, 15279-15286.

[78] Chiche, D.; Chaneac, C.; Revel, R.; Jolivet, J. P. *Phys. Chem. Chem. Phys.* **2011,** *13*, 6241-8.

[79] Wilson, S. J.; Mc Connell, J. D. C. *J. Solid State Chem.* **1980,** *34*, 315-322.

[80] Gribov, E. N.; Zavorotynska, O.; Agostini, G.; Vitillo, J. G.; Ricchiardi, G.; Spoto, G.; Zecchina, A. *Phys. Chem. Chem. Phys.* **2010,** *12*, 6474-6482.

[81] Kovarik, L.; Bowden, M.; Shi, D.; Washton, N. M.; Andersen, A.; Hu, J. Z.; Lee, J.; Szanyi, J.; Kwak, J. H.; Peden, C. H. F., *Chem. Mater.* **2015,** *27*, 7042-7049.

[82] Kovarik, L.; Bowden, M.; Genc, A.; Szanyi, J.; Peden, C. H. F.; Kwak, J. H. *J. Phys. Chem. C* **2014,** *118*, 18051-18058.

[83] Billinge, S. J. L.; Levin, I. *Science* **2007,** *316*, 561-565.

[84] Kwak, J. H.; Peden, C. H. F.; Szanyi, J. N. *J. Phys. Chem. C* **2011,** *115*, 12575-12579.

[85] Saad, A. B. M.; Ivanov, V. A.; Lavalley, J. C.; Nortier, P.; Luck, F. *Appl. Catal., A* **1993,** *94*, 71-83.

[86] Montanari, T.; Matarrese, R.; Artioli, N.; Busca, G. *Appl. Catal., B* **2011,** *105*, 15-23.

[87] Paulis, M.; Peyrard, H.; Montes, M. *J. Catal.* **2001,** *199*, 30-40.

[88] Phung, T.K.; Herrera, C.; Larrubia, M.Á.; García-Diéguez, M.; Finocchio, E.; Alemany, L.J.; Busca, G. *Appl. Catal., A* **2014,** *483*, 41-51

[89] Puralox/Catalox high purity activated aluminas, Sasol, http://www.sasoltechdata.com/tds/puralox_catalox.pdf (accessed May 17,2019).

[90] Clet, G.; Goupil, J.M.; Szabo, G.; Cornet, D. *J. Mol. Catal. A: Chem.* **1999,** *148*, 253-264.

[91] Lieske, H.; Lietz, G.; Spindler, H.; Völter, J. *J. Catal.* **1983,** *81*, 8-16.

[92] Mager-Maury, C.; Chizallet, C.; Sautet, P.; Raybaud, P. *ACS Catal.* **2012,** *2*, 1346-1357.

[93] Wang, S.; Borisevich, A. Y.; Rashkeev, S. N.; Glazoff, M. V.; Sohlberg, K.; Pennycook, S. J.; Pantelides, S. T. *Nat. Mater.* **2004,** *3*, 143-146.

[94] Machida, M.; Eguchi, K.; Arai, H.; *J. Catal.* **1987,** *103*, 385-393.

[95] Kwak, J.H.; Lee, J.; Szanyi, J.; Peden, C.H.F. *Catal. Today* **2016,** *265*, 240-244.

[96] Garbarino, G.; Wang, C.; Valsamakis, I.; Chitsazan, S.; Riani, P.; Finocchio, E.; Flytzani-Stephanopoulos, M.; Busca, G. *Appl. Catal., B* **2017**, *200*, 458-468.

2. Critical role of (100) Facets on γ-Al_2O_3 for Ethanol Dehydration: Combined Efforts of Morphology-Controlled Synthesis and TEM Study

This chapter contains the published result.

Lee, J.; Jang, E.J.; Jeong, H.Y.; Kwak, J.H. *Appl. Catal., A* **2018,** *556*, 121-128.

2.1. Abstract

In this work, the effect of crystal facets on the catalytic behavior of γ-Al_2O_3 was investigated by X-ray diffraction, transmission electron microscopy, temperature-programmed desorption of ethanol, solid-state ^{27}Al NMR, infrared spectroscopy, and ethanol dehydration reaction. A series of platelet γ-Al_2O_3 was synthesized, in which the relative ratio of (100) facets had been systematically increased. Ethylene formation increased with increasing (100) facets, clearly demonstrating the critical role of these facets as active sites for ethanol dehydration on γ-Al_2O_3. This systematic approach is helpful for a better understanding of facet-dependent catalytic properties of γ-Al_2O_3 that arise from the interaction between the supported metal and the crystal facets.

2.2. Introduction

γ-Al_2O_3 is an important catalytic material that has been used as a support for a wide range of applications in petroleum chemistry and automobile emission control.[1-3] Since γ-Al_2O_3 has an intrinsic acidity, it can participate in acid-catalyzed reactions such as alcohol dehydration.[4] For decades, numerous studies have been devoted towards understanding the fundamental nature of Al_2O_3 owing to its practical importance in catalysis.[3,5-14]

The catalytic properties of oxides, such as activity, selectivity, and distribution of active phases on the support, are significantly affected by their surface characteristics because chemical processes mainly occur on the surface.[8-12,14] Thus, considerable research efforts have been made to study the surface characteristics of oxides in detail. In particular, the effect of a crystal facet on catalytic behavior has been thoroughly examined for oxides like TiO_2, CeO_2, and FeO_x that have a well-defined crystalline structure.[15] However, it is difficult to understand the effect of each crystal facet of γ-Al_2O_3 on its catalytic properties due to undefined structures (defect-spinel or non-spinel), which is intrinsically complex.[8,16,17] Therefore, many studies have been performed by indirect methods such as surface science, theoretical calculations, or using relatively crystalline δ, θ, α phases of Al_2O_3 which are obtained by phase-transformation of γ-Al_2O_3.[8,9,18-20] For example, Digne and Sautet et al. have suggested a non-spinel-based γ-Al_2O_3 simulated model and shown that surface dehydroxylation is closely related to both temperature and exposed facets.[8,9] In order to experimentally verify the influence of crystal facets on the catalytic properties of γ-phase, two issues must be addressed. The first issue deals with the sensitivity of the technique or instrument used for characterization of the crystal facets of γ-Al_2O_3. Various tools like X-ray diffraction (XRD),[16,21-23] NMR,[14,24,25] FT-IR,[3,26-29] transmission electron microscopy (TEM),[1,6,30] and other temperature-programmed techniques[31-33] can be utilized to characterize the Al_2O_3 surface. However, a quantitative measurement of the facet ratio using bulk techniques such as XRD is very difficult due to the low crystallinity and small domain size of γ-Al_2O_3.[23,32] The second challenge lies in the preparation of a series of γ-Al_2O_3 samples with systematic variance in morphology. Recent advances in nanotechnology have made it possible to prepare various Al_2O_3 with different morphologies. Since the morphology of γ-Al_2O_3 is determined from boehmite (by topotactic transformation),[9,13,34] the synthesis of the precursor AlOOH were controlled to obtain specific morphologies such as needle, platelet, flower-like, and ellipsoid Al_2O_3.[35-39] However, many studies focus on the characterization of boehmite instead of γ-Al_2O_3. Although some researchers have investigated the crystal facets of γ-Al_2O_3, these studies have been limited to comparisons between its drastically different morphologies, such as rod, platelet, and cuboctahedral.[40-41] Therefore, any approach towards understanding the effects of crystal facets on catalytic properties must involve well-defined γ-Al_2O_3 with systematic morphological change.

In this work, a series of platelet γ-Al_2O_3 samples was synthesized wherein the number of (100) facets increased systematically and then correlated with the catalytic behavior of γ-Al_2O_3 in ethanol dehydration. The catalytic activity of γ-Al_2O_3 in ethylene formation increased with an increase in the relative ratio of (100) facets. This result suggests that the (100) facets play a crucial role in the alcohol dehydration reaction; therefore, careful control of γ-Al_2O_3 morphology is an important aspect of catalyst design.

2.3. Experimental Section

2.3.1. *Preparation of facet-oriented γ-Al_2O_3*

A series of platelet Al_2O_3 was synthesized based on previous reports with modification.[39,42] First, $Al(NO_3)_3 \cdot 9H_2O$ (SAMCHUN, 98.0% purity, 7.15 g) was dissolved in distilled water (80 ml) to form a transparent solution. Then, hydrazine monohydrate ($N_2H_4 \cdot H_2O$, SAMCHUN, 80% minimum purity) diluted in water was dropped into the solution, leading to a milky precipitate. The resultant mixture was transferred into a 125 ml Teflon-lined autoclave, then sealed and kept in the electric oven at 200 °C. After 12 h, the pH was measured by pH meter. The variance of hydrazine monohydrate amounts led to the pH range from 8.3 to 10. Next, the precipitates were collected by centrifugation, repeatedly washed by DI water and isopropyl alcohol, and dried at room temperature with air blowing for 1 day. Another series of platelet Al_2O_3 was synthesized with the addition of glacial acetic acid in controlled amounts, leading to the variance of pH from 4.3 to 7.6. The other procedures were same. The as-prepared powders were calcined in a muffle furnace at 600 °C for 3 h, resulting in the platelet γ-Al_2O_3.

2.3.2. Characterizations

XRD patterns were obtained on a Bruker D8 Advance A25 using Cu Kα radiation (λ = 1.54 Å) in step mode between 2θ values of 5° and 75°, with a step size of 0.02°/s. The morphologies of Al_2O_3 were confirmed by TEM (JEOL JEM-2100). The bright field transmission electron microscopy (BFTEM) image and electron diffraction pattern were obtained by a FEI Titan^3 G2 60-300 at an accelerating voltage of 80 kV. The specific surface area was determined by the Brunauer-Emmett-Teller method using BELSORP-Max instrument. Solid ^{27}Al-NMR experiments were performed at room temperature on a Varian VNMRS 600 MHz NMR spectrometer, operating at a magnetic field of 14.4 T. The corresponding ^{27}Al Larmor frequency was 156.299 MHz. All the spectra were acquired at the spinning rate of 25 kHz, using a 1.6 mm pencil-type MAS probe. Each spectrum was acquired using a total of 256 scans with a recycle delay time of 1 s. All spectra were externally referenced (i.e., the 0 ppm position) to a 1 M $Al(NO_3)_3$ aqueous solution. We normalized the ^{27}Al MAS spectra with the same total NMR peak area for the ease of comparison.

Ethanol TPD was carried out using the same experimental procedures as described in our previous report.[33] Prior to ethanol TPD experiments, 0.05 g of alumina was calcined at 500 °C for 1 h under 20% O_2/He flow (1.0 ml/s). After calcination, the sample was cooled down to room temperature and ethanol adsorption was carried out for 30 min using a 2.0 % ethanol/He gas mixture (1.0 ml/s), followed by a He purge for 30 min in order to remove weakly-bound ethanol molecules. After stabilization of the flame ionization detector (FID) signal of an Agilent 7820A gas chromatograph (GC), a TPD experiment was carried out in flowing He (1.0 ml/s) with a heating rate of 10 °C/min, and the reactor outlet flowing directly to the FID (i.e., no GC column separation).

The in situ diffuse reflectance infrared spectroscopy (DRIFTS) experiments were performed on a Nicolet iS10 FTIR spectrometer equipped with a mercury cadmium telluride (MCT) detector. Al_2O_3 samples were loaded into a high temperature reaction chamber (Harrick Scientific) using ZnSe windows, which is installed in a Praying Mantis diffusion reflection accessory. The loaded sample in the DRIFTS reactor was purged at 500 °C for 2 h with 3 ml/min of He and then cooled down to the room temperature. The pretreatment conditions were confirmed by obtaining the spectrum of commercial γ-Al_2O_3 (Puralox SBA 200). The IR spectrum collected from Puralox SBA 200 after the same treatment showed that the hydroxyl groups were consistent results with a previous study (Supporting information).[12] Then, the spectrum was collected at 25 °C under 3 ml/min of He flow by using harshly dried KBr as a background. Each obtained spectrum was the average 1024 scans at a resolution of 4 cm^{-1}. Each spectrum was normalized with the intensity of 3728 cm^{-1} peak which was assigned to be located on the (110) surface by Digne et al.[8]

2.3.3. *Catalytic activity measurements*

Ethanol dehydration tests were performed in a quartz flow reactor (outer diameter 1/4’’ and inner diameter 3.6 mm) using 0.01 g samples (60-100 mesh) supported by quartz wool. Samples were treated under 20% O_2/He flow at 500 °C for 1 h. The carrier gas (He) was passed through a bubbler containing ethanol (99.5%, Sigma Aldrich) kept at 24 °C and ambient pressure. The ethanol concentration (2%) was controlled by relative He flow rate (total flow rate of He was 2.0 ml/s). Under this reaction flow condition, external diffusion could be neglected.[43] The outlet gases were analyzed by a GC (Agilent 7820A) using an HP-FFAP column and FID. The overall activities for ethanol dehydration were compared at 180 °C and apparent activation energies were obtained in the temperature region ranging from 170 °C to 190 °C under differential condition (< 10% conversion). Another series of activity measurements was carried out at 300 °C with the same protocols. Under this condition, the catalysts exhibited significant deactivation. Therefore, the initial reaction rates were estimated by extrapolation.

2.3.4. *Calculation of the facet ratio by TEM measurements*

Length and thickness of platelet γ-Al_2O_3 particles were measured on TEM images at low magnification. 50 particles were counted for each platelet γ-Al_2O_3 synthesized at different pH condition (4.3 – 10). Usually, the main facets of γ-Al_2O_3 are discussed based on (100), (110) and (111) facets. So, we measured the length and thickness of each particle in order to obtain the relative facet ratio of (100), (110) and (111) facets. The needed length parameters are defined in **Figure 2.1**. The parameter w_1, w_2, and w_3 are the lengths for each corresponding side on exposed planes. t is the thickness of particles. h is the diagonal of (110) facet. h' is the height of (110) facet. θ is the angle between (111) facets on elongated platelet. The aspect ratio was defined as w_3/h (rhombus) and a/h (elongated). The calculation of the facet ratio was done based on the measured parameters. Simply, we can divide into two groups; rhombus and elongated platelet. For rhombus particles, no apparent (100) facet existed. So, (110) and (111) facet was only considered. Although the previous TEM study shows that the {100} facet exists on the rhombus platelet γ-Al_2O_3 due to surface roughness on (110)/(111) facets or internal surface of the pore,[44] the detailed understanding is out of the scope in this work. For elongated particles, (100), (110) and (111) facets all are considered.

< *Rhombus particles* >

S_{110}, the area of {110} facets = $w_3 \times h$ *(rhombus) or* $2 \times w_1 \times h'$ *(parallelogram)*

S_{111}, the area of (111) facets = $2 \times t \times (w_1 + w_2)$

Total area = $S_{110} + S_{111}$

The relative ratio of each facet (%) = $100 \times S_i$ / total area

< *Elongated particles* >

S_{100}, the area of (100) facets = $2 \times w_3 \times t$

S_{110}, the area of (110) facets = $2 \times w_3 \times h + 2 \times w_1 \times w_2 \times \sin(\theta)$

S_{111}, the area of (111) facets = $2 \times t \times (w_1 + w_2)$

Total area = $S_{100} + S_{110} + S_{111}$

The relative ratio of each facet (%) = $100 \times S_i$ / total area

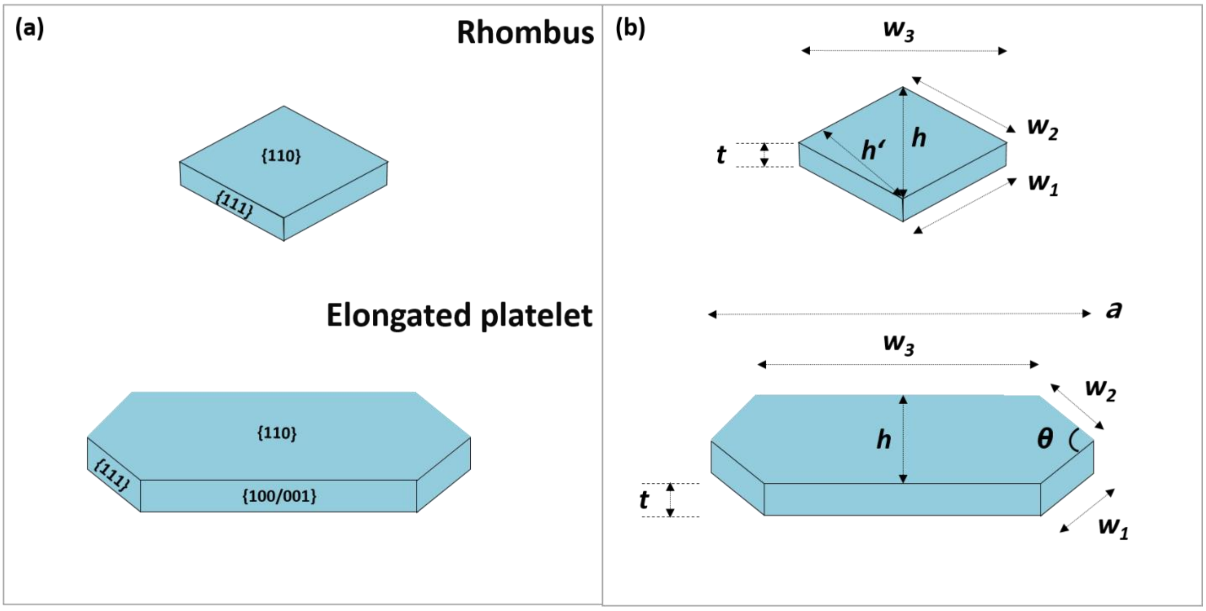

Figure 2.1. (a) Schematic description of platelet γ-Al_2O_3 (rhombus and elongated) with the indexing of the crystallographic planes and direction in a cubic lattice and (b) dimensional parameters of platelet γ-Al_2O_3. The parameter w_1, w_2, and w_3 are the lengths for each corresponding sides on exposed planes. t is the thickness of particles. h is the diagonal of {110} facet. h' is the height of {110} facet. θ is the angle between {111} facets on elongated platelet. The aspect ratio was defined as w_3/h (rhombus) and a/h (elongated).

2.4. Results and Discussion

Figure 2.2 shows the structural and morphological characteristics of AlOOH synthesized by controlling pH with acetic acid and hydrazine. XRD patterns confirmed the formation of orthorhombic γ-AlOOH (JCPDS no. 74-1895) under the entire range of pH used. Representative TEM images for all series of AlOOH synthesized at pH 4~10 are shown in **Figure 2.2b–2.2g**. Boehmite synthesized at pH 10 primarily showed a rhombus shape. Under neutral conditions, hexagonal shapes were obtained and elongated platelets that were truncated at one-side were synthesized under acidic conditions. With decreasing pH, growth in a specific direction was observed.

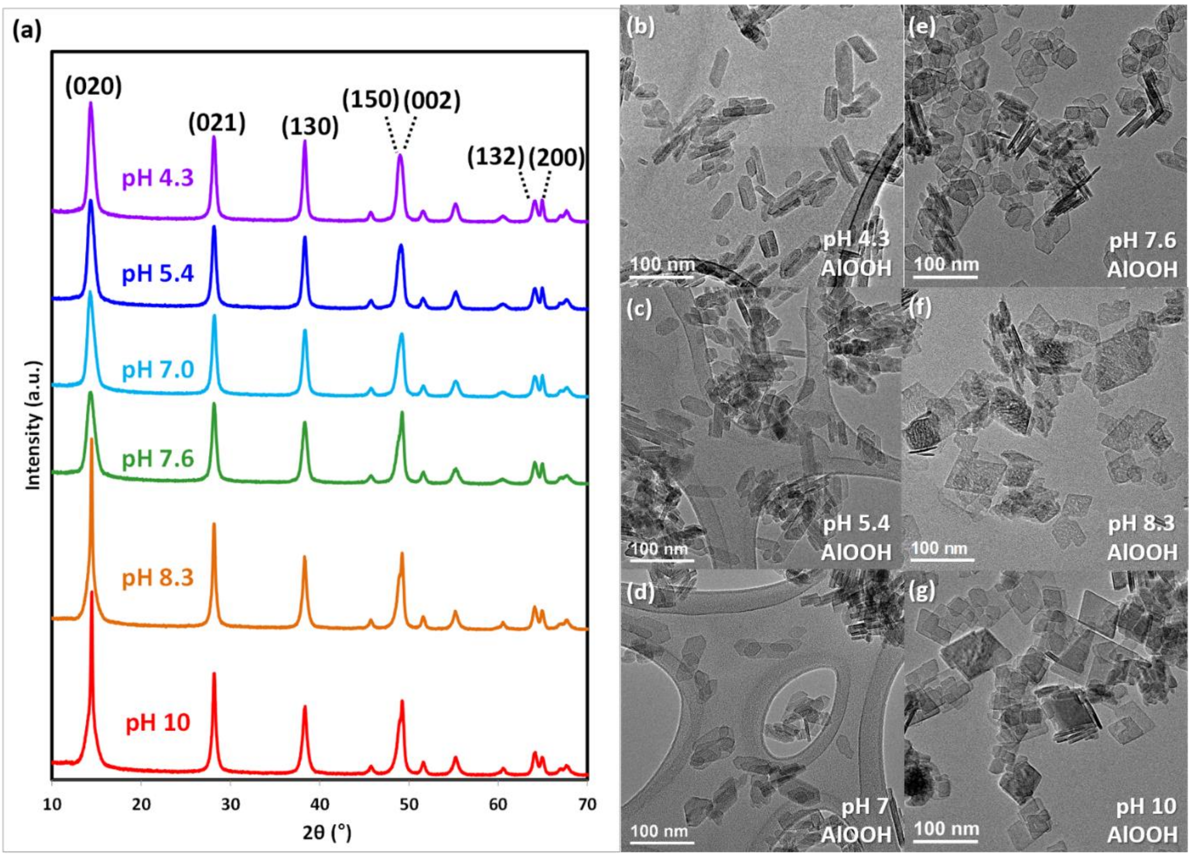

Figure 2.2. (a) XRD patterns for AlOOH synthesized at different pH levels and the low magnification TEM images for AlOOH synthesized at (b) pH 4.3, (c) pH 5.4, (d) pH 7, (e) pH 7.6, (f) pH 8.3, and (g) pH 10.

After thermal treatment at 600 °C, boehmite phase-transformed to become γ-Al_2O_3 (JCPDS no. 10-425), as confirmed by XRD (**Figure 2.3a**). It is noteworthy that there are no apparent differences in the XRD peaks of boehmite and γ-Al_2O_3, even though some differences can be observed for as-prepared γ-AlOOH samples. This observation illustrates the difficulties in applying bulk techniques such as XRD for γ-Al_2O_3, which arise due to its low crystallinity and small domain sizes. The transformation of AlOOH into γ-Al_2O_3 is known to be topotactic, which means that the facets of γ-Al_2O_3 inherit their characteristics from the starting AlOOH.[9,13,34] Compared with initial morphologies of AlOOH, the overall morphology of γ-Al_2O_3 platelet is maintained (**Figure 2.3b–2.3g**), which is consistent with topotactic phase transformation. At pH 10, the particles have a rhombus shape with a length of 30–70 nm. After the shape changes to hexagonal under neutral conditions, Al_2O_3 finally becomes an elongated platelet with the elongated side measuring 30–90 nm and the shorter side 8–25 nm. The aspect ratio of synthesized γ-Al_2O_3 was also measured for more quantitative information, as shown in **Figure 2.4**. A high aspect ratio is observed under acidic conditions, indicating the presence of elongated platelet morphology. Thus, several γ-Al_2O_3 platelets with different morphologies were synthesized by systematically controlling the pH during their synthesis.

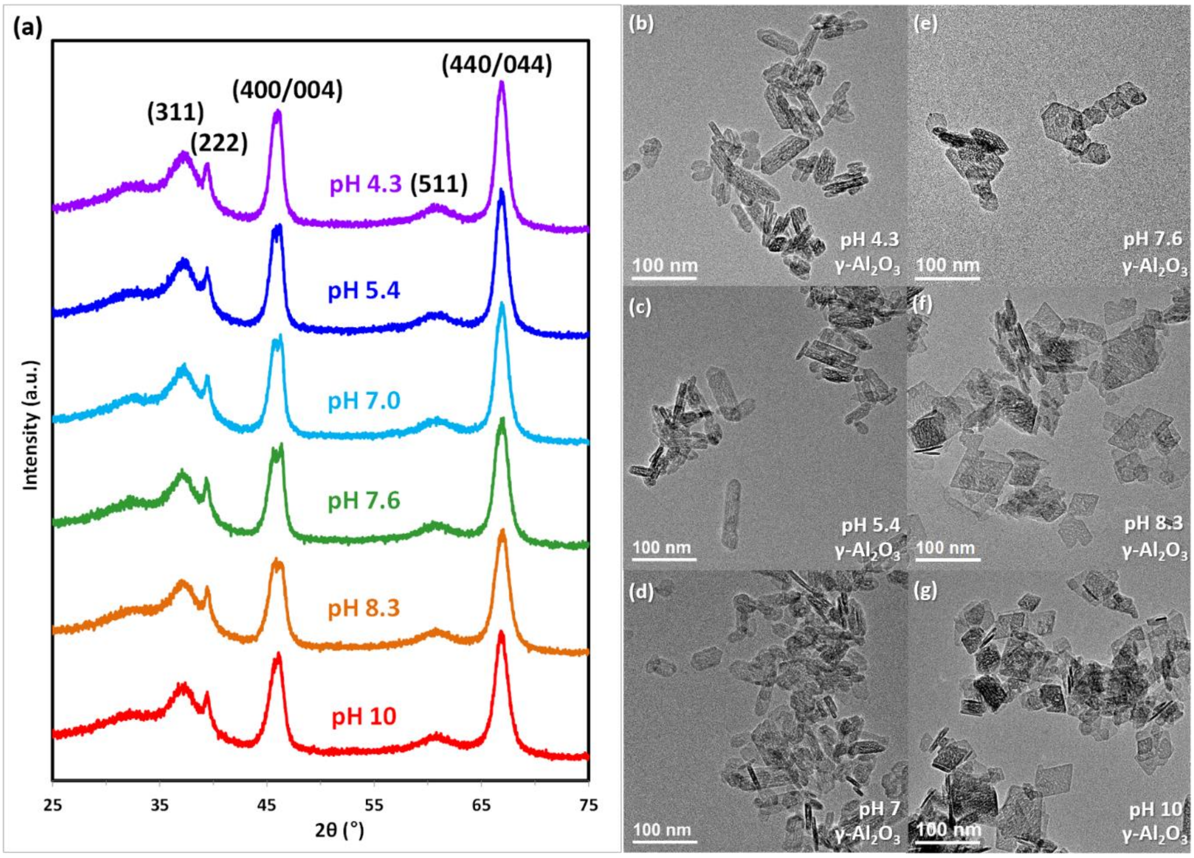

Figure 2.3. (a) XRD patterns for γ-Al_2O_3 synthesized at different pH levels and the low magnification TEM images for γ-Al_2O_3 synthesized at (b) pH 4.3, (c) pH 5.4, (d) pH 7, (e) pH 7.6, (f) pH 8.3, and (g) pH 10.

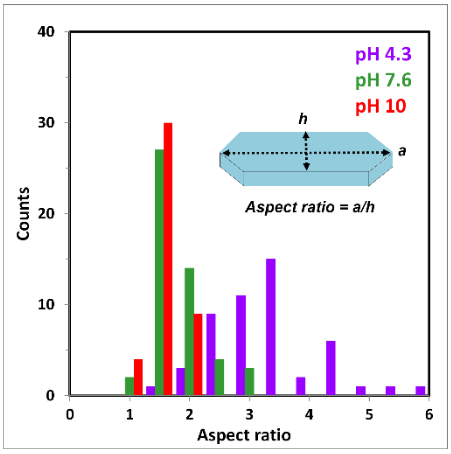

Figure 2.4. Aspect ratio of γ-Al_2O_3 at selected pH (4.3, 7.6, and 10). The aspect ratio is defined as *a*/*h* on the inlet.

In order to identify the detailed crystallographic orientation of synthesized γ-Al_2O_3, bright-field TEM (BFTEM) and electron diffraction studies were performed on individual particles and the results are shown in **Figure 2.5**. Usually, the (010) facet is known to be the most dominating of all facets on AlOOH because the interfacial tension of this facet is the lowest and also independent of the pH.[44] The BFTEM images and selected area electron diffraction (SAED) pattern of AlOOH given in **Figure 2.5a** show that all particles are aligned to the main basal planes perpendicular to the [010] direction. The diagonal planes of the platelet formed at pH 10 are parallel to the (202) facets. The newly elongated planes formed with decreasing pH were found to be parallel to (001), which illustrates the specific growth along (001) facets. After thermal treatment, the SAED pattern for γ-Al_2O_3 (**Figure 2.5b**) showed that the main basal planes were perpendicular to the (110) direction, indicating the change of the (010) facet on AlOOH into a (110) facet of γ-Al_2O_3. The lateral faces of (202) and (002) facets in AlOOH also changed into (111) and (004) facets of γ-Al_2O_3, respectively. These observations are consistent with previous structural correlations between AlOOH and γ-Al_2O_3.[9]

The crystal facets of γ-Al_2O_3 that are mainly discussed in the literature are (100), (110), and (111) facets.[9] Detailed TEM studies were performed to determine the ratio of each of these facets in fifty Al_2O_3 particles. The BFTEM images were analyzed based on the structural model shown in **Figure 2.6a** and the results are summarized in **Figure 2.6b**. The rhombus γ-Al_2O_3 synthesized under basic conditions showed no apparent (100) facet. Previous HR-TEM study of platelet γ-Al_2O_3 reveals that the alumina has the internal surfaces of pore/voids defined by (100) and (111). And based on the epitaxial relationship between Pt and platelet gamma alumina, external surface mainly defined as (110) and (111) facets have (100) facets also, which correlated with some degree of roughness on the (111)/(110) surfaces.[44,46] However, detailed understanding should be further investigated. Considering the apparent morphology, it may be concluded that the (100) facet ratio increased up to 23% with decreasing pH. Thus, there was a systematic increase in (100) facets on γ-Al_2O_3 but the (110) and (111) facet ratio decreased with decreasing pH. Hence, γ-Al_2O_3 synthesized in this work may be considered a suitable model system to investigate the role of (100) facet on the catalytic behavior of γ-Al_2O_3.

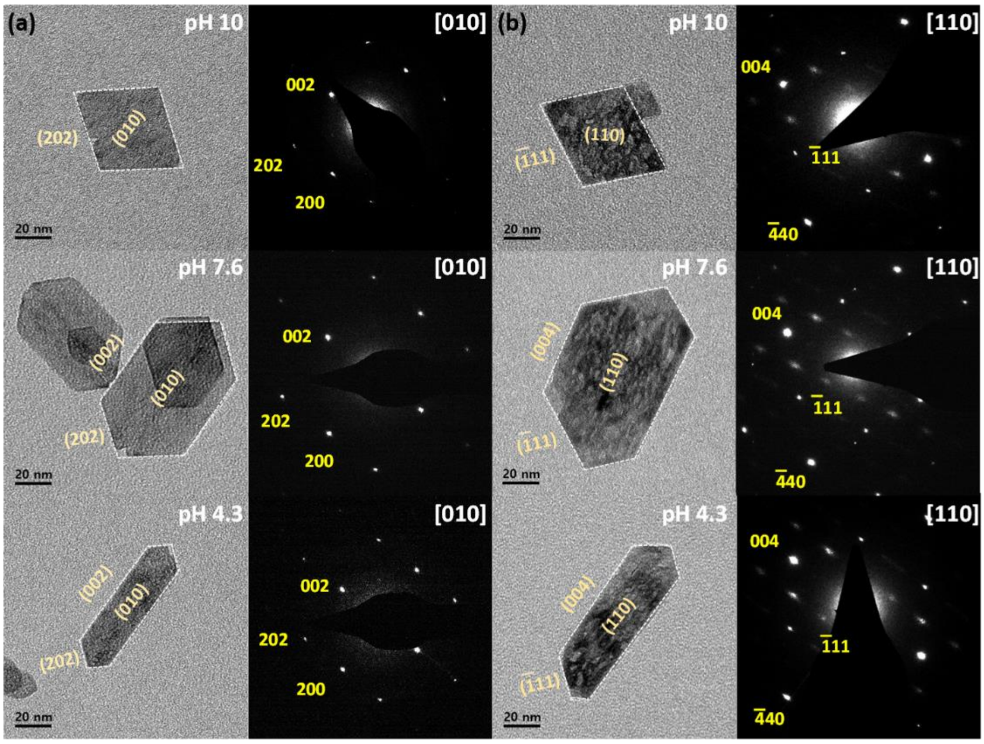

Figure 2.5. BFTEM images and SAED patterns in (a) [010] zone direction of AlOOH and (b) [110] zone direction of γ-Al_2O_3 at selected pH values of 4.3, 7.6, and 10.

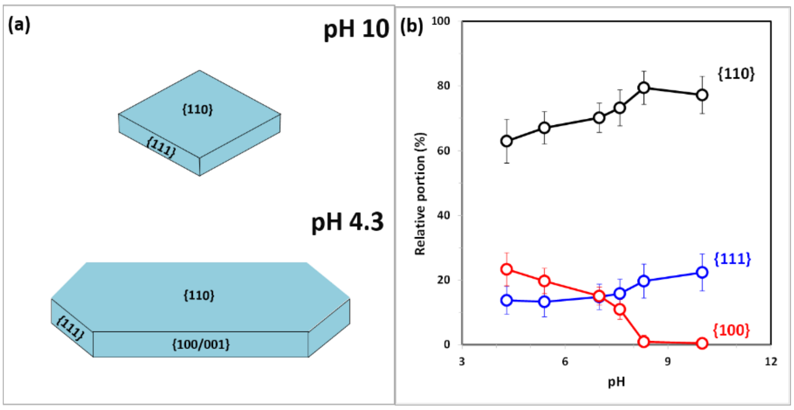

Figure 2.6. (a) Schematic diagram of γ-Al_2O_3 illustrating the different portions of (110), (111) and (100/001) facets at pH 4.3 and 10. (b) Relative portion of (110), (111) and (100) facets by TEM for platelet γ-Al_2O_3 in the entire range of pH. The error bars are shown from the standard derivation from the facet ratio of all counted alumina particles.

Diffuse reflectance infrared Fourier-transform (DRIFT) spectroscopic analysis was performed to investigate the typical properties of the synthesized alumina surface and the changes in surface hydroxyl groups with an increase in the (100) facet ratio. **Figure 2.7a** shows the hydroxyl region of the DRIFT spectrum. It is noteworthy that the peaks at 3766 cm^{-1} and 3660 cm^{-1} increase with increasing (100) facet ratio. Three types of OH groups are known to exist on the surface of γ-Al_2O_3: isolated OH (μ_1), bridged (μ_2) or triply-bridged OH (μ_3), but their exact assignments are still controversial.[3,5,8,9,26,29] Digne et al. have assigned the bands at 3766 cm^{-1} and 3660 cm^{-1} to the isolated hydroxyl group (μ_1) and triply bridged OH groups (μ_3) on the (100) facet, respectively.[8] Meanwhile, Busca has suggested that the band at 3766 cm^{-1} is either associated with or indicates the active sites, and originates from penta-coordinated Al^{3+} cations, or OH groups present in the vicinity of vacant sites, or in the exposed (100)/(110) corners.[3] Although the accurate origin of the band for hydroxyl group observed at 3766 cm^{-1} should be studied further, it is clear that these hydroxyl groups are related to the (100) facet ratio (**Figure 2.7b**). These results are somewhat different to those obtained by Dyan et al. and Busca et al. who have suggested that there are no significant changes in the hydroxyl groups of alumina with different morphologies or exposed surfaces.[3,47] The results of temperature-programmed desorption (TPD) of ethanol, which will be discussed later, suggest that the increase in the intensity of 3766 cm^{-1} and 3660 cm^{-1} peak with the elongation of the (100) facet may be related to the easier desorption as ethylene and increased number of active sites. It has already been shown that specific OH groups located on the surface are related to the alumina facets. Therefore, the acid-base properties of synthesized alumina are affected by the systematically controlled surface facet ratio, as evident by the consistently changing IR spectrum.

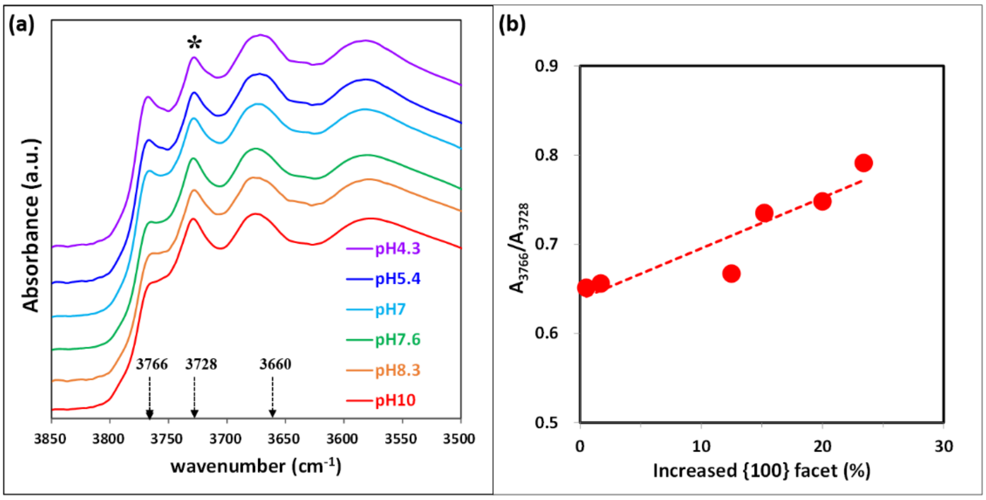

Figure 2.7. (a) DRIFT spectrum of platelet γ-Al_2O_3 measured for the entire pH range after activation at 500 °C and (b) relative absorbance ratio of 3766 cm^{-1} band with respect to 3728 cm^{-1} band as a function of the increased portion of (100) facets. The 3728 cm^{-1} band was shown as the asterisk (*) on **Figure 2.7a**.

The surface characteristics of faceted γ-Al_2O_3 were also investigated by ethanol TPD (**Figure 2.8**). Previous studies reported by our group have shown the ethanol TPD is a sensitive method that can be used to characterize the alumina surface.[32,33,48] Desorption profiles showed two peaks, one is observed below 150 °C, corresponding to the weakly bound ethanol and the other one (>150 °C) is dissociatively-adsorbed ethanol, which desorbed as ethylene. **Figure 2.8c** showed that the maximum desorption temperature of dissociative ethanol (T_d) showed a systematic decrease from 221.4 °C to 206.8 °C with increasing number of (100) facets. On the other hand, the dissociative EtOH sites/nm^2 increased from 1.17 to 1.45 sites/nm^2 with increasing ratio of (100) facets (**Figure 2.8d**). The increase in (100) facet ratio led to both easier desorption as ethylene and increased number of active sites.

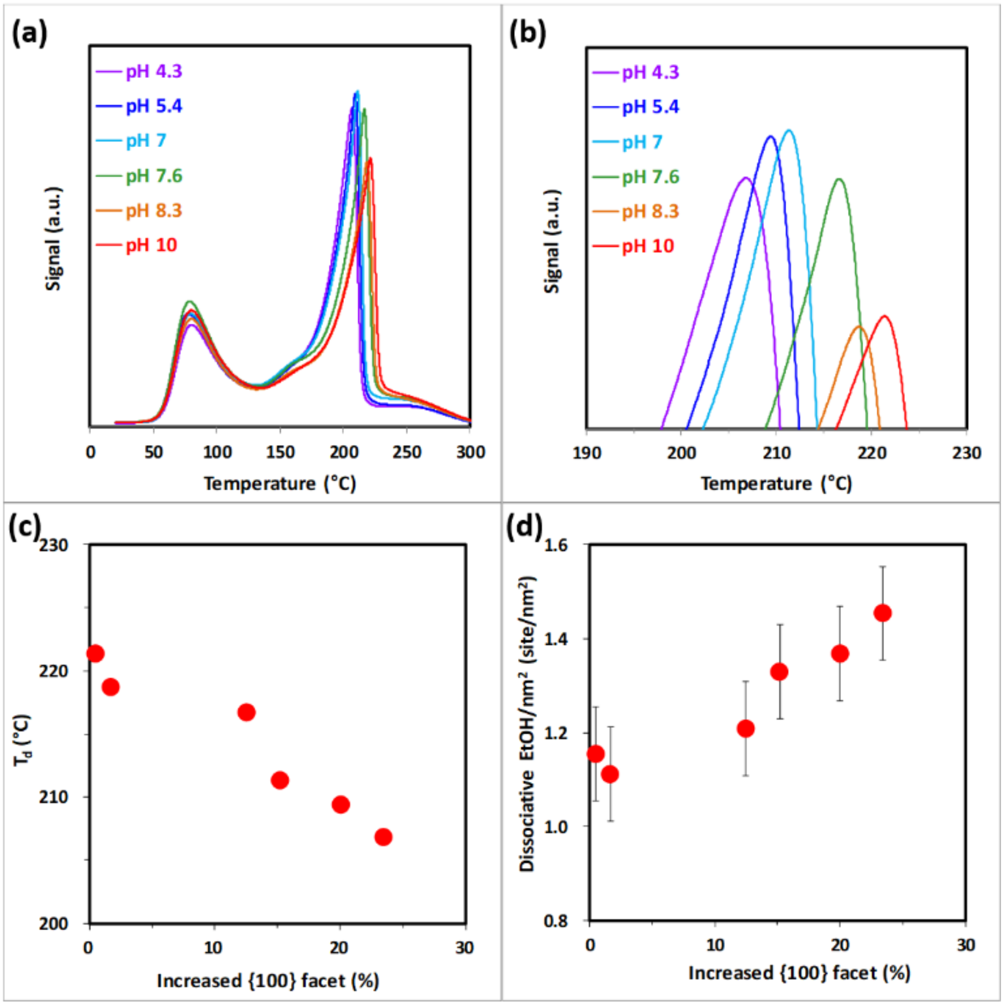

Figure 2.8. (a) Ethanol TPD for platelet γ-Al_2O_3 synthesized at different pH levels and (b) magnified views of maximum desorption rates regions. (c) Desorption temperature (at maximum rates of ethylene desorption, T_d) and (d) number of dissociative EtOH/nm^2 as a function of the ratio of {100} facet.

With the increase in this ratio, it was also expected to change the number of penta-coordinated Al^{3+} sites which are formed by the dehydroxylation of isolated hydroxyls on octahedral Al sites of (100) facets.[8,24] So, we performed solid-state ^{27}Al-NMR shown in **Figure 2.9** for more quantitative information of (100) facets from the number of penta-coordinated Al sites. All samples showed both tetrahedral and octahedral Al^{3+} sites around ~10 ppm and ~69 ppm chemical shifts. The amount of tetrahedral Al^{3+} sites were around 35% (the percentage of the total number of Al^{3+} sites), consistent with typical γ-Al_2O_3 spectrum.[24,41] Penta-coordinated Al^{3+} sites at 35 ppm chemical shift were also observed for three γ-Al_2O_3. However, the meaningful difference and quantification of penta-coordinated Al^{3+} sites were difficult due to lack of sensitivity (600 MHz) and low surface area of platelet γ-Al_2O_3 (**Figure 2.10**).

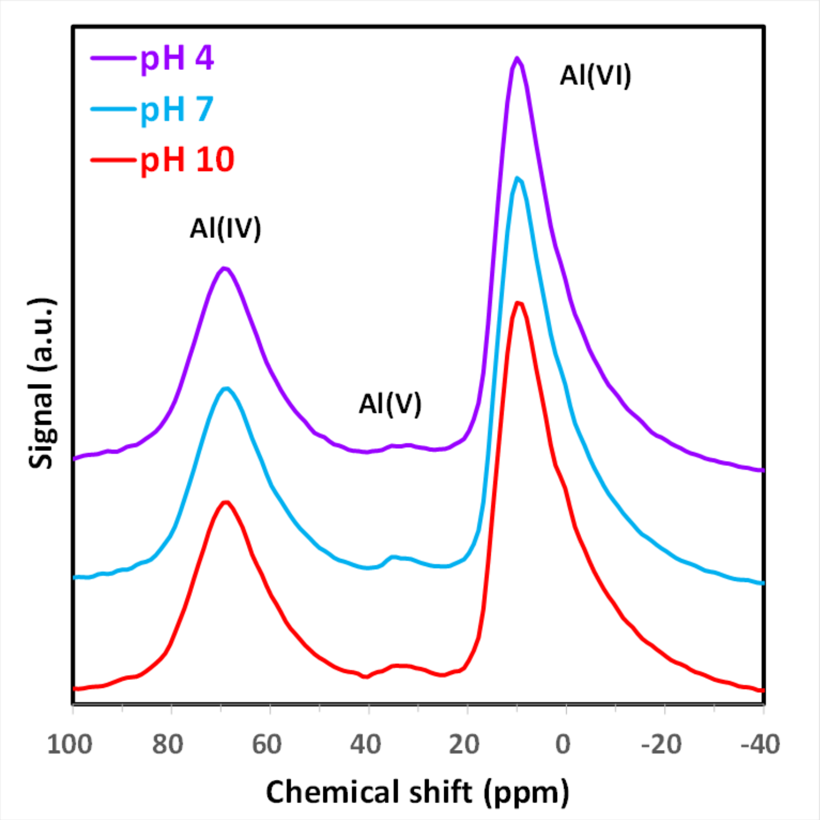

Figure 2.9. Solid ^{27}Al-MAS-NMR of γ-Al_2O_3 synthesized at pH 4, 7, and 10.

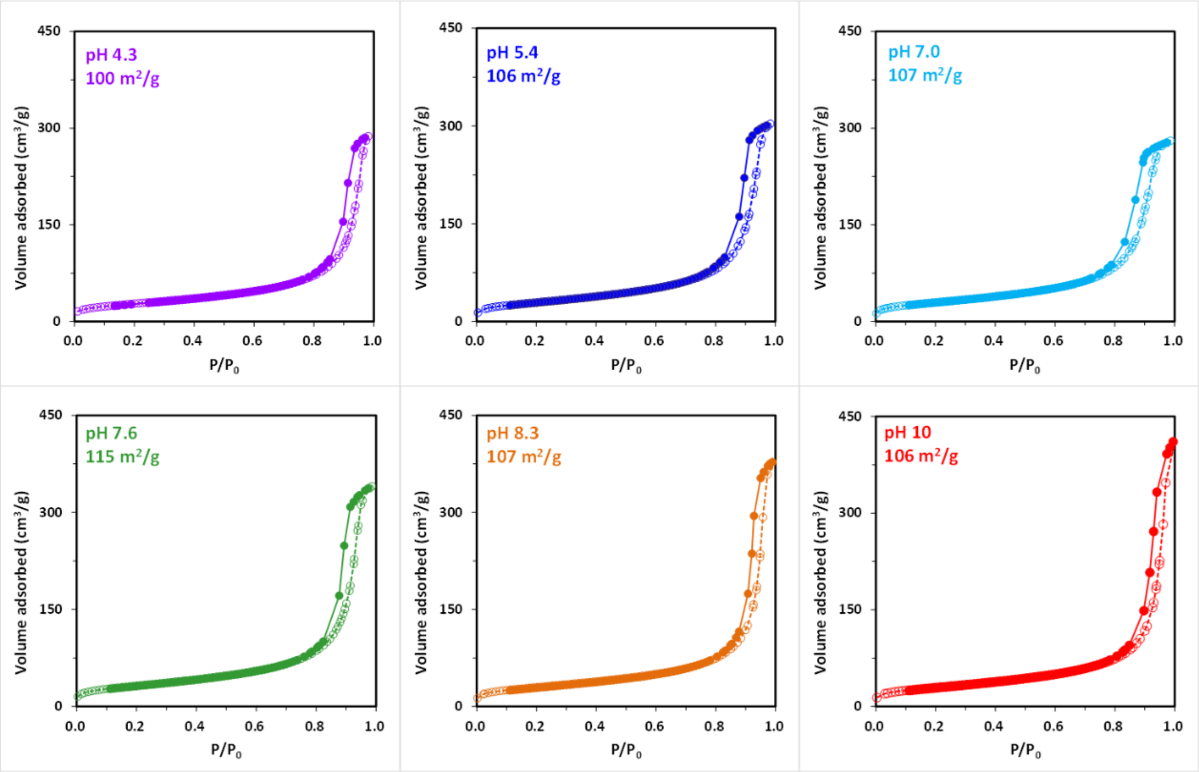

Figure 2.10. N_2 adsorption/desorption isotherms and BET surface areas for platelet γ-Al_2O_3. The isotherm profiles of platelet γ-Al_2O_3 are close to Type IV. BET surface areas were practically the same among platelet γ-Al_2O_3 synthesized at different pH condition.

Various characterization techniques confirmed a systematic increase in (100) facets on platelet γ-Al_2O_3. Next, it is important to investigate the influence of (100) facets on the catalytic activities on γ-Al_2O_3. For this purpose, ethanol dehydration was chosen as the model reaction. Ethanol dehydration on Al_2O_3 proceeds via two pathways, with one producing ethylene via intramolecular dehydration and the other producing ether via intermolecular dehydration.[4] Despite considerable efforts, the nature of the active sites for alcohol dehydration on γ-Al_2O_3 is still unclear.[4,12,33,49-56] **Figure 2.11a** shows the activity of faceted γ-Al_2O_3 for ethanol dehydration reaction at 180 °C and using 2% ethanol. Under these reaction conditions, the dominant product was ether (>98%). Interestingly, overall conversion increased from 2% to 3.9% with increasing (100) facet ratio. In addition, the ethylene yield almost doubled at the maximum but selectivity didn't show a significant difference (1.8–2 %–**Figure 2.11b**). We also carried out ethanol reaction measurements at 300 °C, where ethylene was the major product. **Figure 2.11c** showed an increase in conversion with increasing (100) facet. Under high temperature reaction condition, C_2H_4 yield clearly increased from 36.5 % to 54.6 % with increasing (100) facet. C_2H_4 selectivity also increased from 51.9 % to 70 % (**Figure 2.11d**). Increased selectivity to ethylene is consistent with ethanol TPD which showed easier desorption as ethylene for elongated platelet than rhombus platelet. Note that rhombus platelet where no apparent (100) facets exist showed catalytic activity for ethanol dehydration. Although no apparent (100) facets are shown in rhombus particles, (100) facets related to surface roughness on (110)/(111) facets or internal surface of pore might be related to catalytic activities for ethanol dehydration. The existence of 3766 cm^{-1} on rhombus platelet also might be related to these facets.

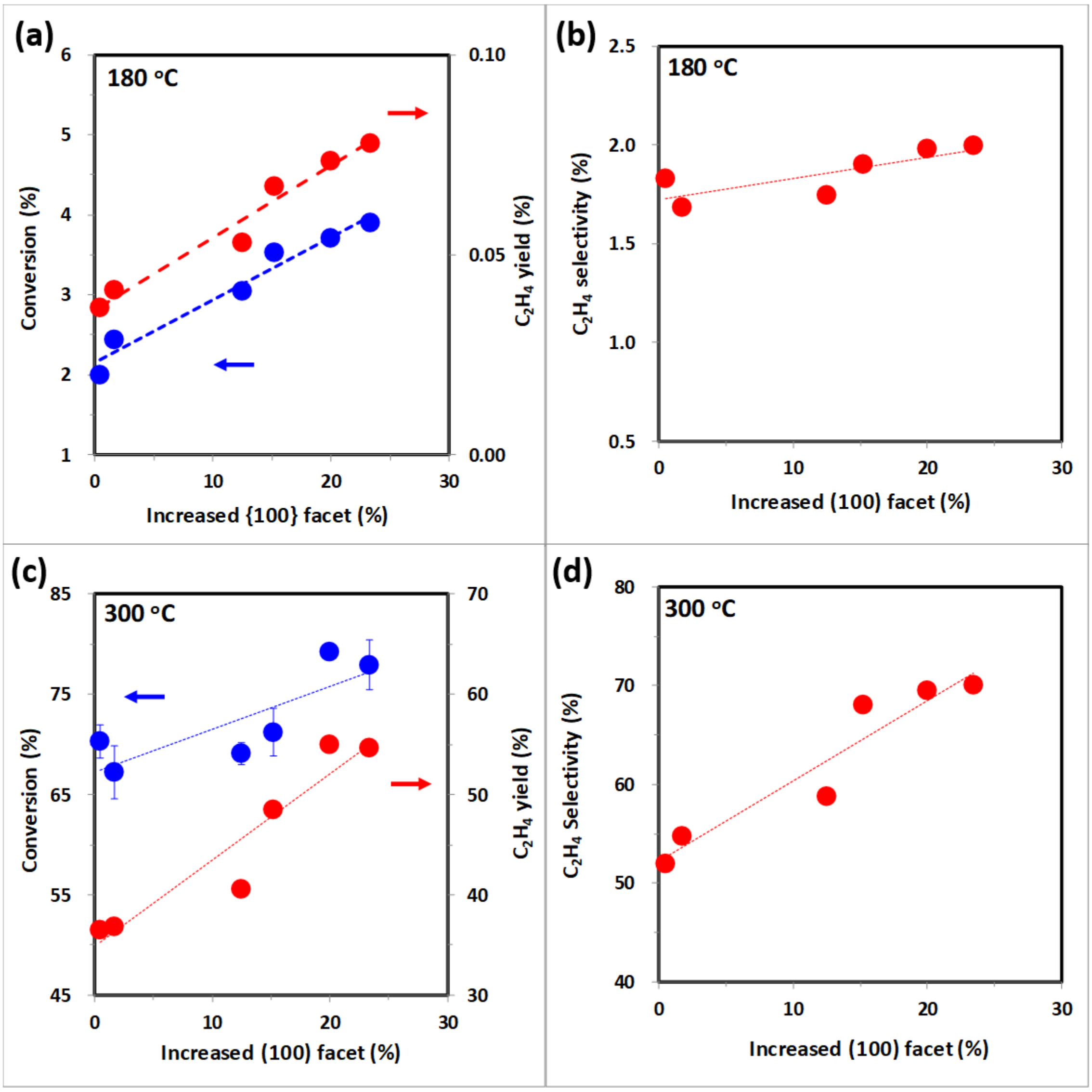

Figure 2.11. (a) Total conversion and ethylene yield and (b) ethylene selectivity for ethanol dehydration as a function of the increased portion of (100) facets at 180 °C. (c) Total conversion and ethylene yield and (d) ethylene selectivity for ethanol dehydration as a function of the increased portion of (100) facets at 300 °C.

The increase in catalytic activity for ethanol dehydration is closely related to the intense hydroxyl bands around 3766 cm^{-1}. Srinivasan et al. have demonstrated a correlation between the intensity of the band at 3770 cm^{-1} with the most reactive transition alumina studied by them.[57] In this work, the ratio of (100) facet was increased by controlling the morphology of γ-Al_2O_3, which also led to the intense band at 3766 cm^{-1} (**Figure 2.7b**) and increase in catalytic activity for ethanol dehydration. These results clearly demonstrate the catalytic role of (100) facet for ethanol dehydration reaction on γ-Al_2O_3. It has been proposed that (100) facet is the active site of the alcohol dehydration reaction. This was confirmed by showing that there is a one-to-one correlation between the number of dissociative ethanol and the penta-coordinated Al sites created by dehydroxylation of hydroxyls on (100) facets.[25, 33] Recently, Larmier et al. have reported based on a combination of experimental and DFT studies that the reaction pathways involved in isopropyl alcohol dehydration require the active sites on (100) facets.[52] However, experimental evidence of facet-dependent activities for ethanol dehydration on Al_2O_3 was still missing. The strong correlation between (100) facet ratio and ethanol dehydration activity given in this work provides the direct evidence of the critical role of the (100) facet for ethanol dehydration on γ-Al_2O_3. Here, we can't exclude the possibility of a catalytic role for defect sites (edge/corner) suggested by Busca group.[3,12] However, these edges of the corner are also closely related with (100) facets. The edges of (100)/(110) also consistently increase with increasing (100) facets on elongated platelet (**Figure 2.12**). In conclusion, (100) facets are closely related to the catalytic activity for ethanol dehydration.

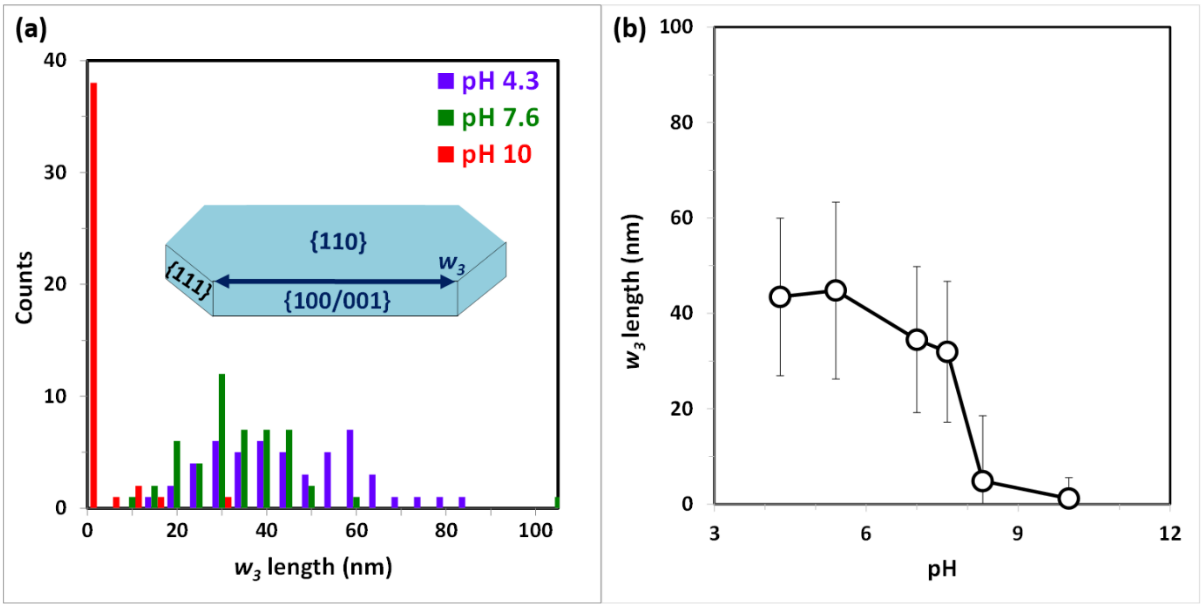

Figure 2.12. (a) Length of w_3 (edge on (100)/(110)) for platelet γ-Al_2O_3 at selected pH. The inset showed the scheme of elongated platelet. (b) Length of w_3 for platelet γ-Al_2O_3 as a function of pH. 50 particles were counted in low magnification TEM images of platelet γ-Al_2O_3.

2.5. Conclusion

We investigated the effect of crystal facets on the catalytic behavior of platelet γ-Al_2O_3 by X-ray diffraction, transmission electron microscopy, temperature-programmed desorption of ethanol, solid-state ^{27}Al NMR, infrared spectroscopy, and ethanol dehydration reaction. A series of platelet γ-Al_2O_3 was synthesized with a systematic increase in (100) facet ratio confirmed by TEM. FT-IR results also showed consistent results supporting a systematic change of (100) facets from the linear relationship between (100) facet and the intensity of 3766 cm^{-1} peak. Ethanol dehydration activity measurements showed that ethylene formation increased with increasing (100) facets, clearly demonstrating the critical role of these facets as active sites for ethanol dehydration on γ-Al_2O_3. The increased (100) facet ratio led to easier desorption as ethylene evidenced by the lower T_d for dissociative ethanol sites from the ethanol TPD study and increased catalytic activities for ethanol dehydration. These results clearly demonstrated the catalytic role of (100) facet for ethanol dehydration on γ-Al_2O_3. These results contribute to the fundamental understanding of crystalline facets on γ-Al_2O_3 and other industrially important catalytic material.

2.6. References

[1] Levin, I.; Brandon, D. *J. Am. Ceram. Soc.* **1998,** *81*, 1995-2012.

[2] Trueba, M.; Trasatti, S. P. *Eur. J. Inorg. Chem.* **2005,** *2005*, 3393-3403.

[3] Busca, G. *Catal. Today* **2014,** *226*, 2-13.

[4] Knözinger, H. *Angew. Chem. Int. Ed.* **1968,** *7*, 791-805.

[5] Peri, J. B. *J. Phys. Chem.* **1965,** *69*, 220-230.

[6] Nortier, P.; Fourre, P.; Saad, A. B. M.; Saur, O.; Lavalley, J. C. *Appl. Catal.* **1990,** *61*, 141-160.

[7] Krokidis, X.; Raybaud, P.; Gobichon, A.-E.; Rebours, B.; Euzen, P.; Toulhoat, H. *J. Phys. Chem. B* **2001,** *105*, 5121-5130.

[8] Digne, M.; Sautet, P.; Raybaud, P.; Euzen, P.; Toulhoat, H. *J. Catal.* **2002,** *211*, 1-5.

[9] Digne, M.; Sautet, P.; Raybaud, P.; Euzen, P.; Toulhoat, H. *J. Catal.* **2004,** *226*, 54-68.

[10] Wischert, R.; Laurent, P.; Coperet, C.; Delbecq, F.; Sautet, P. *J. Am. Chem. Soc.* **2012,** *134*, 14430-14449.

[11] Raybaud, P.; Chizallet, C.; Mager-Maury, C.; Digne, M.; Toulhoat, H.; Sautet, P. *J. Catal.* **2013,** *308*, 328-340.

[12] Phung, T. K.; Lagazzo, A.; Rivero Crespo, M. Á.; Sánchez Escribano, V.; Busca, G. *J. Catal.* **2014,** *311*, 102-113.

[13] Euzen, P.; Raybaud, P.; Krokidis, X.; Toulhoat, H.; Le Loarer, J.-L.; Jolivet, J.-P.; Froidefond, C. Alumina. In Handbook of Porous Solids; Schüth, F., Sing, K. S. W., Weitkamp, J. Eds.; Wiley-VCH Verlag GmbH:Weinheim, 2002; Vol. 3, pp 1591-1677.

[14] Kwak, J. H.; Hu, J.; Mei, D.; Yi, C.-W.; Kim, D. H.; Peden, C. H. F.; Allard, L. F.; Szanyi, J. *Science* **2009,** *325*, 1670-1673.

[15] Li, Y.; Shen, W. *Chem. Soc. Rev.* **2014,** *43*, 1543-1574.

[16] Sun, M.; Nelson, A. E.; Adjaye, J. *J. Phys. Chem. B* **2006,** *110*, 2310-2317.

[17] Pinto, H. P.; Nieminen, R. M.; Elliott, S. D. *Phys. Rev. B* **2004,** *70*, 125402.

[18] Bara, C.; Plais, L.; Larmier, K.; Devers, E.; Digne, M.; Lamic-Humblot, A.-F.; Pirngruber, G. D.; Carrier, X. *J. Am. Chem. Soc.* **2015,** *137*, 15915-15928.

[19] Kovarik, L.; Bowden, M.; Genc, A.; Szanyi, J.; Peden, C. H. F.; Kwak, J. H. *J. Phys. Chem. C* **2014,** *118*, 18051-18058.

[20] Kovarik, L.; Bowden, M.; Shi, D.; Washton, N. M.; Andersen, A.; Hu, J. Z.; Lee, J.; Szanyi, J.; Kwak, J. H.; Peden, C. H. F., *Chem. Mater.* **2015,** *27*, 7042-7049.

[21] Zhou, R.-S.; Snyder, R. L., *Acta Crystallogra.* **1991,** *B47*, 617-630.

[22] Digne, M.; Raybaud, P.; Sautet, P.; Rebours, B.; Toulhoat, H. *J. Phys. Chem. B* **2006,** *110*, 20719-20720.

[23] Billinge, S. J. L.; Levin, I. *Science* **2007,** *316*, 561-565.

[24] Kwak, J. H.; Hu, J.; Kim, D.; Szanyi, J.; Peden, C. *J. Catal.* **2007,** *251*, 189-194.

[25] Hu, J. Z.; Xu, S.; Kwak, J. H.; Hu, M. Y.; Wan, C.; Zhao, Z.; Szanyi, J.; Bao, X.; Han, X.; Wang, Y.; Peden, C. H. F. *J. Catal.* **2016,** *336*, 85-93.

[26] Tsyganenko, A. A.; Mardilovich, P. P. *J. Chem. Soc., Faraday Trans.* **1996,** *92*, 4843-4852.

[27] Szanyi, J.; Kwak, J. H. *Phys. Chem. Chem. Phys.* **2014,** *16*, 15117-15125.

[28] Morterra, C.; Magnacca, G. *Catal. Today* **1996,** *27*, 497-532.

[29] Knözinger, H.; Ratnasamy, P. *Catal. Rev. Sci. Eng.* **1978,** *17*, 31-70.

[30] Rozita, Y .; Brydson, R.; Comyn, T. P.; Scott, A. J.; Hammond, C.; Brown, A.; Chauruka, S.; Hassanpour, A.; Young, N. P.; Kirkland, A. I.; Sawada, H.; Smith, R. I. *ChemCatChem* **2013,** *5*, 2695-2706.

[31] Srinivasan, S.; Narayanan, C. R.; Biaglow, A.; Gorte, R.; Datye, A. K. *Appl. Catal., A* **1995,** *132*, 271-287.

[32] Kwak, J. H.; Peden, C. H. F.; Szanyi, J. N. *J. Phys. Chem. C* **2011,** *115*, 12575-12579.

[33] Kwak, J. H.; Mei, D.; Peden, C. H. F.; Rousseau, R.; Szanyi, J. *Catal. Lett.* **2011,** *141*, 649-655.

[34] Lippens, B. C. TU Delft, Delft University of Technology, 1961.

[35] He, T.; Xiang, L.; Zhu, S. *CrystEngComm* **2009,** *11*, 1338-1342.

[36] Zhang, L.; Jiao, X.; Chen, D.; Jiao, M., *Eur. J. Inorg. Chem.* **2011,** *2011*, 5258-5264.

[37] Pardo, P.; Montoya, N.; Alarcón, J. *CrystEngComm* **2015,** *17*, 2091-2100.

[38] Pardo, P.; Serrano, F. J.; Vallcorba, O.; Calatayud, J. M.; Amigó, J. M.; Alarcón, J. *Cryst. Growth Des.* **2015,** *15*, 3532-3538.

[39] Santos, P. d. S.; Coelho, A. C. V.; Santos, H. d. S.; Kiyohara, P. K. *Mater. Res.* **2009,** *12*, 437-445.

[40] Sakashita, Y.; Araki, Y.; Shimada, H. *Appl. Catal., A* **2001,** *215*, 101-110.

[41] Lee, J.; Jeon, H.; Oh, D. G.; Szanyi, J.; Kwak, J. H. *Appl. Catal., A* **2015,** *500*, 58-68.

[42] Chen, X. Y.; Zhang, Z. J.; Li, X. L.; Lee, S. W. *Solid State Commun.* **2008,** *145*, 368-373.

[43] Lee, J.; Szanyi, J.; Kwak, J. H. *Mol. Catal.* **2017,** *434*, 39-48.

[44] Kovarik, L.; Genc, A.; Wang, C.; Qiu, A.; Peden, C. H. F.; Szanyi, J.; Kwak, J. H. *J. Phys. Chem. C* **2013,** *117*, 179-186.

[45] Jolivet, J.-P.; Froidefond, C.; Pottier, A.; Chanéac, C.; Cassaignon, S.; Tronc, E.; Euzen, P. *J. Mater. Chem.* **2004,** *14*, 3281-3288.

[46] Kovarik, L.; Wang, C.; Peden, C. H. F.; Szanyi, J.; Kwak, J. H.; Genc, A. *Microscopy and Microanalysis* **2012**, *18*, 1302–1303.

[47] Dyan, A.; Cenedese, P.; Dubot, P. *J. Phys. Chem. B* **2006,** *110*, 10041-10050.

[48] Lee, J.; Jang, E. J.; Kwak, J. H. *J. Catal.* **2017,** *345*, 135-148.

[49] DeWilde, J. F.; Chiang, H.; Hickman, D. A.; Ho, C. R.; Bhan, A. *ACS Catal.* **2013,** *3*, 798-807.

[50] DeWilde, J. F.; Czopinski, C. J.; Bhan, A. *ACS Catal.* **2014,** *4*, 4425-4433.

[51] Kang, M.; DeWilde, J. F.; Bhan, A. *ACS Catal.* **2015,** *5*, 602-612.

[52] Larmier, K.; Nicolle, A.; Chizallet, C.; Cadran, N.; Maury, S.; Lamic-Humblot, A.-F.; Marceau, E.; Lauron-Pernot, H. *ACS Catal.* **2016,** *6*, 1905-1920.

[53] Larmier, K.; Chizallet, C.; Cadran, N.; Maury, S.; Abboud, J.; Lamic-Humblot, A.-F.; Marceau, E.; Lauron-Pernot, H. *ACS Catal.* **2015,** *5*, 4423-4437.

[54] Christiansen, M. A.; Mpourmpakis, G.; Vlachos, D. G. *ACS Catal.* **2013,** *3*, 1965-1975.

[55] Jenness, G. R.; Christiansen, M. A.; Caratzoulas, S.; Vlachos, D. G.; Gorte, R. J. *J. Phys. Chem. C* **2014,** *118*, 12899-12907.

[56] Christiansen, M. A.; Mpourmpakis, G.; Vlachos, D. G. *J. Catal.* **2015,** *323*, 121-131.

[57] Srinivasan, S.; Narayanan, C. R.; Datye, A. K. *Appl. Catal., A* **1995,** *132*, 289-308.

3. Acid-base properties of Al_2O_3: effects of morphology, crystalline phase, and additives

This chapter contains the published result.

Lee, J.; Jang, E.J.; Kwak, J.H. *J. Catal.* **2017**, *345*, 135-148.

3.1. Abstract

The acid-base properties of Al_2O_3 with various surface characteristics were studied by XRD, HR-TEM, ethanol TPD, and ethanol dehydration reaction rate measurements. Ethanol TPD showed that the desorption temperature (at a maximum rate of ethylene desorption, T_d) of dissociative ethanol was significantly dependent on morphology, crystalline phase, and additives. Ethylene formation rates, normalized with respect to the amount of dissociative ethanol (quantified by ethanol TPD), exhibited an inverse correlation with T_d on Al_2O_3 with various morphologies, crystalline phases, and additives, which suggests that T_d can be used as a descriptor for acid-base properties of Al_2O_3, irrespective of modification origins. This also indicates that the dissociative ethanol (ethoxide) is the key intermediate of ethylene formation during ethanol dehydration on Al_2O_3. The activities and activation barriers of commercial Al_2O_3 were consistent with our empirical model. This fundamental understanding of the acid-base properties of alumina is helpful for the further development of new catalysts with better activity and selectivity.

3.2. Introduction

γ-Al_2O_3 is one of the most important heterogeneous catalyst materials and is mainly used as a support for catalytically active phases (metal and oxide) owing to its textural properties, such as high surface area and thermal stability.[1-3] Al_2O_3-based catalysts have wide applications, ranging from petroleum chemistry to automobile emission control. In addition, γ-Al_2O_3 itself is a well-known acidic catalyst for alcohol dehydration reactions.[4-12]

The catalytic properties (activity, selectivity, and distribution of active phases on the support) of oxides are directly correlated with their surface characteristics since chemical processes mainly occur on the surfaces of catalysts.[3,5,8,13-23] Therefore, considerable efforts have been devoted to elucidating the surface characteristics of Al_2O_3. Based on the results of infrared (IR) spectroscopy measurements, γ-Al_2O_3 is known to have different types of surface hydroxyls: isolated hydroxyls (coordinated by tetrahedral or octahedral Al sites) and bridging or triply bridging hydroxyls, although the assignments of hydroxyl groups vary among researchers.[3,13-15,17] Later, Digne and Sautet et al. proposed their own γ-

Al_2O_3 model, showing that surface dehydroxylation depends on both temperature and the exposed facets [16, 17]. Moreover, exposure to high temperature leads to the transformation of alumina from the γ- to the δ-, θ-, and finally α-phase, resulting in different catalytic properties.[1,3,19] Finally, the catalytically active phases (Pt, Pd, etc.) supported on γ-Al_2O_3 affect the catalytic properties of Al_2O_3-based catalysts.[21,24,25]

Despite numerous studies, the fundamental understanding of the Al_2O_3 surface is still limited due to the complexity of Al_2O_3-based catalysts.[1-3,16,17,19,26,27] The complexity mainly originates from the unresolved structure of γ-Al_2O_3. The γ-Al_2O_3 model proposed by Digne and Sautet et al. is the most popular, but the vacancies of Al sites are still under debate.[16,17,26,27] Also, γ-Al_2O_3 can be prepared under various conditions (different precursors, pH, thermal treatments, and additives),[19,28] which leads to the modification of Al_2O_3 surface characteristics and makes the rationalization of specific catalytic properties very difficult because characterization of the modified alumina surface (morphology, phase, additives, etc.) is complicated. For decades, various physicochemical methods have been used to characterize the alumina surface.[1,8,14,18,27,29,30] However, the use of well-established techniques, e.g., X-ray diffraction (XRD), was not straightforward due to the small domain size and low crystallinity.[1] Nuclear magnetic resonance (NMR) spectroscopy provides information on Al site environments (tetrahedral, pentahedral, and octahedral).[18,20,31-33] However, low sensitivity prevents the complete description of Al sites on the alumina surface. Recent studies have reported that the visibility of Al sites is still limited because the sensitivities depend significantly on the hydration states of Al sites.[33] High-resolution transmission electron microscopy (HR-TEM) studies have also shown surface reconstruction and Al-defect-rich surfaces,[27,30] indicating that the elucidation of the alumina surface is difficult. Furthermore, it is very difficult to determine the influence of each factor (morphology, crystalline phase, additives) on the surface characteristics separately.

Recently, we reported that ethanol temperature-programmed desorption (TPD) is very sensitive to Al_2O_3 surface properties,[22, 34, 35] being able to detect the early initiation of phase transformations on the surface of Al_2O_3, which is not possible for a bulk analysis technique (XRD).[22] We have also reported that the desorption of dissociative ethanol (mainly as ethylene) was affected by the morphology, phase, and additives.[23, 35, 36] This indicates that the desorption temperature of dissociative ethanol can be used to describe the surface characteristics of Al_2O_3. Narayanan et al. showed that the desorption temperature of isopropanol on the alumina surface (as propene) correlated inversely with the alcohol dehydration activity.[37] Srinivasan et al. further showed that the effect of Na was more significant for modifying catalyst activity than the crystalline phase in alcohol dehydration.[38] However, universal correlation of desorption temperature with catalytic activity among Al_2O_3 catalysts with various surface characteristics (morphology, crystalline phase, additives) is limited because each modification may affect more than one property of the investigated Al_2O_3. A deeper understanding of this correlation will enable the generalization of the effect of each factor (morphology, crystalline phase, and additives) on the surface characteristics of modified Al_2O_3 catalysts.

In this study, we correlated the desorption temperature (at a maximum rate of ethylene desorption, T_d) of dissociative ethanol with the catalytic behavior of Al_2O_3 surfaces with various modification origins (morphologies, phases, and additives) using an acid-catalyzed model reaction (ethanol dehydration). For general insight into the effect of each factor on surface modification, we prepared Al_2O_3 with different morphologies (platelet and rod), transition aluminas, and Al_2O_3 supported by metal oxides. Based on a combined ethanol TPD/dehydration study, we could demonstrate that ethylene TOF was inversely proportional to the T_d of dissociative ethanol independent of the nature of the modification. This empirically correlated trend suggests that T_d can be used as a descriptor for the acid-base properties of Al_2O_3 with various modification origins.

3.3. Experimental section

3.3.1. Materials

Puralox SBA-200 (Sasol) was used as a reference because it is composed of essentially pure γ-Al_2O_3 (with no surface modification by alkali metals (Na_2O 20 ppm)) and has been extensively studied as a γ-Al_2O_3 standard.

We synthesized a series of aluminas with different morphologies (platelet and rod) based on previous reports.[39] Platelet-hexagon Al_2O_3 was synthesized by changing the stirring time (19 days). We also prepared a series of transition aluminas by exposing γ-Al_2O_3 to high temperatures. Puralox SBA-200 samples (1 g) were calcined in air at different temperatures (700, 800, 900, 950, 1000, and 1100 °C) for 3 h using a muffle furnace. After calcination, the presence of the crystalline phase was confirmed by XRD. Finally, we synthesized a series of metal/metal oxide-modified Al_2O_3 samples by using an incipient wetness method using appropriate nitrate-based precursors. With the same incipient wetness method, 1 wt% Pt/SiO_2 was prepared on silica gel (Aldrich, technical grade 40).

We also used commercial aluminas HP-14 (Sasol, Na_2O 20 ppm), Siralox 1.5/100 (Sasol, SiO_2 1.5% and Na_2O 20–100 ppm), Strem 13-2525, and Brockmann I acidic (Aldrich, Na_2O 4000 ppm and Cl 0.14 mmol/g). Information on sample composition was provided by the manufacturers.

3.3.2. Catalyst characterizations

XRD spectra were recorded on a Bruker D8 Advance A25 instrument using Cu K_α radiation (λ = 1.54 Å) in step mode between 2θ values of 5° and 75°, with a step size of 0.02°/s. The morphologies of

Al_2O_3 were confirmed by TEM (JEOL JEM-2100). The specific surface area was determined using the Brunauer-Emmett-Teller (BET) method using a BELSORP-Max instrument (BEL).

Ethanol TPD was carried out using the experimental procedures described in our previous report.[34] Prior to TPD experiments, 0.05 g of alumina was calcined at 500 °C for 1 h under 20% O_2/He flow (1.0 mL/s). Afterward, the sample was cooled to room temperature, and ethanol adsorption was carried out for 30 min using a 2.0% ethanol/He gas mixture (1.0 mL/s), followed by a 30 min He purge to remove weakly bound ethanol molecules. After stabilization of the flame ionization detector (FID) signal of the Agilent 7820A gas chromatograph (GC), TPD experiments were carried out under a flow of He (1.0 mL/s), with a heating rate of 10 °C/min. The reactor outlet was directly connected to the FID (i.e., no GC separation was performed).

We denote the temperature of the maximum rate of ethylene desorption (>150 °C) as T_d in this study. T_d was very sensitive to experimental conditions (pressure drop, reactor, thermocouple contact, etc.). To remove experimental errors and simplify data treatment, we used the difference in desorption temperature, ΔT_d (T_d of sample − T_d of Puralox SBA-200). Reproducibility tests confirmed that the T_d error was ±2 °C.

Ethanol dehydration tests were performed in a quartz flow reactor using 0.01 g samples (60–100 mesh) supported by quartz wool. When the activity was too low to be detected, 0.05–0.08 g samples were used. Samples were kept under a 20% O_2/He flow at 500 °C for 1 h. The carrier gas (He) was passed through a bubbler containing ethanol (99.5%, Sigma Aldrich) at 24 °C and ambient pressure. The concentration of ethanol in the gas mixture (2%) was controlled by the relative He flow rate (total flow rate of He was 2.0 mL/s). The outlet gases were analyzed by GC (Agilent 7820A with an HP-FFAP column and FID). The reaction rates quoted were the initial reaction rates. Since the investigated Al_2O_3 samples mostly showed stable activity profiles, the initial reaction rates were similar to steady-state reaction rates. However, Pt/Al_2O_3 was deactivated during the reaction, making it necessary to use initial reaction rates. The overall activities for ethanol dehydration were compared at the same reaction temperature (180 °C), and apparent activation energies were obtained for a temperature range of 170–190 °C under differential conditions (less than 10% conversion). The turnover frequency (TOF, converted molecules/number of sites·s) was calculated by normalizing the specific reaction rates (molecules/nm^2·s) to the number of sites where ethanol was dissociatively adsorbed (number of sites/nm^2), which was quantified from ethanol TPD.

To characterize the changes in the surface characteristics of alumina after the reaction, ethanol TPD was performed after the reaction at 180 °C for the designated times, and the samples were cooled under He flow. After purging for 30 min, ethanol TPD was carried out as described previously.

The size of Pt clusters in 1% Pt/Al_2O_3 (fresh and reacted) was confirmed by high-angle annular dark-field scanning transmission electron microscopy (HAADF-STEM) imaging using a JEOL JEM-2100F microscope operated at 200 kV. Fresh 1% Pt/Al_2O_3 was calcined at 500 °C for 1 h under 20% O_2/He flow (flow rate = 1 mL/s). After cooling to room temperature, the samples were kept in a desiccator prior to TEM measurements. TEM images of the 1% Pt/Al_2O_3 catalyst were recorded after the ethanol dehydration reaction test was conducted for 90 min at 180 °C. The cluster size distribution was obtained by measuring 130 clusters for both samples.

3.4. Results and Discussion

In this study, our main goal was to correlate the effect of three factors (morphology, crystalline phases, and additives) on the surface characteristics of Al_2O_3. Puralox SBA-200 (Sasol) was chosen as a reference γ-Al_2O_3. All data were interpreted based on comparison with Puralox SBA-200.

3.4.1. *Morphology effects*

To investigate the influence of morphology on the surface characteristics of Al_2O_3, aluminas with different morphologies were synthesized, based on previous studies.[39] XRD analysis confirmed that all synthesized aluminas were γ-phase (**Figure 3.1a**). TEM imaging confirmed the morphological differences between the synthesized aluminas (**Figure 3.1b**). Puralox showed agglomerated nanoparticles with irregular shapes. The synthesized platelet Al_2O_3 had rhombus-shaped particles with 20–80 nm in size. The main surface of platelet Al_2O_3 was defined by the (110) plane, and the side surface was defined by (111) planes.[27] Rod Al_2O_3 had long rod-shaped particles with lengths of 50–170 nm. Rod Al_2O_3 is known to grow in the (111) direction with exposed (100) facets.[39] After prolonged mixing, the morphology of platelet alumina changed to a hexagonal shape. Detailed electron diffraction results confirmed that the amount of (100) facets increased for hexagonal-shaped particles compared to that for the rhombus-shaped ones.[28] Although each facet ratio could not be quantified exactly, it is clear that platelet-hexagon Al_2O_3 had more (100) facets than platelet Al_2O_3.

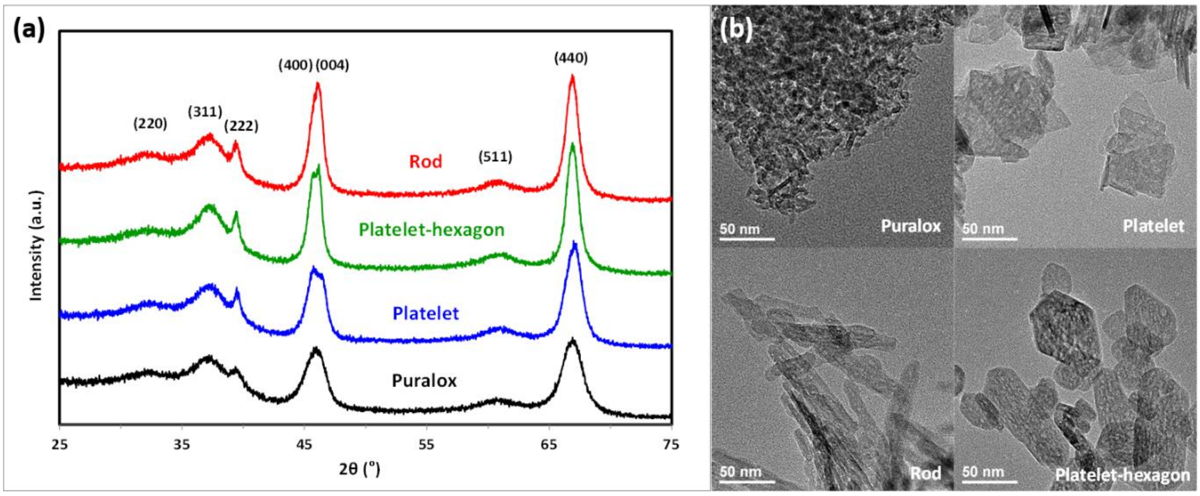

Figure 3.1. (a) XRD patterns and (b) TEM images for Puralox SBA-200 and synthesized platelet, platelet-hexagon, and rod Al_2O_3.

In order to investigate the surface characteristics of γ-Al_2O_3 with different morphologies, ethanol TPD studies were conducted, and two main desorption peaks were observed (**Figure 3.2a**). Similar to our previous studies, the lower-temperature peak (<150 °C) originated from molecularly bound ethanol and the high-temperature peak (>150 °C) stemmed mostly from ethylene formed by dissociative adsorption of ethanol (ethoxide) and the subsequent dehydration on the alumina surface.[34, 35] Here, we focused on the desorption temperature (T_d) of dissociative ethanol. The reference, Puralox SBA-200, exhibited a T_d at 223 °C. Platelet Al_2O_3 had an almost identical T_d, but rod Al_2O_3 exhibited a T_d that was 9 °C lower than that of Puralox SBA-200. Interestingly, platelet-hexagon Al_2O_3 had a T_d that was 4 °C lower than that of platelet γ-Al_2O_3. The order of T_d could be summarized as follows: rod < platelet-hexagon < platelet = Puralox. This order is consistent with results from our previous study (rod < platelet = Puralox).[35] Ethanol TPD demonstrated that the morphology affects the acidity of the γ-Al_2O_3 surface. It can be summarized that T_d decreased with increasing (100) facet exposure.

In this study, our main goal was to correlate T_d with the catalytic behavior of the Al_2O_3 surface. Hence, we correlated T_d with ethanol dehydration reaction rates. To obtain this correlation, the TOF was normalized with respect to the amount of dissociatively adsorbed ethanol (quantified by ethanol TPD). Ethanol dehydration on Al_2O_3 is known to proceed via two pathways, with one producing ethylene through intramolecular dehydration and the other producing ether through intermolecular dehydration. Under the reaction conditions used (180 °C, 2% ethanol), ether was the major product (>97%). γ-aluminas with T_d values lower than those of the reference γ-Al_2O_3 (rod and platelet-hexagon) showed higher ethylene formation TOFs (**Figure 3.2b**). Overall, the TOF of ethylene formation was inversely proportional to T_d. This inverse proportionality between activity (TOF) and T_d was also observed for ether (**Figure 3.2c**).

Next, the relationship between the apparent activation energy barrier (E_a) and T_d was studied. The activation energy barriers for Puralox SBA-200 was 159 kJ/mol for ethylene and 93 kJ/mol for ether formation (**Figure 3.2d**), which are consistent with the results of our previous study.[35] For γ-Al_2O_3 with different morphologies, the activation energy barriers for ethylene and ether formation were similar to those of the reference γ-Al_2O_3. In summary, Al_2O_3 with different morphologies had different surface acidity characteristics ($\Delta T_d < 10$ °C), but exhibited similar E_a for ethylene and ether formation. This can be related to the fact that the T_d difference was too small to investigate the change of apparent activation barriers, which will be discussed later.

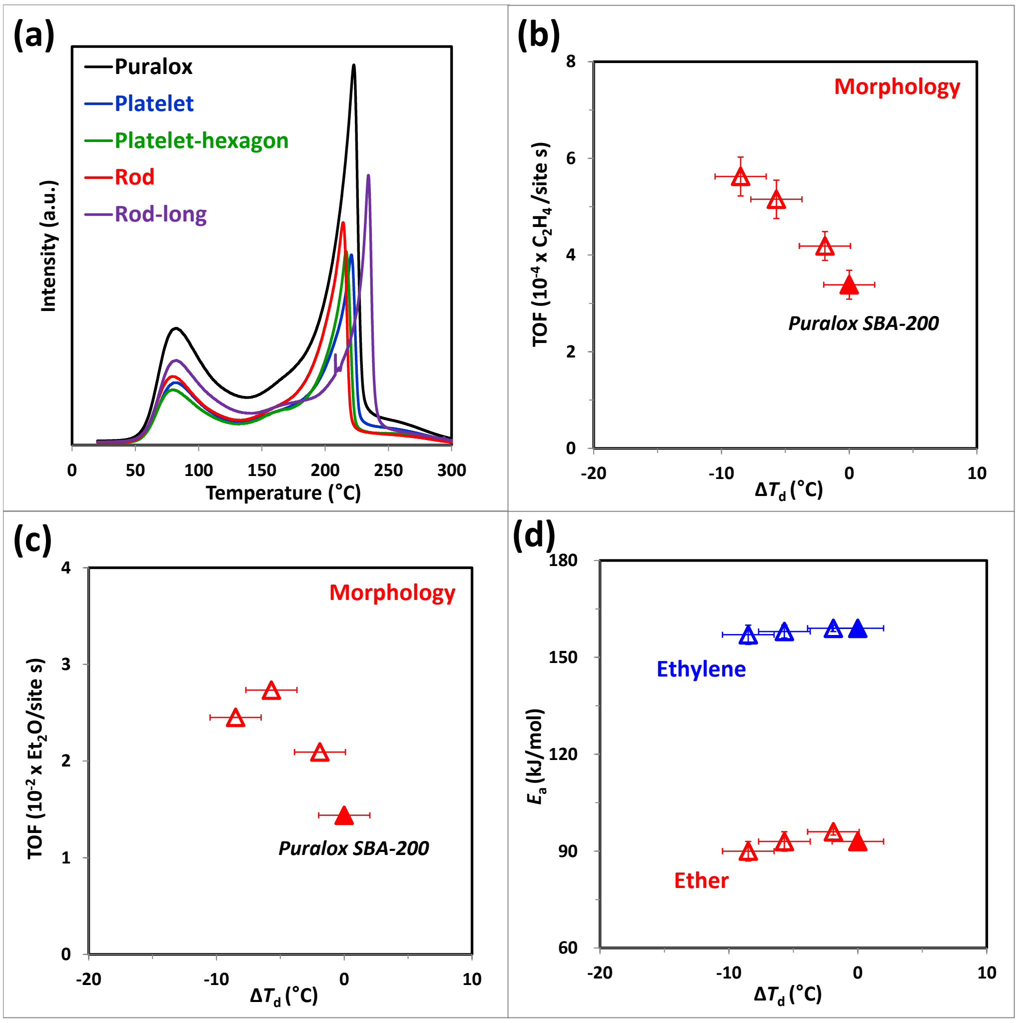

Figure 3.2. (a) Ethanol TPD for Puralox SBA-200 and the synthesized platelet, platelet-hexagon, and rod Al_2O_3. Ethanol dehydration reaction rates normalized with respect to the amount of dissociative ethanol for (b) ethylene and (c) ether, and (d) the apparent activation barriers of ethylene and ether formation for Puralox SBA-200 and Al_2O_3 with different morphologies as a function of ΔT_d.

3.4.2. *Crystalline phase effects*

To investigate the effect of the crystalline phase on the acid-base properties of Al_2O_3, we prepared transition aluminas by exposing the reference γ-Al_2O_3 (Puralox SBA-200) to high temperatures. XRD was used to confirm the crystalline phase of the high-temperature-treated aluminas (**Figure 3.3**). Up to 800 °C, no structural change of γ-Al_2O_3 was observed by XRD. Above 850 °C, a new diffraction peak at $2\theta = 32.9°$ appeared, and the (400)/(004) peak ($2\theta = 46°$) began to split into two peaks (45.6° and 46.6°), indicating the appearance of δ-Al_2O_3. After calcination at 900 °C, δ-Al_2O_3 was mainly observed, which is consistent with previous reports on δ-Al_2O_3 (JCPDS No. 47-1770).[40] After calcination at 950 °C, θ-Al_2O_3 started to appear (peaks at $2\theta = 31.8°$, 51.1°, and 60.3°). Two θ-Al_2O_3 peaks at $2\theta = 44.8°$ and 47.8° were clearly resolved for Al_2O_3 calcined at 1000 °C, indicating the formation of θ-Al_2O_3.[29, 40] Although θ-Al_2O_3 was mainly observed, small peaks were detected at $2\theta = 25.7°$, 43.4°, and 57.6°, characteristic of α-Al_2O_3 (JCPDS No. 010-0173). After calcination at 1100 °C, α-Al_2O_3 was the dominant phase, although some of the θ-Al_2O_3 remained. The BET surface area (12 m^2/g) of the above sample was slightly larger than that of pure α-Al_2O_3 (usually <5 m^2/g) owing to the residual θ-Al_2O_3. It is noteworthy that transitional Al_2O_3 consists of mixed phases since phase transformation is a continuous process.[1]

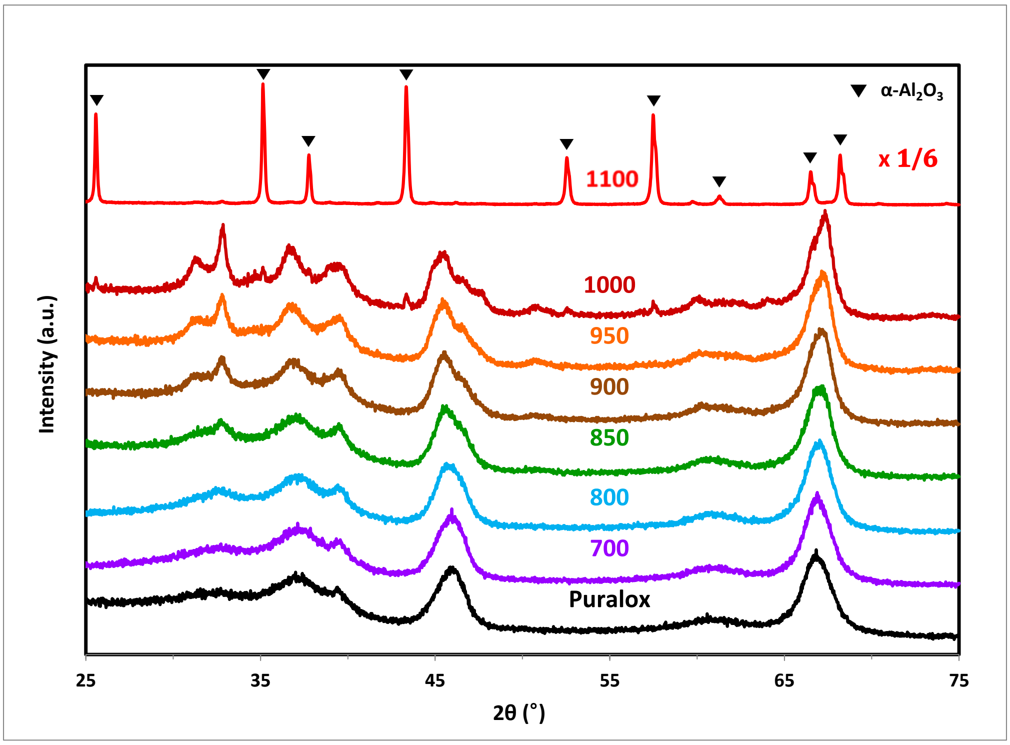

Figure 3.3. XRD patterns of Puralox SBA-200 and transition Al_2O_3. Numbers denote the calcination temperature.

Ethanol TPD profiles collected for transition aluminas (δ-Al_2O_3, θ-Al_2O_3, and α-Al_2O_3) are displayed in **Figure 3.4a**. The T_d increased with increasing calcination temperature above 750 °C. Considering that no structural change was observed by XRD up to 800 °C, the early initiation of the T_d change indicates that the Al_2O_3 surface is influenced prior to bulk alumina, which is consistent with our previous report.[22] XRD analysis of transition alumina revealed that γ-Al_2O_3 was transformed into δ-Al_2O_3 at 900 °C, θ-Al_2O_3 at 1000 °C, and finally α-Al_2O_3 at 1100 °C. In ethanol TPD, the T_d value for γ-Al_2O_3 was 221.8 °C. When γ-Al_2O_3 phase-transformed into other transition aluminas, T_d increased by 21 °C for δ-Al_2O_3, 48 °C for θ-Al_2O_3, and 74 °C for α-Al_2O_3 respectively. Obviously, these phase transformations resulted in less-acidic surfaces compared to that of γ-Al_2O_3.

In transition Al_2O_3, the range of T_d differences was much larger ($\Delta T_d = 74$ °C) than that in γ-Al_2O_3 with different morphologies ($\Delta T_d < 10$ °C). The TOF of ethylene formation and ether showed inverse proportionality to ΔT_d (**Figure 3.4b and 3.4c**), consistent with the results for γ-Al_2O_3 with different morphologies. In our previous report, we showed that the amount of dissociative ethanol decreased with increasing calcination temperature.[35] The results presented in this work confirmed that ethanol dehydration activity also decreased with increasing calcination temperature, consistent with the decreased amount of dissociative ethanol. On the other hand, the apparent activation energy barriers for ethylene and ether formation showed clearly different ΔT_d dependences (**Figure 3.4d**). The E_a of ethylene formation decreased from 159 to 129 kJ/mol with increasing calcination temperature. However, the E_a of diethyl ether formation did not change much (93–104 kJ/mol). These results suggest that the active sites for ethylene and ether formation are potentially different, which will be discussed later.

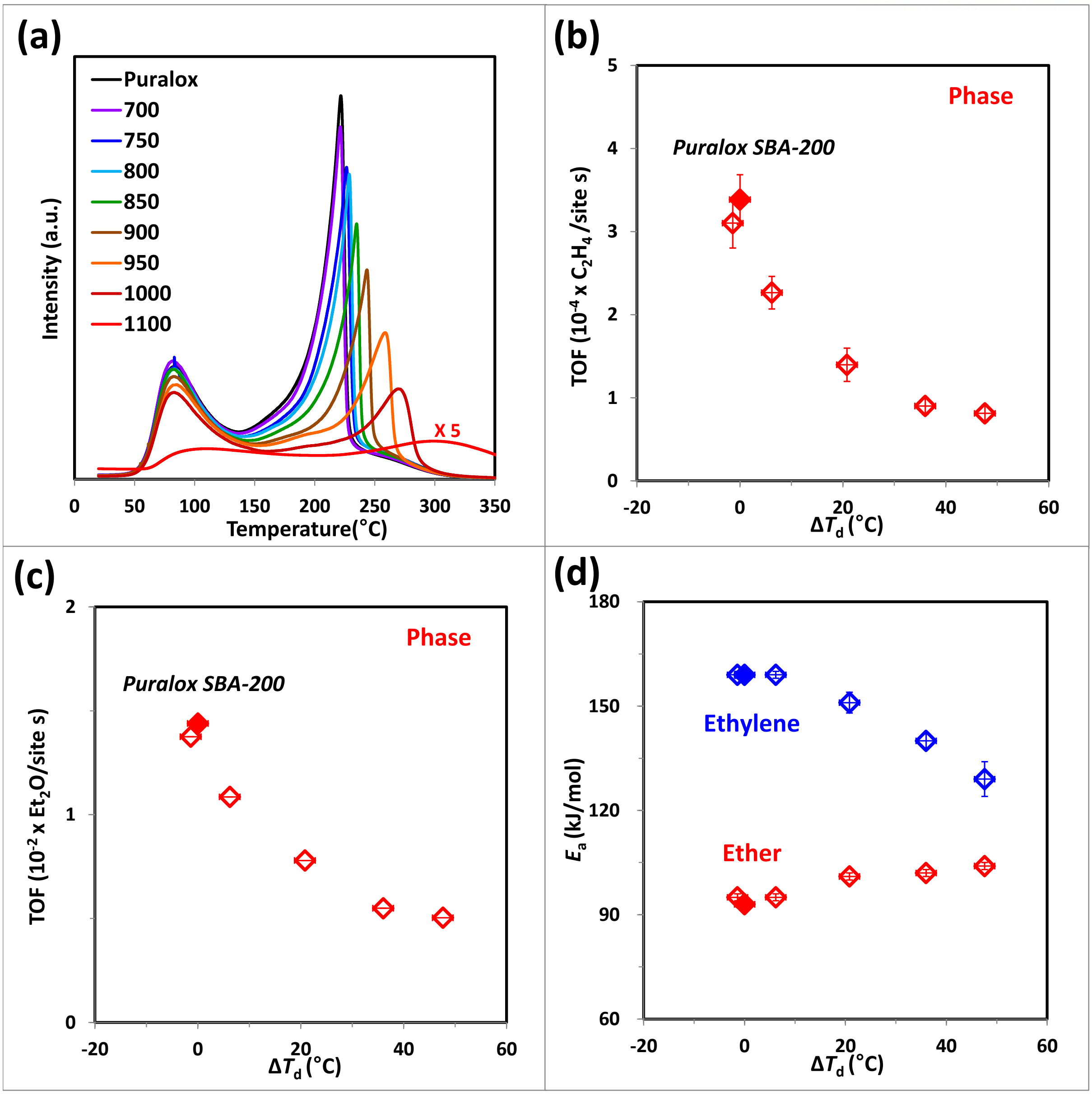

Figure 3.4. (a) Ethanol TPD, normalized ethanol dehydration reaction rates (with respect to the amount of dissociative ethanol) for (b) ethylene and (c) ether, and (d) the apparent activation barriers for ethylene and ether formation for Puralox SBA-200 and transition Al_2O_3 as a function of ΔT_d.

3.4.3. *Effects of additives*

In our previous report, we showed a linear relationship between the desorption temperature of dissociatively adsorbed ethanol and the metal electronegativity of the metal-oxide-modified γ-Al_2O_3.[23] Based on these results, we performed ethanol dehydration reactions on a series of γ-Al_2O_3 modified with metal oxides to clarify the effect of metal oxides on catalytic activity.

The ethanol TPD profile shown in **Figure 3.5a** demonstrates that the T_d of modified γ-Al_2O_3

changed linearly with the electronegativity of additive oxides. Modification with Pt made the surface more acidic (lower T_d), but various alkali metals and metal oxides (La, Zn, Ba, and Na) made it more basic (higher T_d) compared to Puralox SBA-200. It is notable that alkali metals significantly altered the surface of γ-Al_2O_3. A Na level of only 1000 ppm increased the T_d by 42 °C, and 1500 ppm of Na increased it by 72 °C. These findings are consistent with those reported by Srinivasan et al., who showed that 400 ppm of Na in γ-Al_2O_3 increased the propylene desorption temperature by 50 °C in isopropanol TPD.[38]

Ethanol dehydration tests for a series of modified γ-Al_2O_3 (**Figure 3.5b**) showed that the ethylene formation rate was inversely proportional to ΔT_d in a wide temperature range (−35 to 72 °C). Although 1% Pt/γ-Al_2O_3 (lowest T_d) exhibited similar ether formation activity to Puralox SBA-200 (**Figure 3.5c**), its ethylene formation TOF exceeded that of the reference γ-Al_2O_3 by five times. We confirmed that 1% Pt/SiO_2, which has no acidic sites on the support, showed practically no activity in the ethanol dehydration reaction, indicating that the contribution from Pt metal only was negligible. The 0.15% Na/γ-Al_2O_3 sample (highest T_d) showed 30 times less activity for both ethylene and ether formation. Similarly, Srinivasan et al. showed that the addition of only 400 ppm of Na to commercial γ-Al_2O_3 decreased the isopropanol dehydration activity by 75%.[38] In the case of ether, the activity also decreased with increasing T_d (**Figure 3.5c**). This trend indicates that surface modification by additives significantly affected the catalytic behavior of γ-Al_2O_3. Interestingly, a volcano-type plot was observed between the activation barrier for ethylene and ΔT_d, as shown in **Figure 3.5d**. When γ-Al_2O_3 was made more acidic (lower T_d), the E_a value decreased and reached its minimum (87 kJ/mol) at the lowest T_d (35 °C lower than that of γ-Al_2O_3). Similarly, when Al_2O_3 was made more basic (higher T_d), E_a also decreased. At the highest T_d (72 °C higher than that of γ-Al_2O_3), the E_a of ethylene formation was 113 kJ/mol. Interestingly, the maximum E_a of ethylene formation was 159 kJ/mol for pure γ-Al_2O_3. However, the activation barrier for ether formation was independent of T_d (84–103 kJ/mol). It is of interest that the additives affected the activation barriers of ethylene and ether formation in different ways, which suggests that the corresponding active sites are probably different.

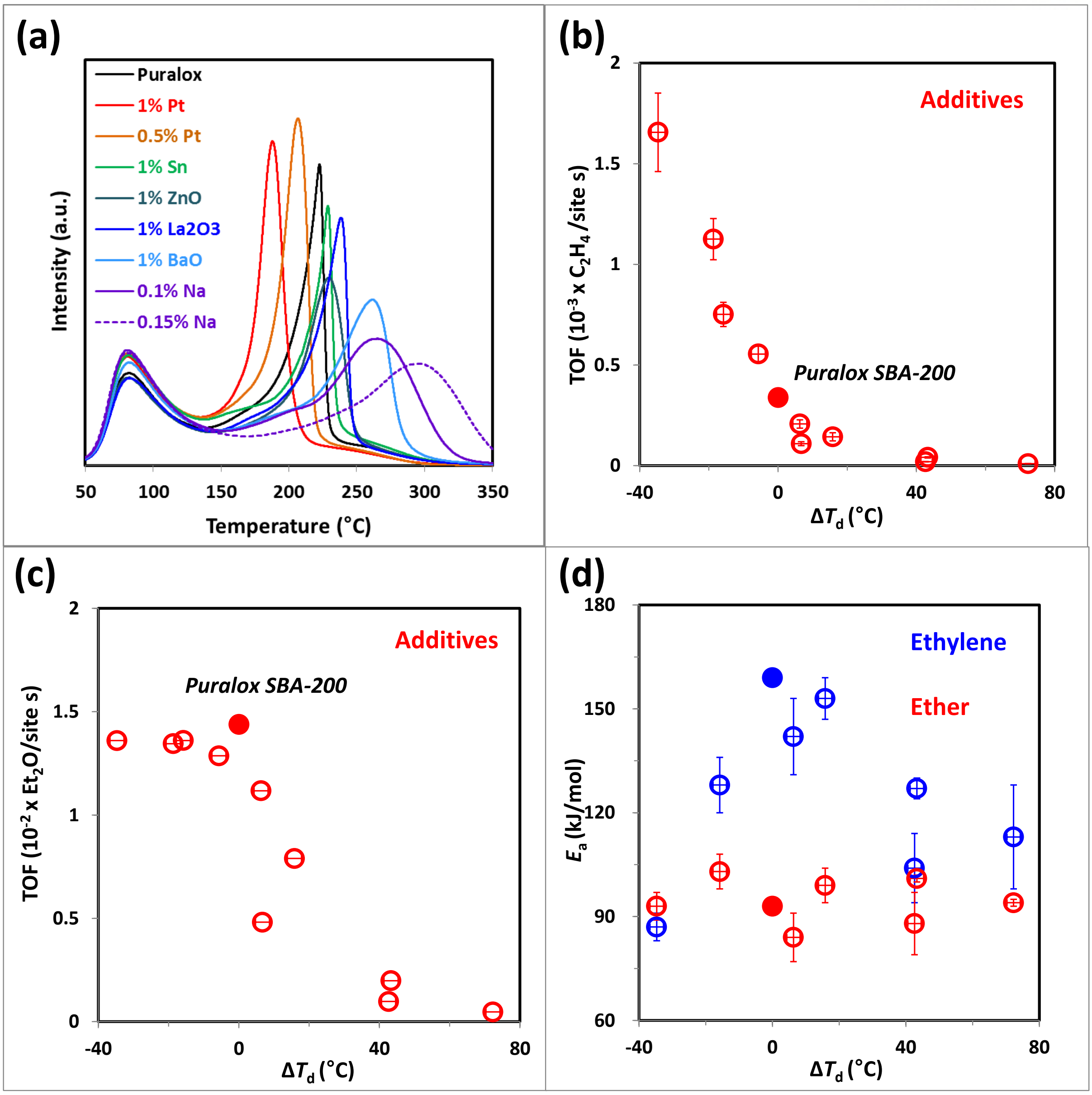

Figure 3.5. (a) Ethanol TPD, normalized ethanol dehydration reaction rates (with respect to the amount of dissociative ethanol) for (b) ethylene and (c) ether, and (d) the apparent activation barriers for ethylene and ether formation for Puralox SBA-200 and Al_2O_3 modified by additives as a function of ΔT_d.

Although 1% Pt/γ-Al_2O_3 exhibited a significantly higher ethylene formation TOF than pure γ-Al_2O_3 (Puralox SBA-200), a competing side reaction (dehydrogenation) produced significant amounts of acetaldehyde. On the other hand, the observed ether formation TOF was slightly lower than that of γ-Al_2O_3. After a 90 min reaction, the production of ethylene decreased by almost 40%, as shown in **Figure 3.6**. The production of acetaldehyde also decreased by almost 50%. However, the production of diethyl ether did not change much. After 7 h, the TOF of ethylene formation decreased by half, but that of ether formation increased by 10%. Here, the TOF was normalized by the BET surface area because the number of dissociative ethanol sites continuously changed due to catalyst deactivation. Notably, a series of γ-Al_2O_3 with different morphologies and transition Al_2O_3 did not show any deactivation during the reaction. Here, the stability of modified γ-Al_2O_3 during ethanol dehydration is important.

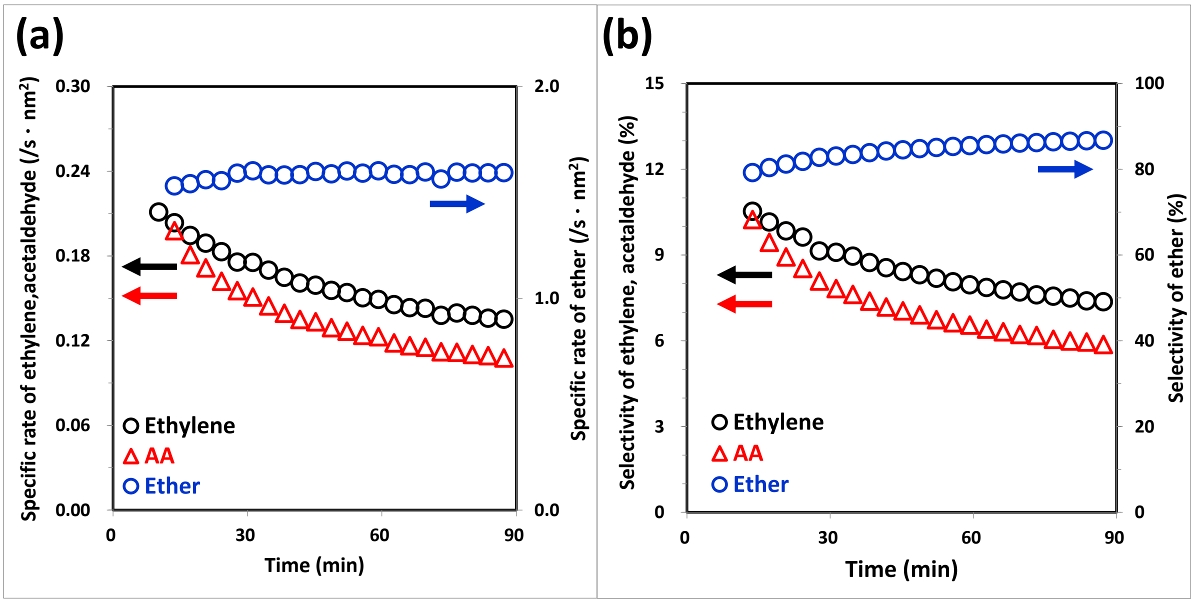

Figure 3.6. (a) Time-on-stream ethanol reaction profiles and (b) selectivity of 1% Pt/Al_2O_3.

In order to characterize the changes of surface characteristics of the modified γ-Al_2O_3 after the reaction, we performed ethanol TPD after the reaction at 180 °C. After 7 h of reaction, the T_d of Puralox SBA-200 was practically unchanged (shown in **Figure 3.7a**), even though the alumina surface was exposed to water produced by ethanol dehydration. The unchanged T_d after long-term exposure to water (7 h) indicates that the Lewis acidic sites (initially calcined at 500 °C for 2 h) were still present on the surface. This is consistent with our previous studies, which showed that the ethanol dehydration activity of two γ-Al_2O_3 samples calcined at 500 and 200 °C remained constant for 90 min with different conversions.[34] Here, the γ-Al_2O_3 surface was stable for 7 h, which constitutes a much longer reaction period compared to that in the previous study. In addition, detailed IR spectroscopy measurements also supported the suggestion that exposure to water did not reconvert Lewis acidic sites to Brønsted acidic sites, suggesting that rehydroxylation of the dehydroxylated γ-Al_2O_3 surface is not a simple process caused by exposure to water.[41]

On the other hand, 1% Pt/γ-Al_2O_3 showed a different TPD profile after the reaction (**Figure 3.7b**), showing a T_d increase of 16 °C, consistent with the deactivation of ethylene formation during ethanol dehydration. We checked whether the change of surface characteristics after the reaction would also be observed for other modified γ-Al_2O_3. Interestingly, 1% BaO showed a similar TPD profile and an almost identical T_d after the reaction, as shown in **Figure 3.7c**. We note here that modification with 1% BaO increased the T_d by 43 °C, but 1% Pt decreased it by 35 °C, compared to that of Puralox SBA-200. The next point to be addressed is the categorization of the T_{d} shift after the reaction into two groups: those of modified γ-Al_2O_3 with more acidic (lower T_{d}) and more basic surfaces (higher T_{d}) than pure γ-Al_2O_3. To confirm the above hypothesis, a series of ethanol TPD measurements were carried out after the reaction. The results summarized in **Table 3.1** revealed that the T_{d} shifts showed clearly different trends for these two groups of modified γ-Al_2O_3 (acidic vs. basic) in a wide ΔT_{d} range (from −35 to 72 °C). The modified γ-Al_2O_3 with a basic surface (higher T_{d}) showed almost identical T_{d} values before and after the reaction. In contrast, the modified γ-Al_2O_3 with an acidic surface (lower T_{d}) showed an increased T_{d} after the reaction test.

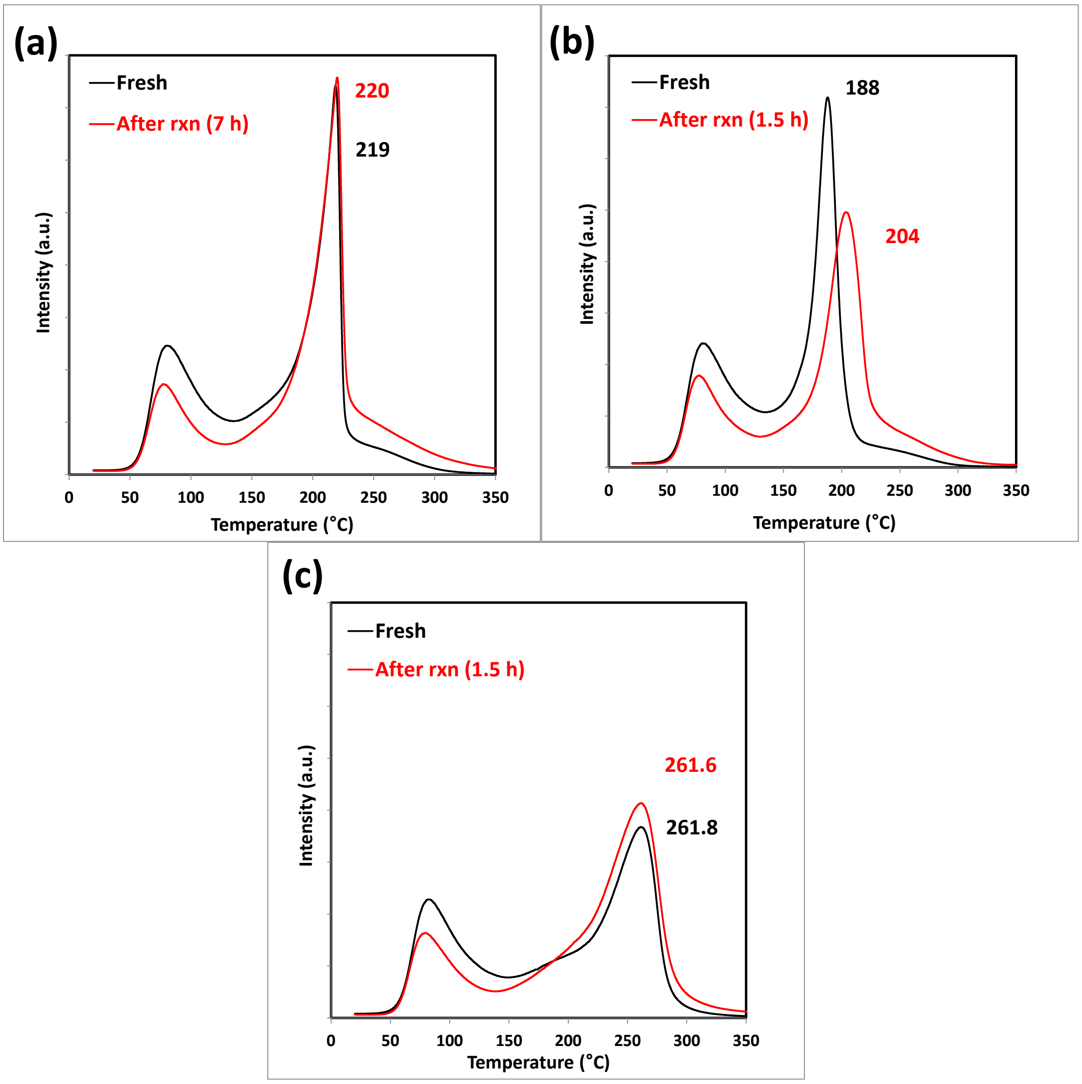

Figure 3.7. Ethanol TPD for (a) Puralox SBA-200, (b) 1% Pt/Al_2O_3, and (c) 1% BaO/Al_2O_3 before and after the reaction.

Catalyst	**T_d (°C)**		
	Fresh	**After reaction***	**ΔT_d**
1% Pt	188	204	16
0.5% Pt	207	217	10
γ-Al_2O_3 (Puralox SBA-200)	219	220	1
1% Sn	229	227	-2
1% BaO	262	262	0
0.15% Na	295	295	0

Table 3.1. Desorption temperatures of maximum rates of dissociative ethanol desorption for Puralox SBA-200 and Al_2O_3 modified by additives. ΔT_d is the difference between T_d values of fresh and post-reaction samples. *The reaction time for post-reaction samples is 1.5 h except for Puralox SBA-200 (7 h).

Intuitively, we expected that the observed T_d shift would originate from the sintering of metals on the γ-Al_2O_3 surface during the reaction, since metals are known to be easily sintered in a humid atmosphere.[42] To confirm this hypothesis, HAADF-STEM images were obtained for fresh and reacted 1% Pt/γ-Al_2O_3 and are shown in **Figure 3.8a** and **3.8b**. The particle size distribution clearly showed that the Pt cluster size increased from ~1 nm (fresh catalyst) to ~1.5 nm (catalyst after 90 min reaction), as shown in **Figure 3.8c**. During ethanol dehydration, the produced water induces the sintering of Pt on γ-Al_2O_3 surfaces; thus, the electronic properties of γ-Al_2O_3 are less affected by supported Pt. We also note here that ethanol TPD could sensitively detect Pt sintering based on the corresponding T_d shift (16 °C).

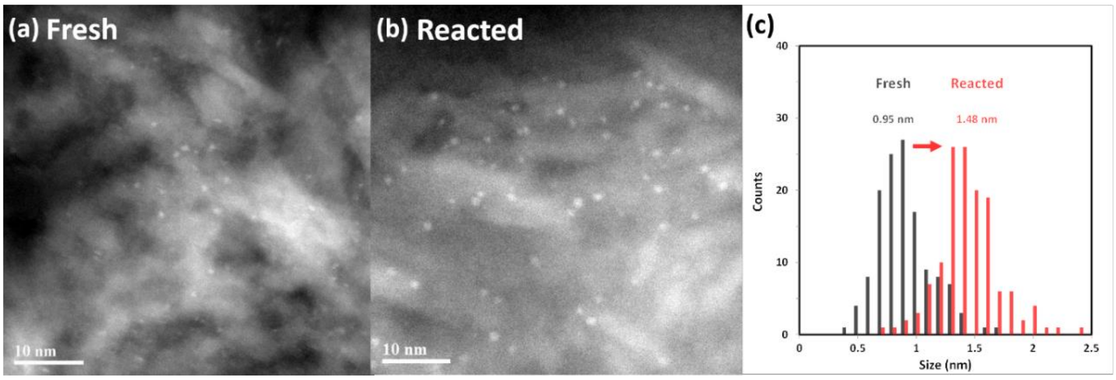

Figure 3.8. HAADF-STEM images for (a) fresh and (b) 1.5 h post-reaction 1% Pt/Al_2O_3 (Puralox SBA-200). (c) Particle size distribution for supported Pt on 1% Pt/Al_2O_3.

3.4.4. *Overall correlations between T_d of dissociative ethanol and ethanol dehydration behavior*

In this study, we attempted to generalize the ethanol dehydration behavior of Al_2O_3 based on three surface characteristics (morphology, crystalline phase, and additives), combining all data obtained for these three variables. Again, we note here that each T_d of dissociative ethanol was normalized with respect to the reference (Puralox SBA-200) value. The specific activity was normalized based on the amount of dissociative ethanol.

Overall, ethylene formation TOF showed a negative correlation with T_d (**Figure 3.9a**). The inverse relationship between T_d and alcohol dehydration activity was reported previously. Srinivasan et al. showed that propylene formation activity correlated inversely with the T_d of propylene for a series of commercial and Na-modified γ-Al_2O_3.[38] Golay et al. also showed that ethanol dehydration activity decreased as the alumina basicity was increased using Mg^{2+}.[43] Recently, Zotov et al. studied Cl-, SO_4-, and Na-modified aluminas using electron paramagnetic resonance (EPR) spectroscopy using spin probes.[44] When the alumina surface was made more acidic (Cl, SO_4), the ethylene formation rates increased. The authors also found a good correlation between the number of weak electron acceptor sites and ethylene formation rates. Still, the universal correlation among Al_2O_3 catalysts with various modification origins was limited.

In this work, we demonstrate that ethylene formation rates, normalized with respect to the amount of dissociative ethanol, showed the inverse correlation with T_d, even though the origins of surface characteristics were completely different (morphology, phase, and additives). The empirically observed trend suggests that the acid-base properties of Al_2O_3 are independent of modification origin. Specifically, the generalized trend for transition Al_2O_3 is consistent with the work of Hu et al., who suggested that Lewis acidic Al^{3+} cations (penta-coordinated) are the active sites for ethanol dehydration, independent of the phase.[36] Herein, we point out that the T_d of dissociatively adsorbed ethanol can be used as a descriptor for the overall acid-base properties of the alumina surface irrespective of the modification origin.

In the case of ether formation, the TOF showed an overall decrease with increasing T_d (**Figure 3.9b**). However, Pt-modified γ-Al_2O_3 showed a much lower TOF than alumina with different morphologies. This observation could be attributed to the decreased ether selectivity of Pt-modified γ-Al_2O_3 (90–96%) compared to those of other aluminas (>97%). When Al_2O_3 was made more acidic (lower T_d), the ethoxide species were more easily desorbed at a lower temperature than in the case of pure γ-Al_2O_3, leading to enhanced ethylene formation (less ether formation). These results are consistent with the study of Golay et al. The authors studied a series of Mg-modified aluminas and suggested that the C_2H_5–O bond is strengthened with increasing basicity, leading to a preferred intermolecular dehydration pathway.[43]

Interestingly, the dependence of the apparent activation barrier on T_d showed clearly different trends for ethylene and ether formation. The apparent activation barrier of ethylene formation showed a volcano-type dependence on T_d (**Figure 3.9c**). The E_a of ethylene formation seemed to be more significantly affected by the crystalline phase and additives than by the morphology. Samples with similar T_d values showed similar E_a of ethylene formation, regardless of how the alumina was modified (i.e., different crystalline phases or additives). On the other hand, the activation barrier of ether formation was almost identical for all of the investigated catalysts in a wide range of T_d values (**Figure 3.9d**). It has been argued that ethylene and ether may be formed at different active sites. [6,11,45-47] In situ titration studies showed that phenol molecules increased ethylene formation rates, but decreased the ether formation rates.[45] However, pyridine titration decreased both olefin and ether formation rates; olefin formation was more inhibited than ether formation.[11, 45, 47] The different dependences of E_a on T_d observed for ethylene and ether formation in this work potentially support these arguments.

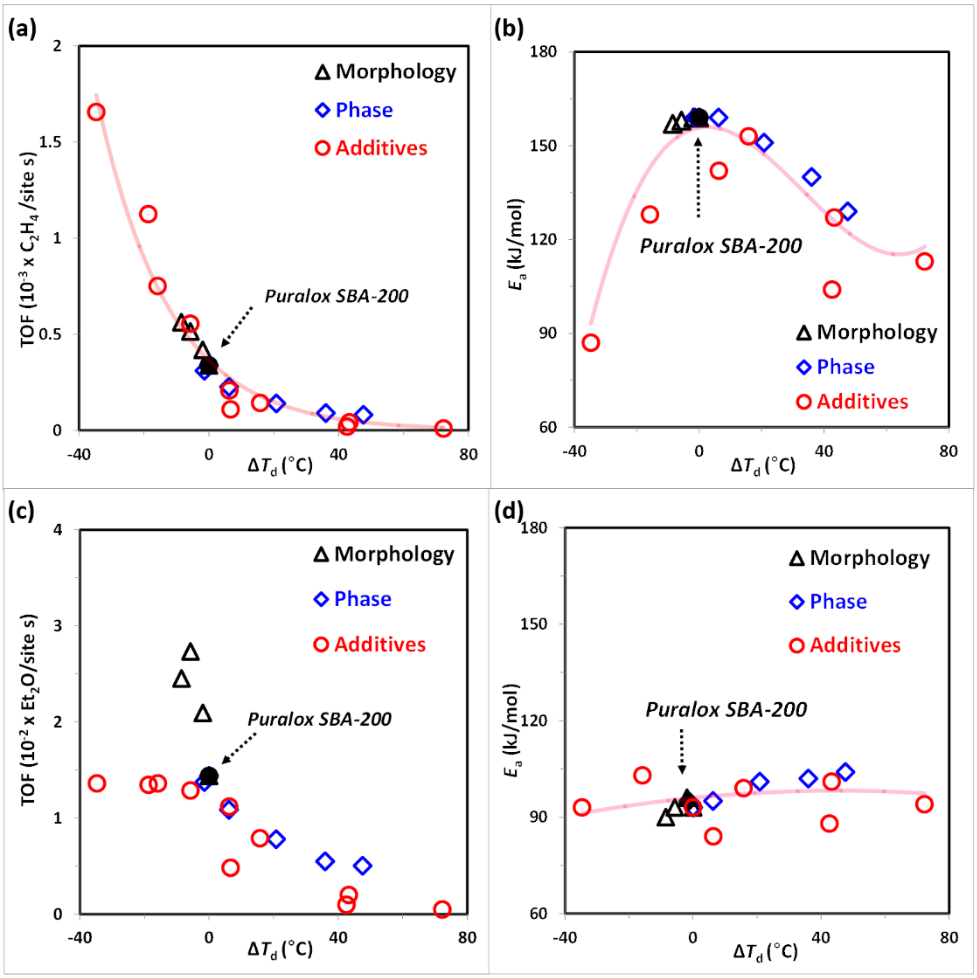

Figure 3.9. Normalized ethanol dehydration reaction rates (with respect to the amount of dissociative ethanol) for (a) ethylene and (b) ether, and apparent activation barriers for (c) ethylene and (d) ether formation on Al_2O_3 with different morphologies, transition Al_2O_3, and Al_2O_3 modified by additives as a function of ΔT_d. The red line was drawn as a guide.

It is notable that the measured E_a in this study is the apparent activation barrier, which depends on both the heat of ethanol adsorption and the intrinsic dehydration barrier ($E_{app} = E_s + \Delta H$). Narayanan et al. suggested that the activation barrier of isopropanol dehydration varied because the adsorption barrier of defect sites depends on the structure of alumina.[37] Future theoretical research will provide further insights for the fundamental understanding of changes in the E_a of ethylene formation.

Although molecularly adsorbed ethanol was still observed by mass spectrometry at the temperature of ethylene desorption in some studies,[48, 49] we removed weakly bound ethanol by He purging during ethanol TPD, and most of the residual molecularly adsorbed ethanol was expected to desorb before the onset of ethylene desorption. Thus, high-temperature desorption (>150 °C) might be due to the dissociatively adsorbed ethanol (ethoxide) on the alumina surface. Higher T_d values indicate that the surface ethoxide is strongly bound, being hard to desorb as ethylene, thus leading to decreased ethylene formation. Based on the correlation between T_d and ethylene formation rates, we can conclude that ethylene formation is directly related to the presence of ethoxide species on alumina surfaces. However, the ether formation rate was less correlated with the ethoxide, which might be related to the more complex nature of intermolecular dehydration. Recently, the Busca group reported that ethoxide was a key intermediate in the formation of both ethylene and ether, based on Fourier transform infrared (FT-IR) spectroscopy and reaction studies, which is consistent with our present work.[8]

Numerous studies have been devoted to modifying aluminas for better catalytic performance.[50-55] Alkali metals or metal oxides have been supported on Al_2O_3, leading to modified acidity or improved thermal stability. However, defining and comparing the modified surface characteristics is difficult. Our empirically correlated model provides a fundamental basis for understanding the surface characteristics of various alumina catalysts from the viewpoint of their acid-base properties, being a guideline for designing better catalysts.

3.4.5. *Commercial Al_2O_3*

To utilize the results of combined ethanol TPD/dehydration activity relationships for characterizing the surface properties of Al_2O_3, we tested a series of commercial aluminas: Puralox SBA-200, HP-14, Strem, Siralox 1.5, and Brockmann I acidic.

Commercial Al_2O_3 is composed of various alumina phases, as shown in **Figure 3.10a**. Puralox SBA-200 and HP-14 were composed of γ-Al_2O_3, while Strem Al_2O_3 showed mixed γ- and δ-Al_2O_3 phases. Siralox 1.5 was close to θ-Al_2O_3, with residual δ-Al_2O_3, and its surface was modified by 1.5% Si. Brockmann I acidic seemed similar to γ-Al_2O_3, but showed different diffraction patterns of the (400)/(004) peaks ($2\theta = 45.7°$ and $46.7°$), indicating a different phase from that of γ-Al_2O_3. Commercial Al_2O_3 also exhibited various morphologies, confirmed by TEM, which are shown in **Figure 3.10b**.

Puralox SBA-200 consisted of agglomerated nanoparticles with irregular shapes (**Figure 3.1b**). HP-14 showed a rod-like particle shape. The Strem and Siralox samples had rectangular particle shapes with two-dimensional morphologies. Brockmann I was composed of agglomerated particles with circular shapes. In summary, commercial Al_2O_3 showed various phases, morphologies, and additives.

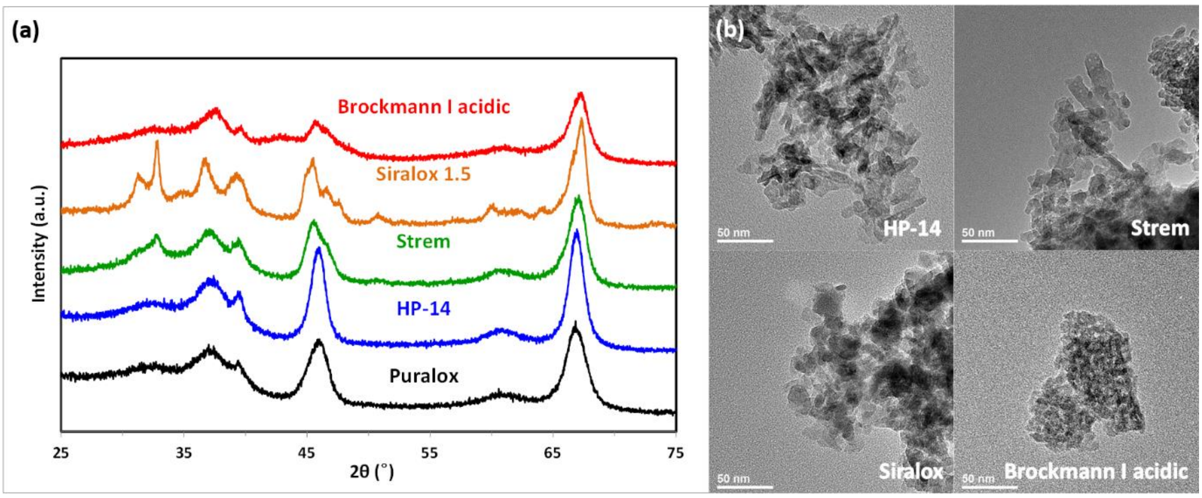

Figure 3.10. (a) XRD patterns and (b) TEM images for commercial Al_2O_3.

The acid-base properties and the amount of dissociatively adsorbed ethanol were determined using ethanol TPD (**Figure 3.11a**). The T_d order was as follows: HP-14 < Puralox < Strem < Siralox 1.5 < Brockmann I. The desorption area in ethanol TPD depended on the surface areas of the alumina samples. However, Siralox 1.5 exhibited an unusually small desorption area compared to Puralox SBA-200, although the BET surface area of Siralox 1.5 was half that of Puralox SBA-200. The low desorption area could be explained by the presence of doped Si atoms on the Al_2O_3 surface, which block the adsorption sites.

Ethanol dehydration rates measured on these commercial aluminas showed that the TOF for both ethylene and ether showed inverse trends with respect to T_d (**Figure 3.11b** and **3.11c**). The activation energy barriers also showed a similar trend to the previously observed trend (**Figure 3.11d**). Siralox 1.5 and Brockmann I showed E_a values of ethylene formation 30–40 kJ/mol lower than those of the other samples, while the activation barrier of ether formation was similar for the investigated T_d.

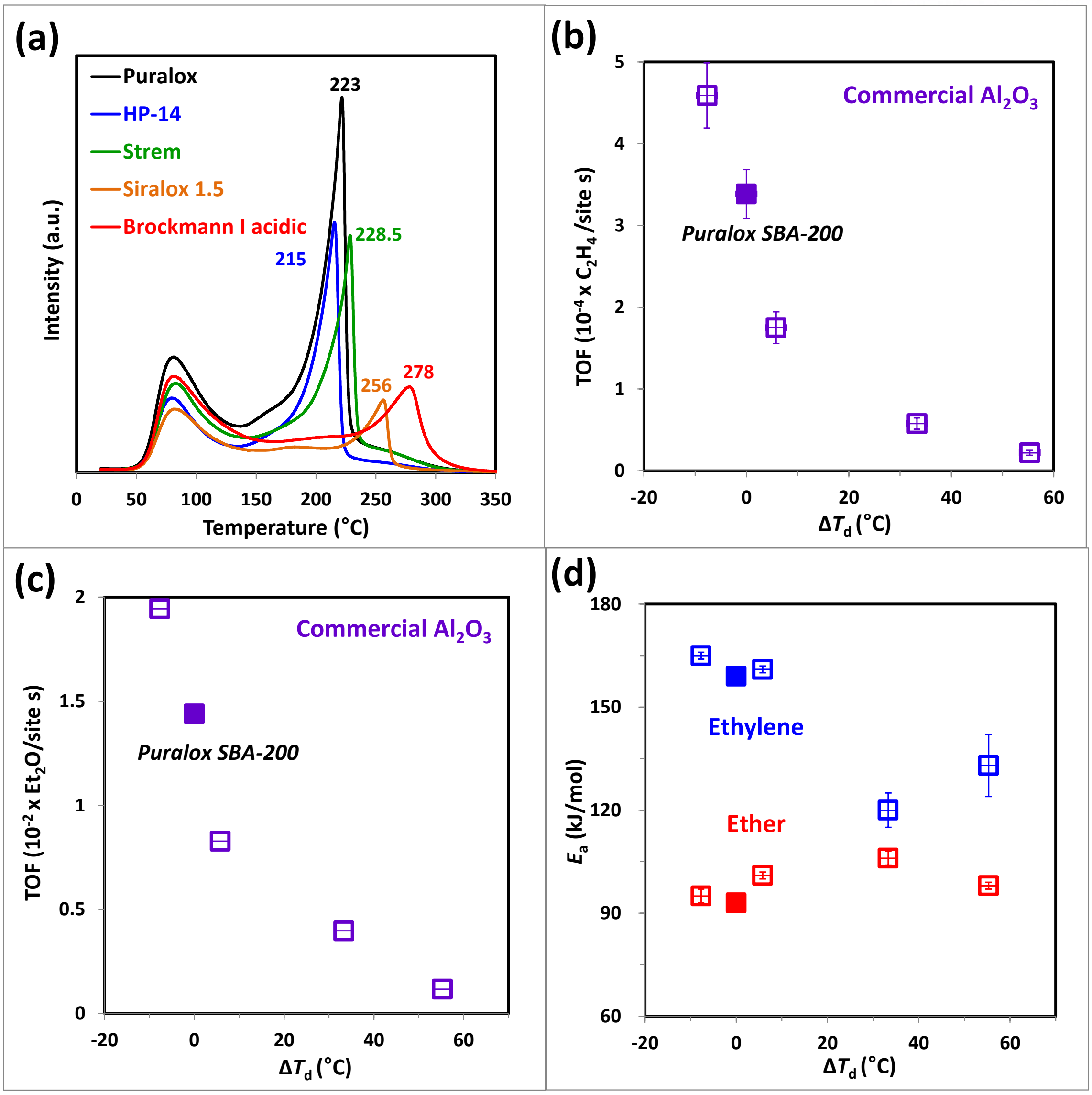

Figure 3.11. (a) Ethanol TPD, normalized ethanol dehydration reaction rates (with respect to the amount of dissociative ethanol) for (b) ethylene and (c) ether, and (d) apparent activation barriers for ethylene and ether formation on commercial Al_2O_3 as a function of ΔT_d.

For comparison of commercial aluminas with reference alumina (Puralox SBA-200), well-defined morphologies, crystalline phases, and additives, we plotted the data collected for commercial aluminas in **Figure 3.9**. As seen in **Figure 3.12**, the ethylene and ether formation rates and activation barriers were completely consistent. These results clearly demonstrated that the acid-base properties of alumina surfaces can be characterized and generalized, despite their drastically different morphologies, crystalline phases, and various additives. This fundamental understanding of the catalytic properties of alumina surfaces is very helpful for the further development of new catalysts with better activity and selectivity.

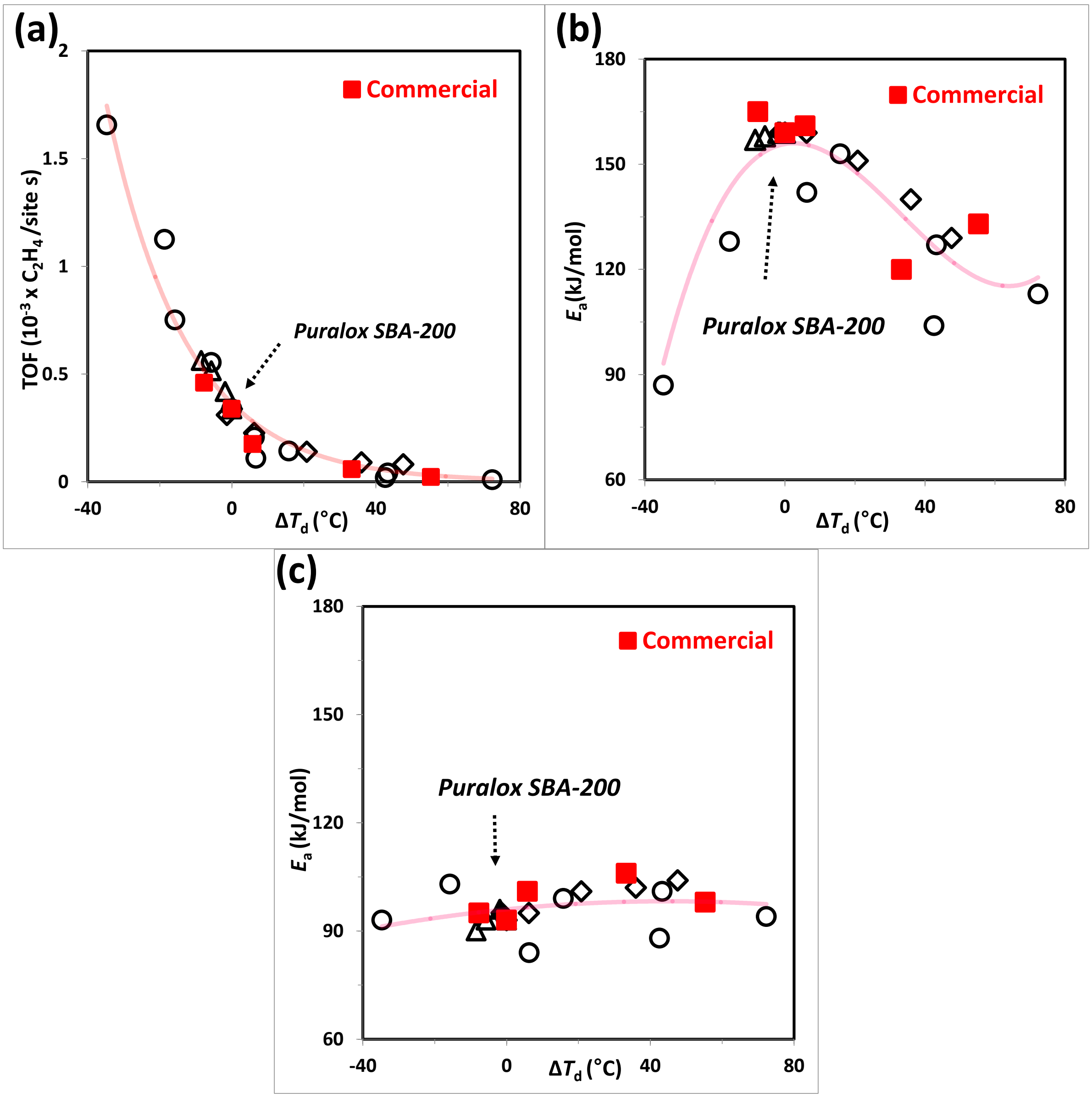

Figure 3.12. (a) Normalized ethanol dehydration reaction rates (with respect to the amount of dissociative ethanol) for ethylene, and the apparent activation barriers for (b) ethylene and (c) ether formation on Al_2O_3 with different morphologies, transition Al_2O_3, Al_2O_3 modified by additives, and commercial Al_2O_3 as a function of ΔT_d.

3.5. Conclusion

In this study, we investigated the surface characteristics of various aluminas with different (morphologies, crystalline phases, and additives) by XRD, HR-TEM, ethanol TPD, and ethanol dehydration reaction rate measurements. The desorption temperature (T_d) of dissociative ethanol, which depends on the morphology, crystalline phase, and additives, changed from 188 °C to 299 °C. The crystalline phase and additives affected T_d more drastically than did the morphology.

The ethanol dehydration rates, normalized with respect to the amount of dissociative ethanol quantified from ethanol TPD, of various modified Al_2O_3 catalysts also changed significantly. The TOF of ethylene formation varied from 9.5×10^{-6} to 1.7×10^{-3} C_2H_4/site·s. Ethylene formation rates showed an inverse correlation with T_d even though the origin of surface characteristics was completely different (morphology, phase, and additives). This suggests that T_d can be used as a descriptor for the acid-base properties of alumina irrespective of modification origin. Additionally, it suggests that ethoxide is a key intermediate in ethanol dehydration on alumina. The TOF of diethyl ether formation showed a similar trend, but Al_2O_3 modified with Pt exhibited a lower ether formation rate than pure γ-Al_2O_3.

The apparent activation barrier for ethylene formation showed a volcano-type relationship with T_d where the maximum E_a was observed on pure γ-Al_2O_3 (159–165 kJ/mol). However, ether showed similar apparent activation barrier (84–106 kJ/mol for all modified Al_2O_3), suggesting potentially different active sites for ethylene and ether formation. Finally, the activities and activation barriers of commercial Al_2O_3 were consistent with our empirically correlated model. This fundamental understanding of the acid-base properties of alumina is helpful for the further development of new catalysts with better activity and selectivity.

3.6. References

[1] Levin, I.; Brandon, D. *J. Am. Ceram. Soc.* **1998,** *81*, 1995-2012.

[2] Trueba, M.; Trasatti, S. P. *Eur. J. Inorg. Chem.* **2005,** *2005*, 3393-3403.

[3] Busca, G. *Catal. Today* **2014,** *226*, 2-13.

[4] Knözinger, H.; Köhne, R. *J. Catal.* **1966**, *5*, 264-270.

[5] Knözinger, H. *Angew. Chem. Int. Ed.* **1968,** *7*, 791-805.

[6] DeWilde, J. F.; Chiang, H.; Hickman, D. A.; Ho, C. R.; Bhan, A. *ACS Catal.* **2013,** *3*, 798-807.

[7] DeWilde, J. F.; Czopinski, C. J.; Bhan, A. *ACS Catal.* **2014,** *4*, 4425-4433.

[8] Phung, T.K.; Herrera, C.; Larrubia, M.Á.; García-Diéguez, M.; Finocchio, E.; Alemany, L.J.; Busca, G.; *Appl. Catal., A* **2014**, *483*, 41-51.

[9] Christiansen, M. A.; Mpourmpakis, G.; Vlachos, D. G. *ACS Catal.* **2013,** *3*, 1965-1975.

[10] Kang, M.; DeWilde, J. F.; Bhan, A. *ACS Catal.* **2015,** *5*, 602-612.

[11] DeWilde, J.F.; Bhan, A.; *Appl. Catal., A* **2015**, *502*, 361-369.

[12] Larmier, K.; Nicolle, A.; Chizallet, C.; Cadran, N.; Maury, S.; Lamic-Humblot, A.-F.; Marceau, E.; Lauron-Pernot, H. *ACS Catal.* **2016,** *6*, 1905-1920.

[13] Peri, J. B. *J. Phys. Chem.* **1965,** *69*, 220-230.

[14] Knözinger, H.; Ratnasamy, P. *Catal. Rev. Sci. Eng.* **1978,** *17*, 31-70.

[15] Busca, G.; Lorenzelli, V.; Ramis, G.; Willey, R.J. *Langmuir* **1993**, *9*, 1492-1499.

[16] Digne, M.; Sautet, P.; Raybaud, P.; Euzen, P.; Toulhoat, H. *J. Catal.* **2002,** *211*, 1-5.

[17] Digne, M.; Sautet, P.; Raybaud, P.; Euzen, P.; Toulhoat, H. *J. Catal.* **2004,** *226*, 54-68.

[18] Pecharroman, C.; Sobrados, I.; Iglesias, J.; Gonzalez-Carreno, T.; Sanz, J.; *J. Phys. Chem. B* **1999**, *103*, 6160-6170.

[19] Euzen, P.; Raybaud, P.; Krokidis, X.; Toulhoat, H.; Le Loarer, J.-L.; Jolivet, J.-P.; Froidefond, C. Alumina. In Handbook of Porous Solids; Schüth, F., Sing, K. S. W., Weitkamp, J. Eds.; Wiley-VCH Verlag GmbH:Weinheim, 2002; Vol. 3, pp 1591-1677.

[20] Kwak, J. H.; Hu, J.; Mei, D.; Yi, C.-W.; Kim, D. H.; Peden, C. H. F.; Allard, L. F.; Szanyi, J. *Science* **2009,** *325*, 1670-1673.

[21] Kwak, J.H.; Kovarik, L.; Szanyi, J. *ACS Catal*. **2013**, *3*, 2094-2100.

[22] Kwak, J.H.; Peden, C.H.F.; Szanyi, J. *J. Phys. Chem. C* **2011**, *115*, 12575-12579.

[23] Kwak, J.H.; Lee, J.; Szanyi, J.; Peden, C.H.F. *Catal. Today* **2016**, *265*, 240-244.

[24] Raybaud, P.; Chizallet, C.; Mager-Maury, C.; Digne, M.; Toulhoat, H.; Sautet, P. *J. Catal.* **2013,** *308*, 328-340.

[25] Hackett, S.F.; Brydson, R.M.; Gass, M.H.; Harvey, I.; Newman, A.D.; Wilson, K.; Lee, A.F. *Angew. Chem. Int. Ed.* **2007**, *46*, 8593-8596.

[26] Pinto, H. P.; Nieminen, R. M.; Elliott, S. D. *Phys. Rev. B* **2004,** *70*, 125402.

[27] Kovarik, L.; Genc, A.; Wang, C.; Qiu, A.; Peden, C. H. F.; Szanyi, J.; Kwak, J. H. *J. Phys. Chem. C* **2013,** *117*, 179-186.

[28] Santos, P. d. S.; Coelho, A. C. V.; Santos, H. d. S.; Kiyohara, P. K. *Mater. Res.* **2009,** *12*, 437-445.

[29] Zhou, R.-S.; Snyder, R. L., *Acta Crystallogra.* **1991,** *B47*, 617-630.

[30] Rozita, Y .; Brydson, R.; Comyn, T. P.; Scott, A. J.; Hammond, C.; Brown, A.; Chauruka, S.; Hassanpour, A.; Young, N. P.; Kirkland, A. I.; Sawada, H.; Smith, R. I. *ChemCatChem* **2013,** *5*, 2695-2706.

[31] Kwak, J. H.; Hu, J.; Kim, D.; Szanyi, J.; Peden, C. *J. Catal.* **2007,** *251*, 189-194.

[32] Lee, D.; Duong, N.T.; Lafon, O.; De Paëpe, G. *J. Phys. Chem. C* **2014,** *118*, 25065-25076.

[33] Wischert, R.; Florian, P.; Copéret, C.; Massiot, D.; Sautet, P. *J. Phys. Chem. C* **2014,** *118*, 15292-15299.

[34] Kwak, J. H.; Mei, D.; Peden, C. H. F.; Rousseau, R.; Szanyi, J. *Catal. Lett.* **2011,** *141*, 649-655.

[35] Lee, J.; Jeon, H.; Oh, D. G.; Szanyi, J.; Kwak, J. H. *Appl. Catal., A* **2015,** *500*, 58-68.

[36] Hu, J. Z.; Xu, S.; Kwak, J. H.; Hu, M. Y.; Wan, C.; Zhao, Z.; Szanyi, J.; Bao, X.; Han, X.; Wang, Y.; Peden, C. H. F. *J. Catal.* **2016,** *336*, 85-93.

[37] Narayanan, C.R.; Srinivasan, S.; Datye, A.K.; Gorte, R.; Biaglow, A. *J. Catal.* **1992,** *138*, 659-674.

[38] Srinivasan, S.; Narayanan, C. R.; Biaglow, A.; Gorte, R.; Datye, A. K. *Appl. Catal., A* **1995,**

132, 271-287.

[39] Chen, X. Y.; Zhang, Z. J.; Li, X. L.; Lee, S. W. *Solid State Commun.* **2008,** *145*, 368-373.

[40] Nguefack M.; Popa, A.F.; Rossignol, S.; Kappenstein, C. *Phys. Chem. Chem. Phys.* **2003,** *5*, 4279-4289.

[41] Szanyi, J.; Kwak, J. H. *Phys. Chem. Chem. Phys.* **2014,** *16*, 15117-15125.

[42] Barbier, J.; Duprez, D.; *Appl. Catal., B* **1994,** *4*, 105-140.

[43] Golay, S.; Doepper, R.; Renken, A. *Appl. Catal., A* **1998,** *172*, 97-106.

[44] Zotov, R.A. ; Molchanov, V.V.; Volodin, A.M.; Bedilo, A.F. *J. Catal*. **2011,** *278*, 71-77.

[45] Jain, J.R.; Pillai, C. *J. Catal.* **1967,** *9*, 322-330.

[46] Christiansen, M. A.; Mpourmpakis, G.; Vlachos, D. G. *J. Catal.* **2015,** *323*, 121-131.

[47] Kang, M.; Bhan, A. *Catal. Sci. Technol.* **2016,** *6*, 6667-6678.

[48] Basagiannis, A.; Panagiotopoulou, P.; Verykios, X. *Top. Catal.* **2008,** *51*, 2-12.

[49] Cordi, E.M.; Falconer, J.L.; *Catal. Lett.* **1996,** *38*, 45-51.

[50] Machida, M.; Eguchi, K.; Arai, H.; *J. Catal.* **1987,** *103*, 385-393.

[51] Ozawa, M.; Nishio, Y.; *J. Alloys Compd.* **2004,** *374*, 397-400.

[52] Konsolakis, M.; Macleod, N.; Isaac, J.; Yentekakis, I.V.; Lambert, R.M.; *J. Catal.* **2000,** *193*, 330-337.

[53] Macleod, N.; Isaac, J.; Lambert, R.M.; *J. Catal.* **2001,** *198*, 128-135.

[54] Clet, G.; Goupil, J.M.; Szabo, G.; Cornet, D. *J. Mol. Catal. A: Chem.* **1999,** *148*, 253-264.

[55] Avgouropoulos, G.; Oikonomopoulos, E.; Kanistras, D.; Ioannides, T. *Appl. Catal., B* **2006,** *65*, 62-69.

4. Effect of number and properties of specific sites on alumina surfaces for Pt-Al_2O_3 catalysts

This chapter contains the published result.
Lee, J.; Jang, E.J.; Jeong, H.Y.; Kwak, J.H. *Appl. Catal., A* **2019,** *569*, 8-19.

4.1. Abstract

In this work, how the number and properties of specific sites on alumina surfaces affect the specific interaction between Pt and alumina was investigated by using X-ray diffraction, ethanol temperature programmed desorption, diffuse reflectance infrared Fourier transform spectroscopy, H_2 chemisorption, scanning transmission electron microscopy and benzene hydrogenation reaction. Here, we chose two sets of model alumina having different number of sites with the identical properties and different properties of sites with the same number based on ethanol TPD. The H_2 chemisorption results for the model aluminas show that H/Pt are all similar for low Pt loadings, but significantly different for high Pt loadings. For 1 wt% Pt/Al_2O_3, the number of specific sites on all the aluminas was sufficient to disperse all the Pt, leading to only highly dispersed Pt clusters (~ 1 nm). However, at 10 wt% Pt/Al_2O_3, the number of Pt atoms is greater than that of the specific sites on the alumina surface, resulting in a bimodal distribution of large agglomerated Pt (> 10 nm) and highly dispersed Pt clusters (< 3 nm) revealed by XRD and TEM. Overall, the results clearly demonstrated that Pt shows higher dispersion with increasing the number of sites and interaction strength because the Pt atoms can interact with specific sites on alumina in greater numbers and more strongly. However, these Pt dispersion changes do not represent the gradual change in Pt cluster sizes, but the relative population change of small (< 3 nm) and large agglomerated Pt clusters (>10 nm). The number of large agglomerated Pt clusters decreased with increasing the number of sites and interaction strength. This fundamental understanding provides an important perspective for designing Al_2O_3-based supported catalysts.

4.2. Introduction

Pt/Al_2O_3 is one of the most important supported heterogeneous catalysts utilized in industries such as automobile exhaust combustion and petroleum refineries.[1-3] Catalytically, Pt/Al_2O_3 is mainly involved in oxidation, dehydrogenation-hydrogenation, and reforming processes.[1-4] Owing to its versatile catalytic applications in the real world, the Al_2O_3-supported Pt catalyst has been of practical and fundamental interest for decades.

The catalytic properties of Pt/Al_2O_3 are affected by various parameters—size, morphology, dispersion, sintering, oxidation state, etc.,—that are closely related to the specific Pt-Al_2O_3 interaction and, ultimately, the surface properties of alumina.[5-10] Therefore, numerous studies have been carried out to understand how the structural, textural, and physicochemical properties of alumina influence the supported Pt.[6,10-14] The various crystalline phases of alumina were investigated by Park et al. and they reported that Pt dispersion was affected more by crystalline structure than the surface area of alumina.[11] Mironenko et al. showed that hydrothermal treatment of alumina increased the number of bridging OH groups, leading to weaker interaction with H_2PtCl_6 (outer-sphere complex) and lower reduction temperature.[10] It indicates that the alumina surface hydroxyl groups affect their interaction with platinum. The properties of these surface hydroxyls are known to be closely related to the activation temperature and crystal facets, as the study of Digne et al. reported.[15, 16] Various effects of crystalline facets have been studied by both experimental and computational methods. Kwak et al. reported that Pt is anchored on penta-coordinated Al^{3+} sites on (100) facets by using solid-state nuclear magnetic resonance spectroscopy, scanning transmission electron microscopy, and density functional theory calculation.[14] Subsequently, Hu et al. reported that Pt_{13} clusters favor the formation of two-dimensional (2D) rafts on dehydrated (100) surfaces, but 3D morphologies on hydroxylated (110) surfaces as revealed by DFT calculations.[6] Furthermore, Agnes et al. showed experimental evidence for the 2D-3D morphologies of Pt clusters on (100) and (110) surfaces, and further morphological changes to hydrogen coverage by combining experimental XANES studies and DFT simulations.[12] Despite intensive research efforts to understand the effect of alumina on Pt-Al_2O_3 interaction, there are still issues to be resolved, because the structural, textural, and physicochemical properties of alumina are closely interrelated.[17-19]

In order to distinguish how each parameter of alumina contributes to the Pt-Al_2O_3 interaction, systematic approaches must involve well-defined model alumina with the sensitive and quantitative characterization of alumina surface properties.[19-23] Recently, we have reported that ethanol temperature programmed desorption (TPD) can sensitively characterize the number and properties of specific sites on various kinds of alumina with different morphologies, crystalline phase, and additives.[24]

In this work, we investigated how the number and properties of specific sites on an alumina surface affect its interaction with Pt. In this regard, we chose two sets of model alumina having different number of sites with the identical properties and different properties of sites with the same number based on ethanol TPD. After loading Pt onto these model aluminas, the Pt dispersion was analyzed by H_2 chemisorption, XRD, and STEM. The results clearly demonstrated that Pt shows higher dispersion with increasing number of sites and interaction strength. This fundamental understanding provides an important perspective for designing Al_2O_3-based supported catalysts.

4.3. Experimental section

4.3.1. Catalyst preparation

We chose four types of model aluminas. Three aluminas were supplied from Sasol company, Puralox TH 100/150, TH 200/110, and TH 500/80, and labeled as T150, T110, and T80, respectively. We calcined T150 aluminas at 1000 °C for 3 h and labeled it T1000.

0.5–10 wt% Pt/Al_2O_3 were prepared by conventional incipient wetness impregnation with $Pt(NH_3)_4(NO_3)_2$ in water and dried at 120 °C overnight. Note that we used $Pt(NH_3)_4(NO_3)_2$ as the Pt precursor in order to remove any additional Cl effect.[25,26] All the samples were calcined at 500 °C for 2 h using 20% O_2/He (1 ml/s) then reduced at 500 °C for 1 h under 10% H_2/He flow (1 ml/s).

4.3.2. Catalyst characterizations

The XRD patterns were obtained on a Bruker D2 phaser diffractometer using Cu Kα radiation ($\lambda = 1.54$ Å) in the step mode between 2θ values of 5 and 80°, with a step size of 0.02 °/s. The tube voltage and current were 30 kV and 10 mA, respectively. The morphologies of Al_2O_3 were confirmed by TEM (JEOL JEM-2100). The specific surface areas were determined by the Brunauer-Emmett-Teller method using BELSORP-Max instrument.

Ethanol TPD was carried out using the same experimental procedures as described in our previous report.[22, 24, 27, 28] 50 mg of alumina was calcined at 500 °C for 1 h under 20% O_2/He flow (1.0 ml/s). After calcination, the sample was cooled to room temperature and ethanol adsorption was carried out for 30 min using a 2.0 % ethanol/He gas mixture (1.0 ml/s), followed by He purging for 30 min to remove weakly-bound ethanol molecules. After stabilization of the flame ionization detector (FID) signal of an Agilent 7820A gas chromatograph (GC), a TPD experiment was carried out in flowing He (1.0 ml/s) at the heating rate of 10 °C/min, and the reactor outlet was directly connected to the FID (i.e., no GC column separation).

Diffuse reflectance infrared Fourier transform spectroscopy (DRIFTS) experiments were carried out on a Nicolet iS50 FTIR spectrometer equipped with a mercury cadmium telluride (MCT) detector to investigate the hydroxyl groups and the relative ratio of Lewis and Brønsted acid sites on alumina surface. 14 mg of Al_2O_3 were loaded into high temperature reaction chamber (Harrick Scientific) with ZnSe windows installed in a Praying Mantis diffusion reflection accessory. All the samples were pretreated using 20 % O_2/He (flow rate = 1 ml/s) at 380 °C (this temperature was calibrated and also the maximum temperature achievable using the current DRIFTS accessory). The FT-IR spectra of the hydroxyl groups were collected at RT with KBr background. Also, in order to observe the acid-base properties on the alumina surface, pyridine adsorption was performed with 1 % pyridine/He flow at 100 °C until the sample was saturated with pyridine. The spectrum was obtained after He purging at the same temperature for 1 h to remove the weakly bound pyridine on the alumina surface by using the spectrum of the pretreated-sample itself under He flow at 100 °C as the background. All the spectra were collected with an average 128 scans at the resolution of 4 cm^{-1}.

Hydrogen (H_2) chemisorption was performed on Belcat-B(BEL Japan, Inc.). 50 mg of a sample was calcined at 500 °C for 2 h under 20% O_2/He (1.0 ml/s) and, subsequently, reduced at 500 °C for 1 h under 10% H_2/He (1.0 ml/s). After purging for 30 min under He (1.0 ml/s), Pt/Al_2O_3 was cooled to 40 °C and chemisorption was carried out by repeated pulse (0.319 ml loop–4% or 10% H_2/Ar). Metal dispersion was calculated based on the stoichiometry of H/Pt = 1. The average diameter of platinum was estimated by the formula of 1.1/(H/Pt).[29] For the reduced samples, high-angle annular dark-field scanning transmission electron microscopy (HAADF-STEM) images were obtained using a JEOL 2100F (JEOL) operated at 200 kV. The particle size distributions were obtained by measuring 400–500 clusters.

4.3.3. Catalyst reaction tests: Benzene hydrogenation

Benzene hydrogenation was performed in a quartz flow reactor using selected Pt/Al_2O_3 samples supported by quartz wool. The samples were calcined at 500 °C for 2 h under 20% O_2/He (1.0 ml/s) and then, reduced at 500 °C for 1 h under 10% H_2/He (1.0 ml/s). After purging for 30 min under He (1.0 ml/s), Pt/Al_2O_3 were cooled to RT and ramped to 80 °C under H_2/He and stabilized before injection of C_6H_6 using a syringe pump. The outlet gases were analyzed by a GC (Agilent 7820A) with a HP-PLOT Al_2O_3 S column and FID. The reaction was carried out under 2% C_6H_6 and 10% H_2 under the total flow rate of 1 ml/s with He balance. During the measurements, catalyst deactivation was observed, so the catalytic activities were compared based on the initial rates by linear extrapolation. The rate measurements were recorded in the absence of diffusion control or thermal gradients by using the Madon–Boudart criterion as described in **Figure 4.1**.[30] The maximum benzene conversion obtained in this work was 13%.

We tested benzene hydrogenation at different temperature and different amounts of samples with two samples (0.5 and 1wt% Pt/Al_2O_3) with the similar dispersion but the different loading (H/Pt = 0.94 for 0.5Pt/Al_2O_3 and 0.86 for 1Pt/Al_2O_3). Based on Madon-Boudart criterion, when the intrinsic activity was plotted with the total available Pt sites, the slope should be close to 1 in order to confirm that the reaction condition is free from heat and mass-transfer limitation. **Figure 4.1a** showed that when the reaction was carried out at 100 ^{o}C with 10 mg amount, the slope is largely deviated from 1, indicating the reaction condition got affected by transfer limitation. But, when using samples 6 mg as shown in **Figure 4.1b**, the slope became close to 1, meaning that the reaction condition is free from heat and mass-transfer limitation.

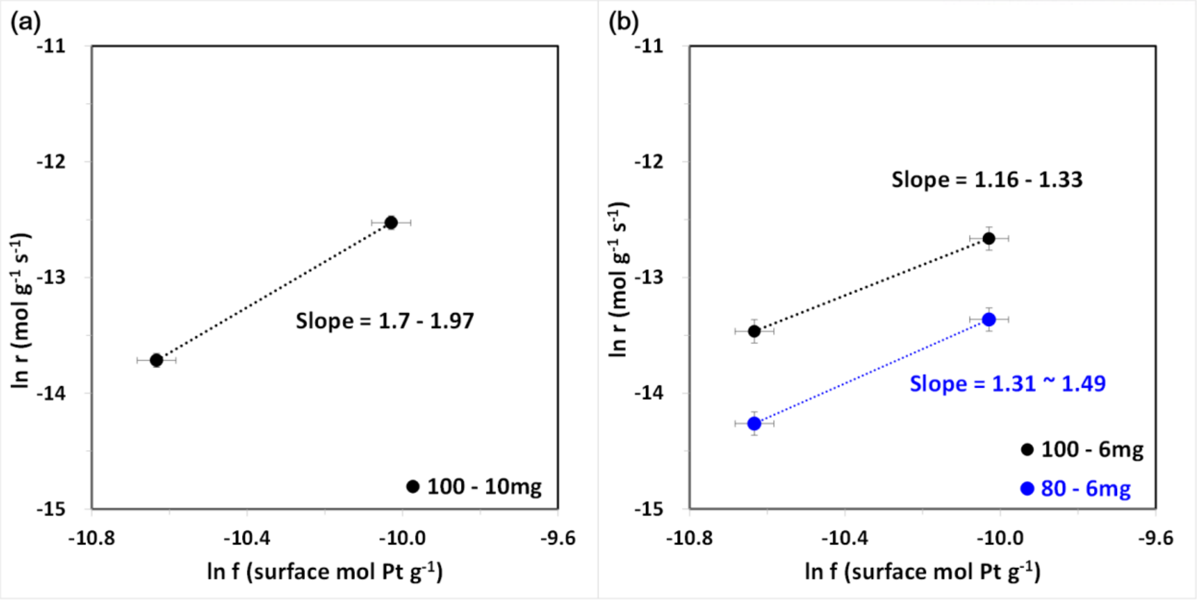

Figure 4.1. Madon-Boudart criterion for benzene hydrogenation under 2% C_6H_6 and 10% H_2 for (a) 0.5 wt% Pt and 1 wt% Pt/Al_2O_3 at 100 °C with 10 mg samples and (b) 80 °C and 100 °C with 6 mg samples after calcination and reduction at 500 °C. H/Pt values for 0.5 wt% Pt/Al_2O_3 and 1 wt% Pt/Al_2O_3 were 0.94 and 0.86 after calcination and reduction at 500 °C, respectively.

4.4. Results and discussion

In order to investigate the effect of the number and properties of specific sites on an alumina surface for Pt-Al_2O_3 interaction, we chose two sets of model aluminas having different number of sites with the identical properties and different properties but with the same number of sites. Recently, we studied the acid-base properties of alumina with various surface characteristics by ethanol TPD and reported that the desorption temperature of dissociative ethanol (at the maximum rate of ethylene desorption, T_d) can be used as a descriptor for the acid-base properties of alumina.[19, 24, 28] The number of sites on an Al_2O_3 surface can be determined by the amount of dissociative ethanol desorbed, and the properties of the sites by the desorption temperature (T_d) from ethanol TPD. With the aid of ethanol TPD, we chose the model aluminas T150, T110, T80 (supplied from Sasol), and T1000 (obtained by calcining T150 at 1000 °C for 3 h), and their characterizations will be detailed in the later sections.

4.4.1. Number of sites

The XRD diffraction pattern in **Figure 4.2a** showed that T150, T110, and T80 all exhibited the same bulk structure as γ-Al_2O_3 (JCPDS no. 10-425). The (222) peak at 2θ = 39.9° and (400)/(004) peaks at 2θ = 45.7–46.7° were sharper for T80 than for T150, indicating bigger crystallites for T80 compared to T150. The BET surface areas of the three aluminas (**Table 4.1**) followed the order T150 > T110 > T80 (T150: 143 m^2/g, T110: 95 m^2/g, and T80: 79 m^2/g). The N_2 adsorption/desorption profiles shown in **Figure 4.2b** revealed very small amounts of microporosity and mesopores, and showed the H3-type hysteresis which originated from the slit-like pores of aggregated platelet particles.[31] All the aluminas had hexagonal platelet morphologies which confirmed by TEM (**Figure 4.3**). The only difference was in their particle size. The particle size was the smallest for T150, the intermediate for T80, and the biggest for T80, which was consistent with the results of XRD and BET surface areas.

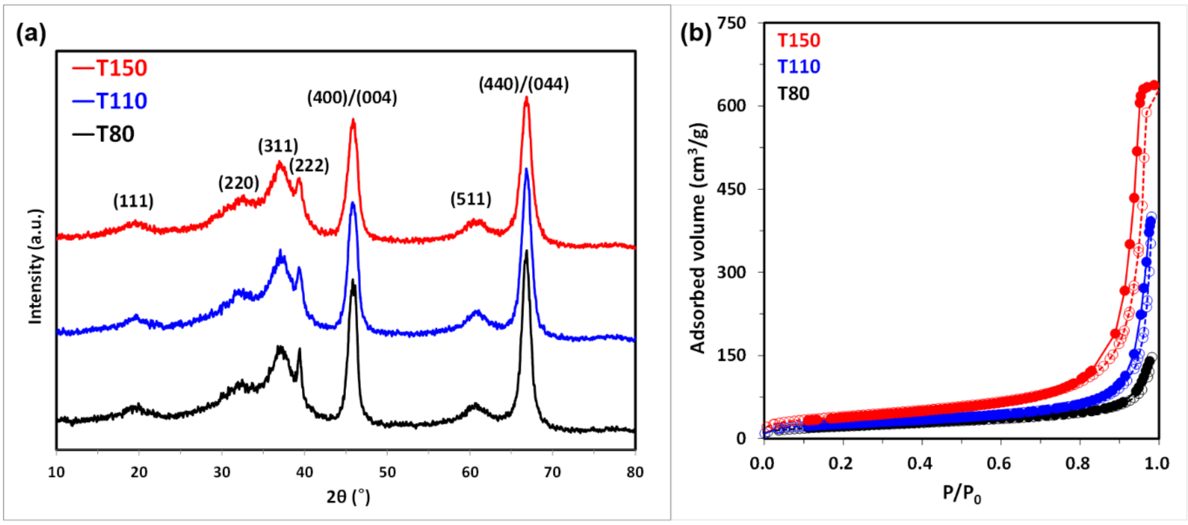

Figure 4.2. (a) XRD patterns and (b) N_2 adsorption/desorption profiles for T150, T110, and T80.

Table 4.1. BET surface area of T150, T110, T80, and T1000.

Sample	BET surface area (m^2/g)
T150	143
T110	95
T80	79
T1000	100

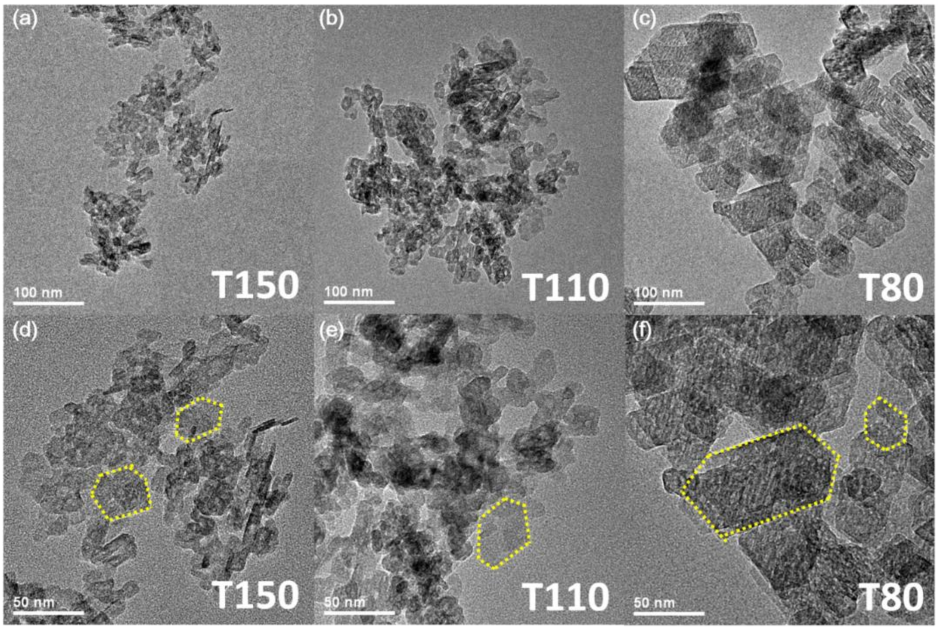

Figure 4.3. TEM images for (a,d) T150, (b,e) T110, and (c,f) T80.

Ethanol TPD for T150, T110, and T80 were performed after activation at 500 °C. The TPD profiles of the three aluminas, shown in **Figure 4.4**, were consistent with the previously reported profiles for γ-Al_2O_3.[22,24,27,32] The desorption profiles showed two peaks, one (at <150 °C) corresponding to weakly bound ethanol and the other (>150 °C) to dissociatively adsorbed ethanol, which was desorbed as ethylene. Interestingly, all three aluminas showed practically the same T_d (208.5–210 °C), with the only difference being the amounts of dissociative ethanol desorbed. The desorption amounts of dissociative ethanol were 3.8×10^{-4} mol/g for T150, 2.4×10^{-4} mol/g for T110, and 2.0×10^{-4} mol/g for T80, which was consistent with the trend in the BET surface area (T150 > T110 > T80).

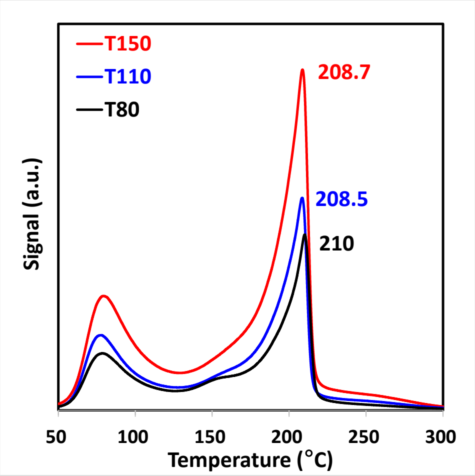

Figure 4.4. Ethanol TPD for T150, T110, and T80.

Figure 4.5a showed the DRIFTS spectra for surface hydroxyl groups for T150, T110, and T80 after activation at 380 °C. All spectra showed the peaks at 3766, 3725, 3670, and 3585 cm^{-1}, which was consistent with typical bands of γ-Al_2O_3.[33,34] Even though the exact assignments of surface hydroxyls on γ-Al_2O_3 are still debated,[16,17,35-39] the relative distributions of each hydroxyl band were similar, indicating the identical distribution of hydroxyl groups on the three aluminas, which exhibited the same bulk structure as γ-Al_2O_3 based on XRD and similar acidic properties, as evidenced by the same T_d obtained from ethanol TPD.

Figure 4.5b and **4.5c** showed the DRIFTS spectra after pyridine adsorption at 100 °C on T150, T110, and T80. **Figure 4.5c** showed two distinctive peaks at 1623 and 1614 cm^{-1}, which were assigned to the pyridine on Lewis acid sites and the weakly acidic surface OH groups of the alumina surface, respectively.[40] The relative ratios between the 1623 and 1614 cm^{-1} peak intensities were similar for the three aluminas. **Figure 4.5b** showed the perturbed surface hydroxyls after pyridine adsorption. Furthermore, the relative ratios between the 3766 and 3722 cm^{-1} peaks for the three aluminas were similar. Overall, the IR results reveal similar acid site distributions among T150, T110, and T80 (similar properties of sites). This is consistent with the same T_d (208.5–210 °C) from ethanol TPD. In addition, the TEM image shown in **Figure 4.3** confirmed that all the aluminas have hexagonal morphologies, but with different particle sizes, indicating the same facet ratio.

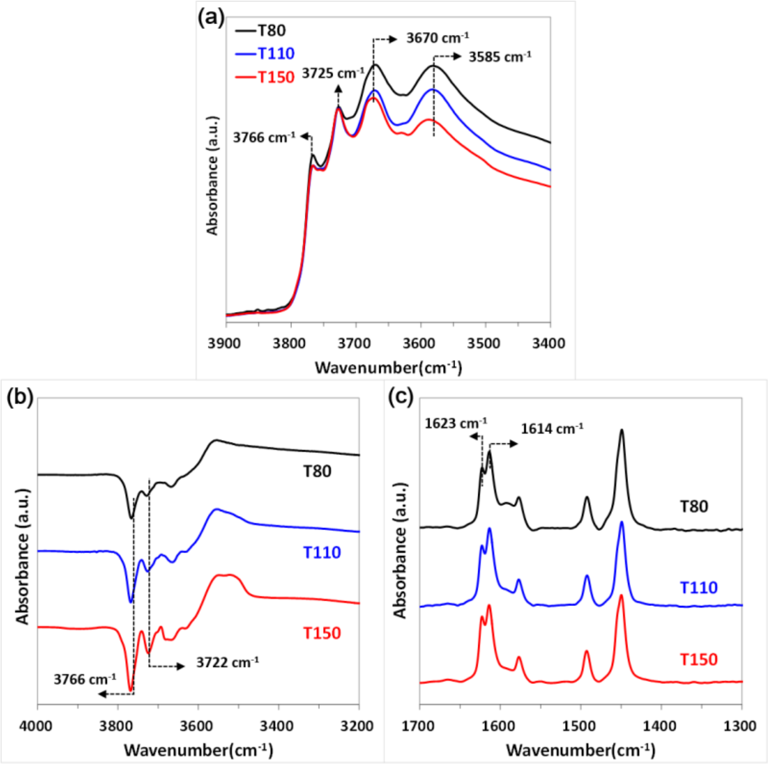

Figure 4.5. (a) DRIFT spectrum of OH regions and (b,c) DRIFT spectrum after pyridine adsorption at 100 °C for T150, T110, and T80.

All the results clearly demonstrate that T150, T110, and T80 can be regarded as model aluminas having different number of specific sites with the same properties. Next, we loaded the active phase (Pt) on these model aluminas by conventional incipient wetness impregnation and studied the effects of the number of specific sites on Pt-Al_2O_3 interaction. We thought, if aluminas have different number of surface sites, then the number of Pt atoms that can interact with the defect sites on the alumina surface would be different, leading to different Pt dispersion.

Figure 4.6 showed H/Pt as a function of Pt loading from 0.5 to 10 wt%, as obtained from H_2 chemisorption after in-situ oxidation and reduction at 500 °C. Overall, H/Pt decreased with increasing Pt loading. At low loading 0.5–1 wt% Pt, H/Pt was practically the same for all the model aluminas. At 1 wt% Pt/Al_2O_3, H/Pt was 0.86 for T150, 0.89 for T110, and 0.86 for T80. However, at higher Pt loading from 2–10 wt%, H/Pt was the highest for T150 and the lowest for T80. At 10 wt% Pt/Al_2O_3, H/Pt was 0.31 for T150, 0.21 for T110, and 0.18 for T80, showing that Pt was better dispersed on T150 than on T80. Overall, the higher the number of specific sites on the alumina, the higher the Pt dispersion.

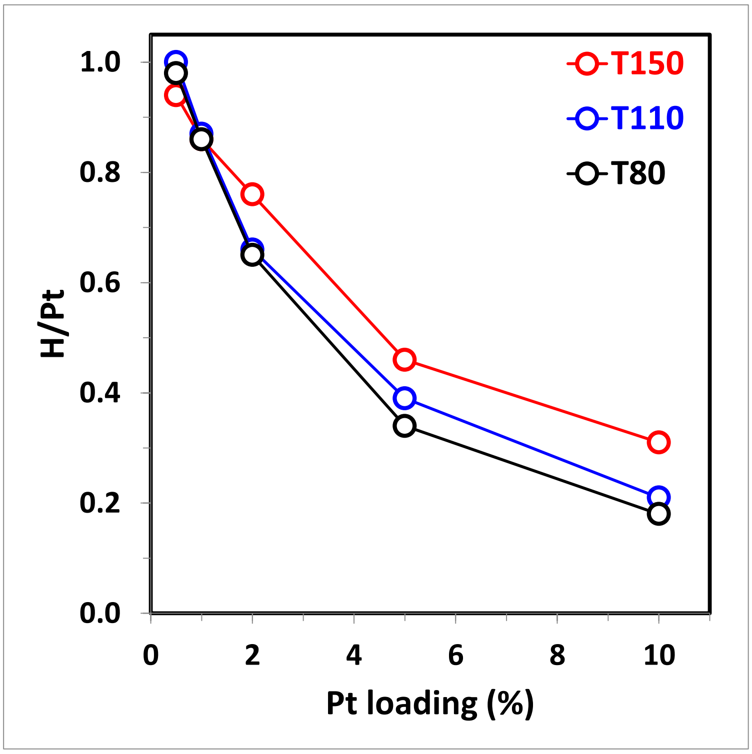

Figure 4.6. H/Pt trend as a function of Pt loading for T150, T110, and T80 after calcination and reduction at 500 °C.

It is well known that Pt dispersion and morphology significantly depend on Pt loading relative to the number of anchoring sites on the alumina surface.[14,42] Quantitative high-resolution ^{27}Al-NMR studies showed that when Pt/Al^{3+}_{penta} (penta-coordinated Al^{3+} sites) is one at 300 °C for calcined 1 wt% Pt/γ-Al_2O_3, Pt exists as atomically dispersed form, but 2D clusters are formed at higher Pt/Al^{3+}_{penta} for higher Pt loading on γ-Al_2O_3 (2–10 wt% Pt). In addition, large agglomerated Pt was detected when Pt loading increased.[42] Despite the different preparation methods used for Pt/Al_2O_3 in this study (150–80 m^2/g γ-Al_2O_3 and 500 °C calcination and reduction), the results consistently showed that H/Pt decreased with increasing Pt loading. At 0.5–1 wt% Pt loading, the three aluminas all have sufficient number of sites to disperse all the Pt atoms. That's why the H/Pt values for T150, T110, and T80 were all similarly close to 1, indicating highly dispersed Pt clusters on alumina surfaces. However, with increasing Pt loading to 10 wt%, the number of Pt atoms became higher than that of the anchoring sites. It leads a gradual decrease of H/Pt with increasing Pt loading up to 10 wt%. The 10 wt% Pt/Al_2O_3 showed H/Pt values of 0.31–0.18, indicating that the Pt cluster size increased compared to that of 1 wt% Pt/Al_2O_3. Although all the Pt could not be highly dispersed at 10 wt% loading, T150 has twice the number of sites as T80, leading to a higher Pt dispersion on T150 (10 wt% Pt/T150: 0.31 and 10 wt% Pt/T80: 0.18), because more Pt atoms can interact with the anchoring sites on the T150 surface. In other words, T80 has less anchoring sites for stabilizing Pt, leading to more Pt sintering compared to T150.

The Pt dispersion was also confirmed by TEM measurements. **Figure 4.7** showed the representative STEM images for 1 wt% Pt/Al_2O_3 after calcination and reduction at 500 °C. Pt clusters around ~ 1 nm were highly dispersed, consistent with the absence of diffraction peak for Pt in XRD (**Figure 4.8**) and also hydrogen chemisorption data. The Pt size distribution by measuring 400 clusters revealed that the average particle diameter was 1.2 nm for T150, 1.0 nm for T110, and 1.0 nm for T80, indicating that the Pt size was similar among the aluminas, which was consistent with the same H/Pt obtained by H_2 chemisorption. At low loading (1 wt% Pt), the number of anchoring sites is sufficient to disperse all the Pt, leading to the formation of highly dispersed small Pt clusters.

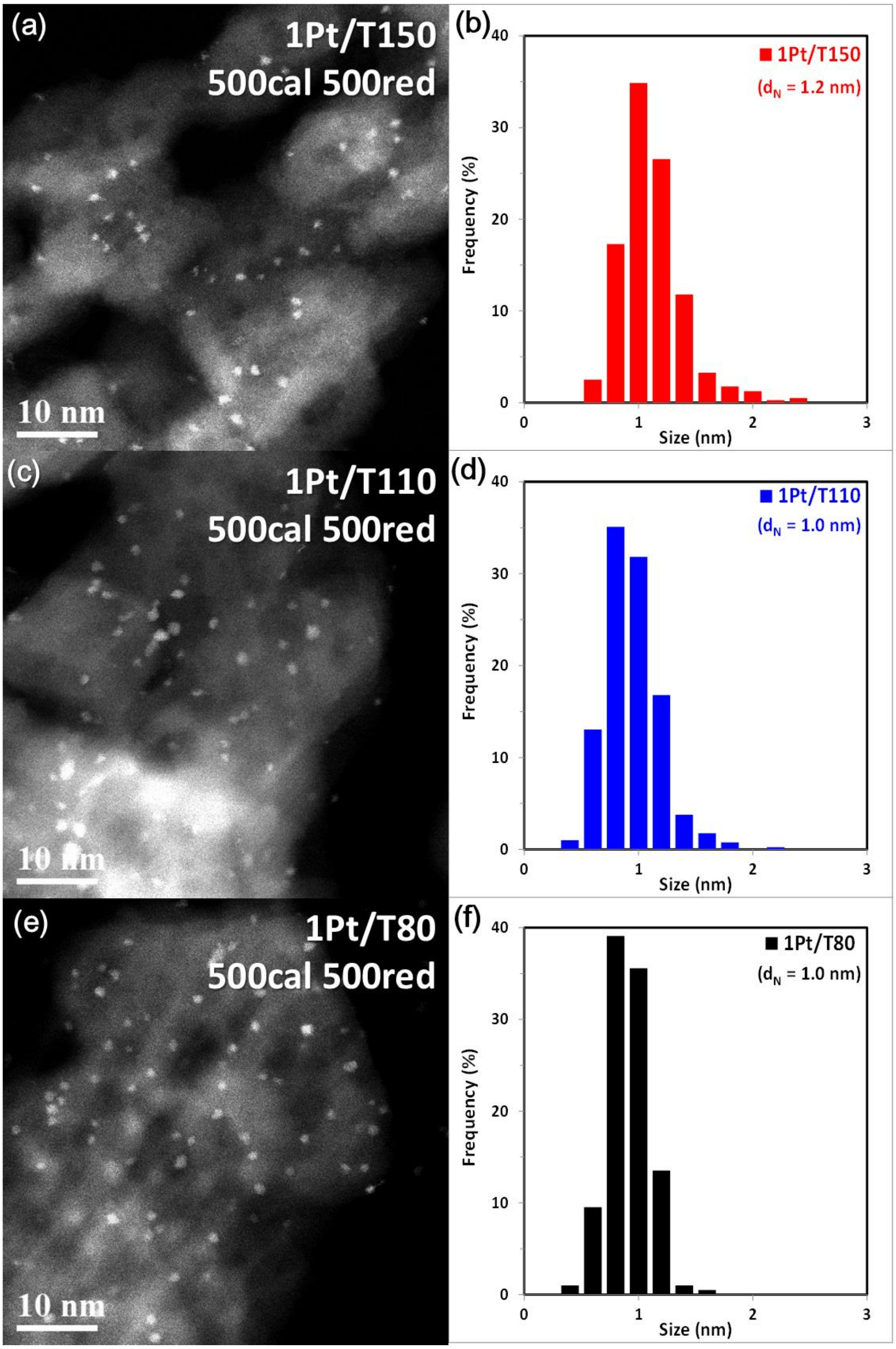

Figure 4.7. STEM images and particle size distribution for (a,b) 1Pt/T150, (c,d) 1Pt/T110, and (e,f) 1Pt/T80.

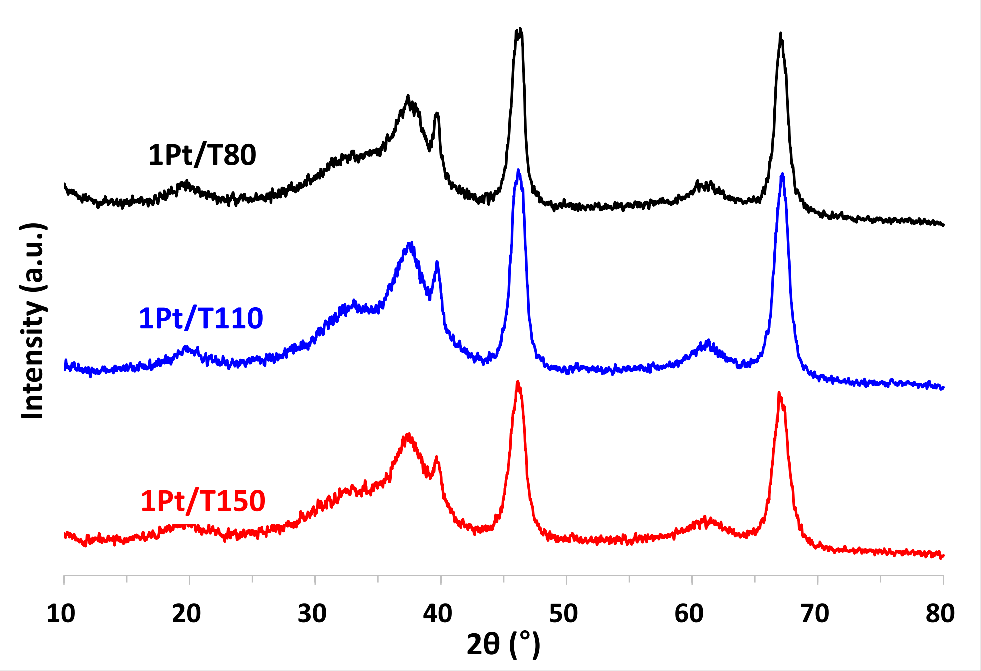

Figure 4.8. XRD patterns for 1Pt/T150, 1Pt/T110, and 1Pt/T80 after calcination and reduction at 500 °C.

Figure 4.9 showed the representative TEM and STEM images for 10 wt% Pt/Al_2O_3 after the same treatments. At high loadings, the number of Pt is much higher than that of the anchoring sites, leading to the agglomeration of Pt atoms and heterogeneous distribution on the alumina surface. The TEM images showed both agglomerated Pt (> 10 nm) and small Pt clusters (< 3 nm), indicating a bimodal distribution of Pt cluster sizes for 10 wt% Pt /Al_2O_3. Here, a significant portion of Pt still existed as highly dispersed Pt with the size around ~1 nm, which was similar to that of 1 wt% Pt/Al_2O_3. When we compare the Pt size distribution up to ~3 nm size, T80 exhibited a greater fraction of bigger Pt clusters than T150 and T110, which was consistent with the trend in H/Pt. However, these size differences are not straightforward when we consider the average Pt size change estimated based on H_2 chemisorption (3.5 nm for T150, 5.2 nm for T110 and 6.1 nm for T80), suggesting the intrinsic limitation of the local properties of TEM characterization. In order to characterize the bigger Pt clusters, we carried out XRD analysis (**Figure 4.10**). The figure showed diffraction peaks for Pt (111) at $2\theta = 39.8°$, Pt (002) at $2\theta = 46.2°$ and Pt (022) at $2\theta = 67.5°$. Although the diffraction peaks of Pt overlap with those of Al_2O_3, we can clearly observe the sharp peak of Pt(111), indicating that agglomerated Pt exists on 10 wt% Pt/Al_2O_3. Here, the Pt(111) peak intensities were the highest for 10 wt% Pt/T80, the intermediate for 10 wt% Pt/T110, and the lowest for 10 wt% Pt/T150, consistently showing that large agglomerated Pt clusters existed on T80 than on T150. The estimation of Pt size using the Scherrer equation was not straightforward owing to the mixed Al_2O_3 peaks and the broad peaks of smaller Pt clusters. Despite a bimodal distribution for 10 wt% Pt/Al_2O_3, all the characterizations showed that T150 exhibit a higher Pt dispersion than T80 for both agglomerated Pt and small Pt clusters, clearly demonstrating that Pt can be more highly dispersed with increasing number of sites of alumina.

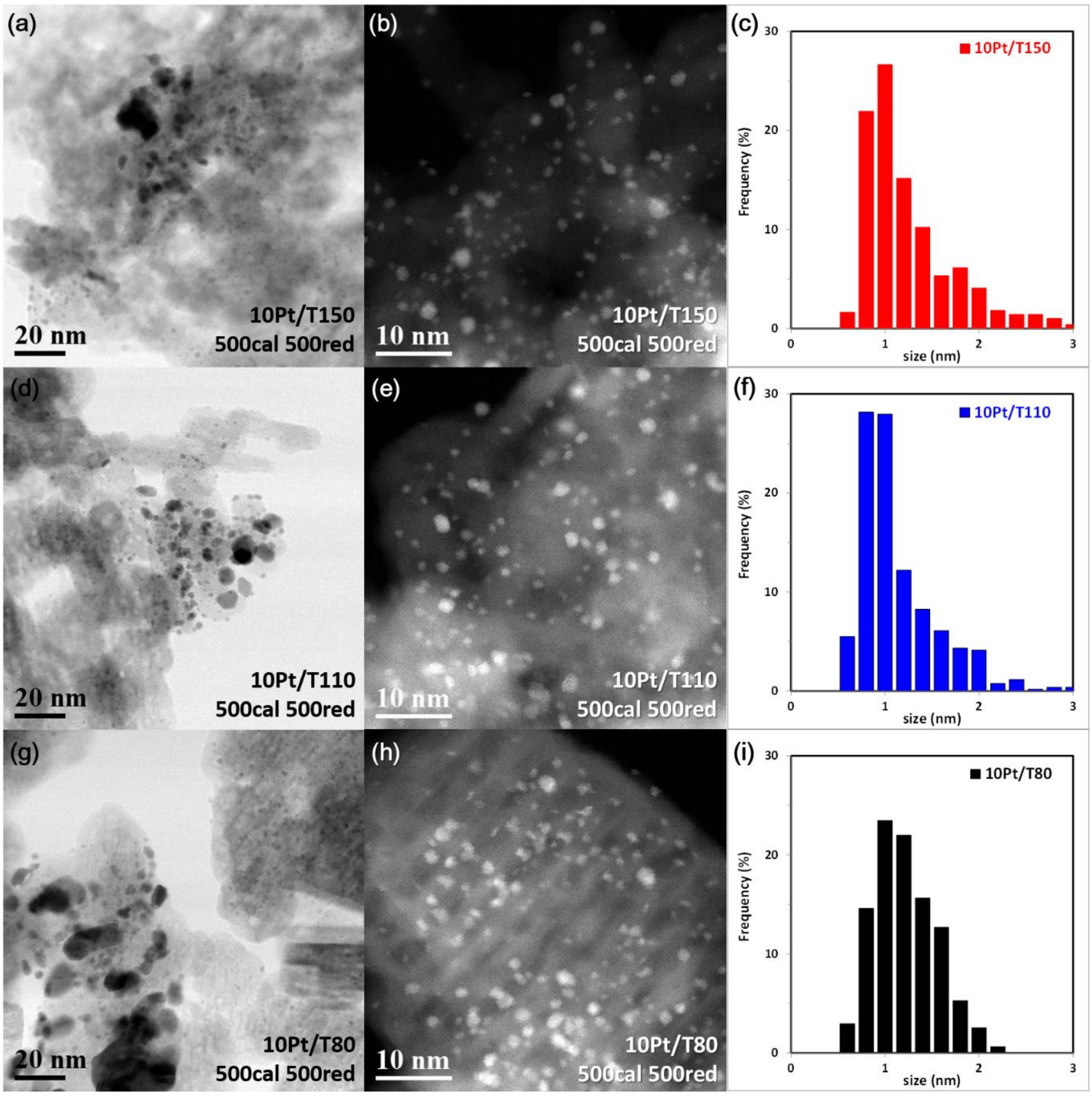

Figure 4.9. Low magnification TEM, STEM images and particle size distribution below ~ 3 nm for (a-c) 10Pt/T150, (d-f) 10Pt/T110, and (g-i) 10Pt/T80 after calcination and reduction at 500 °C.

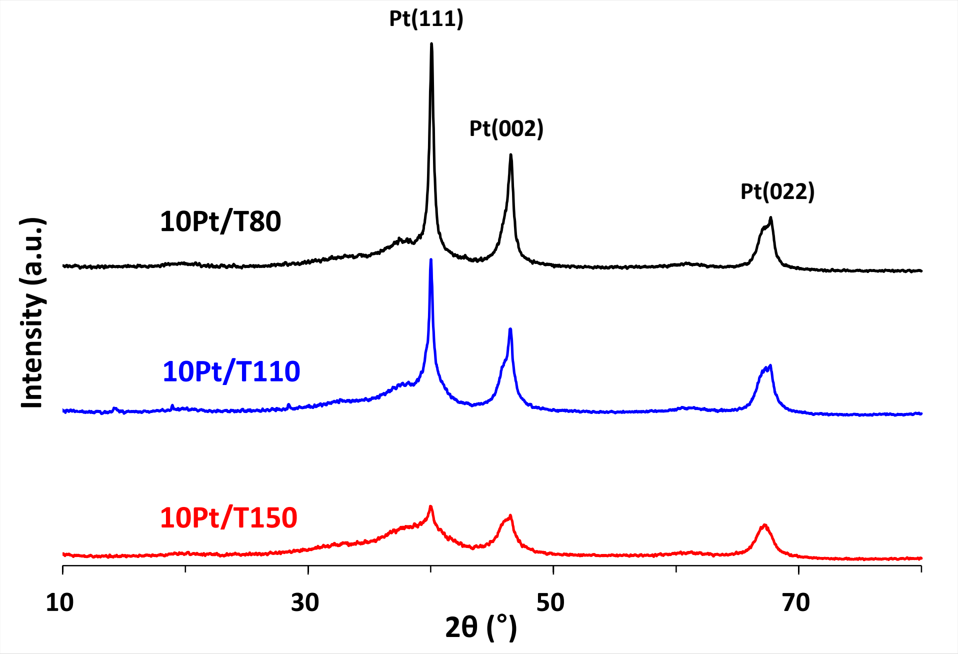

Figure 4.10. XRD patterns for 10Pt/T150, 10Pt/T110, and 10Pt/T80 after calcination and reduction at 500 °C.

Note here that utilizing multiple characterization techniques is important for understanding the heterogeneous nature of Pt/Al_2O_3. While TEM has limitations for Pt size measurements of localized information, XRD reveals only larger Pt crystallites due to the low detectability for small Pt clusters (below ~ 2 nm).[43, 44] H_2 chemisorption shows the ensemble results for Pt dispersion, but a dominant contribution from smaller Pt clusters than agglomerated Pt because only small fractions of Pt are exposed for the agglomerated Pt clusters.[44] Using multiple characterization tools is critical for careful understanding Al_2O_3-supported Pt catalysts.

In summary, increasing the number of specific sites on alumina can increase Pt dispersion. However, the higher Pt dispersion does not arise from a gradual change in Pt cluster size, but from an increased fraction of highly dispersed Pt clusters (< 3 nm) on alumina under bimodal Pt size distribution involving large agglomerated Pt (> 10 nm) and small Pt clusters (< 3 nm).

4.4.2. *Properties of sites*

In order to understand the effect of the properties of specific sites on Pt-Al_2O_3 interaction, we prepared two aluminas having similar number of sites with significantly different properties. We calcined T150 at 1000 °C for 3 h and labeled it as T1000, which was compared with T80.

Figure 4.11 showed the ethanol TPD desorption profiles for T1000 and T80. The desorption temperature at the maximum rates (T_d) for T1000 was 34 °C higher than that of T80 (T150: 244.4 °C, and T80: 210 °C). This was consistent with previous reports that T_d shift into higher temperatures with increasing calcination temperature.[19,24,32] Note here that the amount of dissociative ethanol desorbed was practically the same for T1000 and T80 (1.8×10^{-4} mol/g for T1000 and 2.0×10^{-4} mol/g for T80).

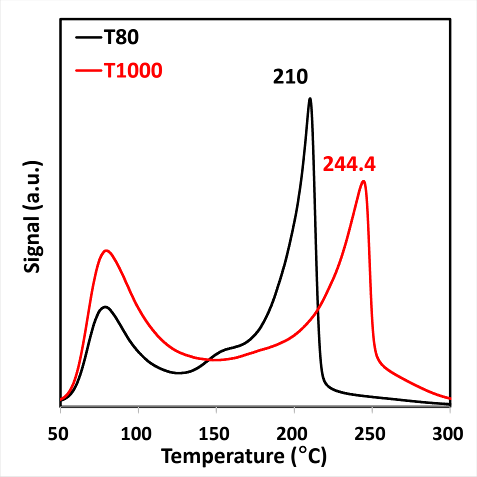

Figure 4.11. Ethanol TPD for T1000 and T80.

The XRD pattern of T1000 (**Figure 4.12a**) showed two θ-Al_2O_3 peaks at 2θ = 44.8° and 47.8° that were clearly visible, apart from the δ-Al_2O_3 peak at 45.8°, indicating that T1000 was phase-transformed into a mixture of δ-Al_2O_3 and θ-Al_2O_3.[45,46] The T80 was previously confirmed as γ-Al_2O_3 (**Figure 4.2a**). The BET surface area of T1000 (**Table 4.1**) was 100 m^2/g, higher than that of T80 (79 m^2/g). The N_2 adsorption/desorption profile for T1000 as shown in **Figure 4.12b** was also similar to that of T80. The TEM images shown in **Figure 4.13** revealed that the morphology and particle size of T1000 were similar to those of precursor T150. The T1000 also had smaller particle size than T80 with the similar morphologies.

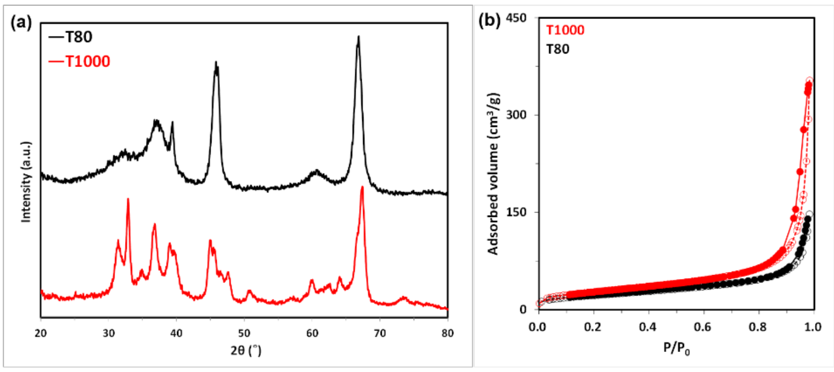

Figure 4.12. (a) XRD patterns and (b) N_2 adsorption/desorption profiles for T1000 and T80.

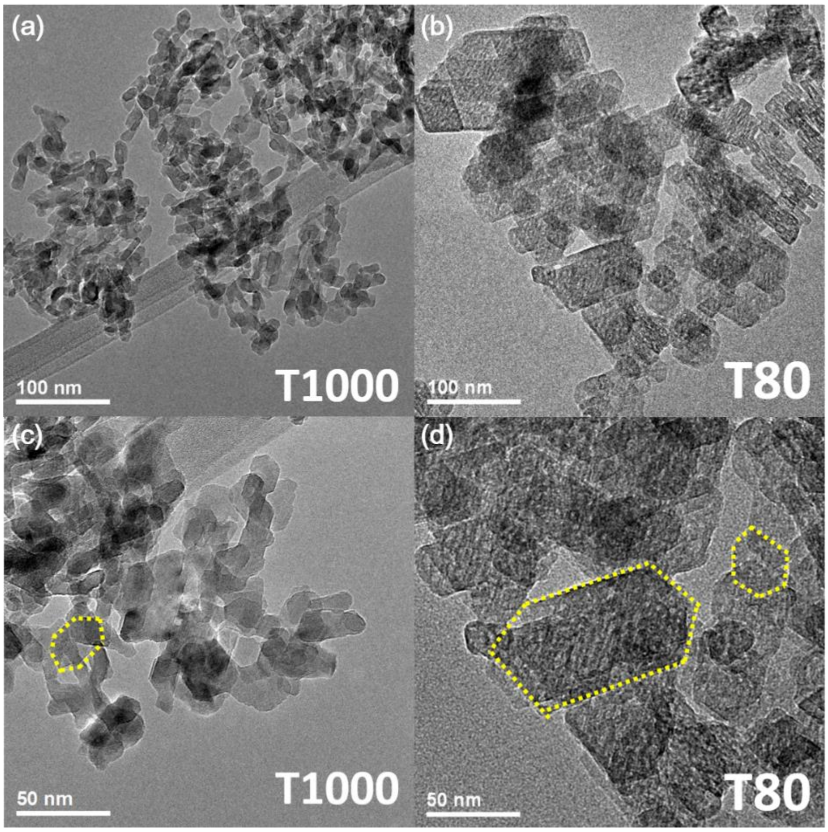

Figure 4.13. TEM images for (a,c) T1000 and (b,d) T80.

Figure 4.14a showed the DRIFTS spectra for the surface hydroxyls of T1000 and T80 after activation at 380 °C. The spectrum of T1000 showed 3790 cm^{-1} bands that appeared with the decrease of the 3766 cm^{-1} peak compared to that of T80 (γ-Al_2O_3), and corresponded to the typical hydroxyl spectra for δ,θ-Al_2O_3, which was consistent with the δ,θ-Al_2O_3 bulk structure by XRD.[33,37] It should be noted that T1000 had a new type of surface hydroxyls at 3790 cm^{-1}, which is assigned as isolated hydroxyls on tetrahedral or octahedral Al species, although the exact assignments are still controversial.[16,17,35,37-39]

Figure 4.14b and **4.14c** showed the DRIFTS spectra after pyridine adsorption at 100 °C on T1000 and T80. **Figure 4.14c** showed that the relative ratio between the 1623 and 1614 cm^{-1} peak intensities for T1000 was lower than that of T80. **Figure 4.14b** showed the perturbed surface hydroxyls during pyridine adsorption. Here, the 3790 cm^{-1} peaks were perturbed only in the case of T1000, also indicating a new type of surface hydroxyl was formed after the phase-transition to δ,θ-Al_2O_3. Overall, T1000 have different acid site distribution compared to T80, which correlates with the higher T_d (34 °C) from ethanol TPD (different properties of sites).

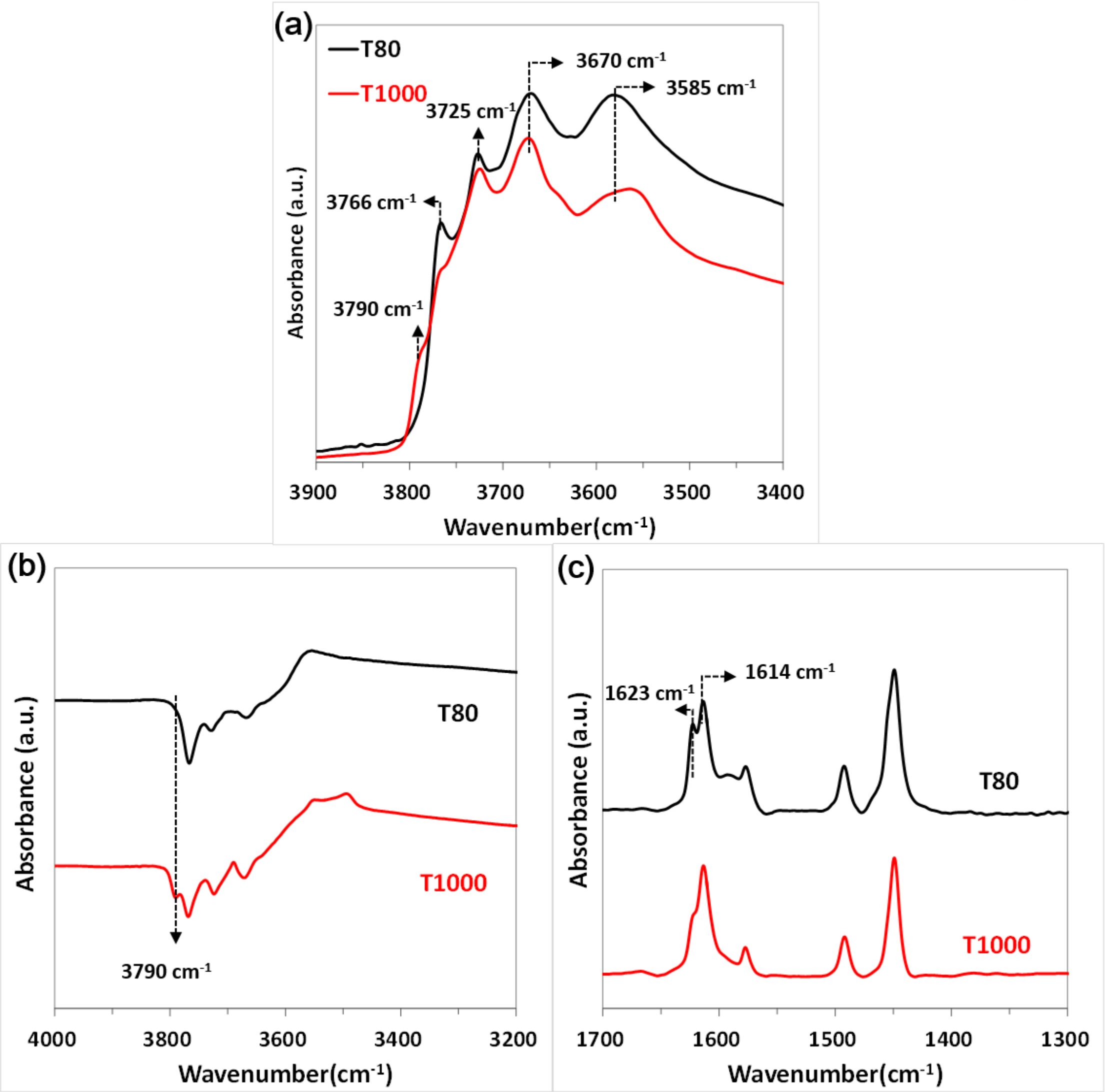

Figure 4.14. (a) DRIFT spectrum of OH regions and (b,c) DRIFT spectrum after pyridine adsorption at 100 °C for T1000 and T80.

In order to investigate the effect of the properties of sites for Pt-Al_2O_3 interaction, H_2 chemisorption was also carried out for Pt/T1000. **Figure 4.15** showed the H/Pt results obtained by H_2 chemisorption as a function of Pt loading from 0.5 to 10 wt%. Similar to the previous trend, H/Pt decreased with increasing Pt loading on T1000. At the loadings of 0.5–2 wt% Pt, H/Pt was practically the same on T1000 and T80. At 1 wt% Pt/Al_2O_3, H/Pt was 0.85 for T1000 and 0.86 for T80. However, interestingly, H/Pt was higher for T1000 than for T80 at higher Pt loading (5–10 wt%). At 10 wt% Pt/Al_2O_3, H/Pt was 0.26 for T1000 and 0.18 for T80, meaning that Pt was more well-dispersed on T1000 than on T80. Overall, the higher the T_d, the higher the Pt dispersion.

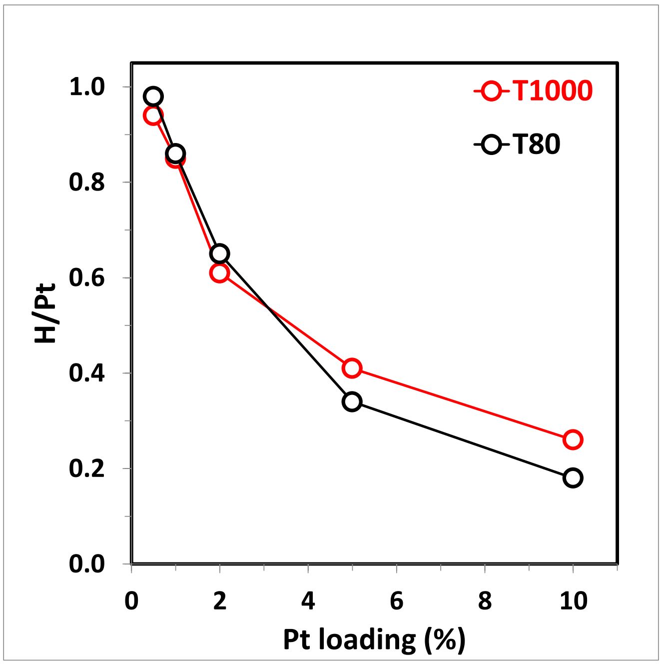

Figure 4.15. H/Pt trend as a function of Pt loading for T1000 and T80 after calcination and reduction at 500 °C.

As previously discussed, T1000 and T80 have enough number of sites to disperse Pt at 0.5–1 wt% Pt. Therefore, the H/Pt value was close to 1, meaning almost all the Pt was exposed to the surface. However, with increasing Pt loading to 10 wt%, the two aluminas have insufficient sites to disperse all the Pt, leading to a decrease in H/Pt below 1. Here, note that T1000 had the same number of sites as T80 but higher T_d (by 34 °C), as revealed by ethanol TPD (**Figure 4.11**). So, higher Pt dispersion on T1000 will be attributed to the properties of the sites on the alumina surface. A higher T_d on the alumina surface means that the Al sites bind ethanol more strongly than those of T80, making it difficult to desorb as ethylene. Similarly, the alumina surface on T1000 anchors Pt more strongly than that of T80 does, and stabilizes Pt, leading to a higher dispersion on T1000 than on T80. Considering the IR data (**Figure 4.14**), T1000 exhibits a new type of isolated surface hydroxyls at 3790 cm^{-1}, which would contribute to a higher Pt dispersion on T1000. Consistently, some studies have reported that these isolated hydroxyls are likely to be related to Pt anchoring.[47] However, more detailed studies on the relationship between Pt and surface hydroxyls are still needed, which will be the future work.

The Pt dispersion was also confirmed by TEM measurements. **Figure 4.16** showed the representative STEM images for 1 wt% Pt/Al_2O_3 after calcination and reduction at 500 °C. The Pt clusters around ~ 1 nm were highly dispersed, consistent with the absence of diffraction peaks for Pt in XRD (**Figure 4.17**). The Pt size distribution by measuring 400 clusters showed that the average particle diameter was 1.1 nm for T1000, and 1.0 nm for T80, indicating that the Pt sizes were similar between the aluminas, consistent with the same H/Pt by H_2 chemisorption.

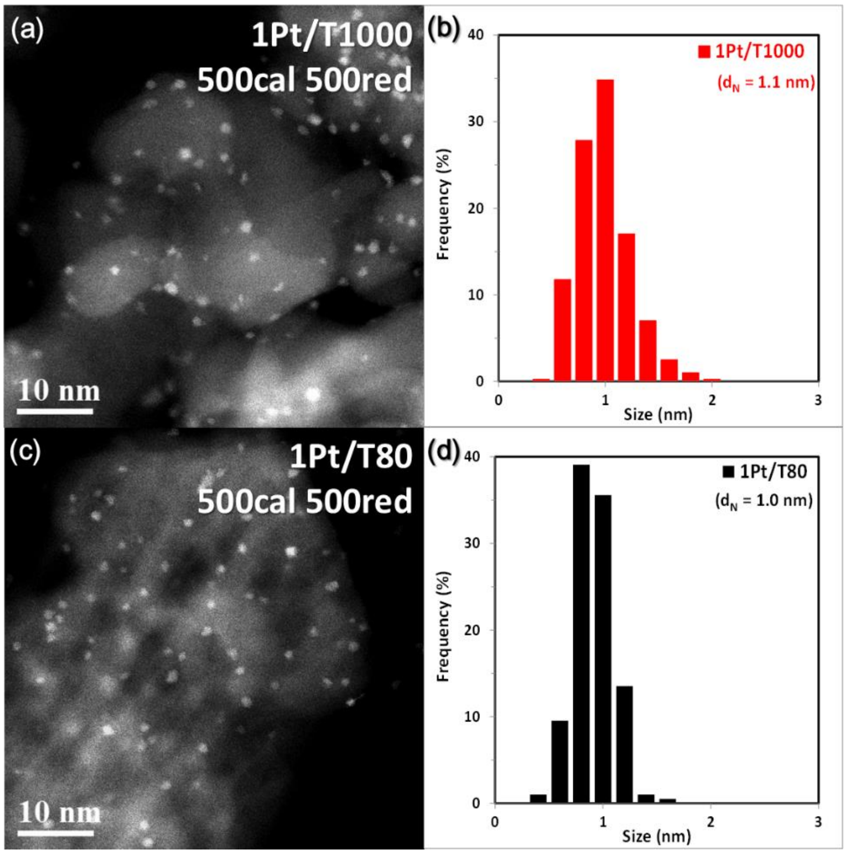

Figure 4.16. STEM images and particle size distribution for (a,b) 1Pt/T1000 and (c,d) 1Pt/T80.

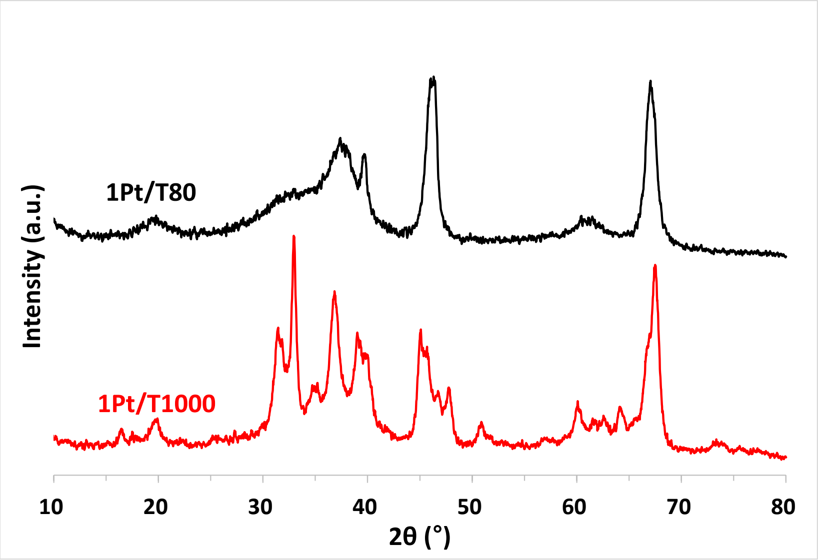

Figure 4.17. XRD patterns for 1Pt/T1000 and 1Pt/T80 after calcination and reduction at 500 °C.

Figure 4.18 showed STEM images for 10 wt% Pt/Al_2O_3 after the same treatment with 1 wt% Pt/Al_2O_3. As the number of sites on T1000 is similar to that on T80, T1000 also showed a bimodal distribution, similar to the case of T80. When we compare the Pt size distribution up to ~ 3 nm size, T80 showed more portion of bigger Pt clusters than T1000, which was consistent with the trend in H/Pt. However, these size differences are not significant when we consider the average Pt size change estimated by H_2 chemisorption (4.2 nm for T1000 and 6.1 nm for T80). So, we carried out the XRD analysis (**Figure 4.19**). The results showed that the Pt(111) peak intensities were higher for 10 wt% Pt/T80 than 10 wt% Pt/T1000, indicating that more agglomerated Pt exists on T80 than on T1000. Again, the Pt size estimation was not accurate due to the overlapping of the alumina peak and underlying broadness of smaller Pt clusters. Despite the bimodal distribution for 10 wt% Pt/Al_2O_3, all the characterizations showed that T1000 has a higher Pt dispersion than T80 for both agglomerated Pt and small Pt clusters, clearly demonstrating that Pt can be more highly dispersed with T_d increase on alumina surfaces.

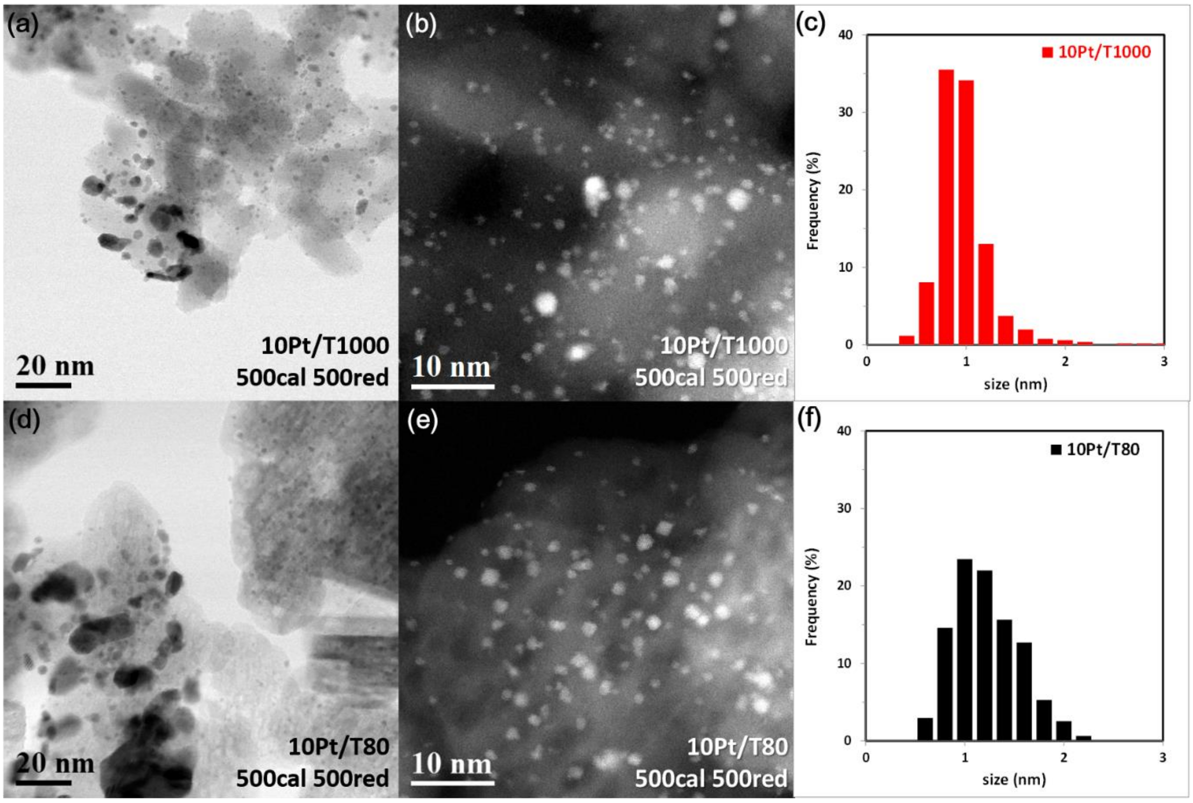

Figure 4.18. Low magnification TEM, STEM images and particle size distribution below ~ 3 nm for (a-c) 10Pt/T1000 and (d-f) 10Pt/T80 after calcination and reduction at 500 °C.

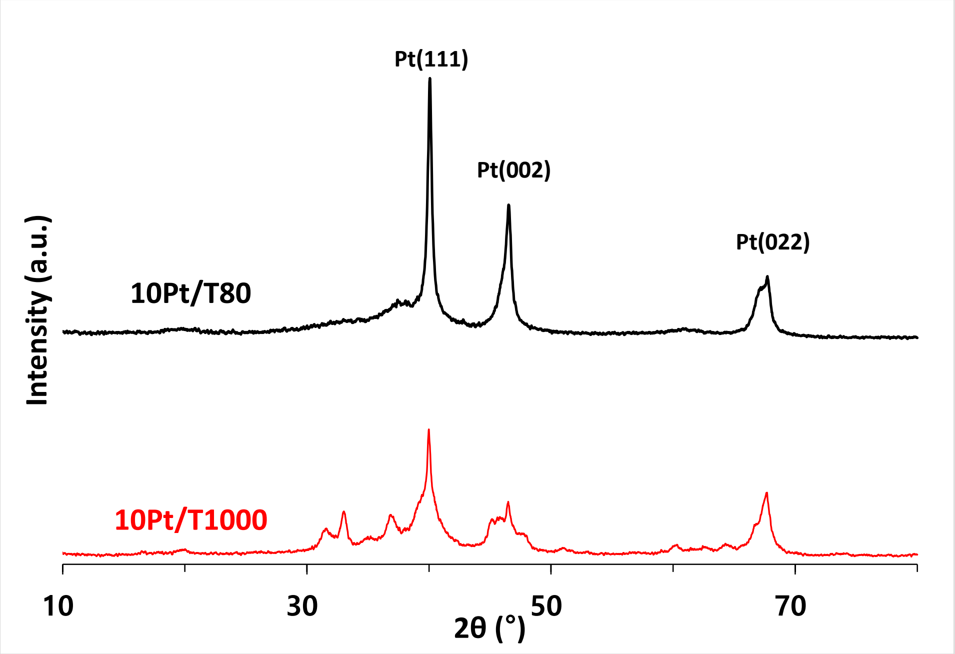

Figure 4.19. XRD patterns for 10Pt/T1000 and 10Pt/T80 after calcination and reduction at 500 °C.

4.4.3. *Catalytic reaction: benzene hydrogenation*

In order to study how the number and properties of sites affect the catalytic properties of Pt/Al_2O_3, we carried out C_6H_6 hydrogenation reaction. C_6H_6 hydrogenation has been one of the typical model reactions for supported metal characterization for decades.[48-52] We chose 1 wt% Pt/Al_2O_3 and 10 wt% Pt/Al_2O_3 for T150, T80, and T1000 model alumina after 500 °C calcination and reduction. C_6H_6 hydrogenation was carried out at 80 °C. Note that for each reaction, the same amount of catalyst was used: 6 mg for 1 wt% Pt/Al_2O_3 and 3 mg for 10 wt% Pt/Al_2O_3.

Figure 4.20a showed the reaction profiles of C_6H_6 hydrogenation for 1 wt% Pt/T150 and 1 wt% Pt/T80. Catalyst deactivation was observed during the reaction, so the initial activity was estimated by linear extrapolation. Both 1 wt% Pt/T150 and 1 wt% Pt/T80 showed practically the same activity profile. The turnover frequency (TOF) normalized by H/Pt (**Table 4.2**) was 0.045 C_6H_6/Pt·s for 1 wt% Pt/T150 and 0.046 C_6H_6/Pt·s for 1 wt% Pt/T80. However, 10 wt% Pt/T150 showed much higher conversion than 10 wt% Pt/T80 as shown in **Figure 4.20b**. The TOF normalized by H/Pt (**Table 4.2**) was practically the same, 0.17 and 0.166 C_6H_6/Pt·s for 10 wt% Pt/T150 and 10 wt% Pt/T80, respectively. Previous characterization data showed that 1 wt% Pt/T150 and 1 wt% Pt/T80 had the same Pt dispersion, as confirmed by H_2 chemisorption and STEM. That's why the same reaction profile and TOF for 1 wt% Pt/T150 and 1 wt% Pt/T80. However, 10 wt% Pt/T150 (H/Pt–0.31) showed higher Pt dispersion than 10 wt% Pt/T80 (H/Pt –0.18). In addition, the XRD and TEM results showed that agglomerated Pt and small Pt clusters coexist on 10 wt% Pt/Al_2O_3. Owing to a very low number of exposed sites on agglomerated Pt, the reaction is typically governed by the highly dispersed Pt clusters (< 3 nm). It suggests that the intrinsic activity of the Pt clusters (TOF) were the same, but the higher conversion for 10 wt% Pt/T150 than for 10 wt% Pt/T80 can be interpreted that more Pt clusters on 10 wt% Pt/T150 contributed the reaction, which contributed dominantly from highly dispersed Pt clusters.

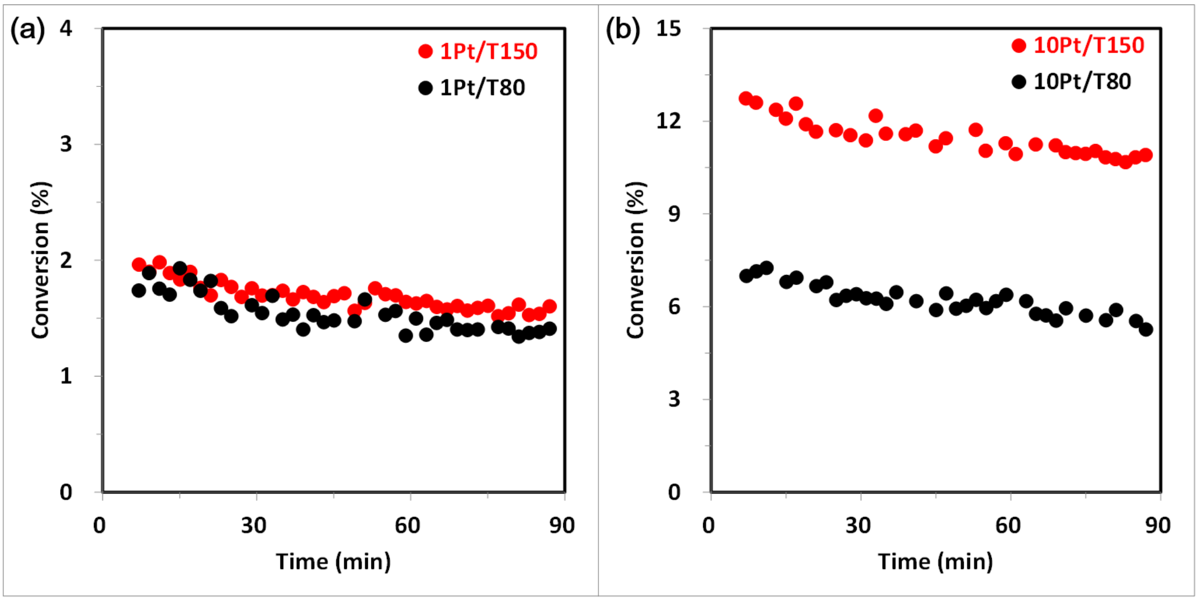

Figure 4.20. Time-on-stream C_6H_6 hydrogenation profiles for (a) 1Pt/T150 and 1Pt/T80 and (b) 10Pt/T150 and 10Pt/T80.

Table 4.2. H/Pt value, benzene hydrogenation conversion and turnover frequencies for 1Pt/T150, 1Pt/T80, and 1Pt/T1000 (top) and 10Pt/T150, 10Pt/T80, and 10Pt/T1000 (bottom). Turnover frequencies were normalized based on H/Pt from hydrogen chemisorption.

Sample	H/Pt	Conversion (%)	TOF (C_6H_6/Pt · s)
1Pt/T150	0.86	1.9	0.046
1Pt/T80	0.86	1.9	0.046
1Pt/T1000	0.85	2.0	0.050
10Pt/T150	0.31	12.5	0.170
10Pt/T80	0.18	7.1	0.166
10Pt/T1000	0.26	9.6	0.156

Subsequently, we studied the effect of the properties of the sites on alumina surfaces for benzene hydrogenation by comparing Pt/T1000 and Pt/T80. **Figure 4.21a** showed the reaction profile for C_6H_6 hydrogenation for 1 wt% Pt/T1000 and 1 wt% Pt/T80. The initial conversion was 2.0% for 1Pt/T1000 and 1.9% for 1 wt% Pt/T80, showing similar activities. The TOF normalized by H/Pt (**Table 4.2**) was 0.050 C_6H_6/Pt·s for 1 wt% Pt/T1000 and 0.046 C_6H_6/Pt·s for 1 wt% Pt/T80. Similar to the earlier case of 1 wt% Pt/T150 and 1 wt% Pt/T80, 1 wt% Pt/T1000 showed Pt dispersion similar to that of 1 wt% Pt/T80, as evidenced from H/Pt and STEM. That's why 1 wt% Pt/T1000 showed the identical activity with 1 wt% Pt/T80. It is also reasonable to conclude that all the 1 wt% Pt/Al_2O_3 investigated for benzene hydrogenation (1 wt% Pt/T150, 1 wt% Pt/T80, and 1 wt% Pt/T1000) had similar Pt dispersions and intrinsic activities (TOF: 0.046–0.050 C_6H_6/Pt·s).

However, as shown in **Figure 4.21b**, 10 wt% Pt/T1000 showed higher conversion than 10 wt% Pt/T80. The H_2 chemisorption results indicated that 10 wt% Pt/T1000 (H/Pt–0.26) showed higher Pt dispersion than 10 wt% Pt/T80 (H/Pt–0.18). When we compare the TOF normalized by H/Pt (**Table 4.2**), the values were 0.156 C_6H_6/Pt·s for 10 wt% Pt/T1000 and 0.166 C_6H_6/Pt·s for 10 wt% Pt/T80, which were practically same. Also, the XRD and TEM results showed that agglomerated Pt and small Pt clusters coexist on 10 wt% Pt/Al_2O_3. It suggests that the intrinsic activities of the Pt clusters were still the same, though the higher conversion for 10 wt% Pt/T1000 can be attributed to the higher number of Pt surface sites on 10 wt% Pt/T1000, which are dominated by the highly dispersed Pt clusters. When we compared this with 10 wt% Pt/T150 activity, 10 wt% Pt/T150 showed the higher conversion (12.5%) than 10 wt% Pt/T1000 (9.6%) because it has more exposed Pt sites (H/Pt is 0.31 for 10 wt% Pt/T150, and 0.26 for 10 wt% Pt/T1000).

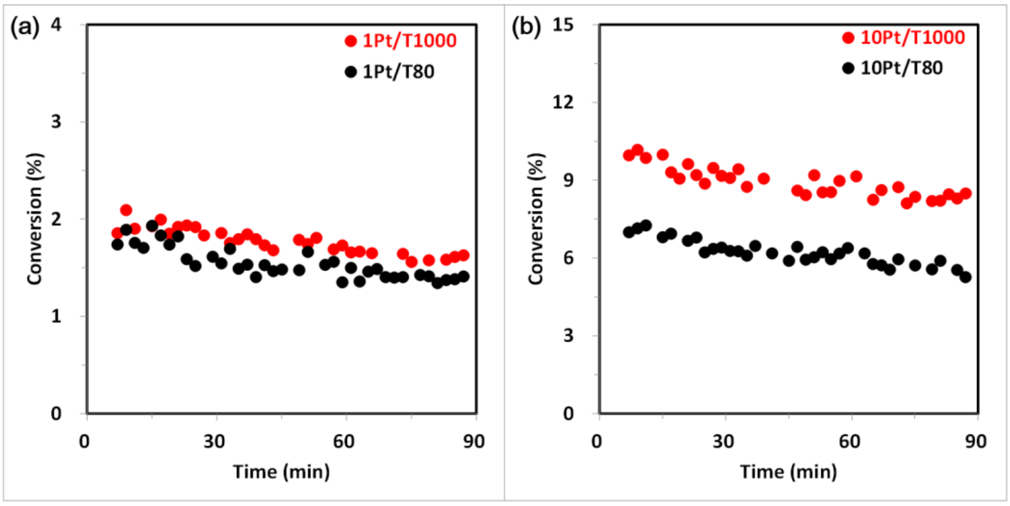

Figure 4.21. Time-on-stream C_6H_6 hydrogenation profiles for (a) 1Pt/T1000 and 1Pt/T80 and (b) 10Pt/T1000 and 10Pt/T80.

Previous studies have reported that benzene hydrogenation is structure-insensitive, which means that the specific activity (TOF) is independent of Pt size.[53,54] However, other studies also reported that benzene hydrogenation is structure-sensitive.[50,51] Flores et al. reported that the structure sensitivity depended on pre-treatment of Pt/Al_2O_3.[51] For high temperature reduction (450 °C), the specific activity increases with decreasing Pt dispersion up to H/Pt = 0.48 (structure-sensitive) and became constant at dispersion lower than H/Pt = 0.48 (structure-insensitive). However, at low reduction temperatures (100–300 °C), the reaction was structure-sensitive at the wide range of H/Pt values (0.04–0.88). Note that in this work our samples were reduced at 500 °C. The TOF at H/Pt = 0.86 was 0.045–0.046 C_6H_6/Pt·s, but increased to 0.166–0.17 C_6H_6/Pt·s at H/Pt = 0.18–0.31. **Figure 4.22** showed that the TOF value increased with decreasing H/Pt, but became constant at low Pt dispersions (H/Pt <0.5), which is consistent with the results of Flores et al..[51] However, detailed studies on whether benzene hydrogenation is structure-sensitive or not are beyond the scope of this work, because our conventional impregnated catalysts have broad size distribution of Pt clusters, and particularly bimodal distribution for 10 wt% Pt/Al_2O_3, which renders the determination of structure sensitivity difficult. The recent work by Somorjai group reported that benzene hydrogenation is moderately structure-sensitive for Pt nanoparticles carefully well-controlled in narrow size distribution.[50]

All the results indicate that the number and properties of sites on the alumina surfaces affect Pt dispersion, leading to different Pt dispersion and catalytic properties for benzene hydrogenation.

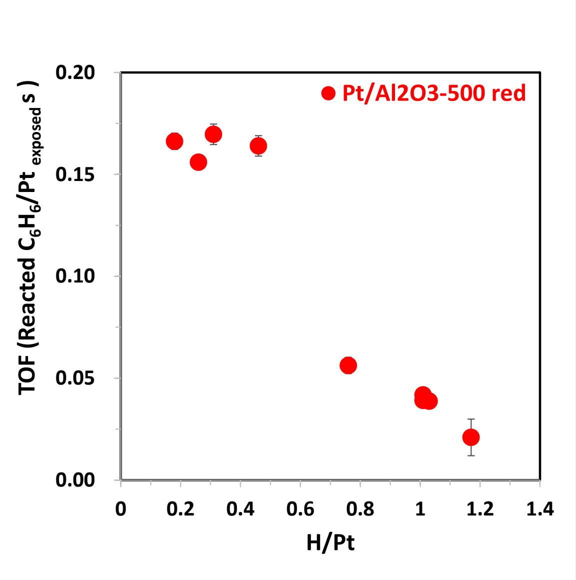

Figure 4.22. Turnover frequency (TOF) of Pt/Al_2O_3 as a function of H/Pt after 500 °C calcination and 500 °C reduction.

4.5. Conclusion

In this work, we investigated the effect of the number and properties of specific sites on alumina surfaces on Pt-Al_2O_3 interaction by using XRD, ethanol TPD, DRIFTS, H_2 chemisorption, STEM and benzene hydrogenation as the model reaction. Here, we chose two sets of model alumina having different number of sites with the identical properties (T150, T110, and T80) and different properties of sites with the same number (T1000, T80) based on ethanol TPD. Ethanol TPD showed that T150, T110, and T80 had similar T_d (208.5–210 °C) but different desorption amounts (3.8×10^{-4} mol/g for T150, 2.4×10^{-4} mol/g for T110, and 2.0×10^{-4} mol/g for T80). The T1000 showed higher T_d (by 34.4 °C) than T80 for the same number of sites (1.8×10^{-4} mol/g for T1000). The DRIFTS of surface hydroxyls showed that T150, T110, and T80 have similar types of surface hydroxyl groups, consistent with the similar T_d obtained from ethanol TPD. However, T1000 have a new type of surface hydroxyl at 3790 cm^{-1}, which is the origin of the different surface properties compared to T80.

After loading 0.5–10 wt% Pt onto these model aluminas, the Pt dispersion was analyzed by various characterization tools (H_2 chemisorption, XRD and STEM). At low Pt loadings (0.5–1 wt% Pt), the number of sites was sufficient to disperse all the Pt, leading to highly dispersed Pt clusters without any aggregated Pt. Therefore, all the model aluminas showed highly dispersed Pt, as evidenced by similar H/Pt values (0.85–0.86) from H_2 chemisorption. However, at higher loading (10 wt% Pt), the number of Pt was higher than that of than anchoring sites, resulting in aggregated Pt evidenced by the sharp Pt(111) peak in XRD, along with small Pt clusters (below ~ 3 nm), revealed by STEM. Under bimodal particle size distribution, both T150 and T1000 exhibited higher Pt dispersion, with the greater portion of smaller Pt clusters and less aggregated Pt, leading to different catalytic properties (higher conversion) for benzene hydrogenation compared to T80. All the results clearly demonstrate that Pt can be more dispersed with increasing number of sites and interaction strength. This fundamental understanding provides an important perspective for designing Al_2O_3-based supported catalysts.

4.6. References

[1] Choudhary, T.V.; Banerjee, S.; Choudhary, V.R. *Appl. Catal., A* **2002,** *234*, 1-23.

[2] Gélin, P.; Primet, M. *Appl. Catal., B* **2002,** *39*, 1-37.

[3] Rahimpour, M.R.; Jafari, M.; Iranshahi, D.; *Appl. Energy* **2013,** *109*, 79-93.

[4] Sattler, J.J.H.B.; Ruiz-Martinez, J.; Santillan-Jimenez, E.; Weckhuysen, B.M. *Chem. Rev.* **2014,** *114*, 10613-10653.

[5] Beck, I.E.; Bukhtiyarov, V.I.; Pakharukov, I.Y.; Zaikovsky, V.I.; Kriventsov, V.V.; Parmon, V.N. *J. Catal.* **2009,** *268*, 60-67.

[6] Hu, C.H.; Chizallet, C.; Mager-Maury, C.; Corral-Valero, M.; Sautet, P.; Toulhoat, H.; Raybaud, P.; *J. Catal.* **2010,** *274*, 99-110.

[7] Vaarkamp, M.; Miller, J.T.; Modica, F.S.; Koningsberger, D.C.; *J. Catal.* **1996,** *163*, 294-305.

[8] Matsuhashi, H.; Nishiyama, S.; Miura, H.; Eguchi, K.; Hasegawa, K.; Iizuka, Y.; Igarashi, A.; Katada, N.; Kobayashi, J.; Kubota, T.; Mori, T.; Nakai, K.; Okazaki, N.; Sugioka, M.; Umeki, T.; Yazawa, Y.; Lu, D. *Appl. Catal., A* **2004,** *272*, 329-338.

[9] Yazawa, Y.; Takagi, N.; Yoshida, H.; Komai, S.-i.; Satsuma, A.; Tanaka, T.; Yoshida, S.;

Hattori, T. *Appl. Catal., A* **2002,** *233*, 103-112.

[10] Mironenko, R.M.; Belskaya, O.B.; Talsi, V.P.; Gulyaeva, T.I.; Kazakov, M.O.; Nizovskii, A.I.; Kalinkin, A.V.; Bukhtiyarov, V.I.; Lavrenov, A.V.; Likholobov, V.A. *Appl. Catal., A* **2014,** *469*, 472-482.

[11] Park, J.E.; Kim, B.B.; Park, E.D. *Korean J. Chem. Eng.* **2015,** *32*, 2212-2219.

[12] Gorczyca, A.; Moizan, V.; Chizallet, C.; Proux, O.; Net, W.D.; Lahera, E.; Hazemann, J.L.; Raybaud, P.; Joly, Y. *Angew. Chem. Int. Ed.* **2014,** *126*, 12634-12637.

[13] Cho, I.H.; Park, S.B.; Cho, S.J.; Ryoo, R. *J. Catal.* **1998,** *173*, 295-303.

[14] Kwak, J. H.; Hu, J.; Mei, D.; Yi, C.-W.; Kim, D. H.; Peden, C. H. F.; Allard, L. F.; Szanyi, J. *Science* **2009,** *325*, 1670-1673.

[15] Digne, M.; Sautet, P.; Raybaud, P.; Euzen, P.; Toulhoat, H. *J. Catal.* **2002,** *211*, 1-5.

[16] Digne, M.; Sautet, P.; Raybaud, P.; Euzen, P.; Toulhoat, H. *J. Catal.* **2004,** *226*, 54-68.

[17] Busca, G. *Catal. Today* **2014,** *226*, 2-13.

[18] Trueba, M.; Trasatti, S. P. *Eur. J. Inorg. Chem.* **2005,** *2005*, 3393-3403.

[19] Lee, J.; Jeon, H.; Oh, D. G.; Szanyi, J.; Kwak, J. H. *Appl. Catal., A* **2015,** *500*, 58-68.

[20] Cai, W.; Zhang, S.; Lv, J.; Chen, J.; Yang, J.; Wang, Y.; Guo, X.; Peng, L.; Ding, W.; Chen, Y.; Lei, Y.; Chen, Z.; Yang, W.; Xie, Z. *ACS Catal.* **2017,** *7*, 4083-4092.

[21] Bara, C.; Plais, L.; Larmier, K.; Devers, E.; Digne, M.; Lamic-Humblot, A.-F.; Pirngruber, G. D.; Carrier, X. *J. Am. Chem. Soc.* **2015,** *137*, 15915-15928.

[22] Lee, J.; Jang, E.J.; Jeong, H.Y.; Kwak, J.H. *Appl. Catal., A* **2018,** *556*, 121-128.

[23] Shi, D.; Wang, H.; Kovarik, L.; Gao, F.; Wan, C.; Hu, J.Z.; Wang, Y. *J. Catal.* **2018,** *363*, 1-8.

[24] Lee, J.; Jang, E. J.; Kwak, J. H. *J. Catal.* **2017,** *345*, 135-148.

[25] Mager-Maury, C.; Chizallet, C.; Sautet, P.; Raybaud, P. *ACS Catal.* **2012,** *2*, 1346-1357.

[26] Paulis, M.; Peyrard, H.; Montes, M. *J. Catal.* **2001,** *199*, 30-40.

[27] Kwak, J. H.; Mei, D.; Peden, C. H. F.; Rousseau, R.; Szanyi, J. *Catal. Lett.* **2011,** *141*, 649-655.

[28] Kwak, J.H.; Lee, J.; Szanyi, J.; Peden, C.H.F. *Catal. Today* **2016,** *265*, 240-244.

[29] Lemaitre, J.L.; Menon, P.G.; Delannay, F. in: F. Delannay (Ed.), Characterization of Heterogeneous Catalysts, Marcel Dekker, 1984, pp. 299-365.

[30] Madon, R.J.; Boudart, M. *Ind. Eng. Chem. Fundam.* **1982,** *21*, 438-447.

[31] Sing, K.S.W.; Everett, D.H.; Haul, R.A.W.; Moscou, L.; Pierotti, R.A.; Rouquerol, J.; Siemieniewska, T. *Pure Appl. Chem.* **1985,** *57*, 603-619.

[32] Hu, J. Z.; Xu, S.; Kwak, J. H.; Hu, M. Y.; Wan, C.; Zhao, Z.; Szanyi, J.; Bao, X.; Han, X.; Wang, Y.; Peden, C. H. F. *J. Catal.* **2016,** *336*, 85-93.

[33] Phung, T. K.; Lagazzo, A.; Rivero Crespo, M. Á.; Sánchez Escribano, V.; Busca, G. *J. Catal.* **2014,** *311*, 102-113.

[34] Phung, T.K.; Herrera, C.; Larrubia, M.Á.; García-Diéguez, M.; Finocchio, E.; Alemany, L.J.; Busca, G. *Appl. Catal., A* **2014,** *483*, 41-51

[35] Busca, G.; Lorenzelli, V.; Ramis, G.; Willey, R.J. *Langmuir* **1993,** *9*, 1492-1499

[36] Peri, J. B. *J. Phys. Chem.* **1965,** *69*, 220-230.

[37] Busca, G.; Lorenzelli, V.; Escribano, V.S.; Guidetti, R. *J. Catal.* **1991,** *131*, 167-177

[38] Knözinger, H.; Ratnasamy, P. *Catal. Rev. Sci. Eng.* **1978,** *17*, 31-70.

[39] Tsyganenko, A. A.; Mardilovich, P. P. *J. Chem. Soc., Faraday Trans.* **1996,** *92*, 4843-4852.

[40] Morterra, C.; Magnacca, G. *Catal. Today* **1996,** *27*, 497-532.

[41] Larmier, K.; Chizallet, C.; Cadran, N.; Maury, S.; Abboud, J.; Lamic-Humblot, A.-F.; Marceau, E.; Lauron-Pernot, H. *ACS Catal.* **2015,** *5*, 4423-4437.

[42] Yao, H.C.; Sieg, M.; Plummer, H.K. *J. Catal.* **1979,** *59*, 365-374

[43] Billinge, S. J. L.; Levin, I. *Science* **2007,** *316*, 561-565.

[44] Spenadel, L.; Boudart, M. *J. Phys. Chem.* **1960,** *64*, 204-207

[45] Kovarik, L.; Bowden, M.; Shi, D.; Washton, N. M.; Andersen, A.; Hu, J. Z.; Lee, J.; Szanyi, J.; Kwak, J. H.; Peden, C. H. F., *Chem. Mater.* **2015,** *27*, 7042-7049.

[46] Nguefack M.; Popa, A.F.; Rossignol, S.; Kappenstein, C. *Phys. Chem. Chem. Phys.* **2003,** *5*, 4279-4289.

[47] Malpartida, I.; Vargas, M.A.L.; Alemany, L.J.; Finocchio, E.; Busca, G. *Appl. Catal.,* **2008,** *80*, 214-225.

[48] Lin, S.D.; Vannice, M.A. *J. Catal.* **1993,** *143*, 539-553.

[49] Lin, S.D.; Vannice, M.A. *J. Catal.* **1993,** *143*, 563-572.

[50] Pushkarev, V.V.; An, K.; Alayoglu, S.; Beaumont, S.K.; Somorjai, G.A. *J. Catal.* **2012,** *292*, 64-72.

[51] Flores, A.F.; Burwell, R.L.; Butt, J.B. *J. Chem. Soc., Faraday Trans.* **1992,** *88*, 1191-1196.

[52] Bratlie, K.M.; Lee, H.; Komvopoulos, K.; Yang, P.; Somorjai, G.A. *Nano Lett.* **2007,** *7*, 3097-3101.

[53] Barbier, J.; Morales, M.; Marecot, P.; Maurel, R. *Bull. Soc. Chim. Belg.* **1979,** *88*, 569-576.

[54] Koussathana, M.; Vamvouka, D.; Economou, H.; Verykios, X. *Appl. Catal.* **1991,** *77*, 283-301.

5. Reduction behavior of Pt on alumina: effect of Pt loading and calcination temperature

5.1. Abstract

The catalytic performances of supported heterogeneous catalysts are significantly affected by the particle size and morphologies, whose properties are critically decided by metal-support interaction. In this work, we studied the reduction behavior of three-dimensional (3D) PtO_2, two-dimensional (2D) PtO_2 and atomically dispersed Pt on industrially relevant Pt/Al_2O_3, related to metal-support interaction. Under oxidizing atmosphere, morphologies and sizes of PtO_2 on Pt/Al_2O_3 are determined by the specific interaction between Pt and Al_2O_3 through Pt-O-Al bond, leading to highly dispersed Pt as ~1 nm 2D-raft PtO_2 and atomically dispersed Pt on Al_2O_3. When all Pt atoms can't interact with anchoring sites on support under high Pt loading or SiO_2 which has weak metal-support interaction, 3D PtO_2 is formed. Due to weak interaction with support, 3D PtO_2 is reduced earlier (-20~-60 °C) than 2D PtO_2 (~110 °C) and atomically dispersed Pt (>300 °C). At high calcination temperature (500-700 °C), PtO_2 is reduced without a reducing agent (auto-reduction) with Pt sintering. Interaction strength also influences auto-reduction when calcination temperature increases. 3D PtO_2 were auto-reduced after 550-600 °C calcination, but 2D PtO_2 were more difficult to be reduced (50 °C higher). So, the interaction strength with the support determines how long Pt oxide can maintain as Pt oxide rather Pt metal. Because 3D PtO_2 is more easily auto-reduced than 2D PtO_2 and atomically dispersed Pt, 3D metallic Pt clusters become less mobile than 2D PtO_2 and atomically dispersed Pt (still, oxidized Pt). So, 3D PtO_2 showed more sinter-resistant behavior than 2D PtO_2 and atomically dispersed Pt. All the results demonstrate that metal-support interaction is important for the reduction behavior of oxidized Pt on Pt/Al_2O_3, suggesting the guideline about a careful activation for the efficient utilization of metallic Pt for catalytic reactions in real-world.

5.2. Introduction

Pt/Al_2O_3 has been one of the most widely used heterogeneous catalysts in industries such as automobile emission control, petrochemistry, and oil refinery.[1-4] Thanks to versatile applications in real-world, there have been numerous studies devoted to understanding the catalytic performances and underlying fundamental aspects of Pt/Al_2O_3.[5-13] The catalytic performances of Al_2O_3-supported Pt catalysts have been reported to be significantly affected by the particle size,[8, 12, 14-15] morphology,[7, 11] and oxidation state[10, 13] of supported Pt in which each parameter also affects each other.[11-12, 16-17] Here, one important factor to determine the geometric and electronic properties of supported Pt is the specific interaction between alumina and Pt,[5-6, 18] whose detailed understanding over atomic scale is still challenging till now.

The specific interaction between Pt and alumina has been intensely investigated under oxidizing or reducing atmospheres, which are common activation condition for supported metal catalysts.[5-7, 9, 19-21] Under the oxidizing condition, Kwak et al. reported that penta-coordinated Al^{3+} sites are anchoring sites for atomically dispersed Pt and two-dimensional raft Pt oxide.[5] When Pt can't interact with the anchoring sites due to too many Pt atoms or inert support which has no anchoring sites such as α-Al_2O_3, 3D-like Pt clusters were observed.[5-6, 22] The next question is how these Pt oxides are reduced and form metallic Pt clusters. Under the reducing condition, metallic Pt clusters can exist as two-dimensional (2D) or three dimensional (3D) morphologies which are critically affected by various factors such as activation temperature,[7, 23] adsorbate coverage,[9, 20, 24] and the degree of interaction with the support.[9, 19] Despite many efforts for the specific interaction of Pt/Al_2O_3, the systematic understanding of the reduction behavior of each oxidized Pt species (3D-like Pt oxide, 2D-like raft Pt oxide and atomically dispersed Pt) into metallic Pt related with the specific interaction is lacking.

The reduction of oxidized Pt species into metallic Pt can be implemented by two ways: One is the reduction by reducing agents such as H_2 (the most typical one) and the other is auto-reduction without reducing agents. For Pt/Al_2O_3, auto-reduction of Pt oxide is driven by the decomposition of Pt oxide into metallic Pt under high temperature condition where Pt metal is the most thermodynamically stable under even oxidizing atmosphere.[25-26] However, high temperature treatments lead to a Pt sintering with concomitant loss of active sites.[27-30] The sintering of supported metal is one major reason for catalyst deactivations and has been intensely studied because harsh operation conditions in many industrial applications usually led to severe sintering of active phases.[31] Despite intense studies, understanding the sintering behavior of 3D-like/2D-like clusters and atomically dispersed Pt during high thermal treatment is still limited.

In this work, we investigated the metal clustering of Pt/Al_2O_3 based on a systematic approach with 3D-like/2D-like PtO_2 and atomically dispersed Pt on Pt/Al_2O_3. Various characterizations (XRD, H_2-TPR, TEM, O_2-TPD, and DRIFTS) demonstrate that 3D-like PtO_2 are easily reduced at -20~-60 °C than 2D-like PtO_2 (~100 °C) and atomically dispersed Pt (>300 °C). That's because 2D-like PtO_2 and atomically dispersed Pt does strongly interact with alumina through Pt-O-Al. When a calcination temperature increases, PtO_2 is auto-reduced into metallic Pt despite the oxidizing atmosphere. During auto-reduction, interaction strength also decides how long Pt oxide can survive as Pt oxide rather metallic Pt. 3D-like PtO_2 are also easily auto-reduced after 550-600 °C calcination than 2D-like PtO_2 (600-650 °C). Thanks to less mobility after reduction into metallic Pt, 3D-like PtO_2 are more sinter-resistant than 2D-like PtO_2 and atomically dispersed Pt. All the results demonstrate that metal-support interaction is critical for reduction behavior of oxidized Pt on industrially relevant Pt/Al_2O_3, suggesting the guideline for efficient utilization of metallic Pt for catalytic reactions in real-world.

5.3. Experimental section

5.3.1. Catalyst preparation

0.1–10 wt% Pt/Al_2O_3 were prepared by conventional incipient wetness impregnation on Puralox TH 100/150 (Sasol) alumina with $Pt(NH_3)_4(NO_3)_2$ in water and dried at 120 °C overnight. Note that we used $Pt(NH_3)_4(NO_3)_2$ as the Pt precursor in order to remove any additional Cl effect.[32-33] 0.5–10 wt% Pt/SiO_2 were prepared on silica gel (Davisil grade 635, Aldrich) by the same methods with Pt/Al_2O_3. All the samples were calcined at 500 °C for 2 h using 20% O_2/He (1 ml/s). We investigated the effect of calcination temperature by changing calcination temperature from 500 °C to 700 °C with 50 °C interval.

5.3.2. Catalyst characterizations

Ex-situ XRD patterns were obtained on a Bruker D2 phaser diffractometer using Cu Kα radiation (λ = 1.54 Å) in the step mode between 2θ values of 10 and 80°, with a step size of 0.02°/s. The tube voltage and current were 30 kV and 10 mA, respectively. The *in-situ* X-ray diffraction patterns were recorded on a high-resolution X-ray diffractometer (Rigaku, Smartlab) operated at 200 kV and 45 mA using CuKα radiation (λ= 1.54 Å) with the step size of 0.02°/s and between 2θ values of 10 and 80°. We calibrated the setting temperature with $NaNO_3$ (melting point–308 °C) where the diffraction patterns of $NaNO_3$ disappeared at the setting temperature 370 °C. H_2 pulse experiments were carried out at RT by H_2 pulses with 10% H_2/Ar (0.997 ml loop). The sample was calcined at setting temperature 560 °C for 2 h in 20% O_2/N_2. Afterward, the sample was cooled to RT and purged under He (100 ml/min). XRD patterns were obtained after injecting H_2 pulses and finally supplying a continuous 10% H_2/Ar flow (60 ml/min). The auto-reduction experiment was carried out from RT to a setting temperature of 800 °C (calibrated temperature-650 °C) with interval 50 °C at 20% O_2/N_2 (100 ml/min).

Bright field transmission electron microscopy (BF-TEM) and High-angle annular dark-field scanning transmission electron microscopy (HAADF-STEM) images were obtained using a JEOL 2100F (JEOL) operated at 200 kV.

Hydrogen (H_2) temperature-programmed reduction was performed on Belcat-B (BEL Japan, Inc.). 50 mg of a sample was calcined under 20% O_2/He (1.0 ml/s) and, purged for 30 min under He (1.0 ml/s). After stabilization under 2% H_2/Ar for 2h, the sample was ramped with 10 °C/min till 700 °C and 5A zeolite trap was used for trapping water. Cryogenic H_2 temperature-programmed reduction was carried out on CATCryo(BEL Japan, Inc.). 50 mg of a sample was calcined under 20% O_2/He (1.0 ml/s) and, purged for 30 min under He (1.0 ml/s). After cooling to -80 °C under He and the stabilization under 2% H_2/Ar for 1h, the sample was ramped with 10 °C/min till 700 °C.

O_2 TPD was carried out in a quartz flow reactor equipped with the mass spectrometer (Pfeiffer vacuum GSD320). After calcination under 20% O_2/He for 2 h, the samples were cooled to RT and purged with He for 30 min. After that, O_2 TPD was started with 10 ºC/min ramping rates till 900 ºC under He atmosphere due to the sensitivity issue.

Diffuse reflectance infrared spectroscopy (DRIFTS) experiments were carried out on a Nicolet iS10 FTIR spectrometer equipped with a mercury-cadmium-telluride (MCT) detector. For the information of hydroxyl groups, 5 mg of Pt/Al_2O_3 sample was loaded into high temperature reaction chamber (Harrick Scientific) with ZnSe windows installed in a Praying Mantis diffusion reflection accessory. After ex-situ calcination at 500 ºC under 20% O_2/He, al the samples were re-calcined using 10 % O_2/He (flow rate = 1 ml/sec) at 400 °C under DRIFTS cell. Right after cooled down to room temperature, the FT-IR spectra of hydroxyl groups were collected with KBr background. Also, to observe the Pt surface properties with different reduction temperature, ex situ pretreated sample was loaded and heated under He flow (1 ml/sec) at 150 °C for water desorption. Then, CO adsorption was conducted with 0.2 % CO/He flow (1 ml/sec) at -30 °C. The spectrum was obtained after He purging at the same temperature to remove weakly bound CO on Pt surface and gas phase CO molecules, using the spectrum of pretreated-sample itself under He flow at -30 °C as a background. All spectra were collected with the average 128 scans at a resolution of 4 cm^{-1}.

Hydrogen (H_2) chemisorption was performed on Belcat-B(BEL Japan, Inc.). 50 mg of a sample was calcined at 500 °C for 2 h under 20% O_2/He (1.0 ml/s) and, subsequently, reduced at 500 °C for 1 h under 10% H_2/He (1.0 ml/s). After purging for 30 min under He (1.0 ml/s), Pt/Al_2O_3 was cooled to 40 °C and chemisorption was carried out by repeated pulse (0.319 ml loop–4% or 10% H_2/Ar). Metal dispersion was calculated based on the stoichiometry of H/Pt = 1.

5.4. Results and Discussion

5.4.1. Specific interaction between Pt and Al_2O_3

0.1, 1 wt% Pt/Al_2O_3 and 1 wt% Pt/SiO_2 were prepared by incipient wetness impregnation and after calcination at 500 °C. **Figure 5.1a** showed the representative HAADF-STEM images. 1 wt% Pt/Al_2O_3 had the highly dispersed small clusters up to ~1 nm and atomically dispersed Pt. High resolution images for 1 nm clusters indicate these highly dispersed clusters consist of 1–2 layer close to two-dimensional (2D) raft-like morphologies, consistent with previous studies.[5, 21, 34-35] When Pt loading was extremely reduced to 0.1 wt%, only atomically dispersed Pt was observed. However, 1 wt% Pt/SiO_2 showed 2–4 nm clusters which showed much bright contrasts, indicating three-dimensional (3D) morphologies. Furthermore, no atomically dispersed Pt was observed on silica. In order to investigate why Pt are highly dispersed on Pt/Al_2O_3 (ultimately up to atomically dispersed Pt) than Pt/SiO_2, we performed H_2-TPR (from room temperature).1 wt% Pt/Al_2O_3 showed two main reduction peaks at 150 °C and 370 °C as shown in **Figure 5.1b**. Interestingly, 0.1 wt% Pt/Al_2O_3 showed only the reduction at 370 °C without the reduction below 300 °C. It can be interpreted that atomically dispersed Pt is reduced at 370 °C. It is also consistent with previous reports showing that clustering of atomically dispersed Pt was observed above 300 °C under H_2 atmosphere.[34-35] The reduction peak at 150 °C can be interpreted as Pt-O-Pt from 2D raft-like oxide, which was consistent with HAADF-STEM images. Previous studies also show that highly dispersed Pt oxide are reduced below ~200 °C.[6, 36-40] 1 wt% Pt/SiO_2 showed only one reduction peak around 120 °C, whose hydrogen consumption amount was much smaller (O/Pt : ~0.2) than that of 1 wt% Pt/Al_2O_3 (O/Pt : 2.0). Considering H_2-TPR of bare support, only Al_2O_3-supported Pt showed the specific reduction at 370 °C clearly. This result suggests that the reduction at 370 °C is closely related to the specific interaction between Pt and alumina which might be Pt-O-Al interaction under oxidizing atmosphere.[5, 21-22, 25] That's why much higher Pt dispersion for alumina than silica due to the specific interaction as Pt-O-Al, whose nature was reported as penta-coordinated Al^{3+} sites by Kwak et. al.[5]

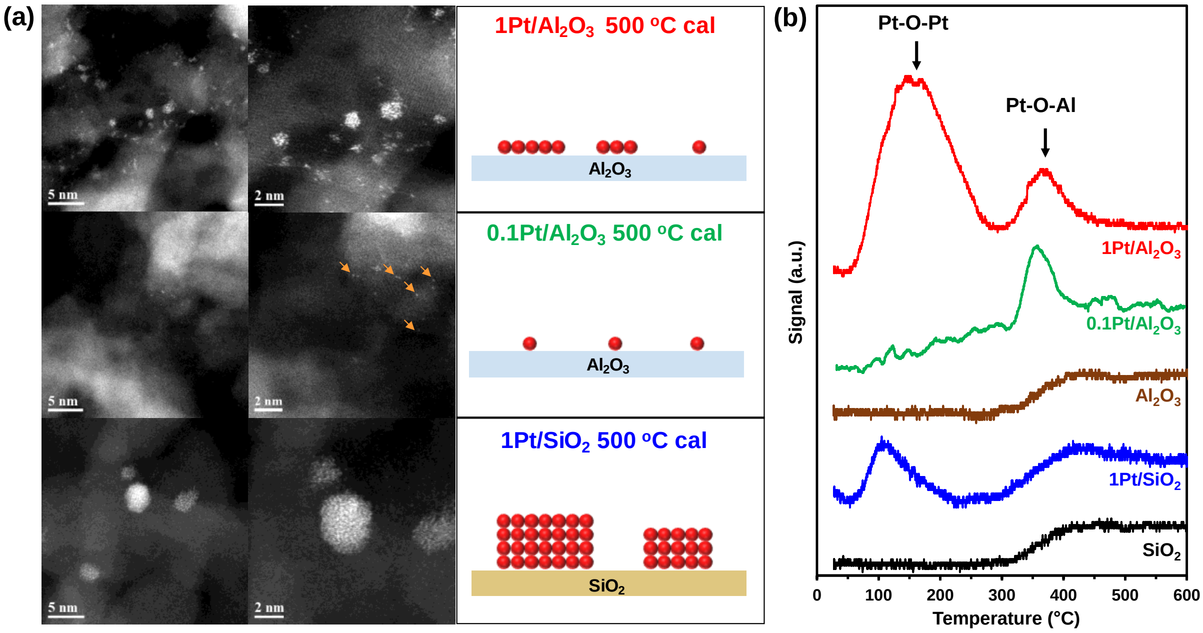

Figure 5.1. (a) HAADF-STEM images and schemes for $1Pt/Al_2O_3$, $0.1Pt/Al_2O_3$ and $1Pt/SiO_2$ after 500°C calcination. (b) H_2-TPR (started from RT) for $1Pt/Al_2O_3$, $0.1Pt/Al_2O_3$, Al_2O_3, $1Pt/SiO_2$ and SiO_2 after 500 °C calcination.

The specific interaction of Pt oxide with alumina surfaces was further demonstrated by DRIFTS results. **Figure 5.2a** showed the gradual decrease of surface hydroxyl at 3766 cm^{-1} with increasing Pt loading after oxidation at 500 ºC. Previous reports suggest that the surface hydroxyl at 3766 cm^{-1} was interpreted that surface hydroxyls on (100) facets that form penta-coordinated Al^{3+} sites when dehydroxylated.[41-42] These results suggest that Pt-O-Al is formed from the anchoring of Pt on the sites of surface hydroxyls on (100) facets. However, after reduction at 500 ºC these hydroxyls reappeared because Pt-O-Al interactions cannot maintain due to the reduction of Pt oxide as shown in **Figure 5.2b**.

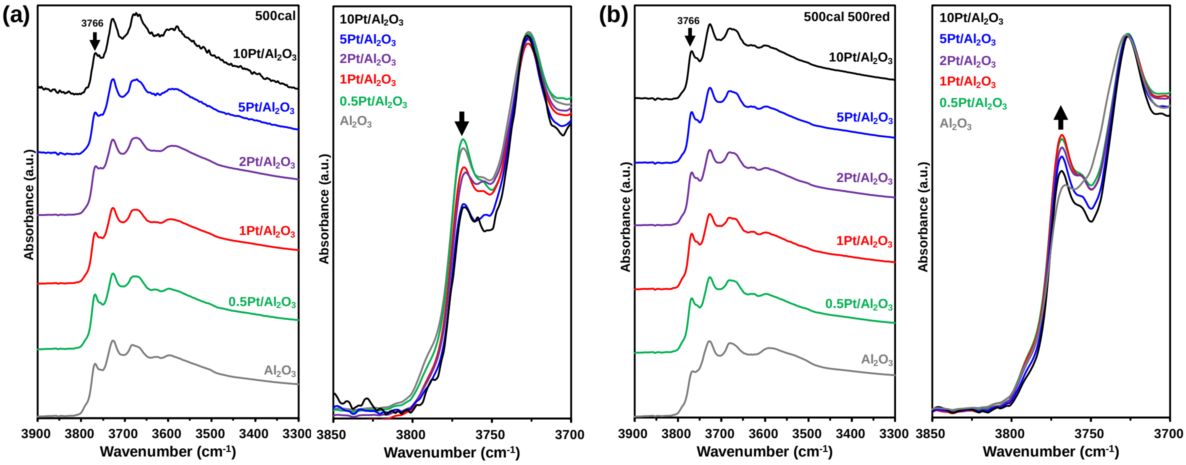

Figure 5.2. DRIFTS spectrum of surface hydroxyl regions for Al_2O_3, 0.5Pt, 1Pt, 2Pt, 5Pt, and 10Pt/Al_2O_3 after (a) 500 °C calcination, (b) 500 °C calcination and 500 °C reduction.

Overall, all the results suggest that specific interaction exists between Pt and alumina and these metal-support interactions can be specific depending on the support. Also, atomically dispersed Pt can be characterized by the ensemble and conventional characterization method, H_2-TPR.

5.4.2. Effect of Pt loading and calcination temperature for the reduction behavior of supported Pt catalysts

The reduction behavior of oxidized Pt into metallic Pt on supported Pt catalysts was investigated by H_2-TPR for a series of Pt/Al_2O_3 with various Pt loading and different calcination temperature as shown in **FIGURE 5.3**. **Figure 5.3a** showed H_2 TPR for 0.5–10 wt% Pt/Al_2O_3 after calcination at 500 °C. The results clearly demonstrate that with increasing Pt loading, the amounts of Pt-O-Pt at 150 °C increased, but that of Pt-O-Al at 370 °C didn't show meaningful change. Next, the calcination temperature was changed from 500 °C to 700 °C with 50 °C interval. **Figure 5.3b–5.3e** showed H_2 TPR profiles for a series of Pt/Al_2O_3 after the calcination at different temperatures. Here, the amounts of Pt-O-Pt decreased with increasing calcination temperature, but that of Pt-O-Al didn't change much till 700 °C calcination. The O/Pt trends for Pt/Al_2O_3 were summarized in **Figure 5.4**. 0.5–1 wt% Pt/Al_2O_3

after the calcination at 500 °C showed 1.7~1.9 values of O/Pt, which was close to PtO_2. With increasing Pt loading under the same calcination at 500 °C, O/Pt decreased to 1.0 (2 wt%) and finally became below 0.5 at 5–10 wt%. It is clear that more Pt was reduced with increasing Pt loading after 500 °C calcination. When the calcination temperature changed, O/Pt values of 0.5–1 wt% Pt/Al_2O_3 slightly decreased from 2.0 to 1.5 up to 600 °C and significantly decreased as PtO at 650 °C. Finally, after 700 °C calcination O/Pt values became below 0.5. Irrespective of initial O/Pt values (PtO_2, PtO, PtO_x ($x<0.5$)), the O/Pt trends decreased with increasing calcination temperature, which was similar with those of Pt loading.

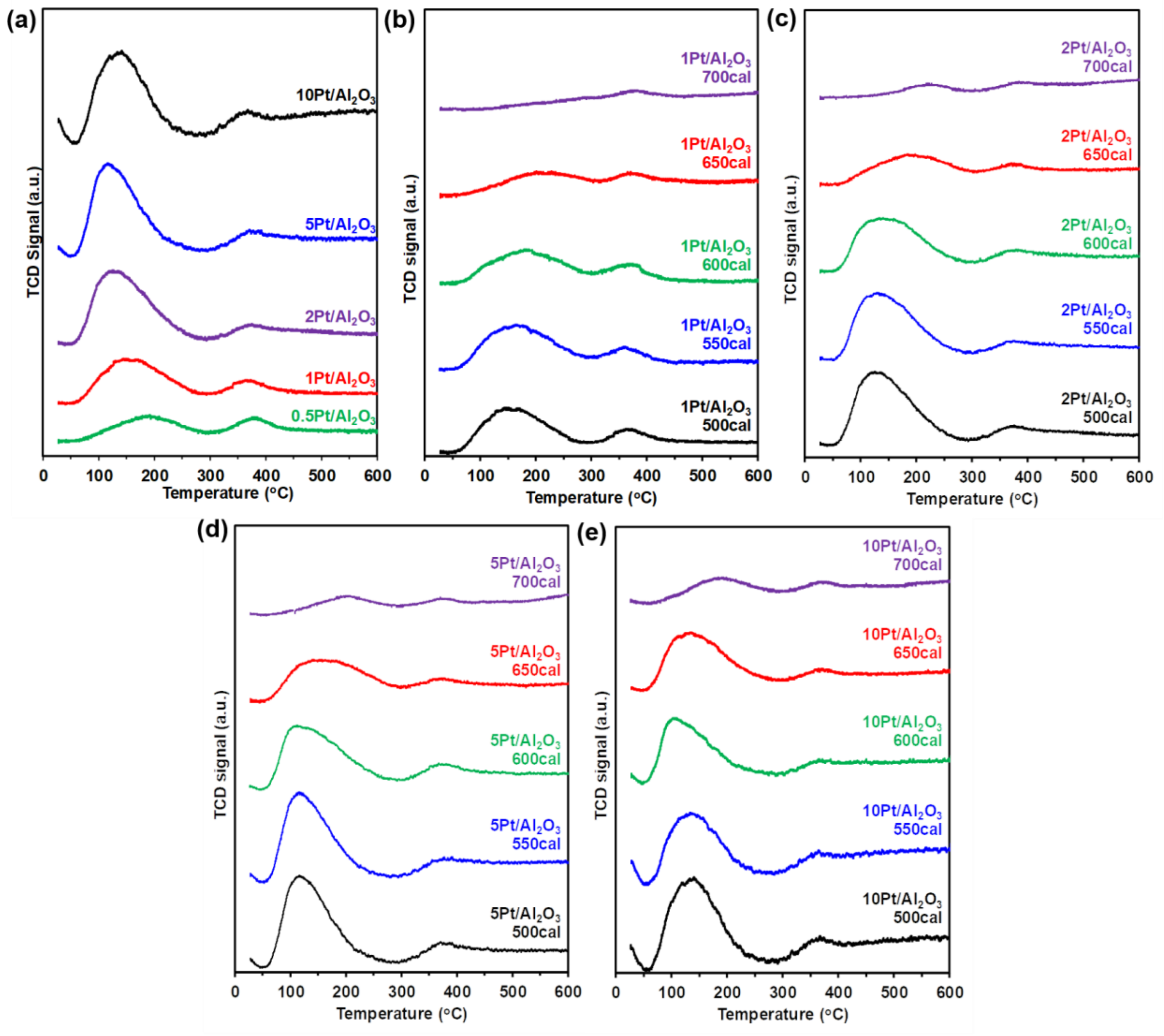

Figure 5.3. (a) RT H_2-TPR for Pt/Al_2O_3 with various Pt loading (0.5–10 wt% Pt) after 500 °C calcination. RT H_2-TPR for (b) 1 wt% Pt/Al_2O_3, (c) 2 wt% Pt/Al_2O_3, (d) 5 wt% Pt/Al_2O_3, (e) 10 wt% Pt/Al_2O_3 after 500–700 °C calcination with 50 °C interval.

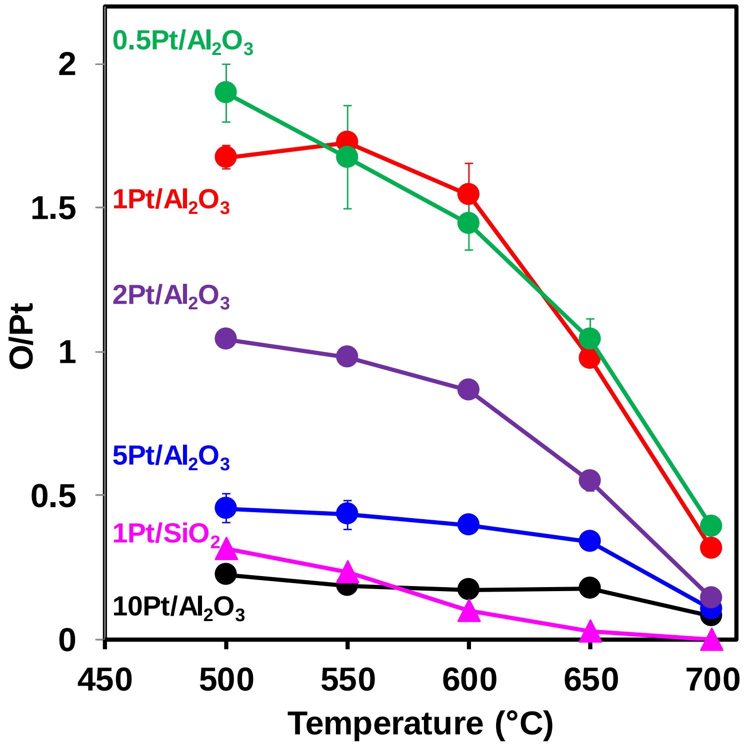

Figure 5.4. O/Pt values from RT H_2-TPR for Pt/Al_2O_3 with various Pt loading (0.5–10 wt% Pt) and 1 wt% Pt/SiO_2 after 500–700 °C calcination.

Pt/SiO_2 was also compared as reference. **Figure 5.5a** showed that all Pt/SiO_2 after 500 °C calcination had the single reduction around 100 °C. **Figure 5.5b** showed that their O/Pt values also decreased with increasing Pt loading, but all O/Pt values were below 0.5, which were much lower than those of Pt/Al_2O_3. It indicates more easier reduction of Pt on SiO_2 than Al_2O_3. When calcination temperatures increased for 1 wt% Pt/SiO_2 as shown in **Figure 5.3c**, single reduction peak around 100 °C continuously decreased till 600 °C and finally become invisible after 700 °C calcination. The O/Pt trends for 1 wt% Pt/SiO_2 was similar to those of 5–10 wt% Pt/Al_2O_3.

Based on H_2-TPR results, we can demonstrate that the reduction behavior of oxidized Pt on Pt/Al_2O_3 can be summarized in two directions: Pt becomes more easily reduced with increasing the Pt loading and the calcination temperature. Then, our next question is how high Pt loading and high calcination temperature can reduce Pt easily, which will be investigated in detail on the next sections.

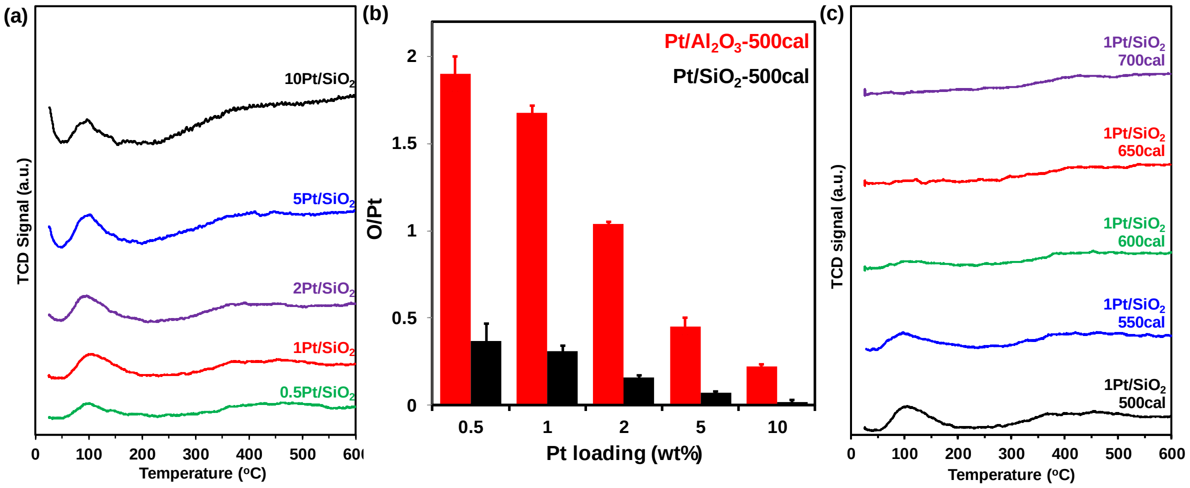

Figure 5.5. (a) H_2-TPR for Pt/SiO_2 with various Pt loading (0.5–10 wt% Pt) after 500 °C calcination. (b) O/Pt values for Pt/Al_2O_3 and Pt/SiO_2 with various Pt loading (0.5–10 wt% Pt) (c) H_2-TPR for 1Pt/SiO_2 after 500–700 °C calcination.

5.4.3. Reduction behavior of 3D-like, 2D-like Pt oxide and atomically dispersed Pt

First question is how increasing Pt loading leads for Pt to be reduced easily after calcination at 500 °C. In order to clarify the origin of decreased O/Pt with Pt loading, detailed characterizations were performed. XRD patterns for a series of Pt/Al_2O_3 was shown in **FIGURE 5.6A**. With increasing Pt loading, increase of PtO_2 peak at 2θ = 33.9° was obviously observed, indicating that Pt oxide exists as PtO_2 rather than other phases (Pt_3O_4 or PtO) on alumina.[39, 43-45] It is consistent with previous reports supporting that PtO_2 as the stable phase in our condition (air, 1 atm, 500 °C).[25] Due to low Pt loading and too small size (~ 1 nm), PtO_2 peaks were below detection limit by XRD for 0.5-1 wt% Pt/Al_2O_3. However, despite invisible PtO_2 peaks, O/Pt values were close to 2, indicating that 0.5-1 wt% Pt/Al_2O_3 also consist of PtO_2. Also, 10 wt% Pt/Al_2O_3 showed the growth of metallic Pt evidenced by sharp Pt peak at 2θ = 39.9° compared to bare γ-Al_2O_3. Note here that the size estimated by Scherr equation indicates that Pt was above 10 nm, which was much larger than PtO_2 (2-3 nm), suggesting the bimodal distribution.[6, 22, 46] For Pt/SiO_2, due to no overlap among diffraction peaks of PtO_2, Pt and SiO_2, Pt related peaks could be clearly visible than Pt/Al_2O_3 as shown in **Figure 5.6b**. Similarly, Pt/SiO_2 showed PtO_2 and metallic Pt at 5-10 wt% Pt.

Interestingly, newly grown PtO_2 were reduced by H_2 even at room temperature directly evidenced by *in-situ* XRD as shown in **Figure 5.6c**. When H_2 pulses were injected at room temperature into calcined 10 wt% Pt/Al_2O_3, the PtO_2 peaks gradually decreased with the simultaneous increase of metallic Pt due to the growth of broad peaks. Finally, when H_2 was continuously supplied, PtO_2 peaks disappeared with the growth of broad metallic Pt peaks. 10 wt% Pt/SiO_2 also showed similar results in

Figure 5.6d. Here, during the reduction of PtO_2 into Pt their peak broadness didn't change, indicating that no apparent size change. Size estimation by Scherrer equation showed that 2-3 nm PtO_2 clusters are reduced into 2-3 nm Pt clusters. These in-situ XRD results clearly show that certain PtO_2 are easily reduced by H_2 (even at room temperature), suggesting that these PtO_2 couldn't be characterized in RT H_2-TPR because they are already reduced during stabilization process before starting H_2-TPR. In order to quantify these easily reduced Pt oxide, we carried out cryogenic H_2-TPR starting from -80 °C for a series of supported Pt catalysts.

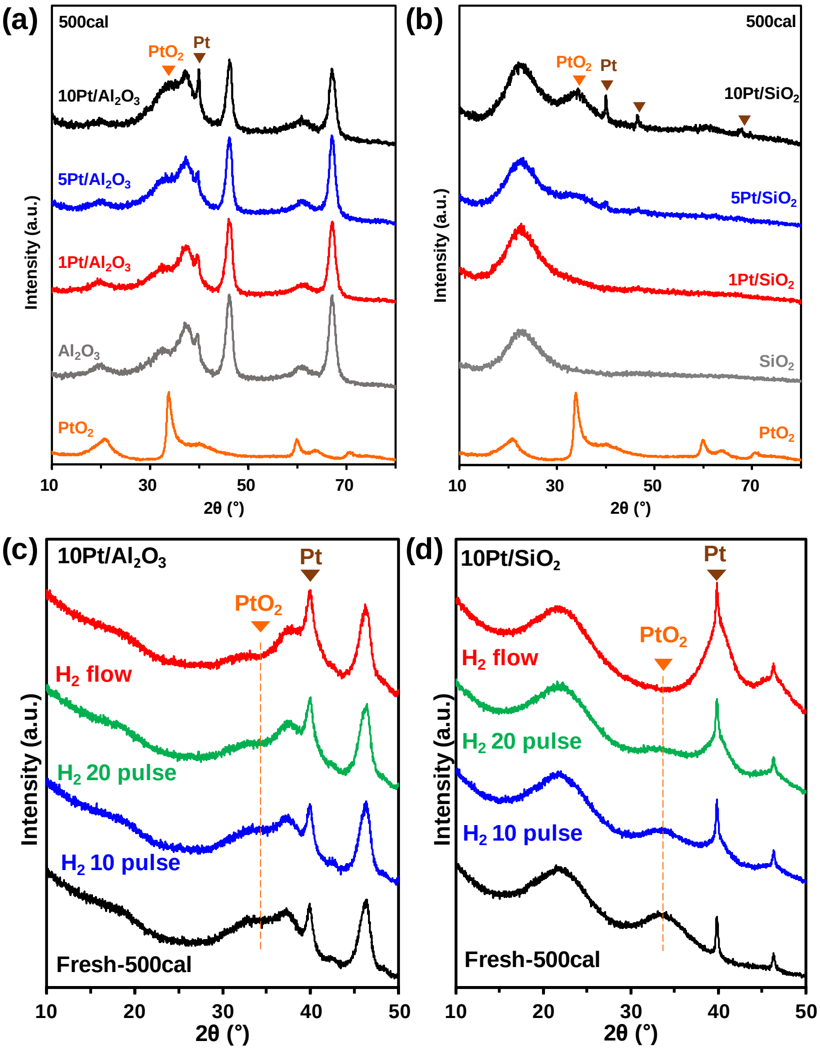

Figure 5.6. *Ex-situ* XRD patterns for (a) Al_2O_3, $1Pt/Al_2O_3$, $5Pt/Al_2O_3$ and $10Pt/Al_2O_3$ and for (b) SiO_2, $1Pt/SiO_2$, $5Pt/SiO_2$ and $10Pt/SiO_2$ after 500 °C calcination. XRD pattern for PtO_2 was obtained as received without pre-treatment. *in-situ* XRD patterns for in-situ reduction at RT by H_2 10 pulses, H_2 20 pulses and H_2 flow for (c) $10Pt/Al_2O_3$ and (d) $10Pt/SiO_2$ after 500 °C calcination.

Figure 5.7a showed cryogenic H_2-TPR profiles for a series of Pt/Al_2O_3. The results showed that 1 wt% Pt/Al_2O_3 had the reduction around 110 °C, but 5-10 wt% Pt/Al_2O_3 had the reduction at much lower temperature around -20~-50 °C, which couldn't be observed on RT H_2-TPR. Thanks to the contribution from the reduction below RT, O/Pt values were much higher (1.3~2.0) than those (0.2~1.0) from RT H_2-TPR for 0.5-10 wt% Pt/Al_2O_3 as shown in **Figure 5.7b**. It suggests that H_2-TPR from RT should be carefully interpreted because certain Pt oxides can be excluded because they are already reduced before ramping from RT during H_2-TPR.[6, 38]

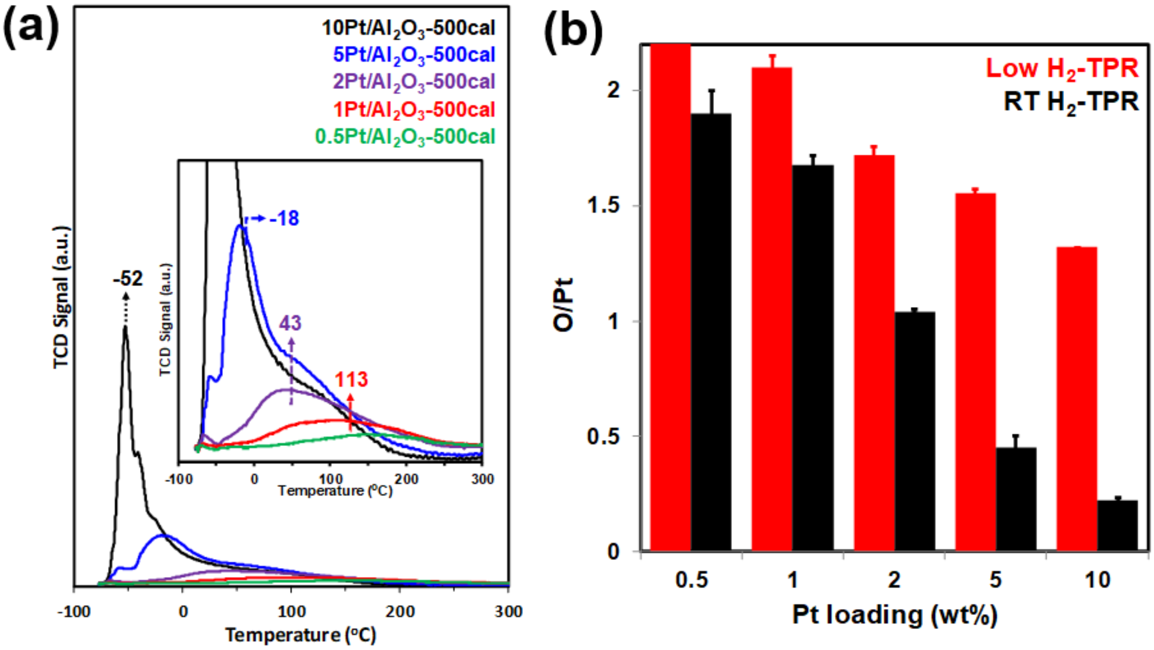

Figure 5.7. (a) Cryogenic H_2-TPR and (b) O/Pt values from RT/cryogenic H_2-TPR for Pt/Al_2O_3 with various Pt loading (0.5-10 wt% Pt) after 500 °C calcination.

HR-TEM on **Figure 5.8** confirmed that 5-10 wt% Pt/Al_2O_3 had additionally 2-3 nm clusters whose morphologies were close to three-dimensional (3D) clusters. Consistently, H_2 chemisorption results in **Figure 5.9** showed that H/Pt decreased from ~1 to 0.5~0.32 with increasing Pt loading, indicating that the average Pt sizes increased at high Pt loading. Compared to 5-10 wt% Pt/Al_2O_3, 1 wt% Pt/Al_2O_3 had only 2D-raft like PtO_2 around 1 nm and atomically dispersed Pt. So, it can be interpreted that reduction below RT comes from 3D-like PtO_2 which were newly formed with increasing Pt loading. The origin for the formation of 3D-like PtO_2 at high Pt loading is that some Pt couldn't interact with the anchoring sites on alumina because total number of Pt are bigger than that of anchoring sites on alumina.[5, 46] However, at low Pt loading (1 wt%), all Pt can do the specific interaction with the anchoring sites on alumina, leading to 2D raft PtO_2.

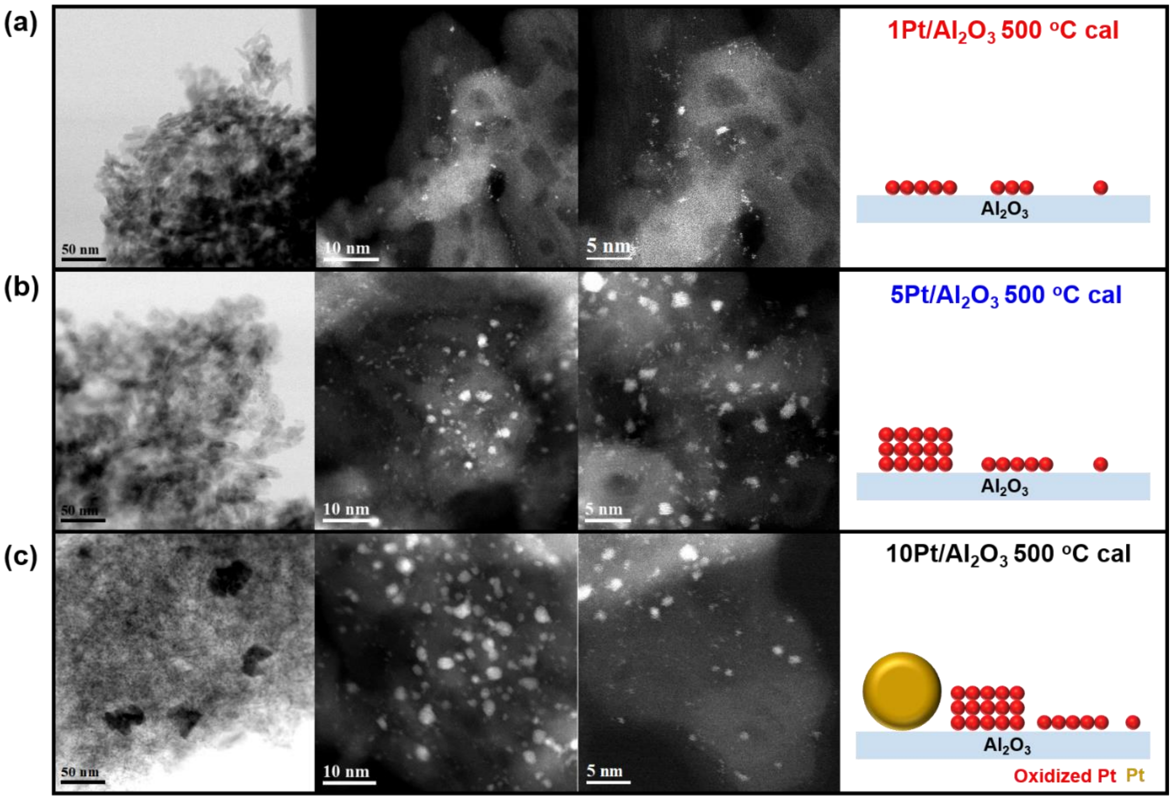

Figure 5.8. Low-magnification TEM and HAADF-STEM images for (a) $1Pt/Al_2O_3$, (b) $5Pt/Al_2O_3$, and (c) $10Pt/Al_2O_3$ after 500 °C calcination.

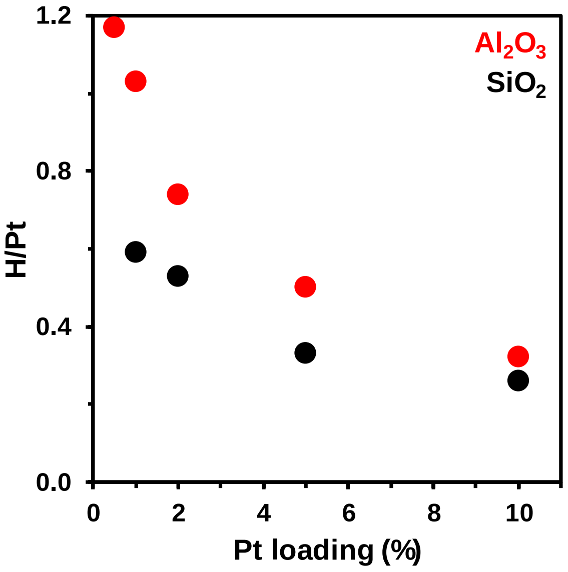

Figure 5.9. H/Pt trend as a function of Pt loading on Al_2O_3 and SiO_2. The samples were calcined at 500 °C under 20% O_2/He and reduced at 500 °C under 10% H_2/He.

Figure 5.10 showed cryogenic H_2-TPR profiles for Pt/SiO_2. Interestingly, Pt/SiO_2 showed the reduction around -40 °C even at 1 wt% Pt. Consistently, 1 wt% Pt/SiO_2 had mainly three-dimensional PtO_2 around 2-4 nm clusters on TEM as shown in **Figure 5.11**. With increasing Pt loading, cryogenic H_2-TPR and TEM showed that 3D PtO_2 clusters exist much more than Al_2O_3. Also, as shown in **Figure 5.9** H/Pt values of Pt/SiO_2 were much lower than those of Pt/Al_2O_3. That's because SiO_2 has very weak metal-support interaction with Pt compared to Al_2O_3.[47-48]

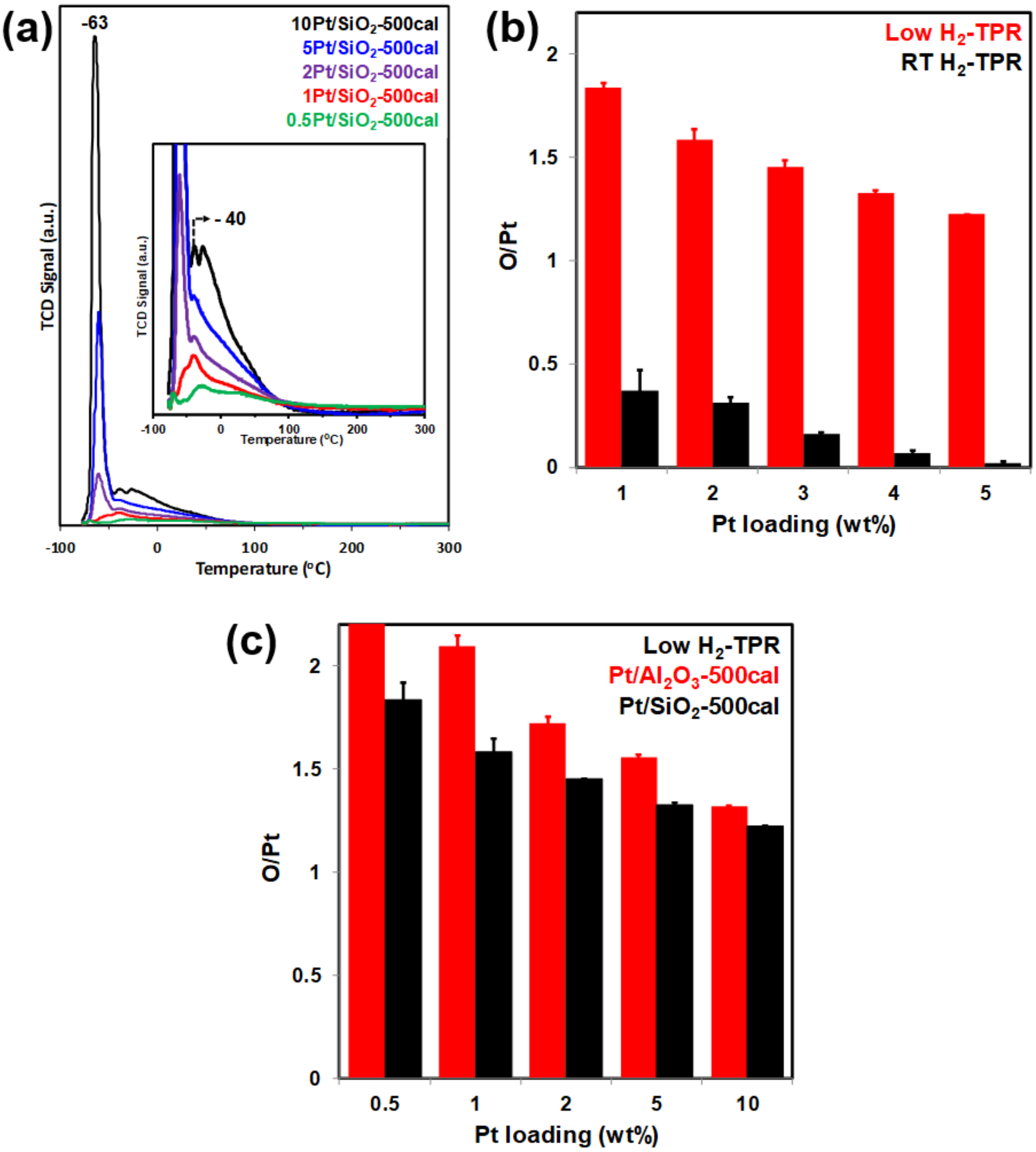

Figure 5.10. (a) Cryogenic H_2-TPR and (b) O/Pt values from RT/cryogenic H_2-TPR for Pt/SiO_2 with various Pt loading (0.5-10 wt% Pt) after 500 °C calcination. (c) O/Pt values for Pt/Al_2O_3 and Pt/SiO_2 from cryogenic H_2-TPR after 500 °C calcination.

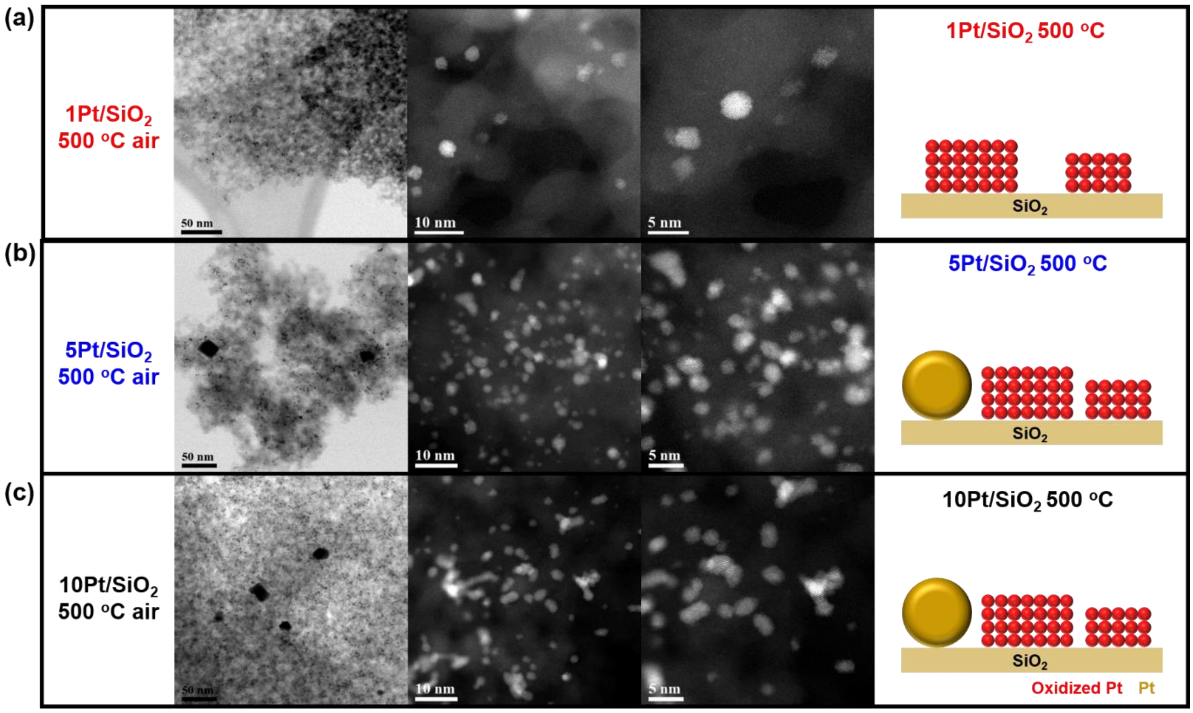

Figure 5.11. Low magnification TEM, HAADF-STEM images and schemes for 1Pt, 5Pt, and 10Pt/SiO_2 after 500 °C calcination.

Finally, DRIFTS experiments after CO adsorption at 243 K were performed for 1Pt/Al_2O_3, 5Pt/Al_2O_3, and 1Pt/SiO_2 after calcination and reduction at RT or 500 °C as shown in **Figure 5.12**. In **Figure 5.12a**, a peak at 2103 cm^{-1} appeared in calcined 1Pt/Al_2O_3, which is assigned as oxidized Pt.[43, 49] There was no apparent difference of IR spectrum on 1Pt/Al_2O_3 after reduction at RT. However, after 500 °C reduction, new peak at 2092 cm^{-1} was observed, corresponding to linearly adsorbed CO on metallic Pt.[11, 50] This indicates the reduction of 2D-like PtO_2 into metallic Pt. **Figure 5.12b** and **5.12c** showed that in 1Pt/SiO_2 and 5Pt/Al_2O_3, the peak at 2089 and 2083 cm^{-1} was observed after reduction at RT, respectively. It indicates that 1Pt/SiO_2 and 5Pt/Al_2O_3 had already metallic Pt even after reduction at RT due to the reduction of 3D-like PtO_2. It is different from 1Pt/Al_2O_3 which retained oxidized Pt after RT reduction. This results also clearly demonstrate the easier reduction of 3D-like PtO_2 than 2D-like PtO_2, consistent with cryogenic H_2-TPR and in-situ XRD.

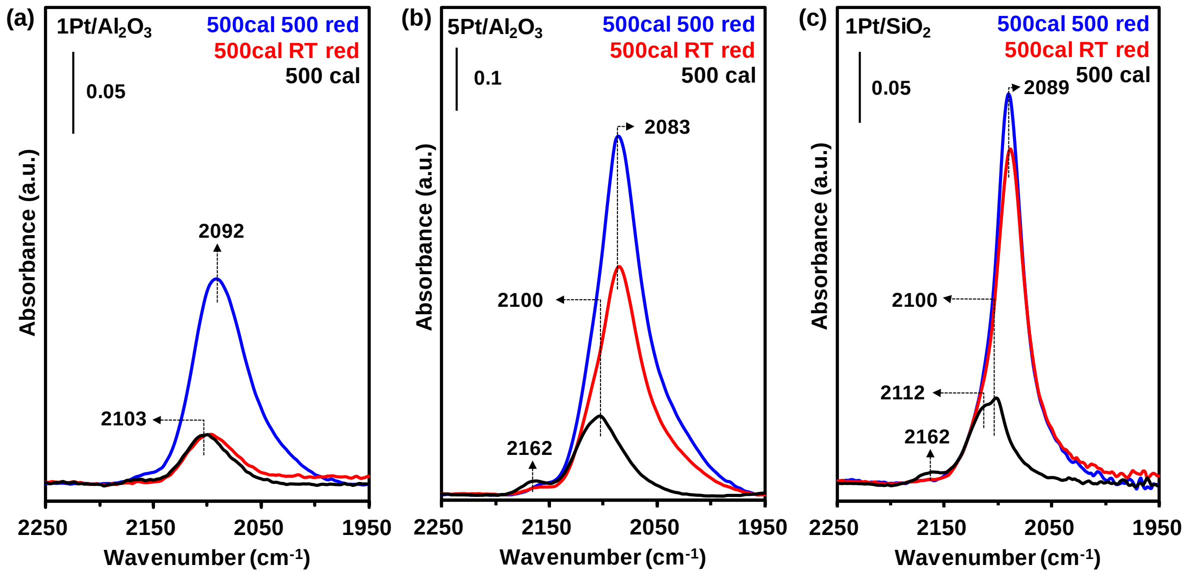

Figure 5.12. CO DRIFTS spectrum at -30 °C for (a) 1Pt/Al_2O_3, (b) 5Pt/Al_2O_3, and (c) 1Pt/SiO_2 after different reduction temperature. After ex-situ activation, the samples were pretreated at 150 °C under He.

Still, O/Pt values (from cryogenic H_2-TPR) decreased with increasing Pt loading on alumina from 2.0 to 1.3 at 10 wt% Pt on **Figure 5.10c**. The decreased O/Pt trends originate from metallic Pt evidenced by sharp metallic Pt peak on XRD. 5-10 wt% Pt/Al_2O_3 and 5-10 wt% Pt/SiO_2 had large metallic Pt crystallites (>10 nm) confirmed by low magnification TEM on **Figure 5.8** and **Figure 5.11**. These large crystallites are related to the intrinsic heterogeneity during the impregnation process. Please note that these large crystallites are not PtO_2 but metallic Pt even under oxidizing atmosphere. When much higher Pt than the number of anchoring sites are loaded on support, some Pt have no interaction with support. These Pt become aggregated, leading to large metallic Pt. So, these large metallic Pt additionally contributes to decreased O/Pt as a function of Pt loading.

In summary, when Pt loading increases on alumina, 3D-like PtO_2 are newly formed. These 3D-like PtO_2 are easily reduced even below RT due to weaker interaction between Pt and alumina. That's why O/Pt decreased with increasing Pt loading on RT H_2-TPR because 3D-like PtO_2 are already reduced at RT. When Pt is loaded on SiO_2 which has very weak metal-support interaction than Al_2O_3, 3D-like PtO_2 are more easily formed. Furthermore, when Pt loading is too high, large metallic Pt crystallites (> 10 nm) are formed on both Al_2O_3 and SiO_2 even under oxidizing atmosphere because these Pt do not interact with the support.

5.4.4. *Auto-reduction behavior of 3D-like, 2D-like Pt oxide and atomically dispersed Pt*

The second question is how increasing calcination temperature leads to easier reduction of Pt. First, we carried out in-situ XRD to know the structural change from PtO_2 to metallic Pt with increasing calcination temperature. **Figure 5.13a** showed XRD patterns for 10 wt% Pt/Al_2O_3 with increasing temperature up to 650 °C under oxidizing atmosphere (20% O_2/He). After 486 °C, 10 wt% Pt/Al_2O_3 had PtO_2 peaks at 2θ =33.9° and also large metallic Pt crystallites (> 10 nm) as previously discussed. From 570~608 °C, the broad PtO_2 peaks at 2θ =33.9° started to decrease and finally disappeared after 650 °C. Simultaneously, the peak intensity of metallic Pt at 2θ =39.9° started to increase sharply at 570 °C and continue to growth till 650 °C. These results suggest that increasing calcination temperature results in the reduction of PtO_2 into metallic Pt even under the oxidizing atmosphere, i.e. auto-reduction. That's because metallic Pt is thermodynamically stable at high temperature despite oxidizing atmosphere.[25-26] Note that the origin for easier reduction of Pt oxide with increasing calcination temperature is clearly different from that with increasing Pt loading, which mainly comes from the newly formed 3D-like PtO_2. Additionally, Pt sintering occurred during high temperature calcination, which was evidenced by the significant size difference by Scherr equation between initial PtO_2 (2-3 nm) and sintered metallic Pt (> 10 nm). However, the reduction of 3D-like PtO_2 by H_2 at RT showed no size change. 10 wt% Pt/SiO_2 was also performed as shown in **Figure 5.13b**. Similarly, auto-reduction of PtO_2 into metallic Pt was observed, but the growth of metallic Pt was severe than 10 wt% Pt/Al_2O_3 due to much weaker metal-support interaction on silica.

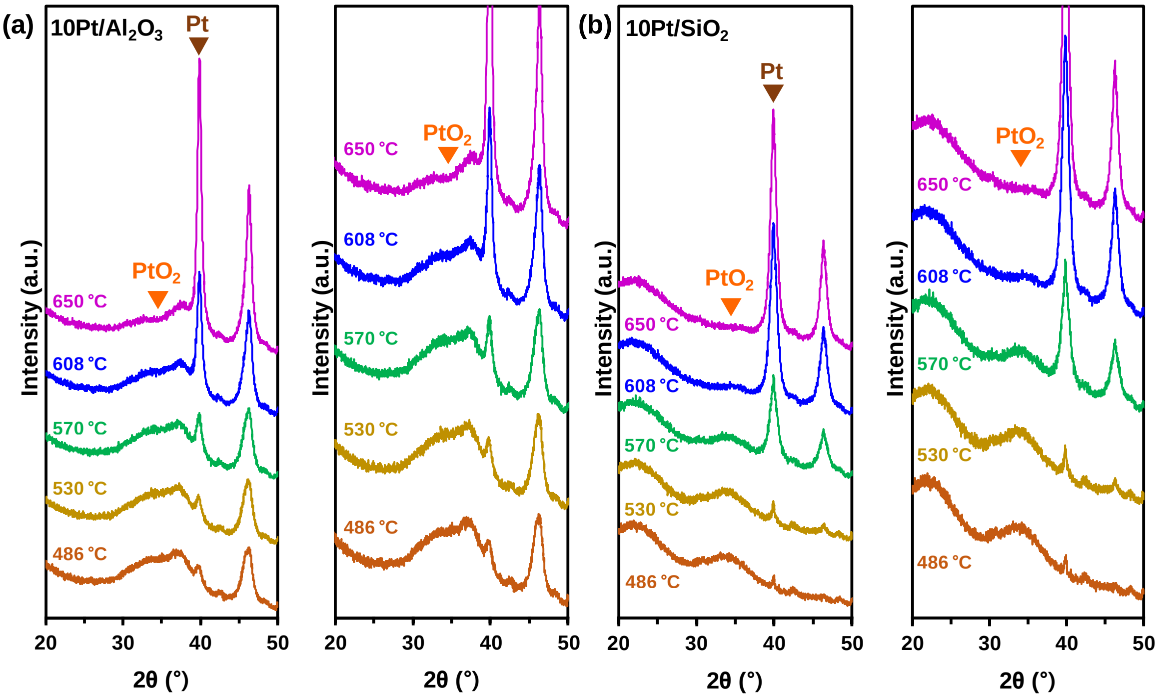

Figure 5.13. *In situ* XRD patterns for (a) $10Pt/Al_2O_3$ and (b) $10Pt/SiO_2$ with increasing calcination temperature under 20% O_2/N_2. The temperature label is calibrated temperature, not setting temperature.

Even though auto-reduction of PtO_2 into metallic Pt was evidenced by in situ XRD, the changes of each oxidized Pt species (3D-like PtO_2, 2D-like PtO_2, and atomically dispersed Pt) with increasing calcination temperature are not clear, which will be further investigated by cryogenic H_2-TPR. On the previous section, cryogenic H_2-TPR demonstrated that 3D-like PtO_2 on Al_2O_3 is easily reduced below RT (-20~-60 ^oC), but 2D-like PtO_2 on Al_2O_3 is reduced much higher temperature around 100 ^oC. **Figure 5.14** showed the cryogenic H_2-TPR profiles for Pt/Al_2O_3 and Pt/SiO_2. Overall, the reduction amounts decreased with increasing calcination temperature, indicating that the amounts of remaining PtO_2 decreased due to auto-reduction of PtO_2 into Pt. Consistently, the growth of metallic Pt with increasing calcination temperature was observed by ex-situ XRD as shown in **Figure 5.15**. **Figure 5.14a** showed the cryogenic H_2-TPR for 1wt% Pt/Al_2O_3. With increasing calcination temperature, $1Pt/Al_2O_3$ showed the drastic decrease of reduction around 600~650 ^oC, suggesting that auto-reduction of 2D-like PtO_2 mainly occurred around 600~650 ^oC. However, **Figure 5.14b** showed that the reduction peaks at -20~-50 ^oC on 5-10 wt% Pt/Al_2O_3 disappeared after 550~600 ^oC calcination. It suggests that 3D-like PtO_2 are auto-reduced at 550~600 ^oC, which was 50 ^oC lower than 2D-like PtO_2. Consistently, XRD results in **Figure 5.15a** and **5.15b** showed that the growth of metallic Pt peak started 50 ^oC earlier for 5wt% Pt/Al_2O_3 than 1 wt% Pt/Al_2O_3. When the O/Pt trend was plotted as a function of calcination temperature as shown in **Figure 5.14d**, 1 wt% Pt/Al_2O_3 showed a drastic decrease of O/Pt values after 650 ^oC, but 5-10 wt% Pt/Al_2O_3 did after ~600 ^oC. Through cryogenic H_2-TPR, we can clarify that 3D-like PtO_2 are auto-reduced more easily around 550~600 ^oC than 2D-like PtO_2 (600~650 ^oC) with the difference of 50 ^oC. Previously, O/Pt values from RT H_2-TPR decreased drastically after 650 ^oC because RT H_2-TPR gives information mainly about 2D-like PtO_2. A series of Pt/SiO_2 was compared as shown in **Figure 5.14e–5.14h**. After 500 ^oC calcination, 1 wt% Pt/SiO_2 had the main reduction at -60 ^oC from 3D-like PtO_2 and these reduction peaks mostly decreased after 550 ^oC. These trends were also observed for 5-10 wt% Pt/SiO_2. Due to weaker interaction with silica than alumina, 3D-like PtO_2 on SiO_2 were 50 ^oC more easily auto-reduced when compared to 3D-like PtO_2 on Al_2O_3.

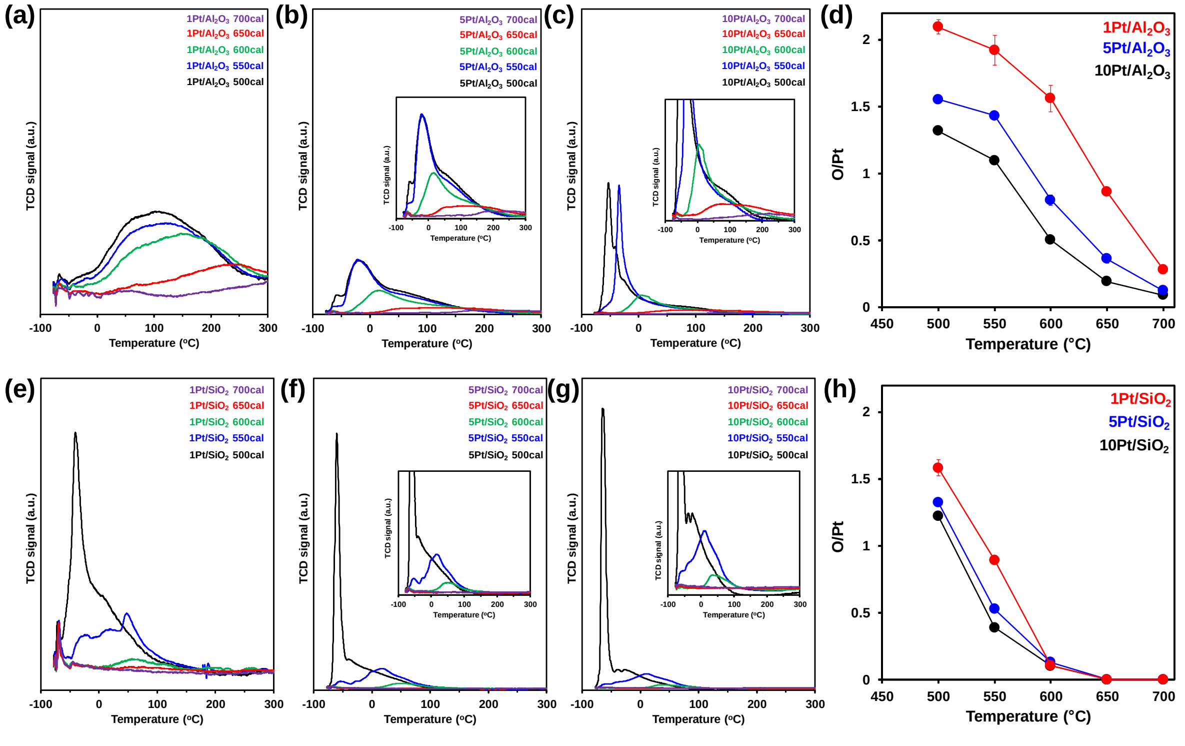

Figure 5.14. Cryogenic H_2-TPR for (a) $1Pt/Al_2O_3$, (b) $5Pt/Al_2O_3$, and (c) $10Pt/Al_2O_3$ after 500–700 °C calcination. (d) O/Pt values for Pt/Al_2O_3 as a function of calcination temperature. Cryogenic H_2-TPR for (e) $1Pt/SiO_2$, (f) $5Pt/SiO_2$, and (g) $10Pt/SiO_2$ after 500–700 °C calcination. (d) O/Pt values for Pt/SiO_2 as a function of calcination temperature.

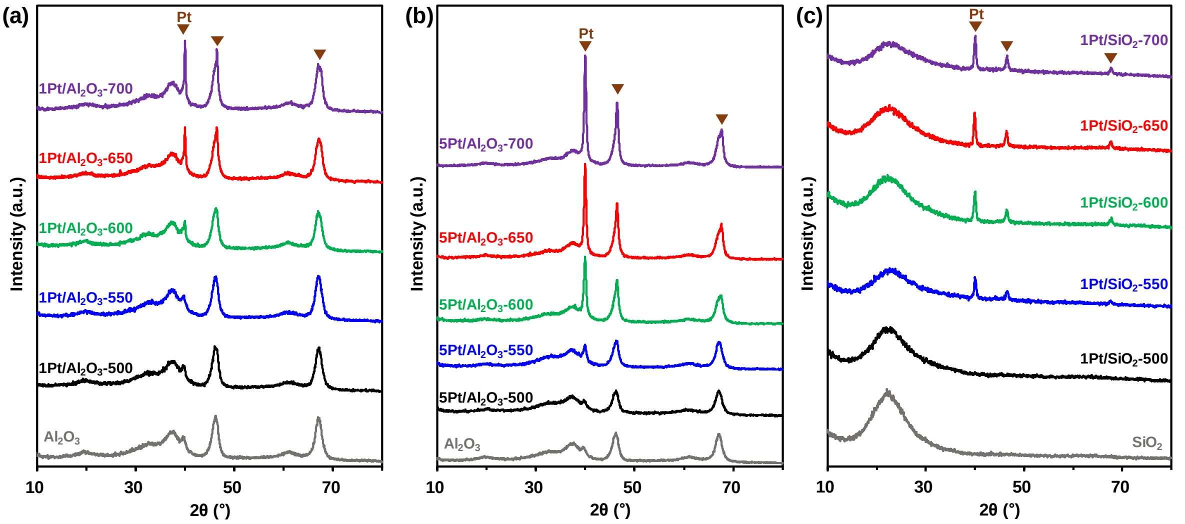

Figure 5.15. *Ex-situ* XRD for (a) $1Pt/Al_2O_3$, (b) $5Pt/Al_2O_3$ and (c) $1Pt/SiO_2$ after 500–700 °C calcination.

Till now, we demonstrate that PtO_2 are auto-reduced into metallic Pt with increasing calcination temperature. Here, the auto-reduction of PtO_2 led to O_2 desorption, which can be characterized by mass spectrometry as O_2 TPD as shown in **Figure 5.16**. Note that O_2 TPD can be only possible under He flow not 20% O_2/He due to the sensitivity problem. Under He atmosphere, PtO_2 are auto-reduced at lower temperature than 20% O_2/He, whose difference was around 90~120 °C for 10 wt% Pt catalysts confirmed by TGA (not shown). **Figure 5.16a** showed O_2 TPD for bare Al_2O_3 and Pt/Al_2O_3 after 500 °C calcination. Bare Al_2O_3 showed a negligible signal for mass 32. 1 wt% Pt/Al_2O_3 showed O_2 desorption at 664 °C. 5 wt% Pt/Al_2O_3 showed increased intensities for the peak at 664 °C and additional peaks for 486 °C and 608 °C. The peak at 486 °C increased for 10 wt% Pt/Al_2O_3. Based on previous characterization results, we can interpret the peak at 486 °C as the auto-reduction of 3D-like PtO_2 and the remaining high desorption temperature peak (608~664 °C) as the auto-reduction of 2D-like PtO_2. So, these results also suggest that auto-reduction of 2D-like PtO_2 are much difficult than 3D-like PtO_2 whose difference around 120~160 °C. This was consistent with previous works.[25, 51] Recently, Sangnier et al. reported that highly dispersed PtO_2 (~1 nm) on alumina showed O_2 desorption above 680 °C, which was much higher than bulk Pt.[25] **Figure 5.16b** showed the results for bare SiO_2 and Pt/SiO_2 after 500 °C calcination. O_2 desorption from 3D-like PtO_2 around 478 °C was observed even on 1 wt% Pt/SiO_2 with another shoulder peak at 620 °C. Here, shoulder peaks around 600 °C might be mainly related with the surface dehydroxylation on silica. Pt/SiO_2 had more amounts of O_2 desorption from 3D-like PtO_2 with a slightly lower temperature than Pt/Al_2O_3 because 3D-like PtO_2 are mainly formed on Pt/SiO_2 due to weak metal-support interaction than alumina. So, O_2 TPD demonstrates that 3D-like PtO_2 showed O_2 desorption at 480~ 500 °C, but 2D-like PtO_2 did at above 600 °C, which was 120 °C higher than 3D PtO_2.

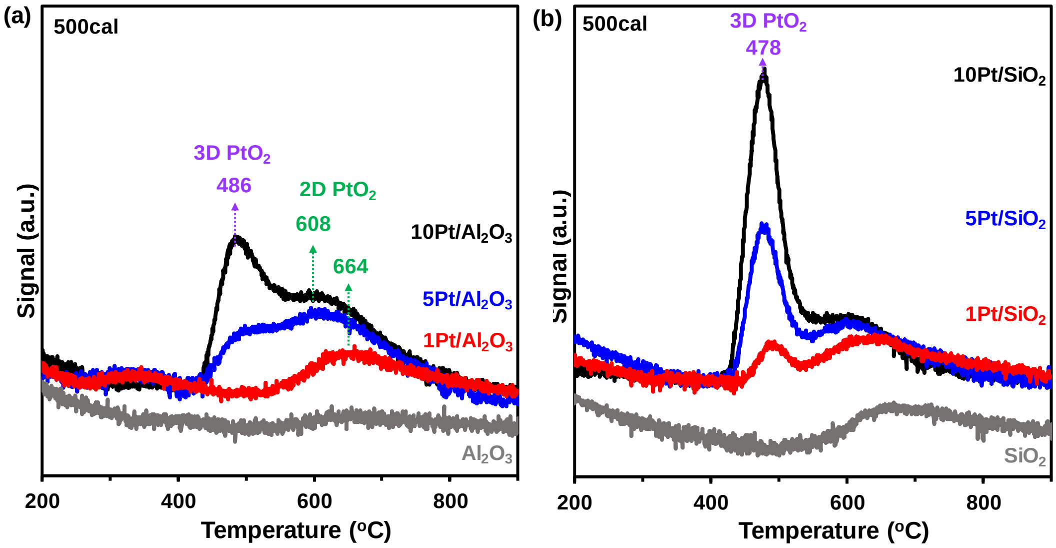

Figure 5.16. O_2 TPD for (a) 1Pt/Al_2O_3, 5Pt/Al_2O_3 and 10Pt/Al_2O_3 and for (b) 1Pt/SiO_2, 5Pt/SiO_2 and 10Pt/SiO_2 after 500 °C calcination.

We extended these results into the effect of calcination temperature as shown in **Figure 5.17–5.18**. **Figure 5.17** showed that O_2 desorption from 3D-like PtO_2 disappeared after 550~600 °C, which was much easier than those from 2D-like PtO_2 on Pt/Al_2O_3 (above 600 °C). Furthermore, 3D-like PtO_2 on Pt/SiO_2 disappeared after 550 °C calcination as shown in **Figure 5.18**. In overall, this was consistent with the results from cryogenic H_2-TPR.

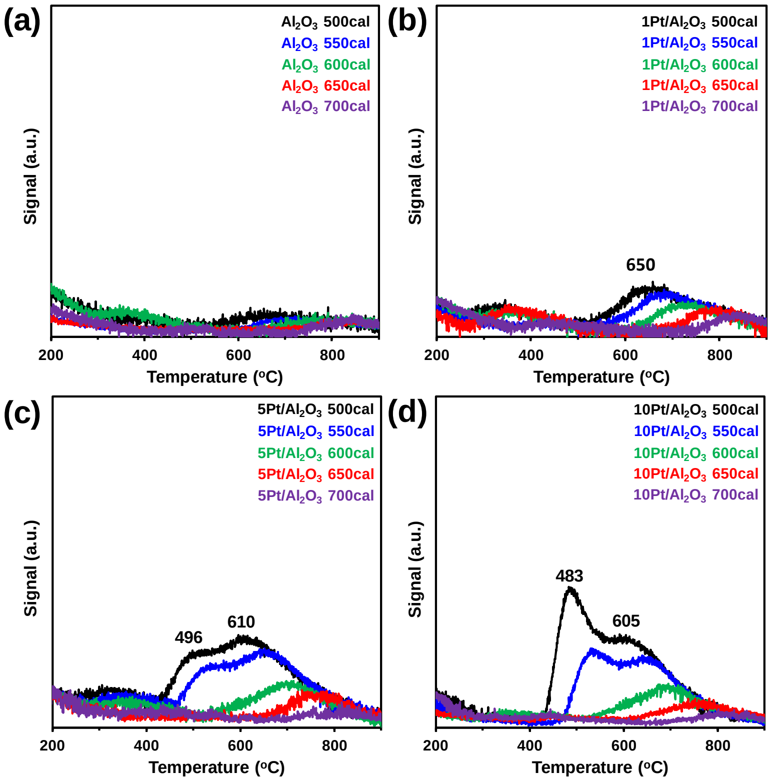

Figure 5.17. O_2-TPD for (a) Al_2O_3, (b) $1Pt/Al_2O_3$, (c) $5Pt/Al_2O_3$ and (d) $10Pt/Al_2O_3$ after 500–700 °C calcination.

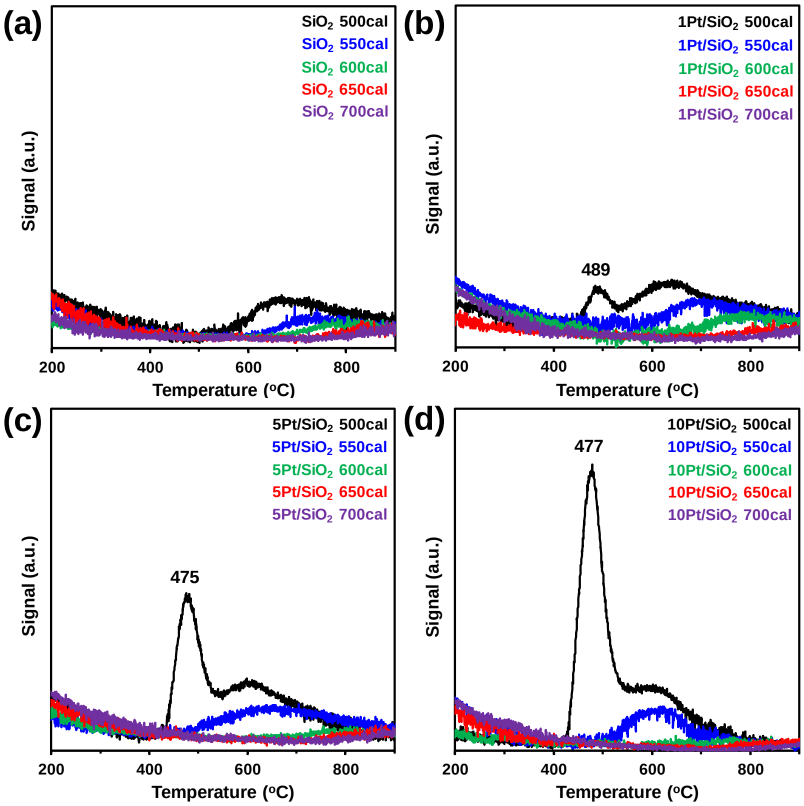

Figure 5.18. O_2-TPD for (a) SiO_2, (b) $1Pt/SiO_2$, (c) $5Pt/SiO_2$ and (d) $10Pt/SiO_2$ after 500–700 °C calcination.

During auto-reduction of PtO_2 into Pt, the sintering behavior of Pt was investigated by TEM as shown in **Figure 5.19** and **Figure 5.20–5.22**. **Figure 5.19a** showed that $1Pt/Al_2O_3$ after 700 ^{o}C calcination had agglomerated Pt around ~100 nm where ~30 nm particles agglomerate together. Interestingly, the whole sizes of Pt on $1Pt/Al_2O_3$ were much larger than those from $5Pt/Al_2O_3$ or $1Pt/SiO_2$ which had 30~40 nm particles. Note that $1Pt/Al_2O_3$ had 2D-like PtO_2 and atomically dispersed Pt, but $5Pt/Al_2O_3$ had additional 3D-like PtO_2 and $1Pt/SiO_2$ had mainly 3D-like PtO_2 only. Additional TEM studies on **Figure 5.20–5.22** observed that Pt sintering started mainly from 600 ^{o}C for $1Pt/Al_2O_3$, but 550 ^{o}C for $5Pt/Al_2O_3$ and $1Pt/SiO_2$, which was also consistent with the growth of metallic Pt peaks in XRD. The Pt sizes by XRD on **Figure 5.19b** show that $1Pt/Al_2O_3$ had twice as large as $5Pt/Al_2O_3$ and $1Pt/SiO_2$. The origin for more Pt sintering of initially highly dispersed Pt during auto-reduction might come from the mobility of 2D-like PtO_2 and atomically dispersed Pt. The 3D-like PtO_2 are auto-reduced into metallic Pt, becoming less mobile than Pt oxide. That's why 3D-like PtO_2 are more stable for Pt sintering. This phenomenon was consistent with the study of Pd/Al_2O_3 by Kang et al. reporting that larger initial Pd sinter more slowly.[52]

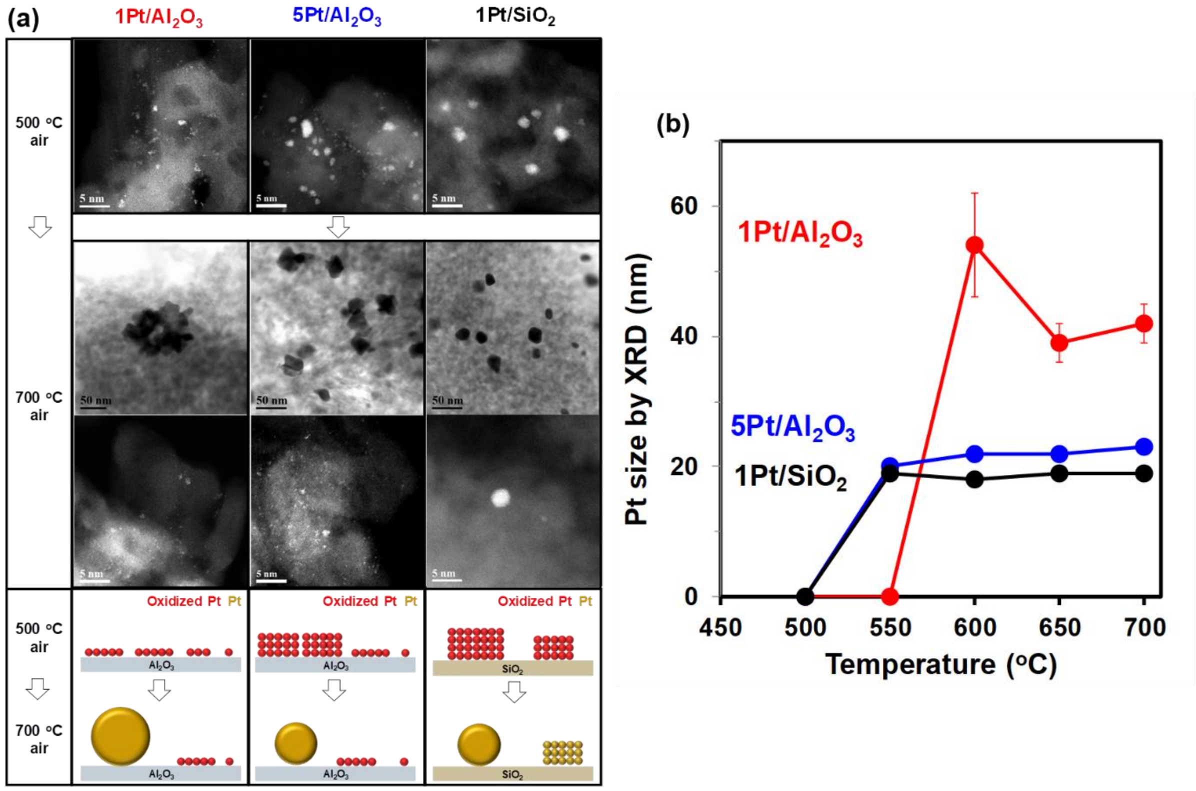

Figure 5.19. (a) TEM and HAADF-STEM images and (b) Pt size estimated by XRD for $1Pt/Al_2O_3$, $5Pt/Al_2O_3$, and $1Pt/SiO_2$ after 500 °C and 700 °C calcination.

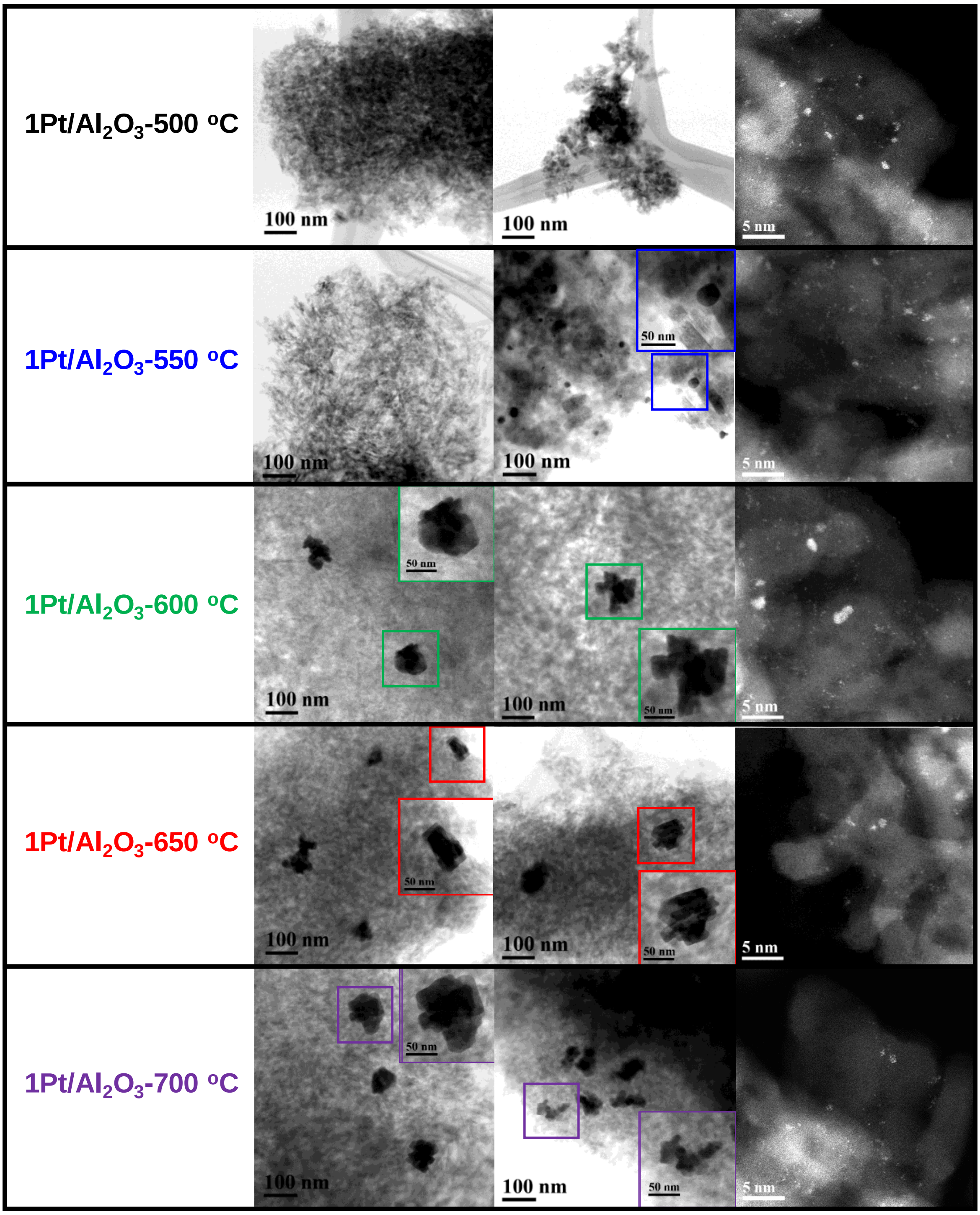

Figure 5.20. Low magnification TEM and HAADF-STEM images for 1Pt/Al_2O_3 after 500–700 ℃ calcination.

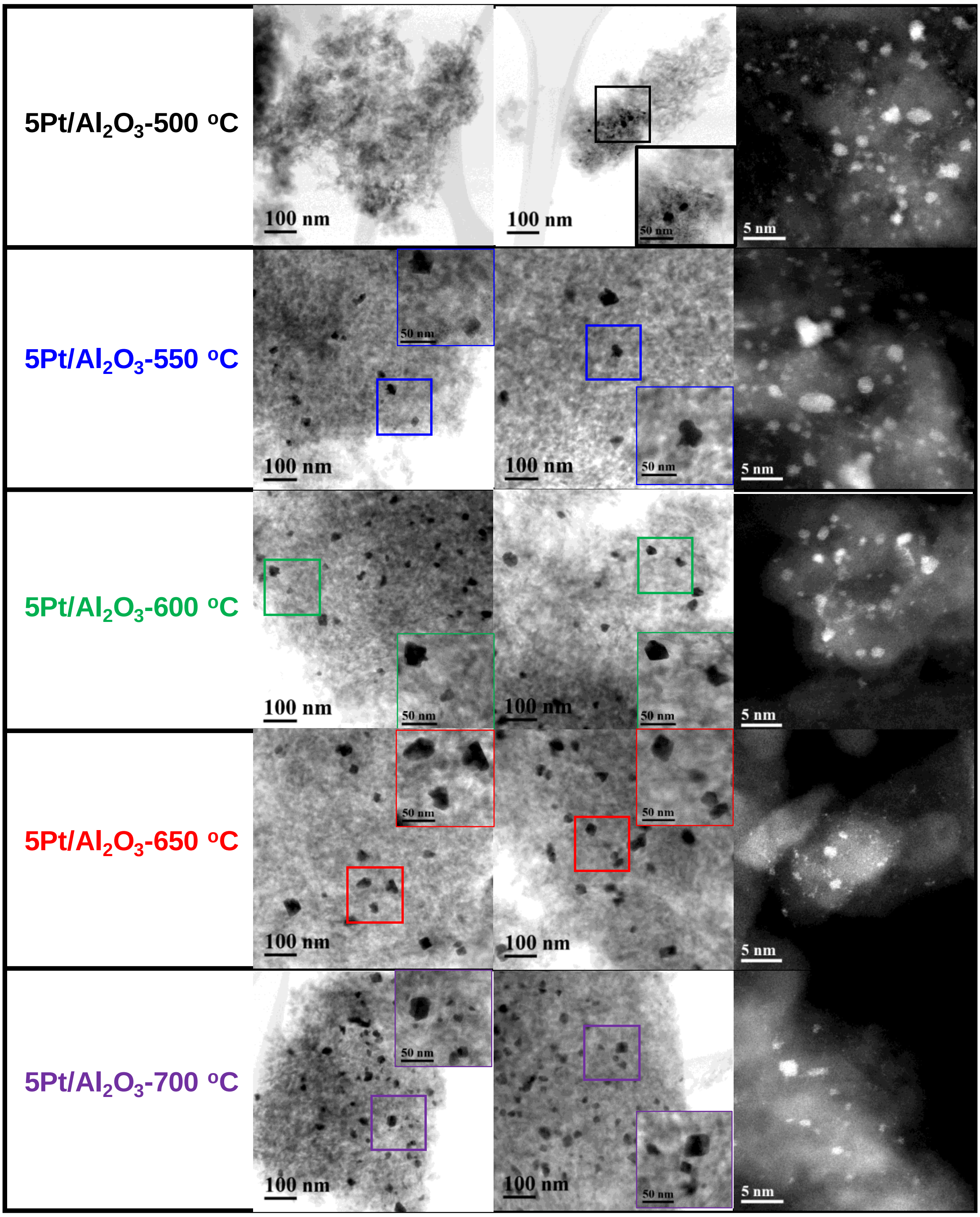

Figure 5.21. Low magnification TEM and HAADF-STEM images for 5Pt/Al$_2$O$_3$ after 500–700 °C calcination.

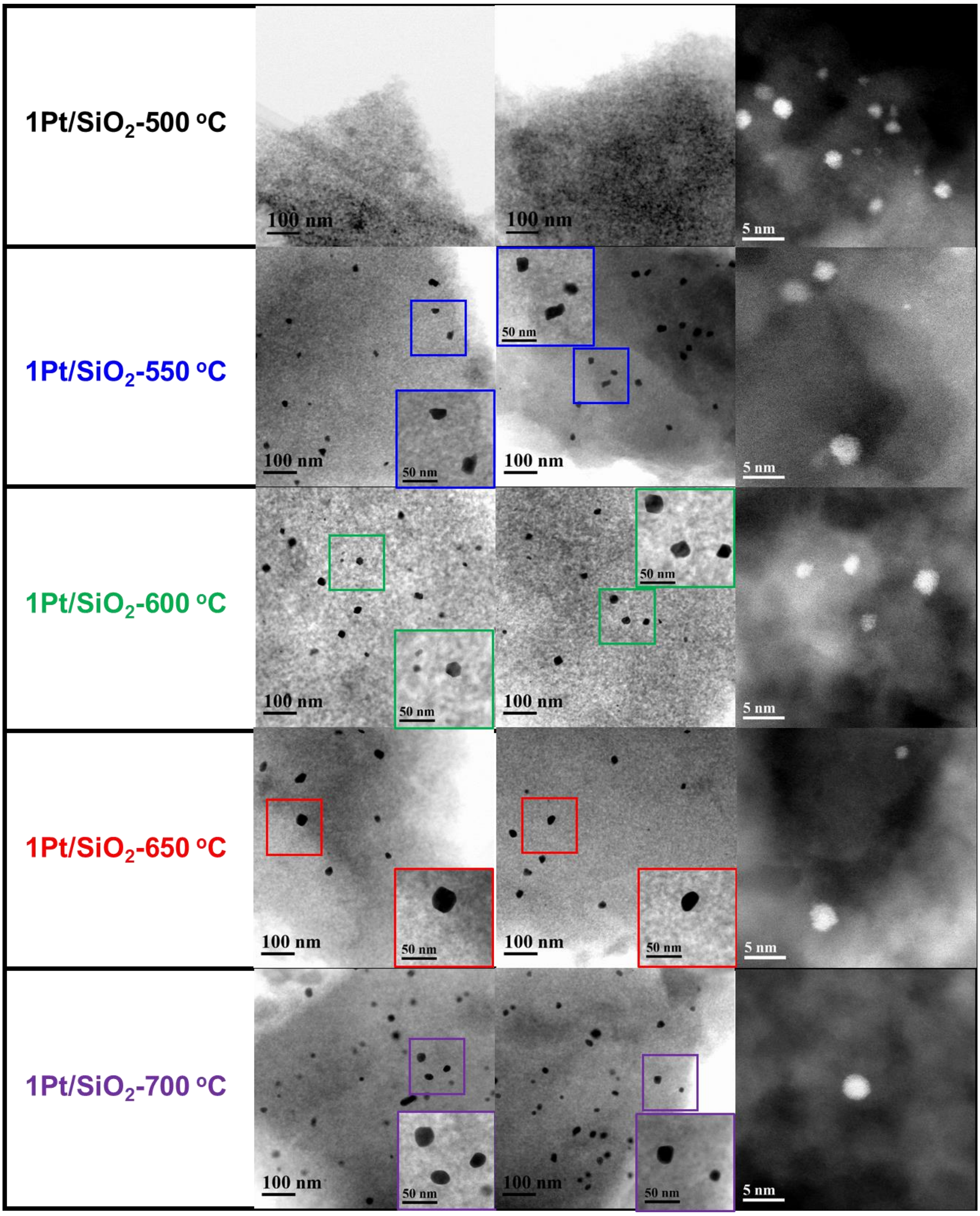

Figure 5.22. Low magnification TEM and HAADF-STEM images for 1Pt/SiO_2 after 500–700 °C calcination.

In addition, the role of atomically dispersed Pt was systematically studied by the variance of reduction temperature for 1Pt/Al_2O_3 on **Figure 5.23–5.26**. **Figure 5.23** showed after reduction around 300 °C, Pt-O-Al peaks disappeared, showing the reduction of atomically dispersed Pt. Consistently, HAADF-STEM (**Figure 5.24**) showed more ~1nm clusters at the expense of atomically dispersed Pt after high temperature reduction (>= 300 °C). After controlled reduction, Pt/Al_2O_3 was aged at 700 °C. **Figure 5.25** showed the sintered Pt whose sizes were estimated above 20 nm by XRD. Interestingly, Pt sizes decreased with increasing the reduction temperature, which was also consistent with low magnification TEM (**Figure 5.26**). The results showed that 1Pt/Al_2O_3 with more atomically dispersed Pt had more Pt sintering after 700 ^{o}C calcination, suggesting the contribution of atomically dispersed Pt into the Pt sintering. All the results suggest that 3D-like PtO_2 is more sinter-resistant than 2D-like PtO_2 and atomically dispersed Pt.

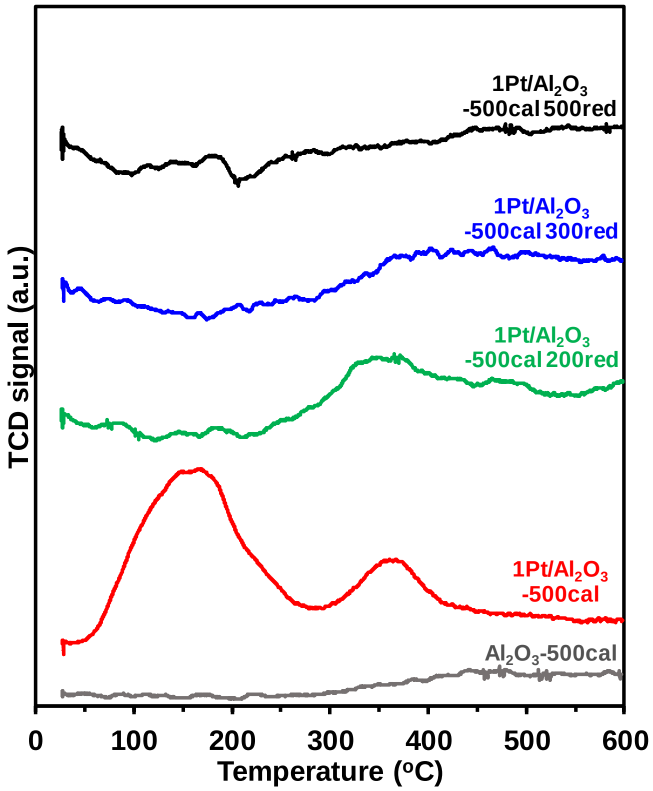

Figure 5.23. H_2-TPR for 1Pt/Al_2O_3 with various reduction temperature.

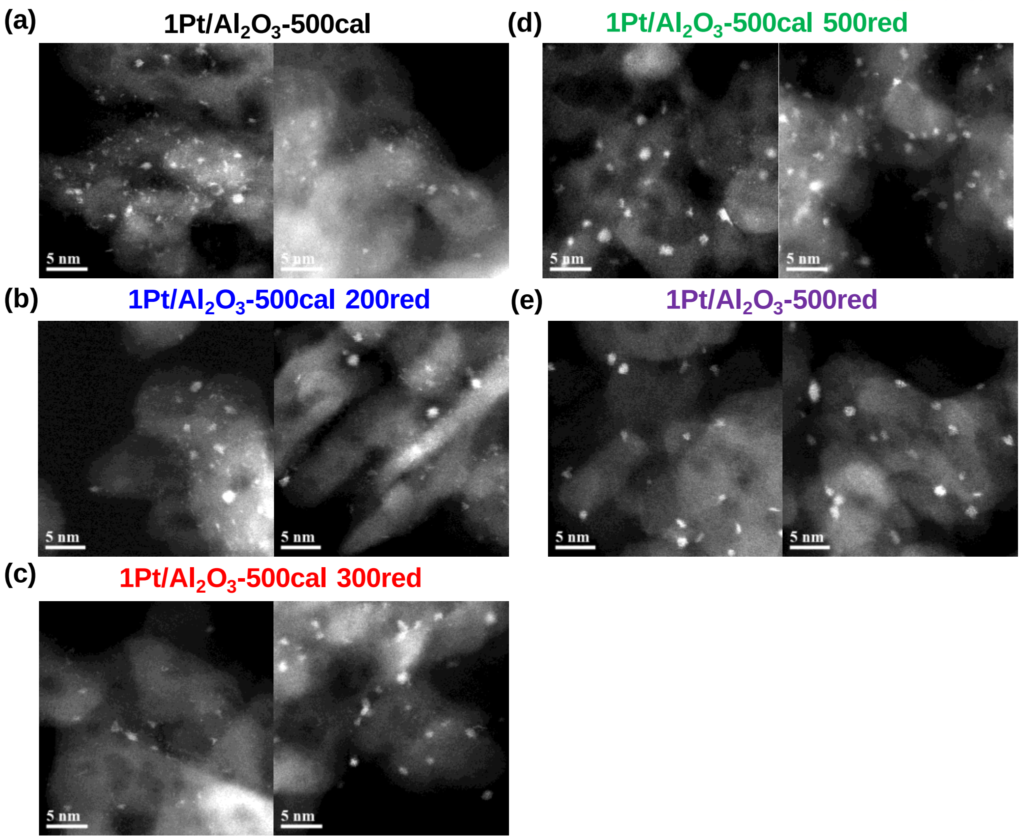

Figure 5.24. HAADF-STEM images for 1Pt/Al_2O_3 with controlled reduction temperature. (a) 500 °C calcination, (b) 500 °C calcination and 200 °C reduction, (c) 500 °C calcination and 300 °C reduction, (d) 500 °C calcination and 500 °C reduction and (e) 500 °C reduction.

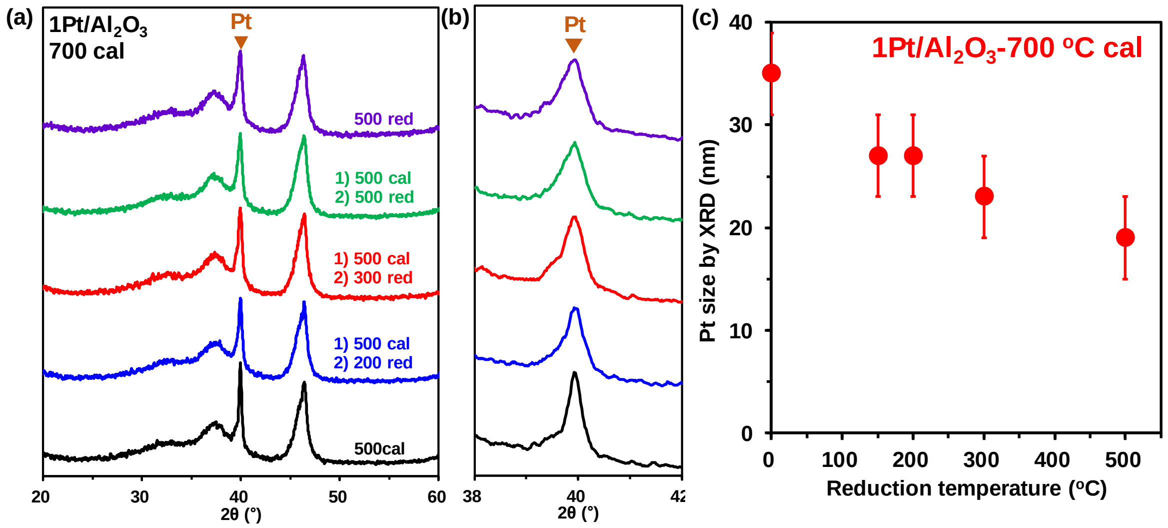

Figure 5.25. XRD patterns for 700 °C aged 1Pt/Al_2O_3 with controlled reduction temperature and (b) magnification at 2θ regions of 38° and 42°. (c) Pt size estimated by XRD as a function of reduction temperature.

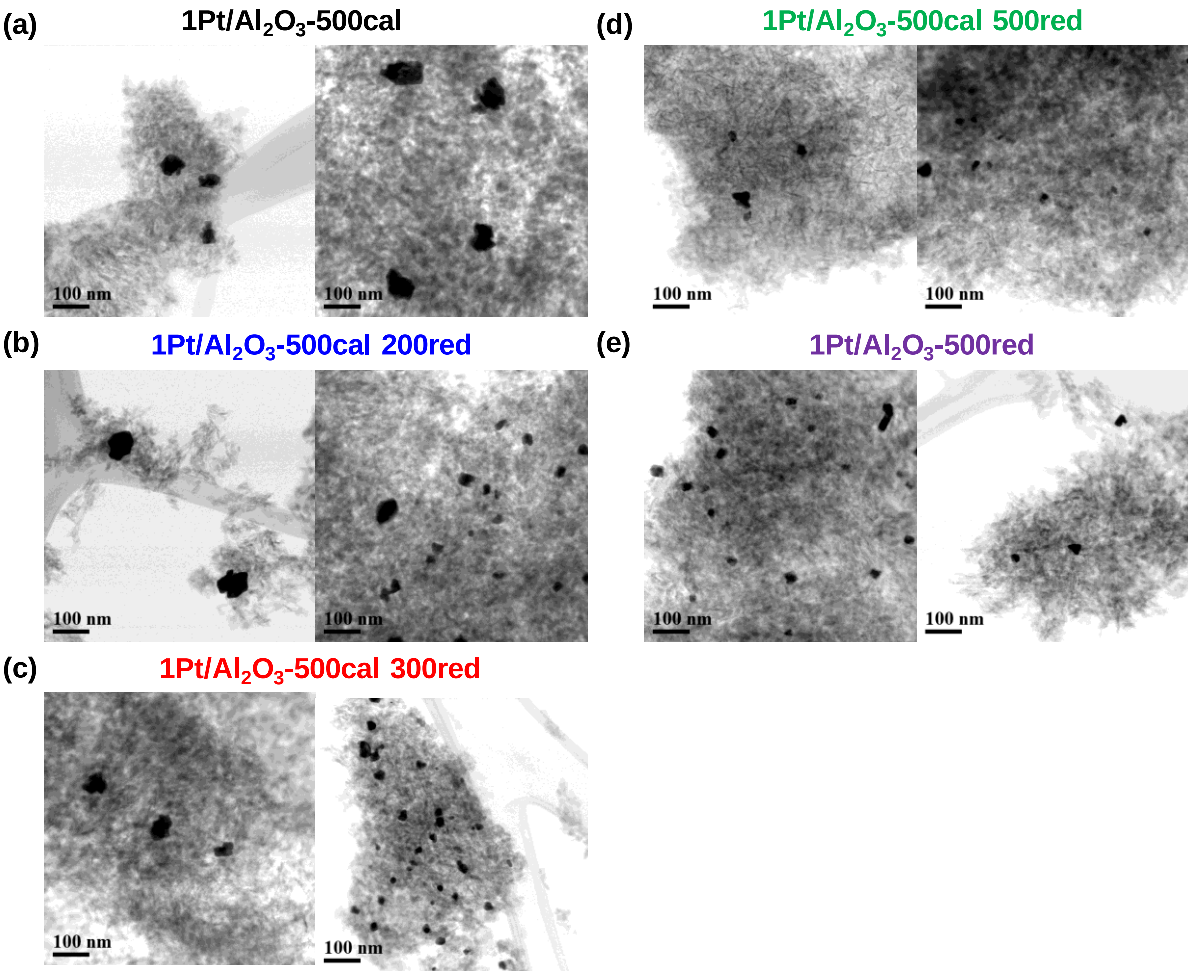

Figure 5.26. TEM images for 700 °C aged 1Pt/Al_2O_3 with controlled reduction temperature – (a) 500 °C calcination, (b) 500 °C calcination and 200 °C reduction, (c) 500 °C calcination and 300 °C reduction, (d) 500 °C calcination and 500 °C reduction and (e) 500 °C reduction.

In summary, when calcination temperature increases from 500-700 °C PtO_2 are auto-reduced into metallic Pt because metallic Pt is thermodynamically stable at high temperature. Cryogenic H_2-TPR and O_2 TPD demonstrate that 3D-like PtO_2 are auto-reduced around 550-600 °C calcination, but 2D-like PtO_2 are auto-reduced at 50 °C higher than 3D-like PtO_2. During the auto-reduction of PtO_2 at high temperature calcination, Pt sintering also occurred. Because 3D-like PtO_2 are more easily auto-reduced than 2D-like PtO_2 and atomically dispersed Pt, 3D metallic Pt clusters become less mobile than 2D-like PtO_2 and atomically dispersed Pt (still, oxidized Pt). So, 3D-like PtO_2 showed more sinter-resistant behavior than 2D-like PtO_2 and atomically dispersed Pt.

5.5. Conclusion

In this study, the reduction behavior of oxidized Pt species (3D-like PtO_2, 2D-like PtO_2, atomically dispersed Pt) on industrially relevant Pt/Al_2O_3 was systematically investigated by XRD, H_2-TPR, TEM,

O_2 TPD, and DRIFTS studies. XRD, H_2-TPR, and TEM results demonstrate that under the oxidizing atmosphere, the morphologies and sizes of PtO_2 on Pt/Al_2O_3 are determined by the specific interaction between Pt and Al_2O_3 through Pt-O-Al. This specific interaction between Pt and Al_2O_3 leads to highly dispersed Pt as 1 nm 2D-like PtO_2 and atomically dispersed Pt at 1 wt% Pt/Al_2O_3. When Pt can't interact with anchoring sites on support by increasing Pt loading (5-10 wt% Pt/Al_2O_3) or using SiO_2 which has very weak metal-support interaction (1 wt% Pt/SiO_2), 3D-like PtO_2 with 2-4 nm are formed. *In-situ* XRD, H_2-TPR, and DRIFTS show that 3D-like PtO_2 are reduced earlier (-20~-60 ºC) than 2D-like PtO_2 (~100 ºC) and atomically dispersed Pt (>300 ºC) due to weak interaction with support. So, H_2-TPR starting from room temperature should be carefully interpreted because 3D-like PtO_2 are not characterized due to the reduction even at RT. All the results suggest that the morphologies and sizes of Pt oxide are decided by metal-support interaction.

When Pt/Al_2O_3 is calcined at high temperature (500-700 ºC), PtO_2 are reduced into metallic Pt. However, this reduction occurred without reducing agent (auto-reduction) because metallic Pt is thermodynamic stable phase rather than Pt oxide at high temperature, which is clearly different from the reduction by reducing agent such as H_2. Here, interaction strength also influences auto-reduction behavior when calcination temperature increases. XRD, H_2-TPR, TEM, and O_2 TPD show that 3D-like PtO_2 are auto-reduced into metallic Pt after 550-600 ºC calcination, but 2D-like PtO_2 are 50 ºC more difficult to be auto-reduced. So, the interaction strength with the support determines how long Pt oxide can maintain as oxidized Pt rather than metallic Pt. During auto-reduction at high calcination temperature, Pt sintering also occurred. TEM and XRD results show that thanks to easier auto-reduction of 3D-like PtO_2, 3D clusters (metallic Pt) become less mobile than 2D-like PtO_2 and atomically dispersed Pt (still, oxidized Pt) So, 3D-like PtO_2 showed most sinter-resistant behavior than 2D-like PtO_2 and atomically dispersed Pt. In addition, when atomically dispersed Pt disappeared by controlling reduction temperature, $1Pt/Al_2O_3$ had less Pt sintering, suggesting the contribution of atomically dispersed Pt for Pt sintering. In summary, metal-support interaction is important for the reduction behavior of oxidized Pt on Pt/Al_2O_3, suggesting the guideline for efficient utilization of metallic Pt for catalytic reaction in real-world by the careful activation process.

5.6. References

[1] Sattler, J. J.; Ruiz-Martinez, J.; Santillan-Jimenez, E.; Weckhuysen, B. M., *Chem. Rev.* **2014,** *114*, 10613-10653.

[2] Rahimpour, M. R.; Jafari, M.; Iranshahi, D. *Appl. Energy* **2013,** *109*, 79-93.

[3] Gélin, P.; Primet, M. *Appl. Catal., B* **2002,** *39*, 1-37.

[4] Koltsakis, G. C.; Stamatelos, A. M. *Prog. Energy Combust. Sci.* **1997**, 23, 1-39.

[5] Kwak, J. H.; Hu, J.; Mei, D.; Yi, C.-W.; Kim, D. H.; Peden, C. H. F.; Allard, L. F.; Szanyi, J.

Science **2009,** *325*, 1670-1673.

[6] Yao, H. C.; Sieg, M.; Plummer, H. K. *J. Catal.* **1979,** *59*, 365-374.

[7] Vaarkamp, M.; Miller, J. T.; Modica, F. S.; Koningsberger, D. C. *J. Catal.* **1996,** *163*, 294-305.

[8] Le Valant, A.; Drault, F.; Maleix, C.; Comminges, C.; Beauchet, R.; Batonneau, Y.; Pirault-Roy, L.; Especel, C.; Epron, F. *J. Catal.* **2018,** *367*, 234-243.

[9] Gorczyca, A.; Moizan, V.; Chizallet, C.; Proux, O.; Net, W. D.; Lahera, E.; Hazemann, J. L.; Raybaud, P.; Joly, Y. *Angew. Chem. Int. Ed.* **2014,** *126*, 12634-12637.

[10] Pakharukov, I. Y.; Stakheev, A. Y.; Beck, I. E.; Zubavichus, Y. V.; Murzin, V. Y.; Parmon, V. N.; Bukhtiyarov, V. I. *ACS Catal.* **2015,** *5*, 2795-2804.

[11] Kale, M. J.; Christopher, P. *ACS Catal.* **2016,** *6*, 5599-5609.

[12] Casapu, M.; Fischer, A.; Gänzler, A. M.; Popescu, R.; Crone, M.; Gerthsen, D.; Türk, M.; Grunwaldt, J.-D., *ACS Catal.* **2017,** *7*, 343-355.

[13] Singh, J.; Alayon, E. M. C.; Tromp, M.; Safonova, O. V.; Glatzel, P.; Nachtegaal, M.; Frahm, R.; van Bokhoven, J. A. *Angew. Chem. Int. Ed.* **2008**, *47*, 9260-9264.

[14] Boubnov, A.; Dahl, S.; Johnson, E.; Molina, A. P.; Simonsen, S. B.; Cano, F. M.; Helveg, S.; Lemus-Yegres, L. J.; Grunwaldt, J.-D. *Appl. Catal., B* **2012,** *126*, 315-325.

[15] Haneda, M.; Watanabe, T.; Kamiuchi, N.; Ozawa, M. *Appl. Catal., B* **2013,** *142-143*, 8-14.

[16] Behafarid, F.; Ono, L. K.; Mostafa, S.; Croy, J. R.; Shafai, G.; Hong, S.; Rahman, T. S.; Bare, S. R.; Cuenya, B. R. *Phys. Chem. Chem. Phys.* **2012,** *14*, 11766-79.

[17] Wang, C.-B.; Yeh, C.-T. *J. Catal.* **1998,** *178*, 450-456.

[18] Small, M. W.; Sanchez, S. I.; Marinkovic, N. S.; Frenkel, A. I.; Nuzzo, R. G *ACS Nano* **2012,** *6*, 5583-5595.

[19] Hu, C. H.; Chizallet, C.; Mager-Maury, C.; Corral-Valero, M.; Sautet, P.; Toulhoat, H.; Raybaud, P. *J. Catal.* **2010,** *274*, 99-110.

[20] Mager-Maury, C.; Bonnard, G.; Chizallet, C.; Sautet, P.; Raybaud, P. *ChemCatChem* **2011,** *3*, 200-207.

[21] Dessal, C.; Sangnier, A.; Chizallet, C.; Dujardin, C.; Morfin, F.; Rousset, J.-L.; Aouine, M.; Bugnet, M.; Afanasiev, P.; Piccolo, L. *Nanoscale* **2019,** *11*, 6897-6904.

[22] Mei, D.; Kwak, J. H.; Hu, J.; Cho, S. J.; Szanyi, J.; Allard, L. F.; Peden, C. H. F. *J. Phys. Chem. Lett.* **2010,** *1*, 2688-2691.

[23] Lisitsyn, A. S.; Yakovina, O. A. *Phys. Chem. Chem. Phys.* **2018,** *20*, 2339-2350.

[24] Mistry, H.; Behafarid, F.; Bare, S. R.; Roldan Cuenya, B. *ChemCatChem* **2014,** *6*, 348-352.

[25] Sangnier, A.; Matrat, M.; Nicolle, A.; Dujardin, C.; Chizallet, C. *J. Phys. Chem. C* **2018,** *122*, 26974-26986.

[26] Nur, A. S. M.; Funada, E.; Kiritoshi, S.; Matsumoto, A.; Kakei, R.; Hinokuma, S.; Yoshida,

H.; Machida, M. *J. Phys. Chem. C* **2018,** *122*, 662-669.

[27] White, D.; Baird, T.; Fryer, J. R.; Freeman, L. A.; Smith, D. J.; Day, M. *J. Catal.* **1983,** *81*, 119-130.

[28] Harris, P. J. F.; Boyes, E. D.; Cairns, J. A. *J. Catal.* **1983,** *82*, 127-146.

[29] Harris, P. J. F. *J. Catal.* **1986,** *97*, 527-542.

[30] Benavidez, A. D.; Kovarik, L.; Genc, A.; Agrawal, N.; Larsson, E. M.; Hansen, T. W.; Karim, A. M.; Datye, A. K. *ACS Catal.* **2012,** *2*, 2349-2356.

[31] Hansen, T. W.; DeLaRiva, A. T.; Challa, S. R.; Datye, A. K. *Acc. Chem. Res.* **2013,** *46*, 1720-1730.

[32] Mager-Maury, C.; Chizallet, C.; Sautet, P.; Raybaud, P. *ACS Catal.* **2012,** *2*, 1346-1357.

[33] Paulis, M. a.; Peyrard, H.; Montes, M. *J. Catal.* **2001,** *199*, 30-40.

[34] Sinkler, W.; Sanchez, S. I.; Bradley, S. A.; Wen, J.; Mishra, B.; Kelly, S. D.; Bare, S. R. *ChemCatChem* **2015,** *7*, 3779-3787.

[35] Bradley, S.; Sinkler, W.; Blom, D.; Bigelow, W.; Voyles, P.; Allard, L. *Catal. Lett.* **2012,** *142*, 176-182.

[36] Lieske, H.; Lietz, G.; Spindler, H.; Völter, J. *J. Catal.* **1983,** *81*, 8-16.

[37] Huizinga, T.; Van Grondelle, J.; Prins, R. *Appl. Catal.* **1984,** *10*, 199-213.

[38] McCabe, R. W.; Wong, C.; Woo, H. S. *J. Catal.* **1988,** *114*, 354-367.

[39] Hwang, C.-P.; Yeh, C.-T. *J. Mol. Catal. A* **1996,** *112*, 295-302.

[40] Veligzhanin, A. A.; Zubavichus, Y. V.; Chernyshov, A. A.; Trigub, A. L.; Khlebnikov, A. S.; Nizovskii, A. I.; Khudorozhkov, A. K.; Beck, I. É.; Bukhtiyarov, V. I. *J. Struct. Chem.* **2010,** *51*, 20-27.

[41] Digne, M.; Sautet, P.; Raybaud, P.; Euzen, P.; Toulhoat, H. *J. Catal.* **2002,** *211*, 1-5.

[42] Lee, J.; Jang, E. J.; Jeong, H. Y.; Kwak, J. H. *Appl. Catal., B* **2018,** *556*, 121-128.

[43] O'Brien, C. P.; Jenness, G. R.; Dong, H.; Vlachos, D. G.; Lee, I. C. *J. Catal.* **2016,** *337*, 122-132.

[44] Muller, O.; Roy, R. *J. Less Common Met.* **1968,** *16*, 129-146.

[45] Seriani, N.; Pompe, W.; Ciacchi, L. C. *J. Phys. Chem. B* **2006,** *110*, 14860-14869.

[46] Lee, J.; Jang, E. J.; Kwak, J. H. *Appl. Catal., A* **2019,** *569*, 8-19.

[47] Yazawa, Y.; Takagi, N.; Yoshida, H.; Komai, S.-i.; Satsuma, A.; Tanaka, T.; Yoshida, S.; Hattori, T. *Appl. Catal., A* **2002,** *233*, 103-112.

[48] Mansour, A. N.; Cook, J. W.; Sayers, D. E.; Emrich, R. J.; Katzer, J. R. *J. Catal.* **1984,** *89*, 462-469.

[49] Primet, M.; Basset, J. M.; Mathieu, M. V.; Prettre, M. *J. Catal.* **1973,** *29*, 213-223.

[50] Avanesian, T.; Dai, S.; Kale, M. J.; Graham, G. W.; Pan, X.; Christopher, P. *J. Am. Chem. Soc.* **2017,** *139*, 4551-4558.

[51] Ono, L. K.; Croy, J. R.; Heinrich, H.; Roldan Cuenya, B. *J. Phys. Chem. C* **2011,** *115*, 16856-16866.

[52] Kang, S. B.; Lim, J. B.; Jo, D.; Nam, I.-S.; Cho, B. K.; Hong, S. B.; Kim, C. H.; Oh, S. H. *Chem. Eng. J.* **2017,** *316*, 631-644.

Acknowledgement

First of all, I would like to appreciate all the guidance from my advisor Prof. Ja Hun Kwak during my Ph.D. degree. It was a great opportunity for me to learn his rare experiences from school, company, and research institutes, helping me to have a balanced view on research, not just biased view in one side. Furthermore, he always says “bloom after your graduation, not during the doctoral degree.” I would like to thank for his effort to give me guidance in terms of long-term growth as independent research rather than short-term performance. Finally, the posture and philosophy of the research that I have heard during lots of talk with him will be a good example for my future research life.

I want to give my gratitude to my parents for continuing encouragement and cheering while their concern about my decision to research life. The calm and sincere attitude of my parents that I have seen so far has become a good example of the necessary attitude in the research which should be carried out for a long time with great patience. Also, I would like to express my great gratitude to my wife, Eun Jeong Jang, who is also my lab colleague who encouraged me to continue to study until now, while giving me uncountable encouragement and support for me during my Ph.D. degree. In addition to experimental help such as important data and discussions for my paper, while collaborating as a researcher, she constantly cheers up and refreshed me when I was in slump due to repeated failures during research. Furthermore, I also appreciate my wife’s parents for offering words of encouragements and rooting for me.

I would like to thank my lab colleagues Dong Gun Oh and Yongseon Kim, including my wife Eun Jeong Jang, who help many things while working together as our lab initial members. During many experiments, we met various unexpected situations and shared those experiences, which was a great help for me. Next, I want to give thanks to Prof. Hu Young Jeong for giving a guidance for me to use TEM, which was really useful for my research, at a more professional level and to interpret the TEM data. I would also like to express my gratitude to my thesis committee members: Prof. Sang Hoon Joo, Prof. Kwangjin An, Prof. Hu Young Jeong, and Prof. Ji-Wook Jang. Thanks to their insightful comments on my research, I could have more ideas and inspiration about the direction of my research and how to deliver my results. The comments on my paper from Dr. János Szanyi (PNNL) were also very helpful. Although I can’t write to everyone here, I would like to thank everyone who give me much encouragement and help.

Finally, I would give applause for myself having done my research for a Ph.D. degree. I want to finish this part with my wish for my career as an independent researcher, giving another inspiration to others.

Curriculum Vitae

Jaekyoung Lee

Personal Information

Molecular Catalysis Lab
School of Chemical Engineering
Ulsan National Institute of Science and Technology (UNIST)
50 UNIST-gil, Ulsan 44919, Republic of Korea
E-mail: jaekyoung@unist.ac.kr
Cellphone: +82-10-4372-4601

Education

2014-2019	**Combined M.S.-Ph.D.** in Chemical Engineering (UNIST) Thesis: Surface properties of Al_2O_3 for understanding metal-support interaction and catalytic properties of Al_2O_3-based catalysts Advisor: Prof. Ja Hun Kwak
2010-2014	**B.S.** Degree in Chemical Engineering (UNIST) GPA Overall: 4.23/4.3 (Rank: 1/88)

Research Interests

- Understanding metal support interaction in atomic scale.
- The role of metal support interaction on its catalytic behavior of supported catalysts.
- Catalyst characterization based on TEM analysis

Publications

1. Eun Jeong Jang, **Jaekyoung Lee**, Hu Young Jeong, and Ja Hun Kwak*
   "Controlling the Acid-Base Properties of Alumina for Stable PtSn-based Propane Dehydrogenation Catalysts"
   Appl. Catal., A **2019**, *572*, 1-8.
2. **Jaekyoung Lee**, Eun Jeong Jang, Hu Young Jeong, and Ja Hun Kwak*
   "Effect of number and properties of specific sites on alumina surfaces for Pt-Al_2O_3 catalysts"
   Appl. Catal., A **2019**, *569*, 8-19.
3. Euiseob Yang‡, Eun Jeong Jang‡, Jun Gyeong Lee, Sinmyung Yoon, **Jaekyoung Lee**, Nathan Musselwhite, Garbor A. Somorjai, Ja Hun Kwak*, and Kwangjin An* (‡ equal contribution)
   "Acidic effect of porous alumina as supports for Pt nanoparticle catalysts in *n*-hexane reforming"

Catal. Sci. Technol. **2018**, *8*, 3295-3303.

4. **Jaekyoung Lee**, Eun Jeong Jang, Hu Young Jeong, and Ja Hun Kwak*
   “Critical role of (100) facets on for ethanol dehydration: Combined efforts of morphology-controlled synthesis and TEM study”
   Appl. Catal., A **2018**, *556*, 121-128.
5. **Jaekyoung Lee**, János Szanyi, and Ja Hun Kwak*
   “Ethanol dehydration on $\gamma\text{-Al}_2\text{O}_3$: Effects of partial pressure and temperature”
   Mol. Catal. **2017,** *434*, 39-48.
6. **Jaekyoung Lee**, Eun Jeong Jang, and Ja Hun Kwak*
   “Acid-base properties of Al_2O_3: Effects of morphology, crystalline phase, and additives”
   J. Catal. **2017,** *345*, 135-148.
7. Ja Hun Kwak*, **Jaekyoung Lee**, János Szanyi, Peden, and Charles H.F. Peden
   “Modification of the acid/base properties of $\gamma\text{-Al}_2\text{O}_3$ by oxide additives: An ethanol TPD investigation”
   Catal. Today **2016,** *265*, 240-244.
8. Libor Kovarik*, Mark Bowden, Dachuan Shi, Nancy M. Washton, Amity Andersen, Jian Zhi Hu, **Jaekyoung Lee**, János Szanyi, Ja Hun Kwak, and Charles H.F. Peden
   “Unraveling the Origin of Structural Disorder in High Temperature Transition Al_2O_3: Structure of $\theta\text{-Al}_2\text{O}_3$”
   Chem. Mater. **2015,** *27*, 7042-7049.
9. **Jaekyoung Lee**, Himchan Jeon, Dong Gun Oh, János Szanyi, and Ja Hun Kwak*
   “Morphology-dependent phase transformation of $\gamma\text{-Al}_2\text{O}_3$”
   Appl. Catal., A **2015,** *500*, 58-68.